Title
Hyperbolic Metamaterials for Super-Resolution Imaging and Deep Sub-Wavelength Cavities

Author
Rho, Junsuk

Publication Date
2013

Peer reviewed|Thesis/dissertation

Hyperbolic Metamaterials for Super-Resolution Imaging and Deep Sub-Wavelength Cavities

by

Jun Suk Rho

A dissertation submitted in partial satisfaction of the

requirements for the degree of

Doctor of Philosophy

in

Engineering - Mechanical Engineering

and the Designated Emphasis

in

Nanoscale Science and Engineering

in the

Graduate Division

of the

University of California, Berkeley

Committee in charge:

Professor Xiang Zhang, Chair

Professor Costas Grigoropoulos

Professor Constance Chang-Hasnain

Spring 2013

Hyperbolic Metamaterials for Super-Resolution Imaging and Deep Sub-Wavelength Cavities

by
Jun Suk Rho

Abstract

Hyperbolic Metamaterials for Super-Resolution Imaging and Deep Sub-Wavelength Cavities

by

Jun Suk Rho

Doctor of Philosophy in Engineering - Mechanical Engineering

and the Designated Emphasis in Nanoscale Science and Engineering

University of California, Berkeley

Professor Xiang Zhang, Chair

Metamaterials, artificially structured nanomaterials, have enabled unprecedented and extraordinary phenomena such as invisibility cloaking due to their unique optical properties which do not exist in naturally available materials or traditional composites materials.

Especially, hyperbolic metamaterials, also known as indefinite metamaterials, have a unique dispersion relation where the principal components of the permittivity tensors do not all have the same signs and magnitudes. Such an extraordinary dispersion relation results in hyperbolic dispersion relations which leads to a number of interesting phenomena, such as the super-resolution effect, in which evanescent waves are transferred to propagating waves at the interface with normal materials. This results in the propagation of electromagnetic waves with very large wavevectors which would otherwise be evanescent waves and thus decay quickly in natural materials.

Thanks to the development of nanofabrication techniques, I have successfully realized such hyperbolic metamaterials into experimental devices. The first hyperbolic metamaterals device is a super-resolution imaging device called the “hyperlens”, which is the first experimental demonstration of near- to far-field imaging using visible light with resolution beyond the diffraction limit in two lateral dimensions. This allows real-time sub-diffractional imaging without any support of image reconstruction and localization. Thus, it would offer a platform to perform very easy and strong biomolecular imaging.

The other unique application of hyperbolic metamaterials is metamaterial optical nanocavities, a key component to scale lasers down to the nanoscale. Unlike traditional dielectric cavities, which resonate at higher frequencies when the cavity size reduces, indefinite cavities with sizes different by several orders may resonate at the same frequency and same mode order.

Furthermore, the size dependence of quality factor due to the radiation loss also shows a reversed behavior compared to traditional dielectric cavities. Large wavevectors supported by hyperbolic metamaterials successfully captured light in 20nm dimension and show a very high figure of merit due to their extremely small mode volume. Such a theoretical and experimental demonstration could have strong potential to achieve a truly nanometer scale low threshold laser whose size is compatible to biomolecules. In addition, the tunable refractive index characteristic of nanocavities is promising for high refractive index surface coatings and cloaking metasurfaces.

I have also studied several interesting metamaterials applications based on various schemes such as negative index, metasurface and plasmonic lens. First of all, I demonstrate a photo-induced chiral switching of reconfigurable negative index metamaterial device as a new class of custom-designed composite with deep sub-wavelength building blocks in response to external optical stimuli. This metamaterial device allows electromagnetic control of the polarization of light and will find important applications in manipulation of terahertz waves, such as dynamically tunable terahertz circular polarizers and polarization modulators for terahertz radiations. Also, with a large scale negative index metasurface, I am able to observe a very strong photonic spin-hall effect, which could provide a route for exploiting the spin and orbit angular momentum of light for information processing and communication. Last, plasmonic nanolithography is studied as a new low-cost high-throughput approach to maskless nanolithography, providing both 22-nm high-resolution direct patterning and 10m/s high-throughput writing speed at the same time.

All topics covered needed very serious effort in nanofabrication technique development. For this reason, I include state-of-the-art nanofabrication techniques and tips which are used to demonstrate such metamaterials and metadevices shown in this dissertation. Utilizing very special top-down and bottom-up processes such as electron beam lithography overlay, super high resolution lift-off process, quantum dot lithography, metamaterial and plasmonic devices that need very high resolution and high-accuracy are demonstrated successfully.

I believe my efforts in developing different types of sub-wavelength metamaterials including hyperbolic metamaterials for extraordinary optical properties and demonstrating the devices experimentally will advance future nanoscale optics and photonics, materials science and broad nanoscience and nanotechnology.

To My Family

Table of Contents

List of Figures

List of Tables

Acknowledgement

I would like to express my sincerest appreciation to my research adviser, Professor Xiang Zhang, for his thorough guidance, critical advice, generous support, deep consideration and warm encouragement through my doctoral study. Without his strong support, I could not achieve my degree. He is not only my academic adviser, but also my mentor and roll model for my future career. I owe tremendous debt to him for my entire life.

I also thank my former and current lab managers, Dr. Guy Bartal, Dr. Xiaobo Yin and Dr. Yuan Wang, who have done very important role in guiding my research path and supporting me in the past five years.

I would like to thank all my former and current teammates, Xiaodong Yang, Yongshik Park, Liang Pan, Shuang Zhang, Yongmin Liu, Zhaowei Liu, Jie Yao, Kevin O'Brien, Yi Xiong, Ania Labno, Ziliang Ye, Haim Suchowski, Alessandro Salandrino, Stefano Palomba, Daniel Kimura and Hyeunsok Choi for all the collaborations, discussions, support and friendship. It has been my great pleasure to work together with them.

I want to extend my thanks to my former and current colleagues in Xlab, Zijing Wong, Chris Gladden, Renmin Ma, Ming Liu, Volker Sorger, Ong Pholchai, Thomas Zentgraf, Jason Valentine, Jeongmin Kim, Shaomin Xiong, Sheng Shen, Majid Gharghi, Peng Zhang, Sunghyun Nam, Seunghoon Han, Bumki Min, David Barth, Nga Thien Bui, and all the other colleagues for their advice, support, and friendship.

I appreciate to my dissertation committee members, Professor Costas Grigoropoulos and Professor Constance Chang-Hasnain, my qualifying exam committee members, Professor Samuel Mao and Prof. David Attwood, and finally my personal mentor and general scientific adviser, Prof. Luke Lee for their thorough guidance and critical advice for my research and future career.

In addition, I appreciate Samsung Scholarship Foundation for the significant financial support during my Ph.D. study.

Finally, I am deeply indebted to my wife Jungyoun Lee and my entire family for their love and support. Any of my successes is impossible without their great love and encouragement.

Curriculum Vitae

Feb 8, 1981	Born in Seoul, Korea
1996 – 1999	Major: English (Minors: French and Chinese) Myungduk Foreign Language High School
1999 – 2007	Bachelor of Science Mechanical and Aerospace Engineering Seoul National University
2007 – 2008	Master of Science Mechanical Science and Engineering University of Illinois, Urbana-Champaign
2008 – 2013	Doctor of Philosophy Mechanical Engineering (Minors: Electrical Engineering and Bioengineering) with designated emphasis in Nanoscale Science and Engineering University of California, Berkeley

Publications

Junsuk Rho, Ziliang Ye, Yi Xiong, Xiaobo Yin, Zhaowei Liu, Hyeunseok Choi, Guy Bartal, and Xiang Zhang, "Spherical hyperlens for two-dimensional sub-diffractional imaging at visible frequencies", *Nature Communications* **1**, 143, 2010

Junsuk Rho*, Xiaodong Yang*, Jie Yao*, Xiaobo Yin and Xiang Zhang, "Experimental realization of 3D indefinite cavities at nanoscale with anomalous scaling law", *Nature Photonics* **6**, 450-454, 2012

Liang Pan*, Yongshik Park*, Yi Xiong*, Erick Ulin-Avila, Yuan Wang, Li Zeng, Shaomin Xiong, Junsuk Rho, Cheng Sun, David B. Bogy, Xiang Zhang, "Maskless plasmonic lithography at 22nm resolution", *Scientific Reports* **1**, 175, 2011

Shuang Zhang*, Jiangfeng Zhou*, Yong-Shik Park*, Junsuk Rho, Hou-Tong Chen, Sunghyun Nam, Ranjan Singh, Abul Azad, Xiaobo Yin, Antoinette J. Taylor and Xiang Zhang, "Photo-induced handedness switching in terahertz chiral meta-molecules", *Nature Communications* **3**, 942, 2012

Xiaobo Yin, Ziliang Ye, Junsuk Rho, Yuan Wang and Xiang Zhang, "Anomalous photonic spin hall effect at metasurface", *Science*, **339**, 1405-1407, 2013

Chapter 1

Introduction

1.1 Introduction to metamaterials

Throughout history, human society has developed along with the accompanying development of new materials [1]. The discovery of stone, bronze and iron each accordingly resulted in great advances in civilization. In the past several decades, the world has developed science and technology greatly through the discovery and synthesis of a number of new materials. One of the categories is optical and photonic materials, which enhance the semiconductor industries and optics industries, boosting the quality of life to humanity. Such materials are very important because they are used to manipulate light, an electromagnetic wave. Good examples include, but not limited to, silicon and silicon oxide. Dielectric materials such as glass, quartz, and sapphire are commonly used in many optical and photonic devices.

The first introduction of a metamaterial showed both negative permittivity and permeability simultaneously, proposed by a Russian physicist Veselago in the 1960's, which had never existed before in nature [2]. Figure 1.1 describes how materials are defined by the sign of their electric permittivity (ε) and magnetic permeability (μ). These properties determine one of the most important optical properties, the index of refraction (n). Most isotropic dielectric materials have both positive permittivity and permeability, and thus allow light to propagate in the medium with positive refractive index. In the case that permittivity and permeability have opposite signs, the refractive index is negative, and thus light becomes an evanescent wave and therefore cannot propagage. The above cases are already shown in natural materials. A material with both negative permittivity and permeability does not exist in the nature, but could exist in artificially made structures. In this case, light can propagate in the material with negative refractive index. This can be explained by Maxwell's equations. A plane waves propagating inside such a material could be described by an electric field intensity vector **E**, magnetic field vector **H**, and wavevector **k**, forming a left-handed triplet, in seeming opposition to wave propagation in conventional media, in which these three quantities form a right-handed triplet. These materials are labeled left-handed media (LHM) and right-handed media (RHM), respectively.

Each case is shown in Figure 1.2. In RHM, the wavevector **k** is in the same direction of the Poynting vector. On the other hand, in LHM, although **E**, **H**, and **k** form a left-handed triplet, **E**, **H**, and **S** maintain a right-handed relationship. Therefore, the wavevector is heading in the reverse direction of the Poynting vector. This results in a backward propagating wave [3]. In such media, the supported backwards waves can be explained by a negative refractive index, which is defined by taking the negative branch of the square root from the definition of the refractive index, $n^2 = \varepsilon\mu$. Consequently, when such media are interfaced with conventional dielectrics, the negative refraction of an incident electromagnetic plane wave is leaded and the Snell's law is reversed. Such a negative index material breaking the law of the nature was the first *metamaterial*, where the prefix '*meta'* means 'beyond' or 'after' in Greek [4].

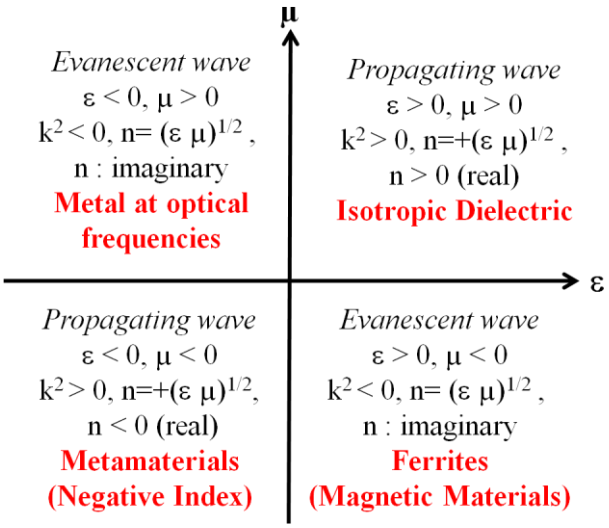

Figure 1.1. Definition of materials with regard to permittivity (ε) and permeability (μ)

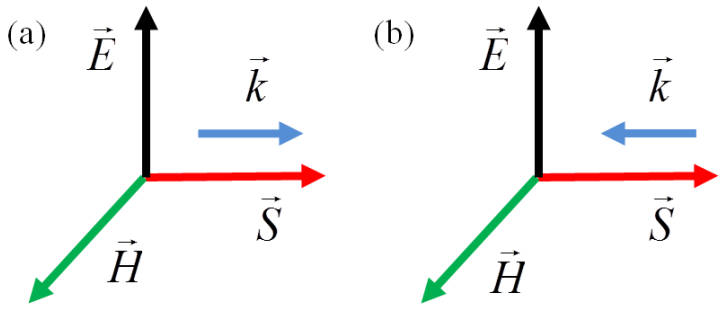

Figure 1.2. Orientation of electric field vector **E**, magnetic field vector **H**, Poynting vector **S**, and wavevector **k** in (a) right-handed media (RHM) and (b) left-handed media (LHM)

Since the first concept of metamaterials was introduced, the term of metamaterials was expanded to many other cases that show extraordinary properties such as ultra-high refractive index, zero index, negative refraction, invisibility cloaking, and super-resolution shown in Figure 1.3. [2, 4, 5, 6, 7, 8, 9, 10] None of these properties exist in natural materials, but can happen in artificially made nanostructures, forming the expanded concept of metamaterials. As shown in Figure 1.4., metamaterials are based on artificial nanoscale atoms, called meta-atoms, much smaller than given wavelengths. The properties of metamaterials rely on their structural arrangements. The positions, stacking order, and combinations of atoms determine the bulk properties of such materials. This is totally different the way we classically distinguish materials depending on the chemical components and chemical bonding. As mentioned above, to meet the criteria classified as metamaterials, the artifical nanomaterials should have unprecedented and extraordinary properties.

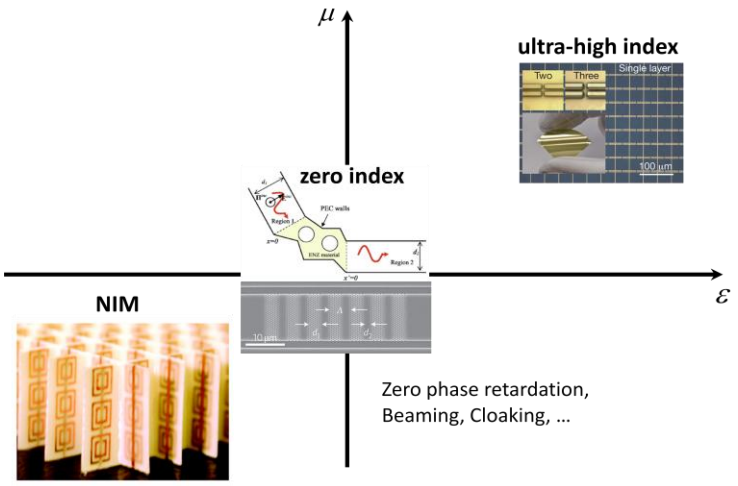

Figure 1.3. Examples of expanded metamaterials

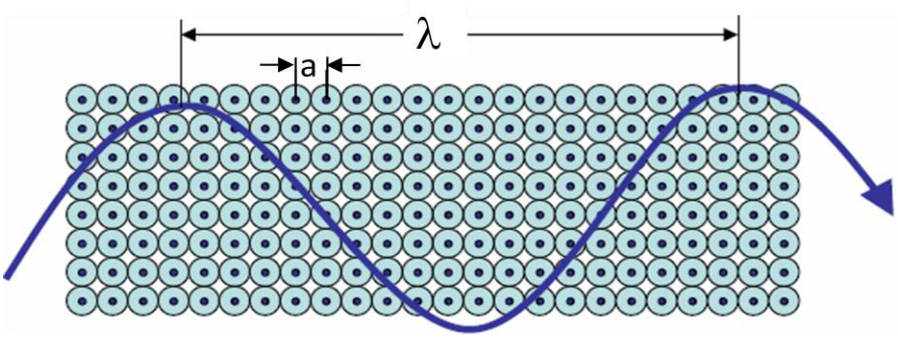

Figure 1.4. Composition of metamaterials based on atoms much smaller than a given wavelength.

1.2 Overcoming diffraction limit with metamaterials

The diffraction limit is the fundamental limitation in optics and photonics restricting the performance of the given systems. For example, as shown in Figure 1.5, when two objects are located further apart than the distance limit Δx, the objects are easily resolved, which means the imaging systems can distinguish the objects as two distinct airy disc peaks of intensity distribution. On the other hand, when the distance between the same two objects gets closer to the distance Δx, the objects become difficult to distinguish. Finally, once they are within Δx, they are not resolved anymore and are seen asshowing one airy disc peak. Here, Δx is called the diffraction limit. The diffraction limit is caused by the electromagnetic characteristics of light. Light consists of two components; one is the propagating wave and the other is the evanescent wave. From the equation (1.1) of electric field distribution, the wavevector k_z is derived according to the equation (1.2).

$$E(x,y,z) = E_0 e^{ik_x x} e^{ik_y y} e^{ik_z z} \tag{1.1}$$

$$k_z = \sqrt{\left(n\frac{\omega}{c}\right)^2 - (k_x^2 + k_y^2)} \tag{1.2}$$

Here, in the case of $(k_x^2 + k_y^2) < (n\omega/c)^2$, k_z becomes real number and this wave constructs a propagating wave in the z-direction. In the case of $(k_x^2 + k_y^2) > (n\omega/c)^2$, k_z becomes imaginary and thus this wave becomes an evanescent wave in which the amplitude of the wave exponentially decays in the z-direction. Figure 1.6 describes a schematic of the object and image plane, and a propagating and evanescent wave. The propagating wave (red colored line) carries larger feature information from the object plane (near-field) to the image plane (far-field). Information from large features is transferred to the far-field without any issue. However, because the evanescent wave (green color line) brings small size feature information to the image plane, this information is not transferred to the far-field due to their evanescent loss in the near-field. That is also known as the near-field effect of the evanescent wave. This is the main reason why the diffraction limit happens in an imaging system.

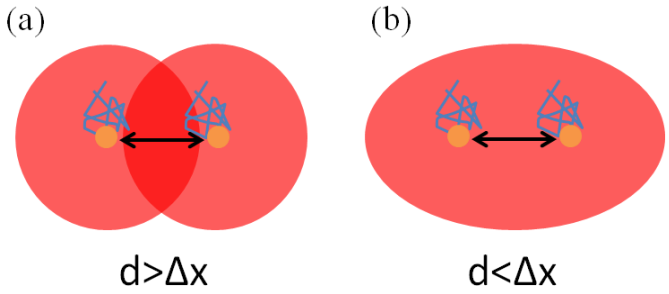

Figure 1.5. Schematic of diffraction limit: (a) when two objects are over diffraction limit, two objects are resolved as two objects to show two peak intensities. (b) when two objects are below diffraction limit, two objects are not resolved as two objects, thus show only one peak intensity.

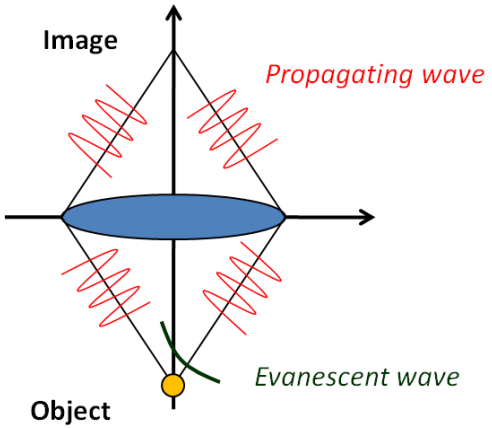

Figure 1.6. Schematic of an imaging system: when the light travels from object plane to image plane, propagating wave carrying big features information are going to the far-field, but evanescent wave carrying small features information exponentially vanish in the near-field.

I also note the Fourier transform process that large features in the spatial domain corresponds to small wavevectors in the k-domain and small features in the spatial domain to large wavevectors in the k-domain. This relation is expressed in Figure 1.7 with the examples of two different sizes of circular slot and intensity profile of the light.

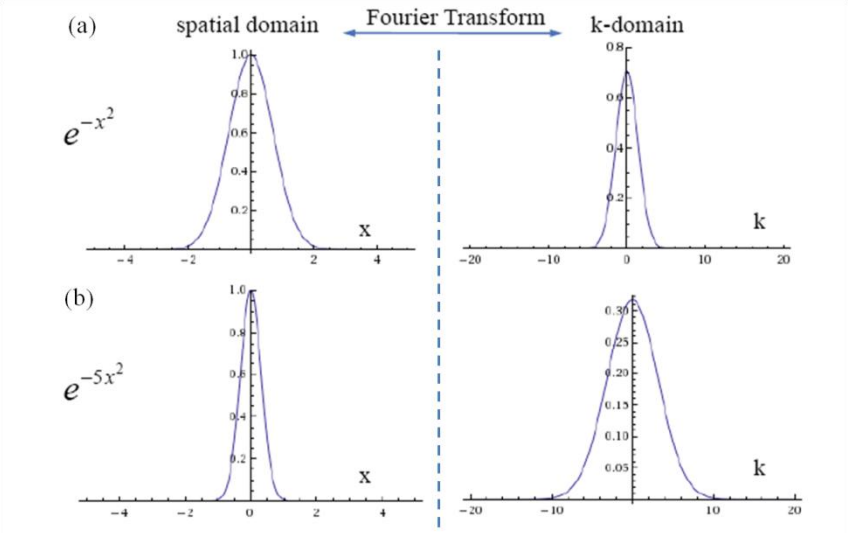

Figure 1.7. Spatial domain and k-domain with Fourier transform: (a) large circular slit in spatial domain has smaller k of 1 in k-domain expressed $\exp(-x^2)$ (b) small circular slit in spatial domain has larger k of 5 in k-domain expressed $\exp(-5x^2)$

In the normal case, the diffraction limit is defined as below [11, 12], and called Rayleigh criteria of diffraction limit. As we can see in equation (1.3), the diffraction limit is proportional to the wavelength and inversely proportional to the numerical aperture, which is a characteristic of a given imaging system.

$$\Delta x = \frac{1.22\lambda}{2NA} \tag{1.3}$$

This diffraction limit has long been an issue in the optics and photonics field as well as many related engineering fields, because the diffraction limit causes critical issues in many cases. For example, not only the resolution of a microscope but also the resolution of lithography, one of the common micro-/nano-fabrication tool, is also limited by this number. Therefore, scientists and engineers have tried to overcome this limit in many ways. Either decreasing wavelength or increasing numerical aperture helped to improve the diffraction limit, but doing such things were still not significant solutions. Basically, those techniques do not have fundamental access to the evanescent wave due to the materials properties of natural materials. As discussed in the previous section, metamaterials have the unique property of controlling permittivity and permeability on demand. They have shown tremendous scientific and technical advances in controlling the electromagnetic properties of light [13, 14]. The way to control and manipulate the properties of light will be discussed in chapter 2 and chapter 3 in detail.

1.3 Control and manipulation of light with metamaterials

As discussed in the previous chapter, natural materials have very limited ability to control light due to the intrinsically fixed optical properties of the materials. One particular example of this is that natural materials have very weak response to the magnetic component of light, so in most cases of this dissertation, metamaterials assume magnetic permeability (μ) as 1 which are considered as optical metamaterials. The other important thing is that because the size of the atoms and molecules are much smaller than the wavelength of light, the detail of the atomic lattice cannot be seen by the light wave and the whole material is treated as a homogeneous single medium. This principle,called effective medium theory, will be discussed in more detail in chapter 2.

Accordingly, the ratio between the lattice constant and the wavelength of electron wave or electromagnetic wave propagation plays a very important role in determining the material properties for different materials. In the semiconductor structure, the electron wavelength is comparable with the period of the atomic lattice. Therefore energy gap is formed due to Bragg diffraction of electrons and leads to all the semiconductor properties. The same effect also happens for electromagnetic waves, where the period of the hole array in a photonic crystal is close to the wavelength of propagating light inside the dielectric. On the other hand, when the wavelength is much larger than the period of the material, the periodic structure cannot be seen and the wave will behave as if it is propagating in a homogeneous media. For example, for visible light propagating in a natural crystal, such as diamond, the light wave cannot differentiate every single atom in the crystal; therefore, the material exhibits a homogeneous optical response. Metamaterials are designed with the same principle.

Pendry first proposed the idea of artificial materials composed of meticulously designed atoms to achieve extraordinary properties that cannot be reached by naturally available materials [15]. Introducing inductance and capacitance with appropriate orientation and magnitude into the artificial atoms was pointed out, so they can interact with the magnetic component of the electromagnetic waves passing through the composite material, therefore create a material with magnetic response at high frequencies. For such materials, magnetic permeability (μ) is not unity any more. For Pendry's structure, it turned out μ values can be also negative. Such a concept of tuning the magnetic response of materials is first discussed in the gigahertz regime, but later the research has been done in a broad range of wavelengths including terahertz [16, 17].

Indeed, Pendry discussed the possibility decreasing the plasmon frequency of a material by using "diluted metal" and therefore controlling a material's electrical response to light in his paper [18]. Although the concept of a metamaterial had not been brought forward in that paper, the basic principle is the same. With both electrical and magnetic response under control, metamaterials enable free tuning of materials' optical properties. The optical properties can be extended into regions that have never been achieved before, where negative refraction of light can be observed. Furthermore, they can also be tuned independently at different locations inside the same material. This powerful ability greatly enhanced our control of the propagation direction and the phase of light propagating in such materials, and built the foundation for the new research field of transformational optics [19, 20]. Many new applications are possible, including the invisible cloaking, which eliminates the scattering of light from an object and makes the object invisible [21, 22, 23, 24, 25, 26, 27].

1.4 Introduction to Plasmonics

Recently, a new concept in electromagnetism of free electron oscillation, surface plasmons (SPs), has been introduced. They are kind of electromagnetic waves trapped at a metallic surface through their interaction with the free electrons of the metal as schematically illustrated in Figure 1.8. The recent discovery of extraordinary transmission through sub-wavelength hole arrays on an opaque metal film has sparked extensive interest in SPs among the scientific community [28, 29, 30, 31, 32]. The observed far-field transmission through a silver holes array in the infrared and visible region can be enhanced by orders of magnitude compared to that of a single hole. This unusual enhancement is attributed to the excitation of SPs on the metal surface which dramatically enhances the optical throughput via the sub-wavelength aperture. Since then, much research focused on the underlying physics and applications of SPs. The use of SPs opens potential applications in nanoscale optical spectroscopy, [33] surface-enhanced spectroscopy, surface plasmon resonance sensing, [34, 35] and plasmonic nanolithography [36, 37].

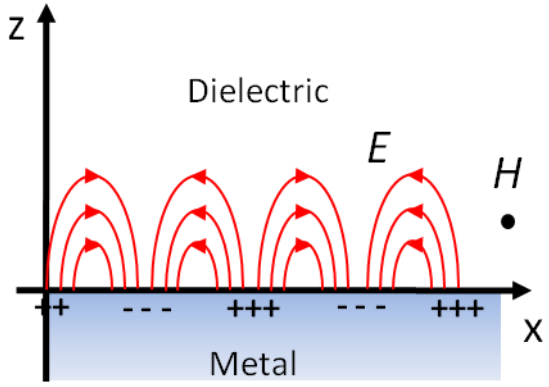

Figure 1.8. Schematic of the charges distribution and the electromagnetic field induced by surface plasmons propagating on a surface in the x direction

The dispersion relation of SPs lies to the right of the light line, indicating the wave vector of SPs is always greater than that of light waves at a given frequency, as shown in Figure 1.9. Because the wave vector in the z direction is imaginary, SPs are nonradiative electromagnetic waves that describe fluctuations of the surface electron density bounded to the metal surface. Therefore, their electromagnetic fields have maximum strength at the surface and decay exponentially into the space perpendicular to the surface. The most interesting property of SPs is their dispersive behaviors, which offer an access to much shorter wavelength of surface waves than the excitation light wavelength. This extraordinary "optical frequency but X-ray wavelength" property of SPs opens up the potential of high-resolution imaging and lithography at a length scale beyond the diffraction limit. One common way to excite SPs by light is using the momentum mismatch between the excitation light to compensate the SPs. As seen in the SP dispersion relation, the momentum of SPs is always larger than that of a free space light. Therefore, a given additional momentum is needed to couple light to SPs. Typically, a grating coupler and an attenuated total reflection coupler, are used to match the momentum mismatch;

therefore, light can be converted into SPs and vice versa. A grating can supply additional wave-vectors (G) which can compensate the momentum mismatch of light and SPs. Figure 1.9 shows the coupling mechanism of a grating coupler. When the wave-vector is matched, the surface plasmon waves can be resonantly excited using light excitation. k_{in} is the incident wave-vector of the light and G is the multiples of 2/a where a is the period of the structure.

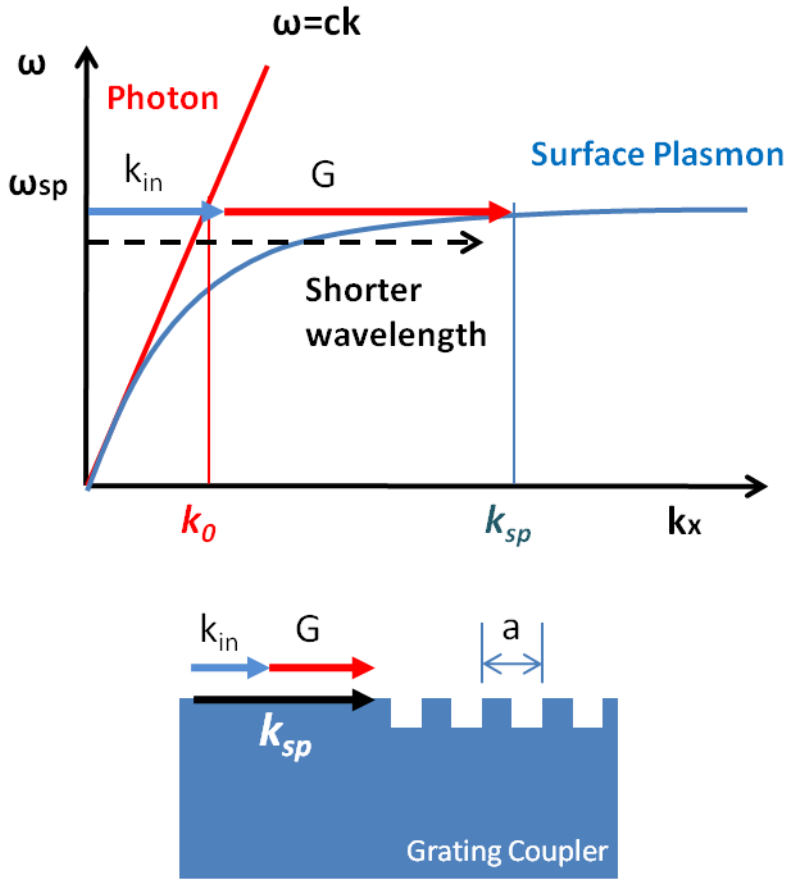

Figure 1.9. The dispersion relation of surface plasmons: The dotted line represents the light line where the SP dispersion curve always lies right of the light line. Normal photons aalways have a linear relationship between wavevector and frequency, but surface plasmons can allow very high wavevector access due to their extraordinary dispersion relation. Bottom figure shows momentum matching through a grating coupler, one of the common ways to excite surface plasmons

1.5 Thesis Organization

This dissertation is for the fundamental physics, design, fabrication and device applications of deep sub-wavelength metamaterials including hyperbolic metamaterials and chiral metamaterials. In addition, it will cover top-down and bottom-up nanofabrication techniques related to the metamaterials and plasmonics research. Finally, manufacturing solutions to scale up current metamaterial and plasmonic devices will be discussed to make metamaterials more useful for engineering applications and end products. This dissertation consists of 8 chapters.

Chapter 1 starts with the introduction and background, which contains the fundamentals such as the definition of metamaterials, dispersion relation, anisotropic media, negative index, negative permittivity, permeability, and refraction.

Chapter 2 describes the unique hyperbolic dispersion relation of anisotropic hyperbolic metamaterial and their fabrication methods to achieve hyperbolic metamaterials.

Chapter 3 focuses on the application of hyperbolic metamaterials, which achieved two dimensional sub-diffraction super-resolution real-time imaging. The design process of achieving hyperbolic metamaterials by thin film multilayer stack, the fabrication of a real device called spherical hyperlens and the experimental demonstration of super-resolution imaging of nanoscale objects are provided.

Chapter 4 presents three dimensional deep sub-wavelength optical nanocavities confining the light in to the truly nanoscale based on the very large wavevectors obtained by the unique hyperbolic dispersion of hyperbolic metamaterials. Both computational and experimental works are presented with design process, materials selection, fabrication and optical experiments.

Chapter 5 discusses chiral metamaterial in the terahertz regime, which can achieve negative refraction without matching negative values of both permittivity and permeability. Also, photo-induced chiral switching, which dynamically control the chirality of metamaterials is discussed in terms of the design, fabrication and experimental results.

Chapter 6 is about several metamaterials applications such as a metasurface to observe very strong spin hall effect and maskless nanolithography overcoming the current lithography limit of resolution and throughput by integrating metamaterials lens and commercial hard drive.

Chapter 7 is dedicated to show the details of the fabrication processes of the devices described in this thesis and the detail of recipes are provided. Also, a variety of top-down and bottom-up nanofabrication techniques used for metamaterials and plasmonics research are shown and discussed for further detail.

Chapter 8 summarizes all the works during my Ph.D. study and discusses the future of metamaterials in terms of advanced nanomanufacturing for more practical devices and manufacturable products.

Chapter 2

Hyperbolic Metamaterials

2.1 Fundamental physics of hyperbolic metamaterials

Hyperbolic metamaterials, also known as indefinite metamaterials are anisotropic materials having hyperbolic dispersion where not all of the principal components of electrical permittivity and magnetic permeability tensors have the same sign. In contrast, all natural materials have both same sign and same magnitude of electrical permittivity and magnetic permeability tensors. In the optical metamaterials case, which I mainly discuss in this dissertation, magnetic permeability is considered as 1. Thus, in all media, two dimensional dispersion relation, relating wavevector **k**, permittivity **ε**, working frequency ω and the light speed in vacuum c, is defined as equation (2.1), and permittivity tensor is defined as (2.2). In detail, k_x and ε_x are wavevector and permittivity components perpendicular to the optical axis, k_z and ε_z are parallel to the optical axis.

$$\frac{k_x^{\,2}}{\varepsilon_z}+\frac{k_z^{\,2}}{\varepsilon_x}=\frac{\omega^2}{c^2} \tag{2.1}$$

$$\varepsilon=\begin{pmatrix}\varepsilon_x & 0 & 0\\ 0 & \varepsilon_y & 0\\ 0 & 0 & \varepsilon_z\end{pmatrix} \tag{2.2}$$

In naturally available normal materials such as air and glass, the permittivity tensor components show all the same sign and same magnitude. An example is shown in equation (2.3), where x, y, z components of permittivity tensor in the principal axes are all positive and all the same number.

$$\varepsilon_{air}=\begin{pmatrix}\varepsilon_{x=y=z}(+) & 0 & 0\\ 0 & \varepsilon_{x=y=z}(+) & 0\\ 0 & 0 & \varepsilon_{x=y=z}(+)\end{pmatrix} \tag{2.3}$$

If I put the permittivity value into the equation (2.1), the iso-frequency contour (IFC) of air is plotted in the shape of circle like in Figure 2.1. In comparison, the dispersion relation of quartz is also plotted in yellow circle. Here, it should be noted that the radius of the circles corresponds to the refractive index of each material, 1 and 1.45. In such isotropic materials, all the wavevectors have same access to the fixed value of the radius, which intrinsically limits the optical performance of the materials. As we discussed in previous chapter, small size objects correspond to a large wavevector. In other words, a large wavevector **k** has more access to the small feature information at the nanoscale for on a given wavelength.

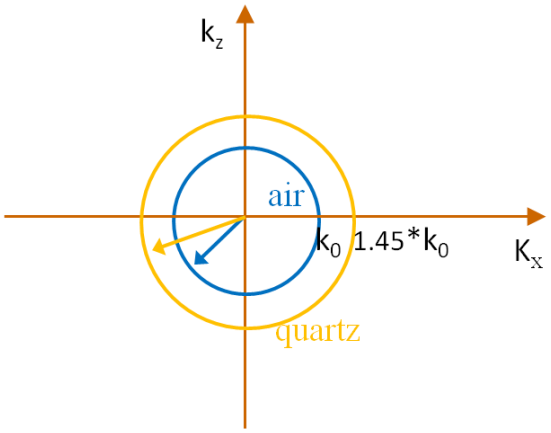

Figure 2.1. The dispersion relation of air and quartz in x-z direction: Air and quartz have an isotropic dispersion relation of circular shape in x-z direction, which can be expanded to a spherical shape in 3D. In each case, the magnitude of the wavevector corresponds to the refractive index of the material. Therefore, they only have access to wavevectors within the circle, where light can propagate, but don't have the access outside of the circle where the light generates evanescent wave.

Although there are materials with larger refractive index, such as silicon and germanium, in nature, the wavevector values are not enough to solve the problems existing in optics and photonics, such as resolution limit and scaling issues. To solve such problems, the larger wavevector can be obtainable, the more flexibility there is to solve these problems. Therefore, the study to engineer permittivity of materials started to achieve an elliptical shape of dispersion, offering access to higher wavevectors in certain directions. That was the first study of changing permittivity to introduce the anisotropy into materials, resulting in artificially made materials called elliptical metamaterials. A dispersion relation of elliptical shape is obtained when permittivity tensors have same sign, but different magnitude along the principal axes. Accordingly, the permittivity tensor is defined as equation (2.4), and the resulting dispersion relation is shown in Figure 2.2. Compared to an isotropic material, air, this metamaterial has anisotropic magnitude of wavevector, specifically a larger wavevector in the x direction in Figure 2.2.

$$\varepsilon_{elliptical} = \begin{pmatrix} \varepsilon_{x=y}(+) & 0 & 0 \\ 0 & \varepsilon_{x=y}(+) & 0 \\ 0 & 0 & \varepsilon_{z}(+) \end{pmatrix} \tag{2.4}$$

Although an elliptical dispersion relation offers significantly extended wavevector access in one direction, there is still a limitation of wavevector access due to the shape of the elliptical IFC. To overcome the limitation, an idea achieving a different shape from the dispersion relation equation (2.1) and (2.2) is shown by Smith and Schurig [38]. They first explored the behavior of wave propagation and various unique effects in indefinite metamaterials. If the permittivity tensor (2.2) has not only a different sign but also different magnitude, the IFC becomes hyperbolic due to the dispersion relation equation (2.1). The permittivity tensor becomes either equation (2.3) or (2.4), which exhibit hyperbolic IFC in either case as shown in Figure 2.3.

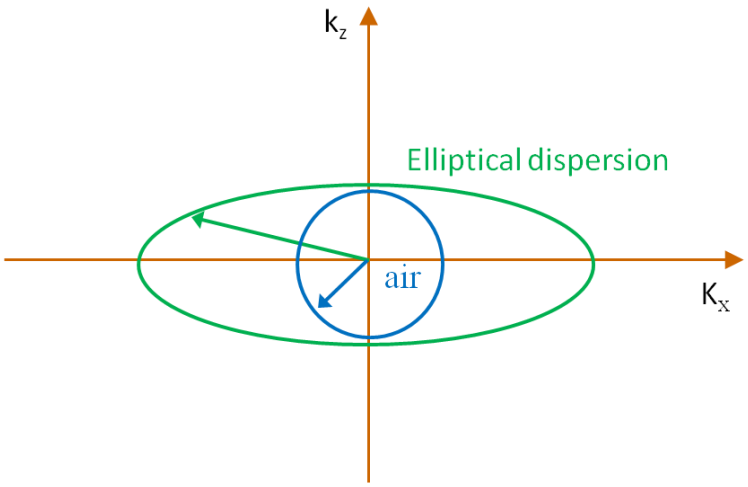

Figure 2.2. Elliptical dispersion relation of anisotropic medium is made by changing the magnitude of permittivity tensor, which allows large wavevector in one specific direction.

$$\varepsilon_{hyperbolic} = \begin{pmatrix} \varepsilon_{x=y}(+) & 0 & 0 \\ 0 & \varepsilon_{x=y}(+) & 0 \\ 0 & 0 & \varepsilon_z(-) \end{pmatrix} \tag{2.3}$$

$$\varepsilon_{hyperbolic} = \begin{pmatrix} \varepsilon_{x=y}(-) & 0 & 0 \\ 0 & \varepsilon_{x=y}(-) & 0 \\ 0 & 0 & \varepsilon_z(+) \end{pmatrix} \tag{2.4}$$

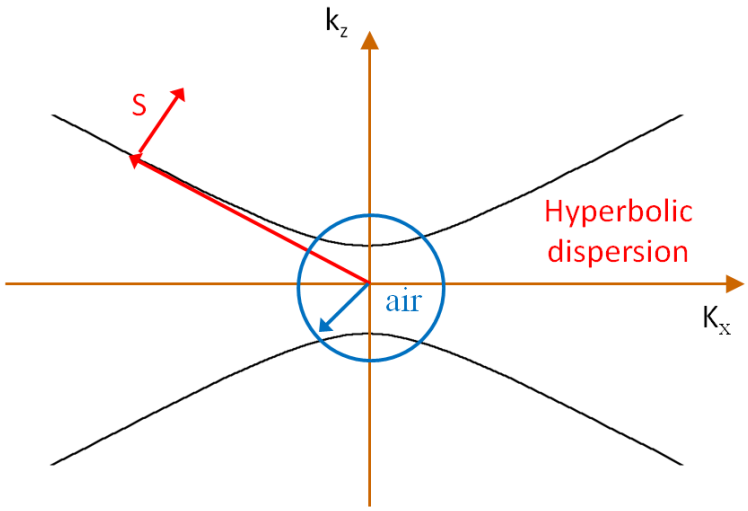

Figure 2.3. Hyperbolic dispersion relation of anisotropic medium is made by changing the sign and magnitude of permittivity tensor, which allow arbitrary unbounded large wavevector in one specific direction. Poynting vector **S** is normal to the wavevector.

Hyperbolic dispersion has unbounded IFC into one direction, x-direction in the case of Figure 2.3, thus it allows arbitrarily large unbounded k_x. This is the most unique property of anisotropic materials having hyperbolic dispersion, subsequently called "hyperbolic metamaterials". For obliquely incident light from free space with a wave vector **k**, the direction of refracted light can be determined from the fact that its group velocity is always normal to the IFC. The tangential wave vector at the interface should be conserved and the causality theorem, that is the energy flows away from the interface, should be satisfied with the Poynting vector **S**, which represents the energy flow direction. Depending on the flatness of the hyperbolic shape, it could show either negative refraction or positive refraction. The latter case is more useful for sub-diffraction imaging, which will be discussed in chapter 3. In former case, when the hyperbolic shape is not flat, the Poynting vector deviates from the wavevector and undergoes negative refraction, although the refraction for the wave vector is still positive.

2.2 Design and fabrication of hyperbolic metamaterials

2.2.1 Nanowire arrayed hyperbolic metamaterials

There are two common methods to realize hyperbolic metamaterials. One is using arrays of parallel metallic nanowires such as silver and gold embedded in a dielectric matrix as shown in Figure 2.4. As long as the period of the nanowire array is much smaller than the working wavelength, one of the critical requirements for building metamaterials, the structure can be characterized as a homogeneous uniaxial anisotropic medium with a permittivity component parallel to the wires (ε_z) and another component perpendicular to the wires (ε_x) [39, 40, 41]. This is an important assumption for hyperbolic metamaterials called the effective medium approximation or effective medium theory [42, 43]. Based on this theory, the new bulk optical property of the hyperbolic metamaterial is defined as equation (2.5), where p is the filling ratio of metal and dielectric, ε_m and ε_d are the permittivity of the metal and dielectric, respectively.

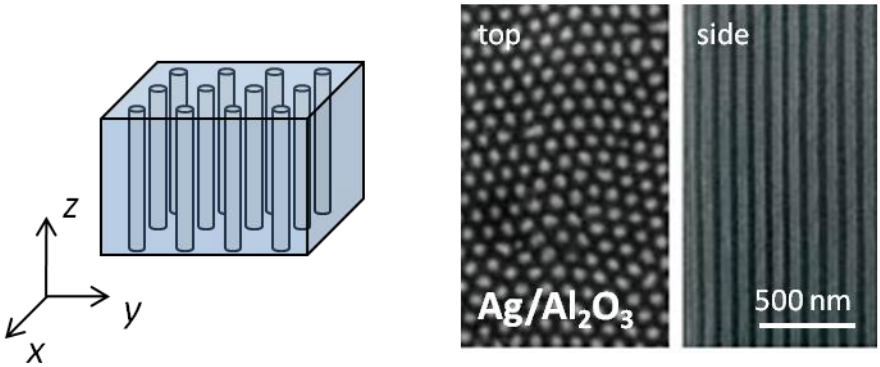

Figure 2.4. An example of hyperbolic metamaterials made by metal nanowire array in dielectric template of Silver and Aluminum Oxide [39]

$$\varepsilon_p(\varepsilon_x = \varepsilon_y) = p\varepsilon_m + (1-p)\varepsilon_d$$
$$\varepsilon_v(\varepsilon_z) = \frac{\varepsilon_m \varepsilon_d}{(1-p)\varepsilon_m + p\varepsilon_d} \quad (2.5)$$

Based on the effective media approximation above, ε_p is negative while ε_v keeps positive over a broad wavelength range from visible to near-infrared when we use a silver and aluminum oxide multilayer stack with filling ratio 0.5. The IFC of light inside such material is therefore hyperbolic and fulfills the requirement for achieving negative refraction. The real parts of ε_p and ε_v as functions of wavelength of EM waves in vacuum are calculated from the equation (2.5). The permittivity of aluminum oxide is ε=2.4 [44, 45] and the permittivity of silver was obtained from literature [46]. Applying the parameters into the equation (2.5), there are broad bands from visible to infrared over which $p\varepsilon$ and $v\varepsilon$ have different signs and therefore a hyperbolic IFC can be realized. This analytical information can be also validated by numerical simulation using a commercial software, COMSOL Multiphysics (a.k.a FEMLAB). Full-wave simulations considering the typical nanowire dimensions and real material permittivies for Al_2O_3 (ε_{Al2O3} = 2.4 [44, 45]) and Ag (ε_{Ag} = -21.6+0.8i [46]) at a visible wavelength of 660nm. The shapes of IFCs obtained from the analytical solution and numerical solution are not perfectly identical, but deviate in high-k region because the analytical solution is based on approximation. This issue of when the effective medium approximation is valid will be discussed further in chapter 4.

2.2.2 Multilayer stacked hyperbolic metamaterials

The nanowire array method discussed in previous section provides a way to demonstrate negative refraction thanks to its unique hyperbolic dispersion. The deeply curved IFC of hyperbolic dispersion allows deviation of the Poynting vector to the negative direction, which is a very interesting observation allowing many potentially useful applications. However fabrication difficulty and limitations prevent more practical applications. Therefore, the other method of stacking a metal-dielectric multilayer shows potential to construct hyperbolic metamaterials in a more practical manner [17, 47, 48]. The principle is the same as in the nanowire array and follows the same effective medium approach described in equation (2.5).

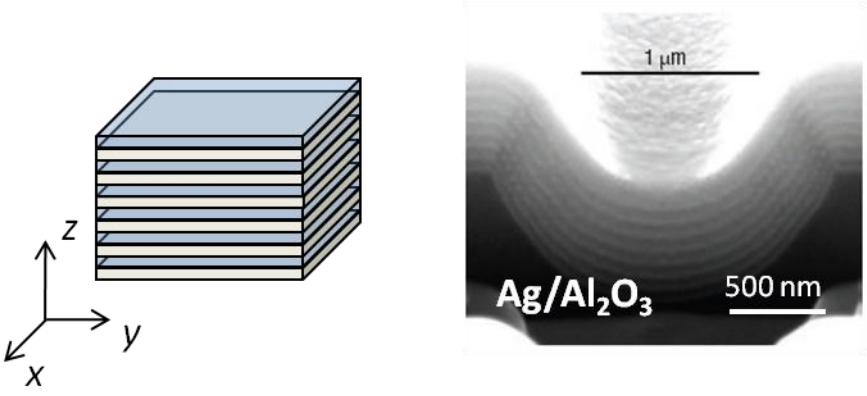

Figure 2.5. An example of hyperbolic metamaterials made by metal-dielectric multilayer of Silver and Aluminum Oxide [14]

The materials selection has a lot of flexibility depending on the working wavelength. The silver and Aluminum Oxide combination works mainly for ultra-violet wavelengths. A case suitable for visible frequency range will be discussed in chapter 4 and one for near-IR will be discussed in chapter 5. Also, another possibility using new semiconductor materials such as zinc oxide and indium tin oxide will be introduced later [49]. In terms of fabrication effort, the multilayer method is far superior to the nanowire array method as long as the quality of the multilayer is smooth and thin enough. Because effective medium theory is valid only if each component, in this case the thin film layers, is much thinner than a given frequency, the thickness control of each layer is very important. However, due to current nanofabrication limit, if the metal and dielectric film is grown too thin, they do not act as bulk materials. Therefore, controlling those two parameters is very important to ensure the validity of the multilayer method for hyperbolic metamaterials. Details will be discussed in next two chapters.

2.3 Conclusion

This chapter explained the theoretical background of hyperbolic metamaterials, which covers the principle of hyperbolic dispersion, including the physics, design and fabrication methods. Based on the effective medium approximation, the electric permittivity tensor of the metamaterials composed of a metal nanowire array embedded in dielectric template and a metal-dielectric multilayer stack can have both different sign and magnitude of permittivity components over a broad frequency range. Due to the hyperbolic dispersion relation for the hyperbolic metamaterials, very large wavevector access is possible and this unique property will be essential to overcome diffraction limit in many applications, which will be covered in the next two chapters. Depending on the material selection of metal and dielectric, filling ratio of the materials, totally different new materials are built in the concept of metamaterials. Consequently, a great advantage of such metamaterials is that we can engineer the optical properties of materials on demand, so that we can control the light beyond diffraction limit more actively. Recently, a new concept of a metasurface including hyperbolic metasurface, enhancing some limit of metamaterials is also introduced in several works in the literature [50] and will be discussed in a later chapter.

Chapter 3

Hyperbolic metamaterials for super-resolution hyperlens imaging

3.1 Diffraction limit and resolution issue

The resolution of conventional imaging systems is inherently restricted by the diffraction limit, where the spatial information of features smaller than one half of the wavelength is confined to non-propagating light and cannot be projected to the far-field. [11, 12] The detail of fundamental about diffraction limit and resolution of imaging systems is already discussed in introduction chapter 1. To overcome diffraction limit in optical imaging science and engineering, indeed a lot of approaches and methods have been studied and demonstrated. While near-field scanning optical microscopy can surpass this limit by collecting the evanescent field in close proximity to the object [51, 52], the slow scanning speed and near-field perturbation from the scanning tip prevent its application in real-time imaging and biological systems. A superlens [13], following Pendry's proposal [5], which projects the sub-diffraction limited images at the near-field of the lens, was the first step toward real-time sub-diffraction resolution imaging. The major breakthrough emerged with the concept of an optical hyperlens [14, 47, 48], showing the first proof-of-principal for magnifying sub-diffraction scale objects to the far-field as propagating waves. Utilizing alternating dielectric and metallic multilayer in a curved geometry, this metamaterial-based optical device achieves strong optical anisotropy that supports the propagation of waves with very large spatial frequency and, due to the cylindrical geometry, adiabatically compresses its lateral wave vector while the wave is propagating outward along the radial direction [47, 53]. Consequently, the sub-diffraction details of the objects are magnified to be above the diffraction limit and can be transmitted to the far field. Since the first experimental demonstration of the cylindrical hyperlens in one dimension [14], newly improved designs as well as fabrication techniques, such as the impedance matched [54], flat [55], oblate [56, 57], the aperiodic [57] and acoustic [59] hyperlens, have been proposed in the framework of transformational optics [60, 61, 62]. Nevertheless, all the experimental demonstrations of hyperlenses so far were limited to one dimensional magnification and UV wavelengths, whereas for any practical imaging applications it is critical to demonstrate two-dimensional imaging with resolution below the diffraction limit in the visible spectrum. In this chapter, I will present a novel approach called optical hyperlens for super-resolution imaging overcoming current diffraction limit far beyond with using hyperbolic metamaterials. Especially, with novel design of sphere shape and new materials combination, full two dimensional magnification imaging and visible frequency operation which are never achieved before will be demonstrated. Also, very easy integration with commercial confocal microscope and metamaterial hyperlens will be shown as a good example for practical device application of metamaterials. In addition, detailed design process to achieve the most optimized system, device fabrication and further metamaterial devices manufacturing will be discussed extensively.

3.2 Design of spherical hyperlens

3.2.1 Mathematical studies for anisotropic materials design for light propagation

The issue about diffraction limit we discussed in chapter 2 is the loss of evanescent wave in normal materials. In this small chapter, I want to discuss propagation of waves in isotropic materials and anisotropic materials for further design process of hyperbolic metamaterials. Figure 3.1 is schematic of field distribution of arbitrary located two objects in x-y plane propagating along z-direction. Field distribution of two objects in x-y plane is expressed by equation (3.1) when z position is zero. If I want to those two objects propagate into z-direction, it's very clear that I want two objects are propagating into z-direction linearly which is represented by Figure 3.2. And, in mathematical form, it is expressed by equation 3.2 which means the given field distribution in arbitrary z position while the objects are moving to z-direction is proportional to the original field distribution when z position is zero. This exactly means transferring field distribution from one plane to another without diffraction.

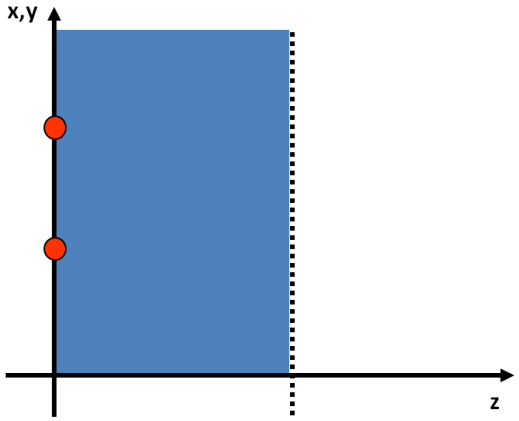

Figure 3.1. Field distribution of two objects in x-y plane

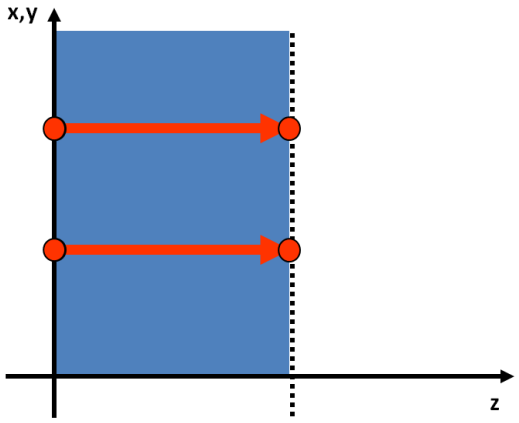

Figure 3.2. Field distribution of two objects in x-y plane propagating to z-direction

$$\Phi(x, y, z = 0) \tag{3.1}$$

$$\Phi(x, y, d) = C\Phi(x, y, 0) \tag{3.2}$$

In other words, to prevent diffraction limit, the field distribution is linearly transferred from the original plane (object plane) to the other plane (image plane) without any disturbance or change at every single point shown in Figure 3.3.

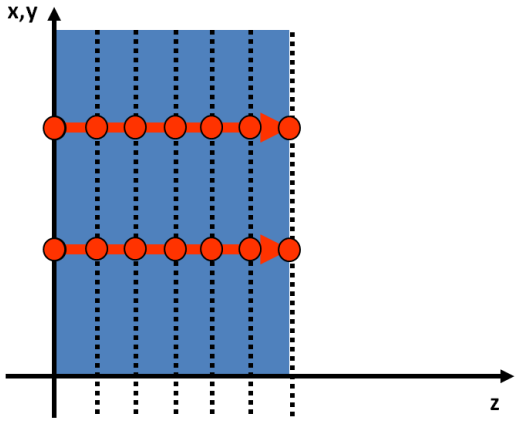

Figure 3.3. Field distribution of two objects propagating to z-direction at every single point

My goal at this moment is finding or designing proper materials which allow such linear propagation relation in z-direction (or any propagating direction). From the rules of propagation in electromagnetic, an equation for propagation of electromagnetic waves is expressed as below equation (3.3) in the case of z-directional propagation. Green color component represents the relationship between z-directional wavevector and x-y directional wavevectors.

$$\Phi[x, y, d] = \int_{x'}\int_{y'} \Phi[x', y', o]\left(\int_{k_x}\int_{k_y} e^{ik_x(x-x')} e^{ik_y(y-y')} e^{ik_z[k_x,k_y]d}\, dk_x dk_y \right) dx' dy' \tag{3.3}$$

Isotropic materials have a dependency between three wavevectors k_x, k_y and k_z. Therefore, k_z is also related with k_x and k_y. And, its relation is represented by equation (3.4) which is actually same form with equation (1.2) in chapter 1.

$$k_z[k_x, k_y] = \sqrt{n^2 k_0^2 - k_x^2 - k_y^2} \tag{3.4}$$

$$\Phi[x, y, d] = \int_{x'}\int_{y'} \Phi[x', y', o]\left(\int_{k_x}\int_{k_y} e^{ik_x(x-x')} e^{ik_y(y-y')} e^{i(i\alpha+\beta)d}\, dk_x dk_y \right) dx' dy' \tag{3.5}$$

With applying equation (3.4) into (3.3), equation (3.5) is obtained, but it failed to satisfy making independent k_z with regard to k_x and k_y., especially in the case of $k_x, k_y \gg nk_0$. Therefore, it could not make the condition (3.2), so it could not propagate in isotropic materials resulting in

evanescent wave in this given materials. Therefore, I had to find a solution making k_z apart from k_x and k_y, which means k_z is independent from two other axes. One strong anisotropic case giving independency to k_z with regard to k_x and k_y is the condition like equation (3.6)

$$k_z[k_x, k_y] = (i\alpha + \beta) = C \tag{3.6}$$

In above case, equation (3.3) becomes (3.7) which is simplified to the equation (3.8) and (3.9), consequently, because $e^{i(i\alpha+\beta)d}$ is independent from x and y. And, this equation (3.8) exactly matched to the equation (1.2) which satisfies propagating condition into z-direction.

$$\Phi[x, y, d] = \int_{x'}\int_{y'} \Phi[x', y', o] \left(\int_{k_x}\int_{k_y} e^{ik_x(x-x')} e^{ik_y(y-y')} e^{i(i\alpha+\beta)d} dk_x dk_y \right) dx' dy' \tag{3.7}$$

$$\Phi[x, y, d] = e^{i(i\alpha+\beta)d} \int_{x'}\int_{y'} \Phi[x', y', o] \left(\int_{k_x}\int_{k_y} e^{ik_x(x-x')} e^{ik_y(y-y')} dk_x dk_y \right) dx' dy' \tag{3.8}$$

$$\Phi[x, y, d] = e^{i(i\alpha+\beta)d} \Phi[x, y, 0] \tag{3.9}$$

3.2.2 Design of hyperbolic metamaterials as an anisotropic material

Only remaining question is how to make such strong anisotropic materials. Here, I introduce one way to build hyperbolic metamaterials by thin film stacking method. From the previous chapter, we learned how we define new permittivity tensor along x, y and z directions based on effective medium theory in metal-dielectric thin film stack. Figure 3.4 shows an example of consisting of material 1 and 2 with their own optical properties such as permittivity.

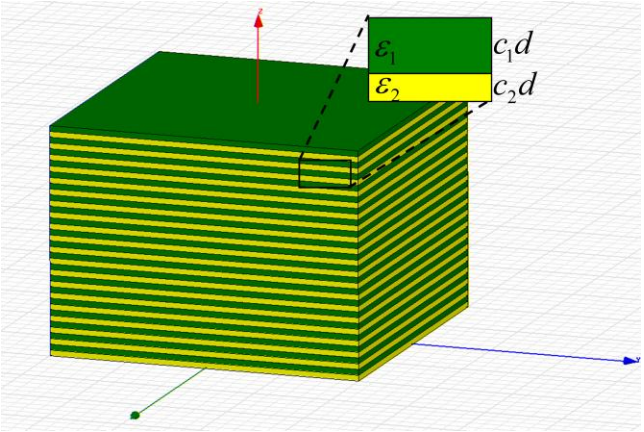

Figure 3.4. An example of multilayer stack consisting with two alternating materials. ε is permittivity, c is filling ratio of thickness d

Depending on their permittivity and thickness (filling ratio to two materials), new permittivity with regard to three axes are defined by effective medium approximation. Now, this stacked

material is considered as a totally new material 3, which has different permittivity to the axis. In this case, in-plan permittivity x and y are same, and propagating direction permittivity z is different. This is the way how we make anisotropic materials, which also will be used to build hyperbolc dispersion relation with controlling the sign and magnitude of new permittivity on demand as we discussed in chapter 2. New permittivity equation is already represented in equation (2.5). If we specify them following Figure (3.4), it is represented as below equation (3.10). By changing the filling ratio of two materials and find the permittivity of two materials depending on the working wavelength, negative permittivity of ε_z and positive permittivities of ε_x and ε_y with different magnitude can be obtained and thus can construct hyperbolic dispersion at certain frequency range.

$$\varepsilon_x = \varepsilon_y = \frac{c_1\varepsilon_1 + c_2\varepsilon_2}{c_1 + c_2}, \quad \varepsilon_z = \frac{(c_1 + c_2)\varepsilon_1\varepsilon_2}{(c_2\varepsilon_1 + c_1\varepsilon_2)} \tag{3.10}$$

3.2.3 Design of spherical geometry for far-field hyperlens imaging

Based on the equations in previous chapter, hyperbolic dispersion relation could be successfully obtained. However, there is still a practical issue of acquiring image of propagating light in the hyperbolc metamaterials.

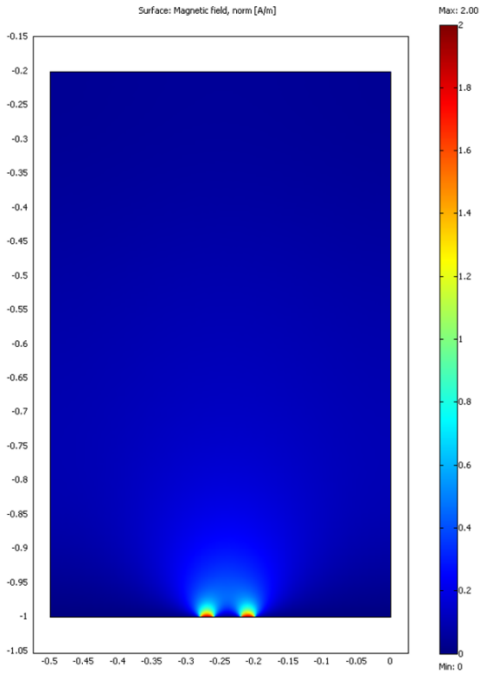

Figure 3.5. Simulation for light propagation of two very small nanoscale objects in normal isotropic materials (blue color), and their distance is within diffraction limit.

Let say there are two nanoscale objects locating with a distance beyond the diffraction limit, for example, two 50nm diameter holes are 50nm apart from each other in the normal isotropic material such as air and wavelength 410nm. When light shine from the bottom in Figure 3.5, light pass through two objects and tries to propagate to the air. However, it does not happen because 50nm distance is far beyond diffraction limit at 410nm wavelength. In this condition, air does not have enough wavevector access due to its limited dispersion relation of k_x, k_y and k_z. Under the condition, light becomes evanescent wave, thus light cannot propagate to the z-direction in the air. This is normally what happened in isotropic materials available in nature.

On the other hand, if a hyperbolic metamaterial are filled with the air, the light can propagate through the metamaterial because it has enough high-k vector access into x-y direction to support the light to propagate into the z-direction. The schematic and light propagation are shown in Figure 3.6. A very important observation from Figure 3.6 is light decays exponentially after escaping hyperbolic metamaterial even though two objects successfully propagates in the matematerial assisted by large wavevector in-plane direction due to hyperbolic dispersion. This is a critical limitation preventing detection of images on the image plane. Several techniques to detect such small object smaller than diffraction limit exist like Near-field Scanning Optical Microscope (NSOM). However, far-field imaging technique with light propagation into the arbitrary space is essential to achieve convenient and practical super-resolution imaging.

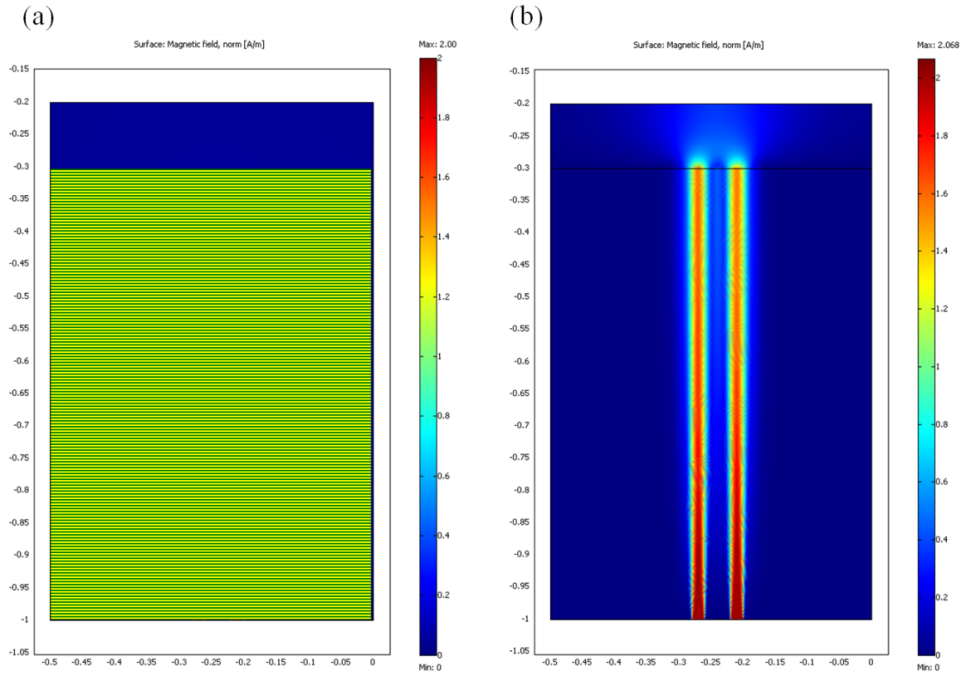

Figure 3.6. (a) Multilayer stacked hyperbolic metamaterial for light propagation two objects beyond diffraction limit (yellow/green color) (b) Simulation for light propagation of two very small nanoscale objects in a multilayer stacked hyperbolic metamaterial. Blue area is filled with hyperbolic metamaterials. Distance beyond diffraction limit is not decaying, but propagating along z-direction without diffraction. As soon as light goes out of hyperbolic metamaterial (marked as a black line), it decays exponentially since it becomes evanescent wave in the air.

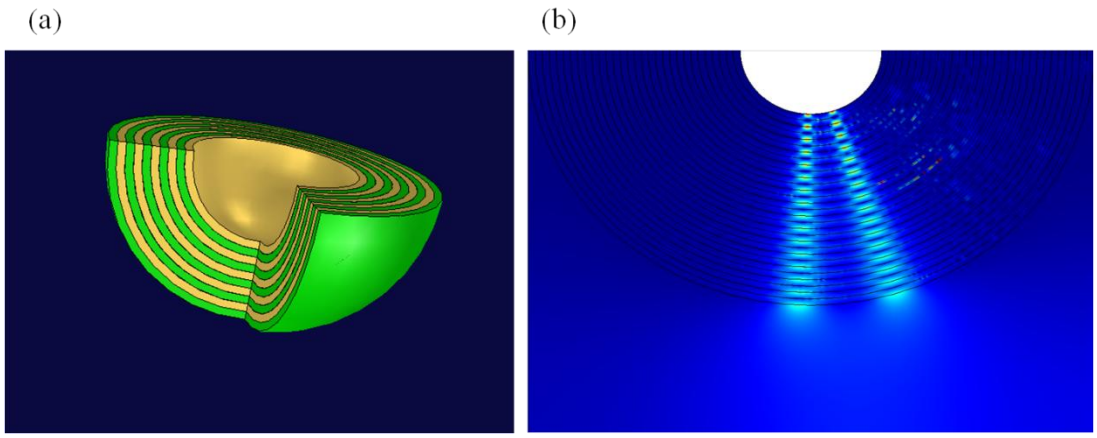

Figure 3.7. (a) Sphere geometry shaped hyperbolic metamaterial based on metal-dielectric multilayer stack (b) Sub-diffraction limited objects are propagating into the radial direction (r) with gradual magnification along in-plane direction (Θ and ϕ)

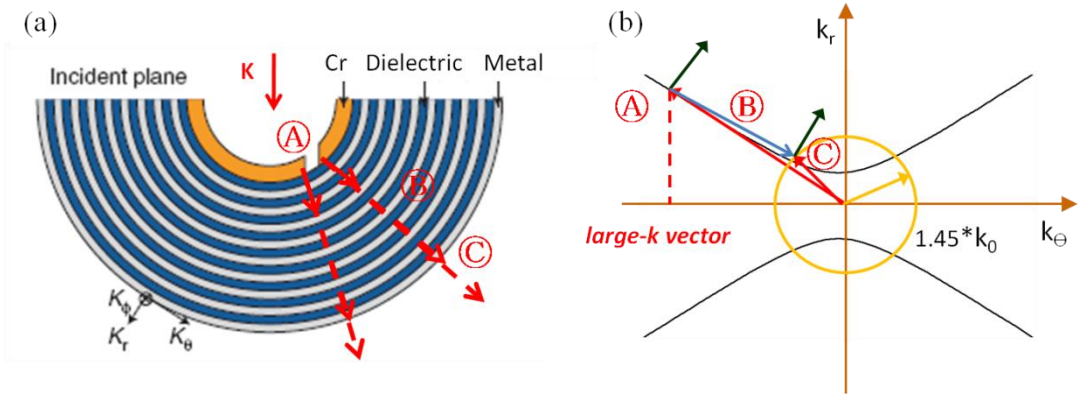

Figure 3.8. (a) Detailed cross section of hyperlens of half-sphere shaped multilayer stack. Each position matches to ones in (b). The sub-wavelength objects are carved in a chromium layer atop the metal-dielectric oxide multilayer. The transverse magnetic (TM) component of unpolarized light relative to the plane is labeled by K (b) Corresponding positions in IFC

To solve above issue, I developed a special geometry of half-sphere shaped hyperbolic metamaterial. As shown in Figure 3.7, hyperbolic metamaterial allows propagating light into the radial direction supported by large in-plane wavevectors. And the spherical geometry gives the gradual magnification along in-plane direction, so that the objects are over diffraction limit when they escape the hyperbolic metamaterial. At the boundary between metamaterial and outside background, two objects are not diffraction limited anymore, so it can be detected by conventional microscopes or other easy techniques. This is the main working principle how hyperlens magnifies sub-diffraction limited objects and project them to the far-field without diffraction. Detailed principle is explained in Figure 3.8. Position A is the case sub-diffraction scale objects are supported by large wavevectos k_Θ and k_ϕ, resulting in starting propagating into

the radial direction, comparing that they become evanescent wave in normal materials. Position B is describing k_Θ and k_ϕ is gradually compressed along the hyperbolic curve coreesponding the radial position changed. This is because optical momentum k_{in} times r is conserved at every point. While propagating along r-direction, the radius becomes larger, then k_{in} get smaller. When the light arrived at the position C, the distance of two objects becomes far enough, which is not diffraction limited anymore, so that they can be supported by dispersion relation of normal material, in this case glass substrate. Therefore, the light can propagate to free space even after getting out of hyperbolic metamaterial, and it can be easily detected by conventional microscope.

3.2.4 Materials selection for hyperlens at visible frequencies

One important thing to design hyperlens is materials selection. Because permittivity of materials changes depending on the given wavelength, I had to select materials combination carefully for my designated frequency range. Particularly, in this work, target wavelength range is full visible wavelength spectrum, so I tried to find the optimized selection which gives the broadest range of hyperbolic dispersion in visible frequencies. Especially, this hyperlens let the light propagating into z-direction, thus hyperbolic dispersion as flat as possible would be better in terms of energy transfer by Poynting vector. Visible wavelength operation requires a high-index dielectric material to match the magnitudes of permittivities in the metal and dielectric at the operation frequency [63]. Therefore, we choose titanium oxide to be the dielectric material with a dielectric constant of 5.83 at 410nm, where the permittivity of silver in this wavelength is -4.99+0.22i [46]. The filling ratio is chosen to be 1:1 with a layer thickness of 30nm. The ultimate resolution limit is set by the magnification as well as the thickness of each layer, below which the multilayer cannot be considered as an effective medium. Being less than 1/10 of the wavelength, the effective medium approximation is met and the effective radial and tangential permittivities can be derived: ε_r = -64-19.83i and ε_θ = 0.42-0.11i. The high contrast between the radial and tangential permittivities results in an ultra-flat unbound dispersion relation over a large range of wave vectors, allowing the subwavelength information to propagate in the hyperlens. This metal-dielectric combination gives the flattest hyperbolic dispersion ensuring propagation without diffraction into the radial direction like Figure 3.9.

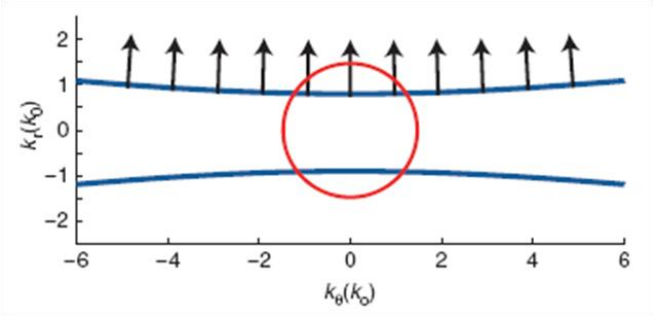

Figure 3.9. Flat hyperbolic dispersion made by silver and titanium oxide combination at visible frequencies. The IFC for the TM modes in the hyperlens compared with isotropic medium made of silicon oxide. The arrows, which are of unit length and on the ultraflat curve, show that all the k components (including those much larger than the wave vectors available in dielectrics) propagate along the same radial direction, indicating the lack of diffraction.

One other consideration for materials selection is choosing proper titanium oxide source. Titanium oxide has several compositions depending on their original status of the source. TiO, TiO_2, Ti_2O_3 and Ti_3O_5 are common composition we could grow with electron beam evaporator system. To find the highest refractive index at visible frequencies, I did ellipsometry to measure the refractive index of two different titanium oxide source TiO_2 and Ti_3O_5 in 50nm thick thin film. Each data of measured refractive index of N and K value is as shown in Figure 3.10 and Figure 3.11, respectively. The value of refractive index at 410nm is plotted, and it was confirmed Ti_3O_5 has higher index than TiO_2. Also, in literature, it's well known Ti_3O_5 has the most stable in the shape of thin film [64]

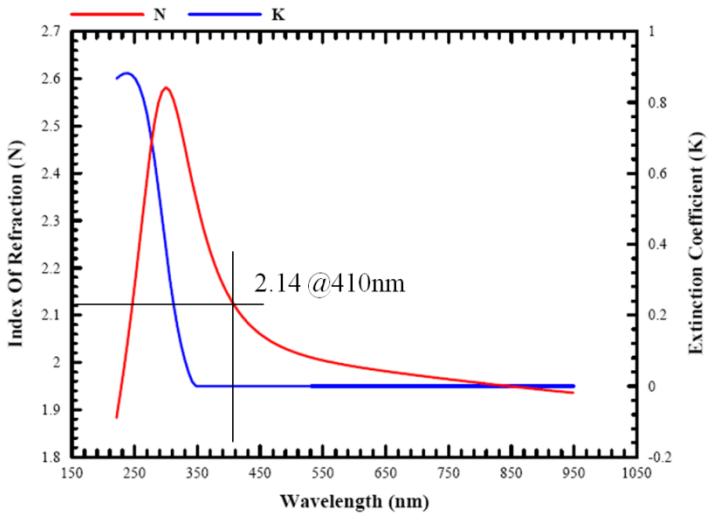

Figure 3.10. Measured refractive index of TiO_2 shows 2.14 at 410nm

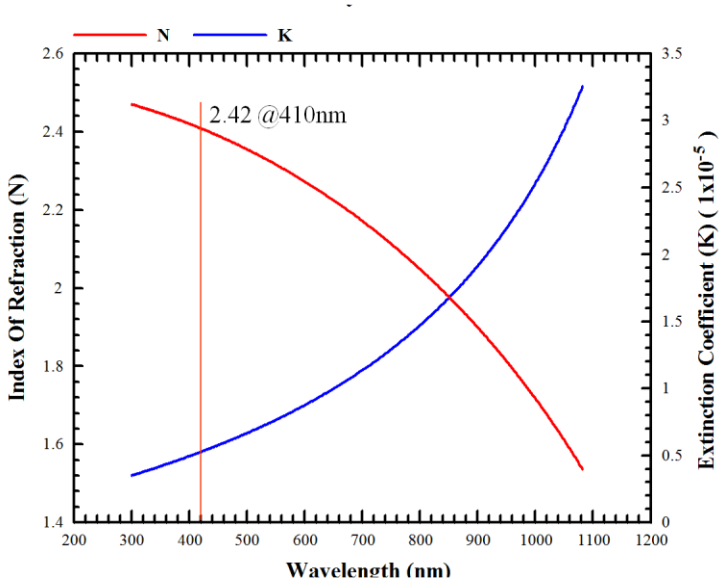

Figure 3.11. Measured refractive index of Ti_3O_5 shows 2.42 at 410nm

3.2.5 Final design confirmation of spherical hyperlens

The spherical hyperlens is arranged in hemi-sphere geometry with alternating metallic and dielectric layers as shown in Figure 3.12. When the thickness of each layer is much thinner than the wavelength of the incident light, the effective permittivity of the multilayer device can be described as the composite average, $\varepsilon_r = \frac{2\varepsilon_{Ag}\varepsilon_{Ti_3O_5}}{\varepsilon_{Ag} + \varepsilon_{Ti_3O_5}}$ in the radial (normal to the metal-dielectric interfaces) direction and $\varepsilon_\theta = \varepsilon_\phi = \frac{\varepsilon_{Ag} + \varepsilon_{Ti_3O_5}}{2}$ in the tangential direction (along the metal-dielectric interfaces). $\hat{r}$, θ and ϕ follow the conventional definitions of the radial, polar and azimuth directions in spherical coordinates, as shown in Figure 3.8 (a). A small positive ε_θ together with a large negative ε_r, results in the propagation of a transverse magnetic (TM) wave being governed by a flat hyperbolic IFC shown in Figure 3.9, which allows the propagation of waves with much larger spatial frequencies than in natural media. On the other hand, the transverse electric components, having no electric field along the radial direction, propagate through the hyperlens as a low-index isotropic medium such that the non-zero spatial frequencies are filtered out. Hence, the objects can only be magnified in one direction under linear polarized illumination. We overcome this restriction by illuminating the sample with unpolarized light, which contains TM components spanning the whole two dimensional reciprocal space, thus supports propagation of sub-wavelength features in both dimensions. At the same time, the spherical geometry, along with the diffraction control enabled by the flat dispersion, result in a gradual magnification of the sub-wavelength objects during the radial transmission, where the evanescent waves are adiabatically transformed into the propagating waves. Consequently, a magnified image is formed at the output plane of the hyperlens, which can be subsequently acquired though a conventional optical microscope.

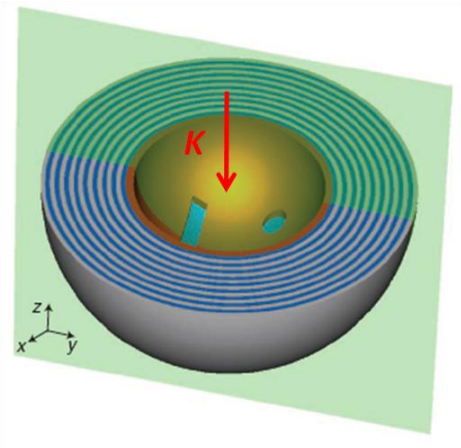

Figure 3.12. Schematic drawing of the final design of spherical hyperlens with sub-diffraction features on the top layer of hyperlens and TM light excitation from the top

3.3 Numerical study for spherical hyperlens

3.3.1 Full-wave three-dimensional simulation

To further support our experimental results, we performed a full-wave three-dimensional electromagnetic simulation with commercial Finite Element Analysis software (COMSOL). The radii of the inner and outer spherical surfaces of the hyperlens are taken as 210nm and 500nm, respectively, making the designed magnification ratio 2.4. Figure 3.14 shows the hyperlens imaging of three apertures with 150nm separation inscribed on the inner surface. The electric field distribution at the outer spherical surface of the hyperlens clearly shows how the three apertures at the inner surface are magnified to three bright spots with separation of 360 nm in a good agreement with the analytical calculations, showing a magnification of 2.4 in both x-y directions. By increasing the ratio between the inner and outer radius of the hyperlens, the magnification and resolution can be further improved while reducing the transmission of the hyperlens.

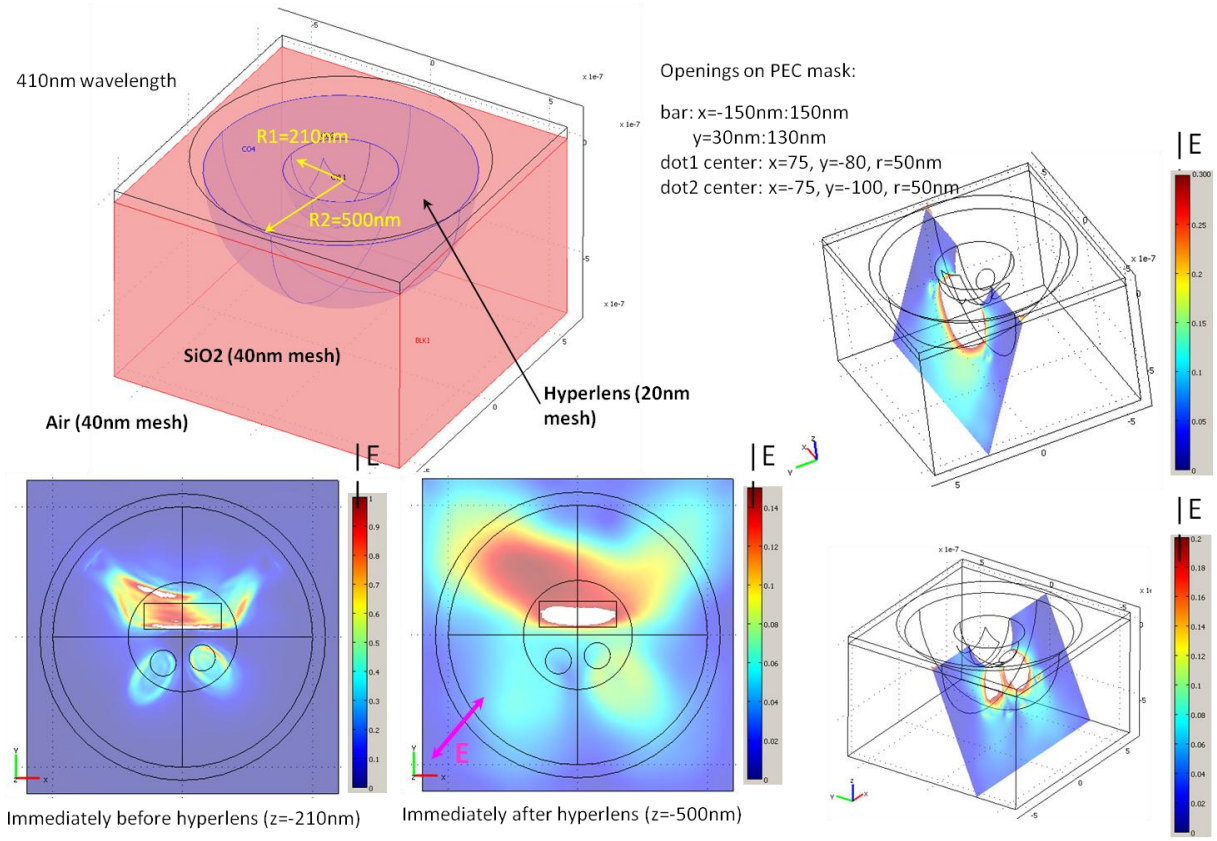

Figure 3.13. Full-wave simulation of the working hyperlens for complex structure to confirm distortion and aberration depending on the arbitrary object shape. Smiling face consisting of two dots and one bar is simulated in 3D. Due to the complexity of structure and different height where the patterns locate, there is a distortion along the radial direction.

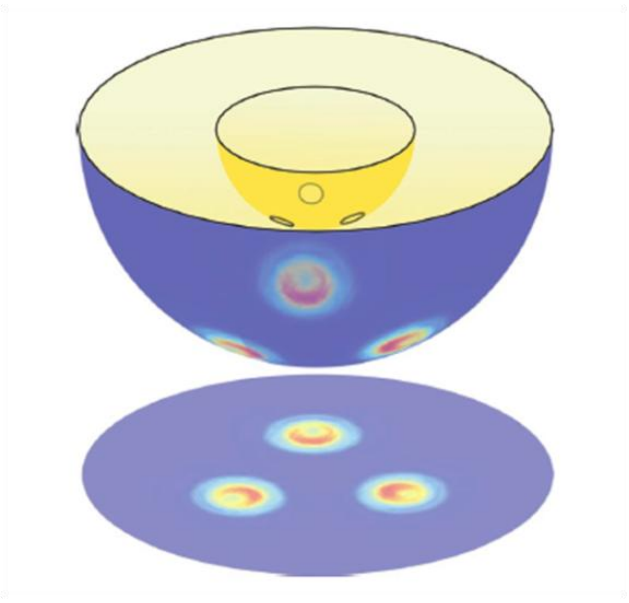

Figure 3.14. Full-wave simulation of the working hyperlens. A FEM analysis shows the magnified image of sub-diffraction limited objects. The objects are composed of three circular openings on perfect electric conductor. The diameter of each circle is 50 nm, and the distance between the circles is 150 nm. The working wavelength is 410 nm. At the image plane, the distance between the circles increased to 360 nm, which corresponds to the magnification of 2.4.

3.3.2 Simulation method

The full-wave three-dimensional electromagnetic simulation (Figure 3.13 and Figure 3.14) is performed in COMSOL. The hyperlens is represented by an effective medium with permittivity tensor (3.11) in the Cartesian coordinate:

$$\ddot{\varepsilon}(x,y,z)=\begin{pmatrix} \cos^2\phi(\varepsilon_r\sin^2\theta+\varepsilon_\theta\cos^2\theta)+\varepsilon_\phi\sin^2\phi & \cos\phi\sin\phi(\varepsilon_r\sin^2\theta+\varepsilon_\theta\cos^2\theta-\varepsilon_{\phi\phi}) & \sin\theta\cos\theta\cos\phi(\varepsilon_r-\varepsilon_\theta) \\ \cos\phi\sin\phi(\varepsilon_r\sin^2\theta+\varepsilon_\theta\cos^2\theta-\varepsilon_\phi) & \sin^2\phi(\varepsilon_r\sin^2\theta+\varepsilon_\theta\cos^2\theta)+\varepsilon_\phi\cos^2\phi & \sin\theta\cos\theta\sin\phi(\varepsilon_r-\varepsilon_\theta) \\ \sin\theta\cos\theta\cos\phi(\varepsilon_r-\varepsilon_\theta) & \sin\theta\cos\theta\sin\phi(\varepsilon_r-\varepsilon_\theta) & \varepsilon_r\cos^2\theta+\varepsilon_\theta\sin^2\theta \end{pmatrix} \quad (3.11)$$

where (r,θ,ϕ) is the Spherical coordinate triplet, meanwhile ε_r, ε_θ *and* ε_ϕ are defined in the result section. The surrounding medium in Figure 3.13 is silicon oxide. The objects at the inner surface is composed of three circular openings in a Perfect Electric Conductor (PEC). The distance between the circles is 150 nm, which is smaller than the diffraction limit at 410 nm wavelength. In the simulation, the radial polarized illumination condition is applied to represent the unpolarized light used in the experiment. In addition to above simple case of three dots locating in triangle position, more complicated nanoscale objects are simulated to confirm the performance of hyperlens as shown in Figure 3.14. Detailed experimental result will be discussed in next chapters.

3.3.3 Optimization of magnification and transmission

To realize optical hyperlens for sub-diffractional imaging, one important thing to consider is optimization of magnification and transmission. Unlike normal lens system, this metamaterial based hyperlens uses metal and dielectric thin films. Especially, due to the reflecting characteristic of metals, hyperlens intrinsically reflect light while it transmits some portion of light. Magnification is defined as the ration of the projected image distance and original object distance. In the case of spherical hyperlens, from the sphere geometry, it is determined by the relation of $M = \frac{outer\ d}{inner\ d}$, and this is proportional to the number of total thin film layers. At the same time, due to the reflecting property of the metal, transmission is inverse proportional to the number of thin film layers. In other words, the more layers give, the less transmission and the higher magnification are offered to the hyperlens. To optimize two parameters for ideal performance of hyperlens, two designs are considered at the design stage. The first design is magnification priority model shown in Figure 3.14 (a), in this case, total 44 layers are simulated to give magnification value 4.85 which can provide 80nm resolution. However, in this design, transmission through 22 layers is only 6%, which is very difficult to detect the transmitted light at the far-field. In the transmission priority design (Figure 3.14 (b)), 18 layers are stacked to give magnification of 4.17 with the resolution of 110nm and yet keep 25% transmission, which is high enough to detect with EM-CCD camera at the far-field. Even though the resolution and magnification decreased 15%, transmission increased nearly 5 times, so the transmission priority design is selected for the final design.

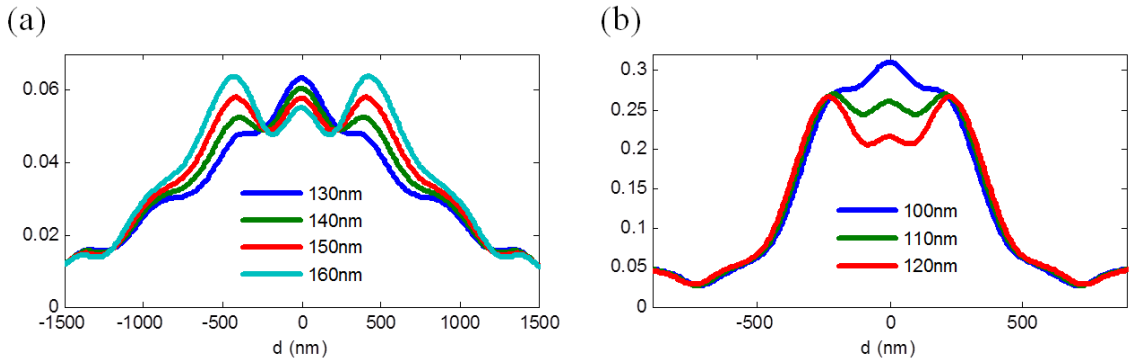

Figure 3.15. (a) Magnification priority design. Hyperlens consists of 22 pairs of silver-titanium oxide. The inner radius is 400nm and the outer radius is 1940nm, which gives magnification of 4.85. (b) Transmission priority design. Hyperlens consists of 9 pairs of silver-titanium oxide. The inner radius is 210nm and the outer radius is 875nm, which gives magnification of 4.17.

3.4 Hyperlens device fabrication

The fabrication process is schematically shown in Figure 3.16 (a)-(e). Initially, the half-spherical geometry of the hyperlens is formed by isotropic wet-etching into the quartz substrate. Nine pairs of silver and titanium oxide thin film layers were subsequently deposited with layer thickness of 30nm. Finally, the arbitrary sub-diffraction limited features are inscribed on an additional chromium layer by focused ion beam milling to serve as objects for imaging. The final structure is confirmed by cutting a cross section of the spherical hyperlens (Figure 3.17). In detail, spherical hyperlens fabrication starts with a highly refined quartz wafer. (Fused Silica Corning 7980 of UV Grade 1" square x .006" ± .001" thick) To prevent the pinholes made from deposition, at least 100nm-thickness chromium is necessary for the etching mask. Circular opening as small as 50nm is followed by focused ion beam milling (Strata 201XP, FEI). The half-spherical geometry of the hyperlens is formed by isotropic wet-etching into the quartz substrate with 10:1 buffered oxide etchant. The shape of the lens is defined by the etching mask, and the diameter is precisely controlled by the etching time. The spherical shape of the etched cavity is examined by atomic force microscope (Dimension 3100, Veeco). After removing chromium mask layer by another wet etching with CR-7 etchant, Electron beam evaporation system (EB-4P, Torr) was used to deposit the silver and titanium oxide multilayer. To reduce the scattering from the surface roughness, vacuum condition is kept at 10^{-7} Torr and the film growth rate is kept as slow as 0.1nm/s. As the last step, one additional layer of 50nm chromium is deposited, and the arbitrary sub-diffraction limited features such as nanometer-sized apertures and slots are inscribed by focused ion beam milling. The surface roughness of the final structure is < 1.5nm RMS. SEM image (Figure 3.17) is taken after short BOE soak to give high contrast.

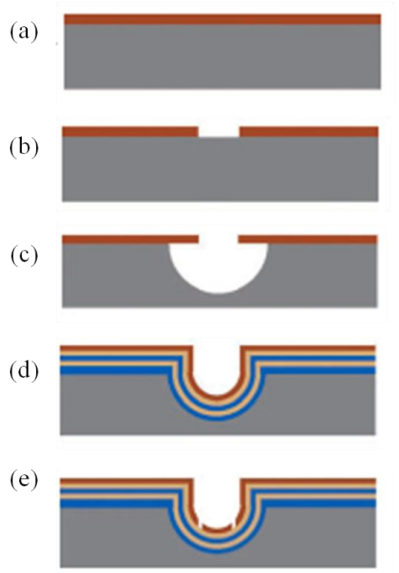

Figure 3.16. Structure and fabrication procedure of the spherical hyperlens. (a) Chromium hard mask layer is deposited on a quartz wafer. (b) Opening window is made by focused ion beam milling. (c) Isotropic wet etching defines a half-spherical geometry, and the mask layer is removed. (d) A total of 18 layers are conformally deposited onto the hyperlens structure. (e) On the top of 18 silver-dielectric stack, chromium layer is deposited to engrave arbitrary objects.

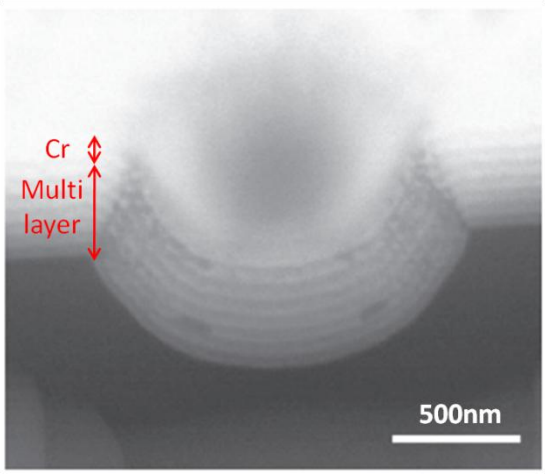

Figure 3.17. A scanning electron microscope (SEM) image of the cross-sectional view of spherical hyperlens. The multilayer stack is clearly seen layer by layer.

3.5 Experiment of optical measurement

3.5.1 Experimental setup

The experiment is operated in a normal transmission optical microscopy system, where the objects on the inner hyperlens surface are illuminated by a normally-incident and unpolarized white light source (XE120, EXFO) with a 10nm band pass filter centered at 410nm. A magnified image on the outer surface is then imaged through the objective (100X oil immersion objective, NA=1.3, Zeiss) and captured by EM-CCD camera (NS-H9100-02, Hamamatsu). Multiple exposures are taken and averaged to increase the signal-to-noise-ratio.

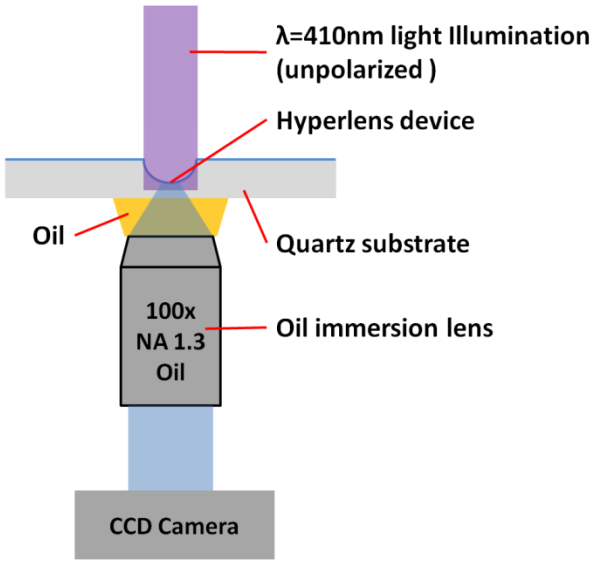

Figure 3.18. Hyperlens experimental set-up integrated into the conventional confocal microscope

3.5.2 Confirming practical diffraction limit as a control experiment

Theoretical diffraction limit of imaging system shown in Figure 3.18 is determined by Rayleigh criteria that we discussed in Chapter 1 and Chapter 2 and calculated as below equation 3.12. To confirm this value really works, control experiment verifying diffraction limit is executed. Control objects are three dots patterned on 50nm thick thin chromium layer, as keeping the same condition with real hyperlens experiment except the geometry.

$$\Delta_x \text{ or } \Delta_y = \frac{0.61\lambda}{NA} = \frac{0.6\times 410nm}{1.3} = 192nm \tag{3.12}$$

We decreased the distance with 10nm step from 400nm to 100nm. When the distance is far larger than expected diffraction limit, they are clearly resolved like Figure 3.19. However, once the distance arrived at 270nm, three dots are about to be seen as a circular aperture, which means not resolving properly. Further, in the case of 160nm obviously beyond given diffraction limit, they are not resolved and showed very high intensity of one circular aperture. From this experiment, we can conclude the practical diffraction limit of this imaging system is around 270nm, corresponding λ/NA as some literature claim diffraction limit criteria. [14]

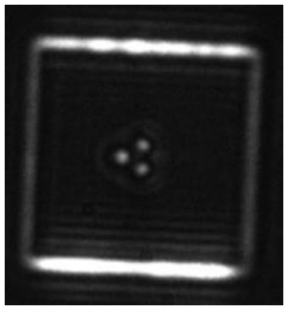

Figure 3.19. Control experiment of three dots in flat metal layer of which distance is 380nm. Because the distance is far over diffraction limit at 410nm wavelength, they are clearly resolved.

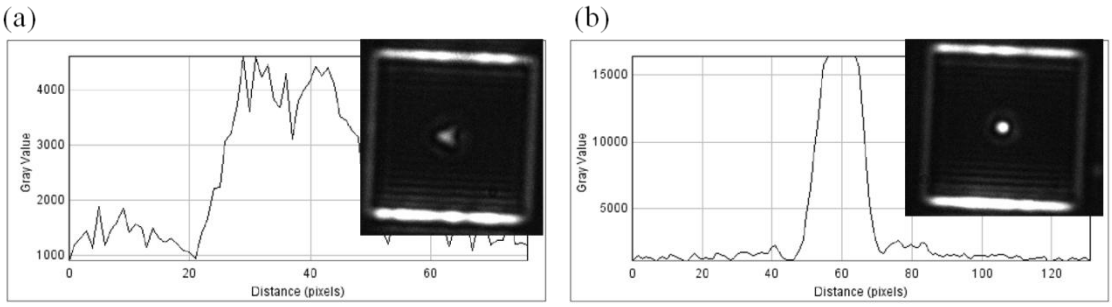

Figure 3.20. Control experiment of three dots in flat metal layer of which distances are (a) 270nm and (b) 160nm. (a) Objects start not to be resolved. It can be considered as a practical diffraction limit of current imaging system. (b) Beyond diffraction limit, obviously not resolved.

3.6 Results and discussion

3.6.1 Observation of resolution beyond the diffraction limit

The hyperlens is placed in a transmission optical microscopy system such that it serves as an integral part of the microscope with the ability to deliver the sub-wavelength features into the propagation regime, where they can be collected by the objective lens. Figure 3.21 (1.5D) and Figure 3.22 (1.5D and 2D) depicts three sets of the magnified images of sub-diffraction limited objects, obtained by CCD camera at the image plane. The objects shown in Figure 3.22 (a) consists of two apertures of 100nm diameter and a slot of 100nm width, which are separated by 160nm and 180nm respectively. The magnified optical image on the hyperlens is shown in Figure 3.22 (b). The result indicates that the separation of 160nm and 180nm are clearly resolved in the experiment, despite being below the diffraction limit of the 410nm illumination wavelength. Figure 3.22 (c) presents the cross section along the red line in Figure 3.22 (b) showing a measured distance between dots and bars of 346nm and 363nm, corresponding to magnifications of 2.02~2.16. A different objects, made of three apertures located in triangular configuration with 160nm, 170nm and 180nm spacing in three sides (Figure 3.22 (d)) is also clearly resolved at the far field (Figure 3.22 (e)); the separation of the two apertures is measured to be 333 nm in the cross-sectional analysis shown in Figure 3.22 (f). Given the fabricated distance of 160nm, the averaged magnification ratio is 2.08. This ratio is smaller than the designed value, which is mainly due to non-conformal deposition and inaccurate thickness control of the layer, resulting in deviation of the concentricity of the hyperlens and a position dependent magnification power. In addition the hyperlens magnifies the image of the objects onto a spherical surface, resulting distortions in subsequent conventional microscope image are shown in Figure 3.22 (b) and Figure 3.22 (d). Adapting thin film deposition techniques with improved conformality, thickness and roughness control can considerably improve the quality of the hyperlens, and in principle, these image aberrations can be compensated by introducing more corrections conventionally employed in lens design.

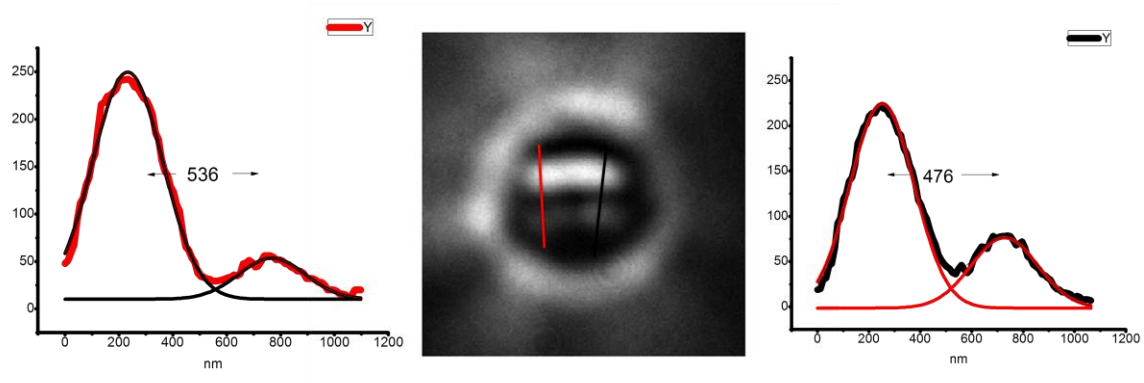

Figure 3.21. Measurement result with the magnifying hyperlens. Image taken of the object being magnified by the hyperlens. The sub-diffraction-limited objects (same gap of 180nm and 160nm) were clearly resolved by the spherical hyperlens. Along the red dash line, a cross section is taken to calibrate the performance of the hyperlens. Cross-sectional analysis shows separation by 536 and 476 nm, respectively, corresponding to ×2.97 magnification.

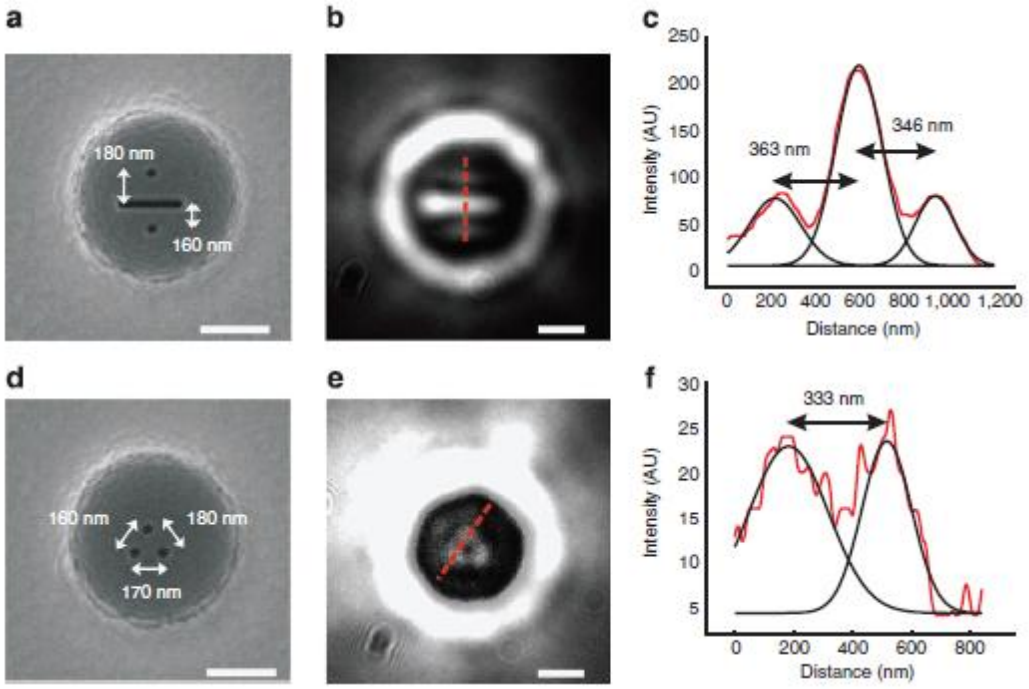

Figure 3.22. Measurement result with the magnifying hyperlens. (a) SEM image of object 1: two 100 nm diameter dots separated by a 100 nm wide bar. The gap sizes are 180 and 160 nm. All scale bars shown in the figure are 500 nm. (b) Image taken of the object being magnified by the hyperlens. The sub-diffraction-limited objects were clearly resolved by the spherical hyperlens. Along the red dash line, a cross section is taken to calibrate the performance of the hyperlens. (c) Cross-sectional analysis showing separation by 363 and 346 nm, respectively, corresponding to ×2.16 magnification. (d) SEM image of object 2: three dots positioned triangularly with gaps of 180, 170 and 160 nm. (e) Image taken of the object being magnified by the hyperlens. The sub-diffraction-limited objects were clearly resolved by the hyperlens. (f) Cross section of the object along the red line after being magnified. Magnified distance is 333nm, corresponding to x2.08.

3.6.2 Control experiment to confirm the hyperlens performance

One concern raised during hyperlens experiment is that the magnification effect happens only by geometry effect from sphere shape. To make sure this concern, I executed one control experiment verifying the performance of hyperlens. One sample is a hyperlens we used for optical measurement, and the other is a lens made with same thickness (540nm) of titanium oxide layer only. Same sub-diffractional objects of three dots used in Figure 3.22 (d) are carved on the top chromium layer of both lenses. As shown in Figure 3.22 (e), the spherical hyperlens successfully resolved images far smaller than diffraction limit. However, a normal lens shows only a spot which means three objects are not resolved due to diffraction limit. This control experiment confirms magnification is not just from geometry effect, but from the unique hyperbolic dispersion relation supporting large wavevector transferring evanescent waves to propagating waves, which is the fundamental physics of hyperlens.

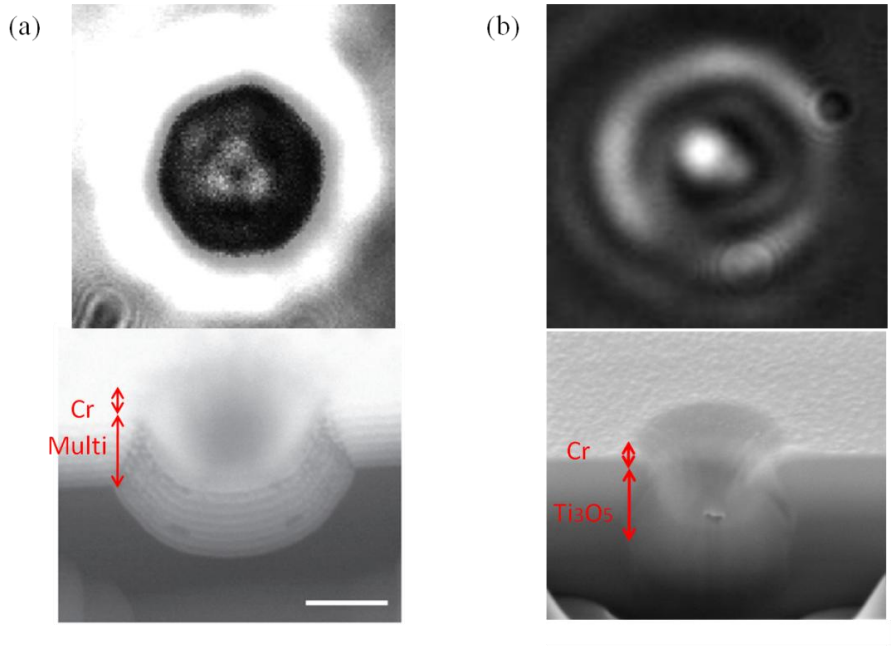

Figure 3.23. Control experiment confirming hyperlens performance. (a) Hyperlens resolve the object overcoming diffraction limit. (b) Non-hyperlens sample consisting of only titanium oxide layer with same thickness does not resolve the same size objects due to diffraction limit.

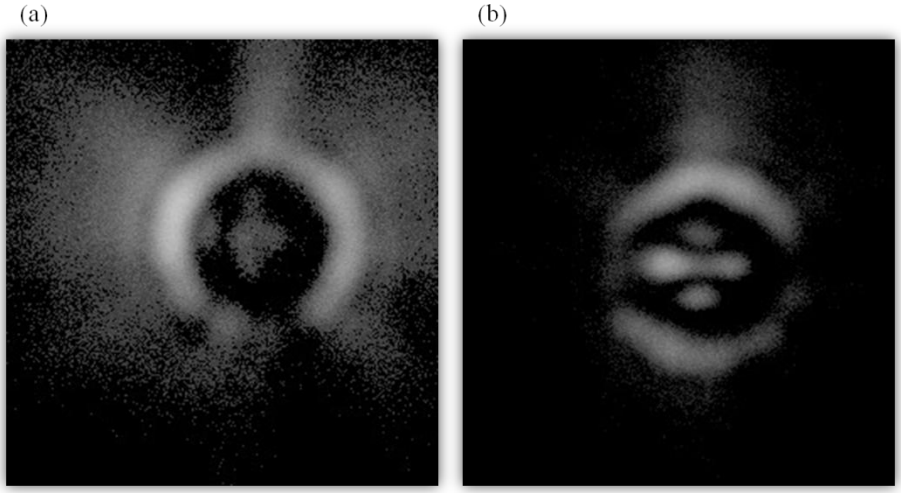

Figure 3.24. 1.5D sub-diffraction objects magnified through hyperlens experiment with (a) vertically polarized light (b) horizontally polarized light

3.6.3 Polarization dependency experiments

To confirm our experiments with unpolarized light, I also conducted the same experiments with polarized light. In Figure 3.24 and Figure 3.25, (a) is done with vertically polarized light,

which shows magnification only happens in y-direction, and (b) is done with horizontally polarized light, which shows magnification only happens in x-direction. In other words, magnification with polarized light exists along the polarization direction, which is the limitation of previous hyperlens workingwith only TM polarized light [14]. Using unpolarized light, spherical hyperlens can have hyperlensing effect in two lateral dimensions regardless of directionality, which is one of the original finding of this work.

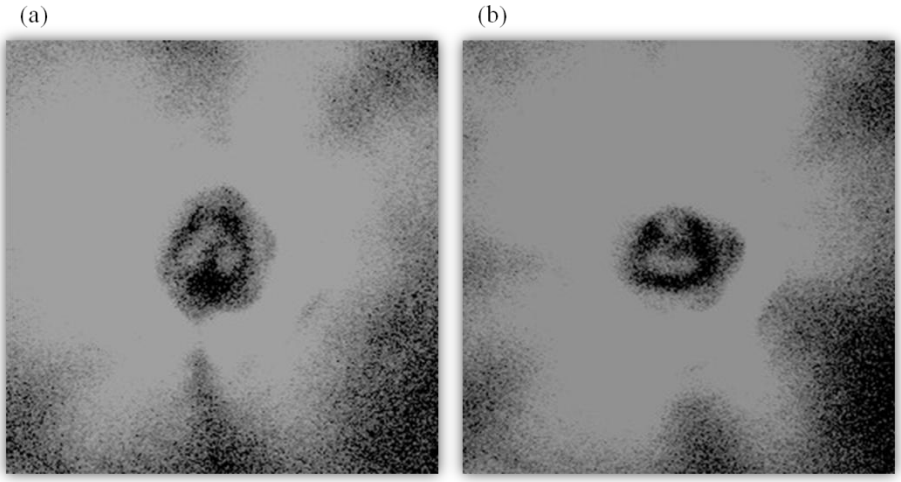

Figure 3.25. 2D sub-diffraction objects magnified through hyperlens experiment with (a) vertically polarized light (b) horizontally polarized light

3.7 Summary

In this chapter, I present the first spherical hyperlens for two-dimensional sub-diffraction limited real-time imaging at visible frequencies without the need for optical scanning or image reconstruction [65]. By implementing the principle of hyperbolic dispersion into the innovative spherical geometry, we have designed and demonstrated the first hyperlens that projects an optical image onto the far-field with resolution beyond the diffraction limit in both lateral directions on the object plane. Our results indicate that with real material and practical fabrication techniques, the hyperlens can be operated at the visible frequency, which is of vital importance to biological applications. Improved thin film deposition techniques will eliminate the distortion found in the current experiments to a considerable extent. This spherical hyperlens can be readily integrated with optical microscopes as the magnified images from the hyperlens are comprised of propagating waves and can be further manipulated by conventional optics in real-time. The unique sub-diffraction imaging capability and visible frequency operation of the presented hyperlens make it competent for next generation optical metrology, molecular imaging and nanolithography. Transforming scattered evanescent waves into propagating waves, the hyperlens produces a magnified image at the far-field where it could be further processed by conventional optics. The visible wavelength operation with sub-diffraction resolution opens new avenues towards optical nano-scope and real-time biomolecular imaging in living cells.

Chapter 4

Hyperbolic metamaterials for nanoscale optical cavities

4.1 Introduction to optical cavity and diffraction limit issue

Diffraction limit in optical science and engineering is intensively described in previous chapters, and metamaterials have provided several solutions on this matter. Among many extraordinary effects of various metamaterials, hyperbolic metamaterials have a particularly great potential to access sub-diffraction scale light. Super-resolution imaging by utilizing high-k vector is demonstrated by hyperlens allowing sub-diffraction light propagating into the far-field. Similar phenomena but the different application is possible by the same hyperbolic metamaterials using unique property of sub-wavelength light access. In this chapter, I will introduce an application of hyperbolic metamaterials into optical cavity science and engineering which overcomes the limitations of current state-of-the-art in the field.

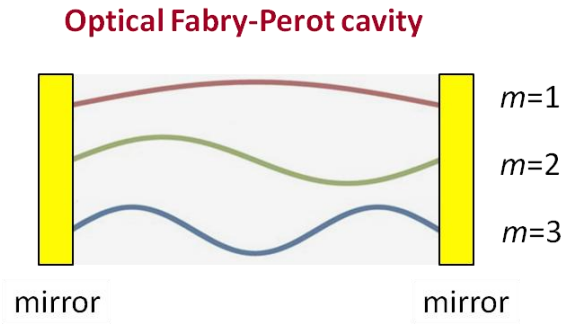

Figure 4.1. Schematic of optical Fabry-Perot cavity with three different modes

Optical cavity is basically the fundamental component confining light and enhancing the energy level to make laser beam. Optical cavity consists of two mirrors and light is travelling inside the cavity by reflecting each mirror. As shown in Figure 4.1, once light is introduced inside the cavity, the light continues travelling and reflecting on the mirrors until they are vanished due to loss. The loss is made when the light hits each mirror. While they are travelling in the cavity, the energy level increases and gets unstable when reflecting the mirrors. Once the level is high enough, an external force pushes the light to make a laser beam as the energy level goes back to the ground state. This is the basic principle laser beams are made. Thus, the key issue to make laser beams is how the cavities captured the light efficiently, increase the energy level without loss and eventually make laser beam with less external pump force.

The resonance condition of optical cavity is expressed in equation (4.1). In the conventional cavity, by solving the electromagnetic wave equation, the standing waves supported between two mirrors will have the resonance frequency condition which is proportional to the mode order m, and inverse proportional to the cavity size L and the refractive index n. c is the light speed in vacuum, so it can be assumed as a constant value. Therefore, we can change the frequency f by tuning the index n or tune the size L. f is inversely proportional to n, so wavelength is proportional to refractive index n. For example, with natural material having same refractive index, larger cavity has lower frequency and longer wavelength (normal dispersion), and higher order mode has higher frequency and shorter wavelength corresponding smaller refractive index n (normal dispersion). In this equation, one important point is that size and index are independent to each other, and this is the most different case of metamaterials cavities which will be discussed in later this chapter.

$$f_m = \frac{m}{2L}\left(\frac{c}{n}\right) \tag{4.1}$$

By squeezing light into a smaller dimension, the photonic density of state can be substantially enhanced due to the reduced mode volumes. This leads to a much faster emission process, and straight forwardly brighter and faster optoelectronics. The enhancement is determined by so called Purcell factor, which is the ratio of the artificially tailored photonic density of states and the density of states when the emitter is sitting in vacuum. Ever since the development of cavity QED in 80's, people know how to intervene the spontaneous emission process of an emitter. In stead of reducing the mode volume, people typically introduce a high quality factor cavity to enhance the photonic density of states by reducing the spectral line-width.

For optical cavity, one important parameter is the quality factor Q, which is defined as electromagnetic energy stored inside the cavity divided by the energy dissipated per cycle, it represents the optical loss (how long the optical energy can be stored); and modal volume V is defined as total electromagnetic energy divided by the maximum energy density, it gives the size of the optical confinement, (how tight the optical energy can be localized). The large Q/V ratio represents low loss and small size (represents both long photon lifetime and strong optical intensity,) and is the figure of merit Q/V for the enhancement of light matter interaction. And those relations are expressed as equation (4.2) and (4.3). Finally, to determine the performance of optical cavities, Q/V called figure of merit is evaluated for general method of cavities science and engineering.

$$Q = 2\pi \times \frac{Electromagnetic\ \ Energy\ \ Stored}{Energy\ \ Dissipated\ \ \ per\ \ cycle} \tag{4.2}$$

$$V = \frac{Total\ \ Electromagnetic\ \ Energy}{\max(Electromagnetic\ \ Energy\ \ Density)} \tag{4.3}$$

In addition to the quality factor in cavity, general criteria determining enhancement of light-matter interactions is introduced in equation (4.4). Therefore, finding larger figure of merit in various cavities is very important and this is able to be achieved by achieving either higher quality factor or smaller mode volume, or both.

– Purcell factor for spontaneous emission : Q / V
– Optical forces and trapping & Biosensing : Q / V
– Strong coupling for cavity QED : $Q / \sqrt{V}$ (4.4)
– χ^3optical nonlinearities : Q^2 / V

Figure 4.2 is a diagram of state-of-the-art different micro- and nanoscale cavities with regard to Q and V. Silica microsphere and microtoroid have highest Q and largest modal volume as well. With high index material, such as silicon, we can make smaller microdisk and microring resonators, with lower-Q too. High-Q photonic crystal cavities with modal volume of single cubic wavelength can be also designed, but it is still diffraction limited so it cannot achieve small mode volume. With the help of surface plasmons, recent plasmonic cavities such as plasmonic microdisk, FP cavity, and plasmonic nanostructures achieve sub-wavelength mode volume V, so the Q/V ratio is quite high even the Q is low due to the metal loss. However, it could not achieve high performance cavities compatible to conventional dielectric cavities due to their small quality factor. Main reason they could not overcome diffraction limit is that all these cavities are made from natural materials such as silica (silicon oxide), silicon, plasmonic materials, whose materials properties, especially dispersion relation, are limited discussed in chapter 1 and 2.

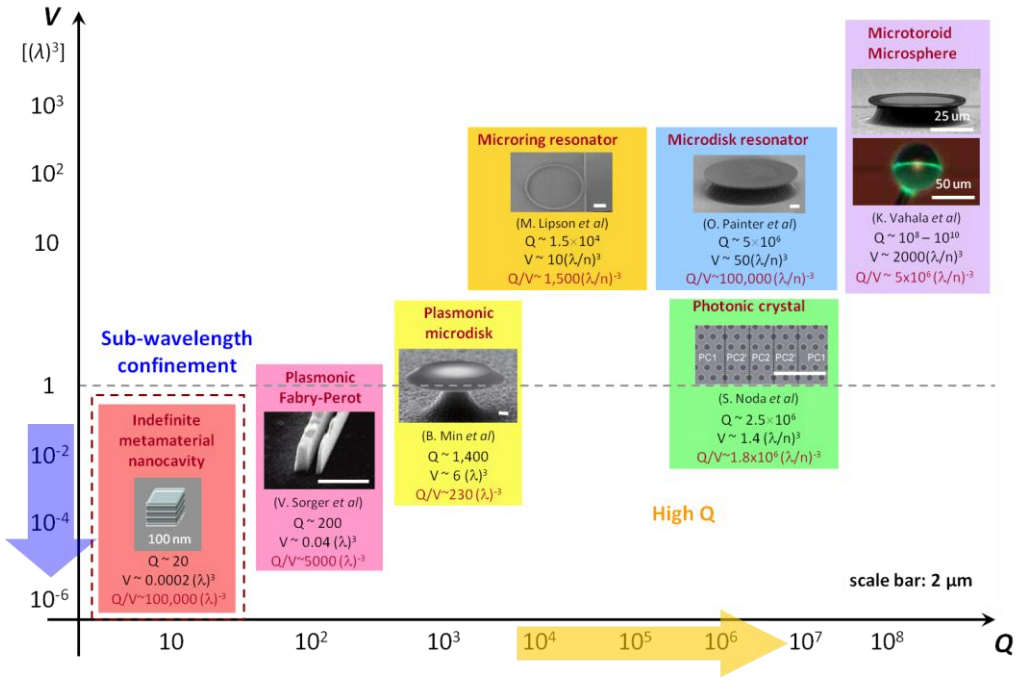

Figure 4.2. Diagram of current microscale and nanoscale optical cavities depending on Q and V

To overcome above size issue, metamaterials can be utilized. For example, if refractive index n is related to the cavity size, then the resonance frequency might show some anomalous dispersion. Quality factor and modal volume V can also be significantly influenced. In next

sections of this chapter, I want to show new kind of nanocavity made with hyperbolic metamaterials, which has deep sub-wavelength and anomalous dispersion, and high radiation Q. In optical cavities, the radiation loss from total internal reflection strongly depends on the cavity size. For optical cavities with size larger than wavelength scale, such as microsphere, microdisk, TIR induced radiation Q increases as the mode volume gets larger due to the smaller surface curvature and the reduced radiation leakage. On the other hand, a novel deep sub-wavelength nanocavity based on hyperbolic metamaterials I will show in this chapter has unique phenomena not only radiation Q increases dramatically when the cavity is even shrank, but also the resonance frequency is independent on the cavity size.

4.2 Metamaterials for optical cavities scaling down to nanoscale

As we studied in previous chapters, metamaterials have allowed extraordinary electromagnetic properties that are not attainable in nature [2, 6, 7, 15, 19, 21, 22, 25, 66]. Indefinite media with hyperbolic dispersion called hyperbolic metamaterials, in particular, have found intriguing applications [14, 38, 47, 48]. The miniaturization of optical cavities increases the photon density of states and therefore enhances light–matter interactions for applications in modern optoelectronics. However, scaling down the optical cavity is limited to the diffraction limit and by the reduced quality factor. In this chapter, I will show experimentally demonstrated optical cavity made of indefinite metamaterials that confines the electromagnetic field to an extremely small space. The experiments reveal that indefinite cavities demonstrate anomalous scaling laws: cavities with different sizes can resonant at the same frequency, and a higher-order resonance mode oscillates at a lower frequency. We also demonstrate a universal fourth power law for the radiation quality factor of the wave vector. Cavities with sizes down to l/12 are realized with ultrahigh optical indices (up to 17.4 experimentally and up to 39.5 theoretically), a feature that is critically important for many applications [55, 62, 67, 68, 69]. The strong optical field confinement in optical cavities such as microspheres, microtoroids and photonic-crystal cavities [70, 71, 72] has led to numerous exciting applications in areas including integrated photonics, nonlinear optics, quantum electrodynamics and optomechanics [73, 74, 75, 76]. Owing to the limited refractive indices of naturally available materials, the physical sizes of these cavities are limited to the wavelength scale for efficient light confinement. Most recently, metamaterials with an ultrahigh refractive index (in the terahertz regime) have been explored [8, 77, 78]. However, the experimental implementation of such a metamaterial at optical frequencies is difficult because of fabrication constraints. Another approach for achieving nanoscale optical cavities that makes use of nanowire metamaterials has been theoretically investigated [79]. In this chapter remained, I will show experimentally demonstration of hyperbolic metamaterials with optical refractive indices as large as 17.4, which is far beyond that found in natural materials. With such a high optical index, three-dimensional optical cavities with dimensions down to l/12 and unprecedented properties are demonstrated. Unlike conventional cavities where the resonant frequencies depend strongly on size, indefinite cavities support exactly the same resonant frequency in cavities with drastically different sizes as the result of their size-dependent effective indices. This cavity is found to scale anomalously such that a higher-order mode will resonate at a lower frequency. In contrast to the commonly understood principle, the radiation quality factors of the cavities scale inversely with cavity size, and we find experimentally there is a universal fourth power law between the radiation quality factor and the resonating wave vector.

4.3 Design of nanoscale metamaterials optical cavities

4.3.1 Hyperbolic metamaterials for optical cavities

The metamaterial structure consists of alternating thin layers of silver (Ag) and germanium (Ge) (Figure 4.3 (a)). When the multilayer period is much less than the wavelength, the multilayer can be considered as an effective medium described by the Maxwell-Garnet theory. The permittivity tensor of such metamaterials is uniaxial and the real parts of its principal components can have different signs, resulting in a 3D hyperboloid iso-frequency contour (IFC) (Figure 4.3 (b)). A spherical IFC of air with radius of k_0 is plotted for comparison ($k_0 = 2\pi/\lambda_0$). As the results of the open-curved hyperboloid dispersion, the indefinite medium allows wave with extremely large wave vector to propagate and the giant momentum mismatch between the metamaterial and the air causes the total internal reflection (TIR) at the interface. By cutting the metamaterial into a subwavelength cube, 3D optical Fabry-Pérot cavity can be formed with an effective refractive index $n_{eff} = k/k_0$. Since theoretically extreme large wave vectors can be reached along the unbound IFC hyperboloid, the cavity size can be ideally squeezed into nanometer scale.

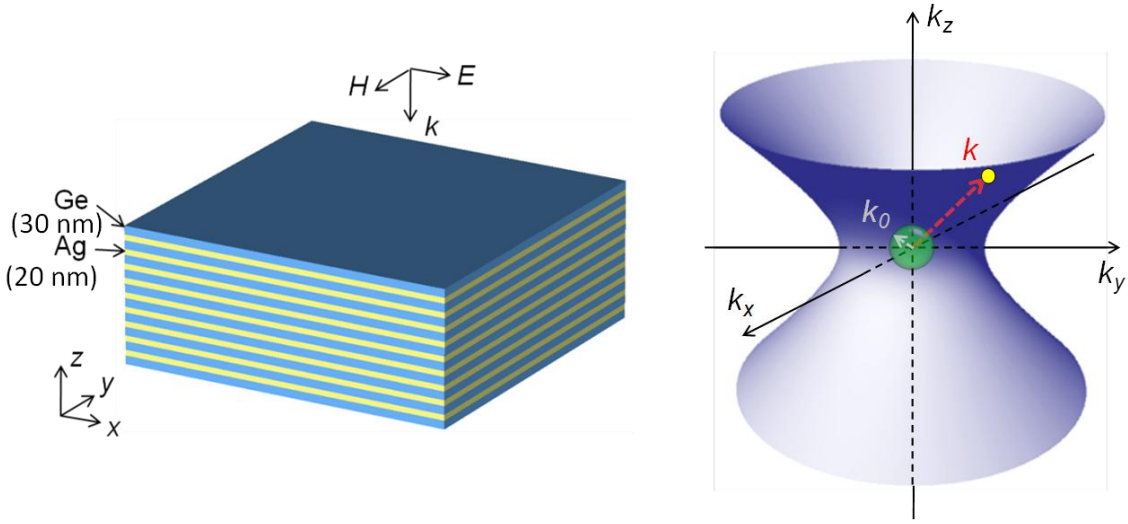

Figure 4.3. Schematic of multilayer hyperbolic metamaterial structure and its hyperboloid IFC. (a) Indefinite metamaterial with alternating silver and germanium multilayers. The permittivity components are negative along the x- and y-directions and positive along the z-direction (obtained from effective medium theory). A three-dimensional hyperbolic metamaterial optical cavity can be created based on TIR at the interface between the metamaterial and air. (b) Hyperboloid IFC of the multilayer metamaterial calculated from the dispersion relation (blue surface) and the spherical isotropic IFC of air with radius k_0 (green surface). The yellow dot located on the hyperboloid shows the resonating wave vector k inside the cavity, which is much larger than k_0, indicating an ultrahigh effective refractive index $n_{eff} = k/k_0$.

4.3.2 Permittivity and dispersion relation for hyperbolic metamaterials

The multilayer metamaterial can be treated as a homogeneous effective medium and the anisotropic permittivity tensor components can be determined from the Maxwell-Garnet theory [86, 87].

$$\varepsilon_p(\varepsilon_x = \varepsilon_y) = p\varepsilon_m + (1-p)\varepsilon_d$$
$$\varepsilon_v(\varepsilon_z) = \frac{\varepsilon_m \varepsilon_d}{(1-p)\varepsilon_m + p\varepsilon_d} \tag{4.5}$$

Here p is the filling ratio of metal, m and d are the permittivity of metal and dielectric, respectively. The optical properties of silver are obtained from the Drude model where $\varepsilon_{Ag} = \varepsilon_\infty - \omega_p^2 / \left(\omega^2 - i\omega\gamma\right)$ with background dielectric constant ε_∞=5.0, plasma frequency ω_p = 1.38×10^{16} rad/s, and collision frequency γ = 5.07×10^{13} rad/s [46]. The permittivity of germanium is around 16. Figure 4.4 shows the calculated permittivity components from equation (4.5), which show negative along x and y directions (parallel to the multilayers) and positive along z direction (vertical to the multilayers). For example, at the frequency of 191 THz (1.5um), ε_x & ε_y are -41+2.2i and ε_z is 29.1+0.1i. The dispersion relation for this uniaxial anisotropic material in x-z cross section is expressed in equation (4.6).

$$\frac{k_x^{\,2}}{\varepsilon_z} + \frac{k_z^{\,2}}{\varepsilon_x} = \frac{\omega^2}{c^2} \tag{4.6}$$

For the three-dimensional Fabry-Pérot type metamaterial cavities, the resonant condition is that the round-trip phase $2k_iL_i$ equal to $2m_i\pi$ in all three directions, where L_i is the cavity size along i direction, m_i is the mode order and i = x, y, z. The resonating wave vector of cavity mode is then approximately $k_i/k_0 = m_i\lambda_0/2L_i$.

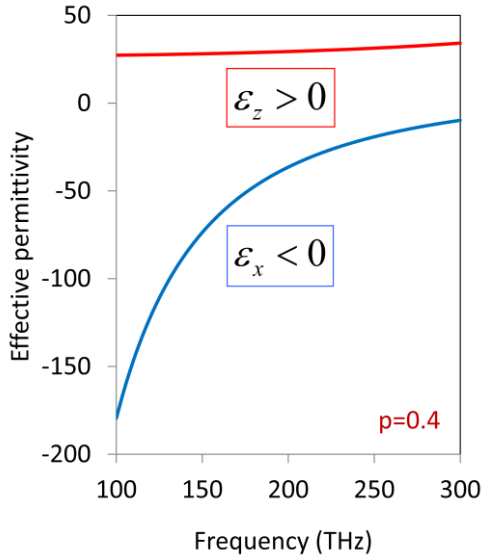

Figure 4.4. The principal components of permittivity tensor for the metamaterial consisting of alternating thin layers of Ag and Ge, calculated from the effective medium approach with a metal filling ratio of 0.4. This makes hyperbolic dispersion over broad frequency range.

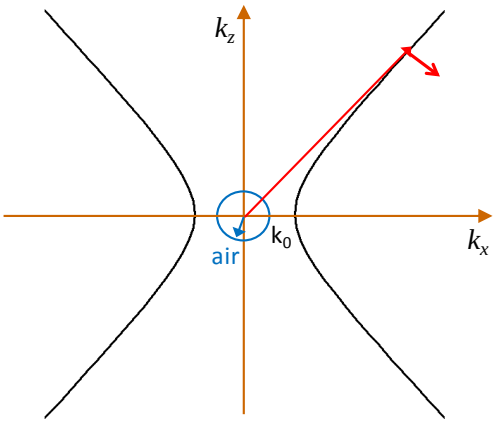

Figure 4.5. Hyperbolic IFC of hyperbolic metamaterials, which can confine light into x-y direction (type II), comparing z-directional propagation (type I)

Figure 4.5 shows dispersion relation of hyperbolic metamaterials derived from Figure 4.4. Unlike the hyperlens case in chapter 3, this hyperbolic IFC has 90° degree rotated hyperboloid shape. Comparing hyperlens has (+, +, -) sign of permittivity tensor, above hyperbolic metamaterials has (-, -, +) sign of permittivity tensor. Therefore, it would confine light in x-y direction rather than propagate into z-direction. For the clarification purpose, we simply classify hyperlens case as hyperbolic metamaterials type I, and cavity case type II. Simple comparison is show in Figure 4.6.

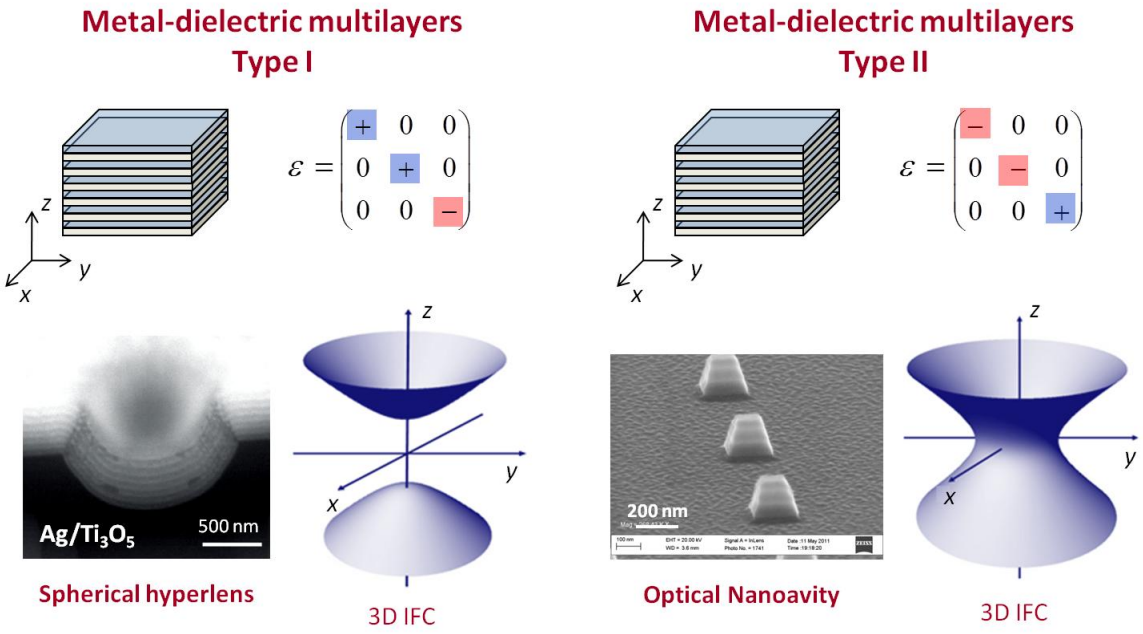

Figure 4.6. Comparison of hyperbolic metamaterials type I and II

4.3.3 Total internal reflection mechanism

As shown in Figure 4.3 (b), due to the nature of hyperbolic dispersion, the 3D hyperboloid supports large wave vectors including components in all *x*, *y*, *z* directions, where k_z can have the same order of magnitude with k_x or k_y. By cutting the indefinite medium into small cubes, 3D Fabry-Pérot cavities are formed with the TIR at the interface of air and indefinite medium. The hyperbolic IFC shown in Figure 4.3 does not form a closed curve and therefore propagating modes in certain directions are forbidden, resulting in different TIR conditions for different directions of propagation. For the top and bottom facets parallel with the multilayer, there is no mode in air that matches k_p (the momentum parallel with the multilayer) in the indefinite medium, and therefore these facets totally reflect light with any allowed incident angles. On the other hand, the TIR critical angle θ_c of the side walls is given by $\arctan\theta_c = \sqrt{\frac{\varepsilon_p}{\varepsilon_v\left(\varepsilon_p - 1\right)}}$ from the condition of $k_v > k_0$, based on the dispersion relation, equation (4.5). The permittivity tensor components parallel with ($\varepsilon_p = \varepsilon_x = \varepsilon_y$) and perpendicular to ($\varepsilon_v = \varepsilon_z$) the multilayer can be estimated using effective medium approximation as shown in equation (4.4). Figure 4.7 shows schematic how TIR happens in this metamaterial cavities.

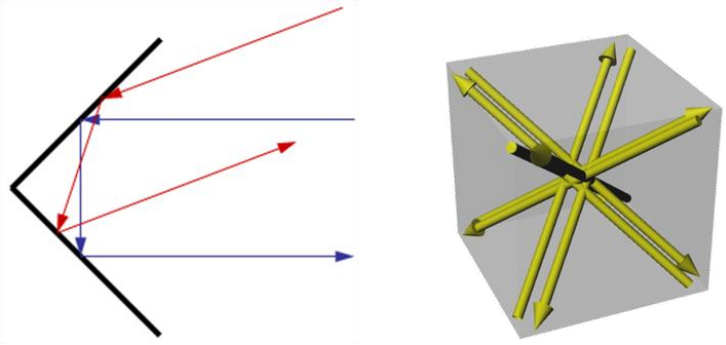

Figure 4.7. Schematic of TIR mechanism to construct cavity

4.4 Numerical study for metamaterial optical cavities

4.4.1 Simulation for ideal design case

Figure 4.8 shows the calculated cavity modes in indefinite optical cavities. The cross-section of the IFC at 150 THz was obtained from a spatial Fourier analysis of finite-difference time-domain (FDTD) calculations, which matches the effective medium calculation well (Figure 4.8 (a)). It is clear that the five cavities with different size combinations (width, height) support identical optical modes with the same resonant frequency and the same mode order (m_x, m_y, m_z) = (1, 1, 1) (Figure 4.8 (b)). The resonating wave vectors of these cavity modes locate on the same hyperbolic IFC in Figure 4.8 (a). For conventional optical cavities made of natural materials, the resonant frequency of a cavity mode is strongly dependent on cavity size because the available wave vector is limited to a circular or elliptical IFC in isotropic or anisotropic materials. In

contrast, indefinite cavities with drastically different sizes resonate at an identical frequency as long as the resonating wave vectors share the same IFC. This is due to the fact that, when the cavity scales down, the resonating wave vector increases along the unbounded hyperbolic dispersion. For example, an optical cavity with size (width, height) of (45, 30) nm, equivalent to (l/44, l/67), supports a wave vector of $k = 39.5k_0$ for the (1, 1, 1) mode, which corresponds to $n_{eff} = 39.5$. Furthermore, among the first five eigen-modes along the z-direction for a cavity with dimensions of (160, 150) nm (Figure 4.8 (c)), the higher order mode is found at a lower resonant frequency, displaying anomalous dispersion in relation to the mode orders due to the opposite signs of the principal components of the permittivity tensor. Such behavior is also observed when using the effective medium calculation (Figure 4.9).

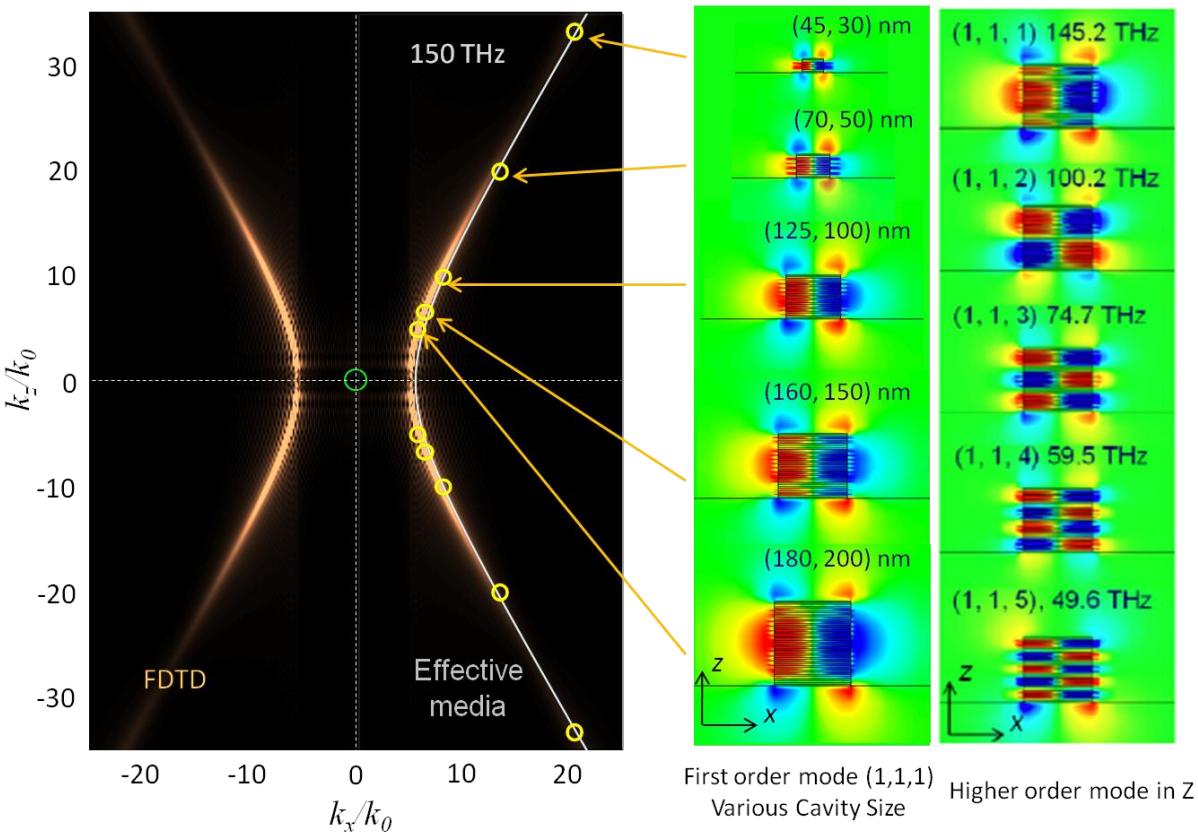

Figure 4.8. FDTD-calculated IFC of the multilayer metamaterial and mode profiles of indefinite optical cavities. (a) Cross-sectional view of the hyperbolic IFC for 4 nm silver and 6 nm germanium multilayer metamaterial at 150 THz (bronze curve), which matches the effective medium calculation (white line). The yellow circles represent the resonating wave vectors of the cavity modes shown in b, and the green circle represents the light cone of air. (b) FDTD-calculated electric field (Ez) distributions of the (1,1,1) mode for cavities made of 4 nm silver and 6 nm germanium multilayer metamaterial with different size (width, height) combinations but at the same resonant frequency of 150 THz. c, FDTD-calculated Ez distributions of the first five cavity modes along the z-direction for the (160,150) nm cavity.

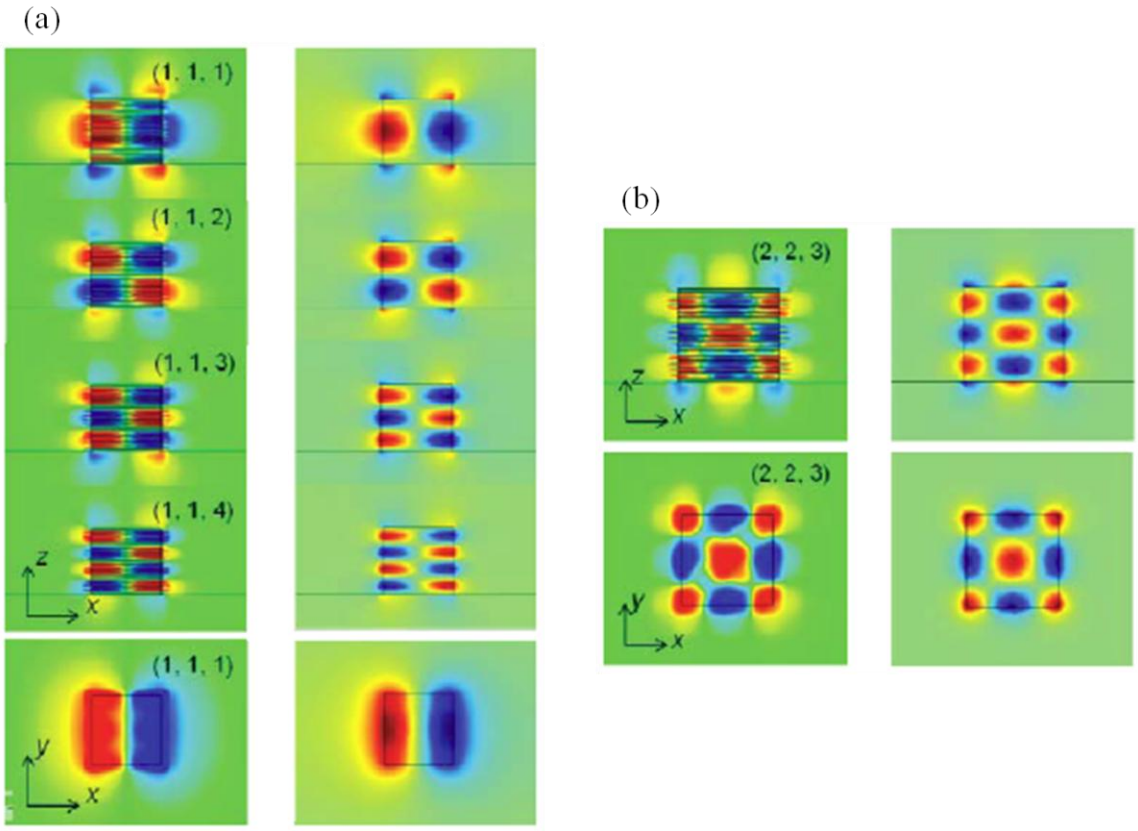

Figure 4.9. Cavity mode profiles obtained from the multilayer metamaterial calculation and the effective medium approach. (a) the electric field E_z distributions of the first four cavity modes along z direction for cavity with size of (160, 150) nm, with both the multilayer metamaterial calculation and the effective medium approach. The cavity modes calculated from these two methods match very well. (b) The electric field *Ez* distributions of the (2, 2, 3) mode at 183.6 THz supported in the same cavity.

4.4.2 Simulation for real design case

The metamaterial cavities were fabricated by alternating layers of 20nm Ag and 30nm Ge considering practical fabrication limit we can obtain from electron beam evaporator. Original design of 4nm Ag and 6nm Ge is too thin to achieve good quality of film from current state-of-the-art thin film deposition tools. Therefore, we choose more relaxed design we can reproduce the good quality of thin film stack consistently. A scanning electron microscope (SEM) image of cavity arrays (dimensions, (170, 150) nm) consisting of three pairs of silver–germanium multilayers, as well as close views of three cavities of different sizes. The side walls of the cavities are tilted (~75°) as a result of the lift-off process in the electron-beam lithography step. To make sure this relaxed design is OK to same cavity effect, we did same FDTD simulations confirming that cavity modes still exist in cavities with tilted side walls as shown in Figure 4.10 and 4.11, although the resonant frequencies shift higher (will be discussed later in this chapter).

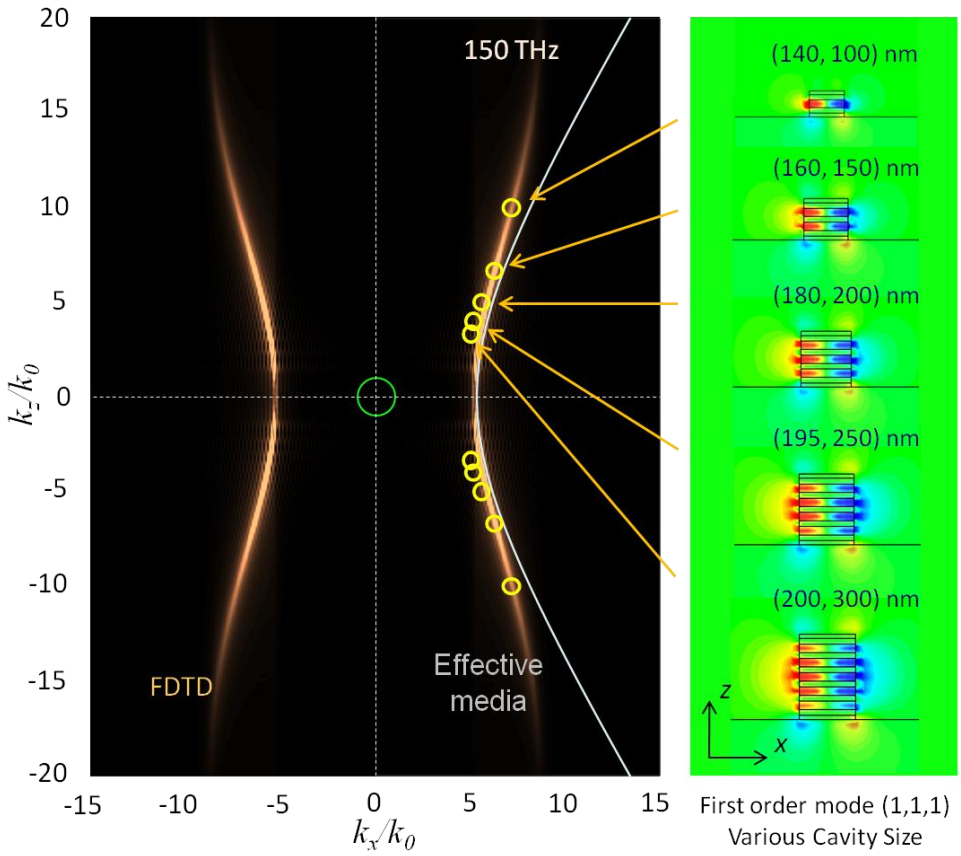

Figure 4.10. FDTD calculated IFC of multilayer metamaterial and mode profiles of metamaterial optical cavities. (a) The calculated IFC at 150 THz for multilayer metamaterial consisting of 20 nm silver and 30 nm germanium thin films (bronze colored curve), which matches the effective medium simulation (light blue colored curve) at low k region ($k << 2\pi/a$). At high k region, as the wavelength is close the period of the multilayer a, the dispersion curve deviates from the effective medium calculation at the edge of the first Brillouin zone. The yellow circles represent the resonating wave vectors of the cavity modes shown in b and the green circle is the light cone of air. (b) The electric field E_z distributions of the (1, 1, 1) mode for cavities with different (width, height) combination but the same resonant frequency at 150 THz.

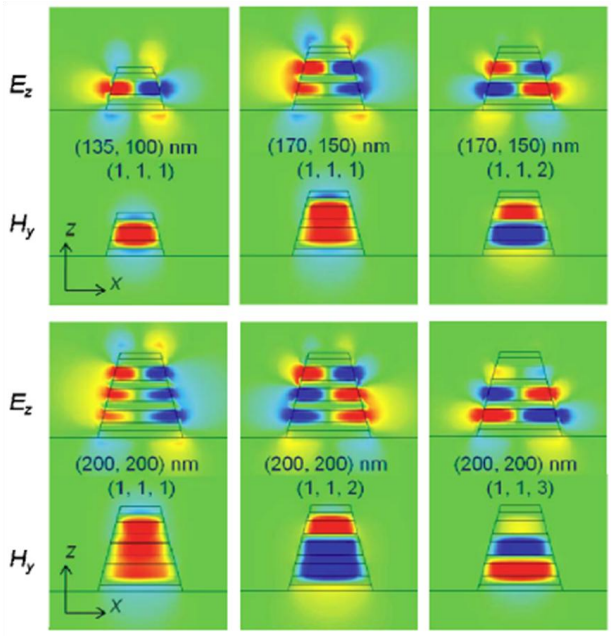

Figure 4.11. The FDTD calculated electric field E_z and magnetic field H_y distributions of the cavity modes for the three cavities. The cavity modes show magnetic dipole-like modes.

4.4.3 Simulation of FTIR measurement for metamaterial cavities

Transmission simulation (FTIR) is done and the result is shown in Figure 4.12.

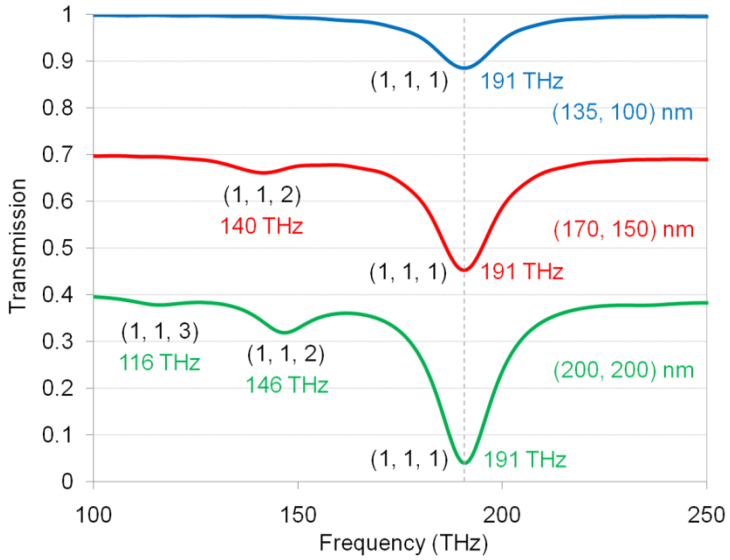

Figure 4.12. The FDTD simulated transmission spectra through the metamaterial optical cavities array with 5% cavity area filling ratio for cavities with different (width, height) combination. The collision frequency of 3γ is used in the Drude model of silver.

4.5 Fabrication of metamaterial nanocavities

The metamaterial optical cavities are fabricated by high-resolution electron-beam lithography (EBL), multilayer electron-beam evaporation and lift-off on a quartz substrate (Eagle XG). Indium-Tin-Oxide (ITO) as a conductive layer is deposited on top of the quartz substrate by a sputter (Auto 306, Edwards) for EBL. In order to minimize the optical absorption, only 2 nm ITO is sputtered. For clean sidewall and high aspect ratio lift-off process, bi-layer photoresist with 500 nm thick methyl methacrylate (MMA-EL8) and 50nm thick polymethyl-methacrylate (PMMA-A2) is used as electron-sensitive polymer. MMA is spin-coated at 5000rpm and soft-baked for 5 min at 150℃. PMMA is then coated at 2000rpm and followed by a 5 min soft-bake at 180℃. Since MMA is more sensitive than PMMA for the EBL exposure, the cavity square patterns will be defined with larger sizes in the bottom MMA layer while the top PMMA layer still maintains the designated sizes. This technique benefits the lift-off process and the sidewalls of cavities can be very clean. After defining the cavity square patterns in the MMA and PMMA bilayer with EBL (CABL-9000C, Crestec), extremely low temperature PMMA development at 4 ℃ is followed. Electron beam evaporation system (Solution, CHA) is then used to deposit the alternating 20nm Ag and 30nm Ge multilayer. To reduce the scattering from the surface roughness during the evaporation process, ultrahigh vacuum condition is kept at 10^{-7} Torr and the film growth rate is set as slow as 0.1nm/s. Finally, sample is soaked in acetone to lift off the photoresist layer. Due to the nature of electron-beam evaporation and lift off process, the side walls of cavities show 75° tilted angle which results in the cavity size difference between the top and the bottom. Since Ge has high surface energy and produces a good wetting effect for Ag growth [84, 85], the multilayer deposition is ultra-smooth and the top surface roughness is less than 1 nm after the deposition of four pairs of Ag-Ge multilayer, which is demonstrated from the AFM measurements. The roughness on the cavity surface in the SEM of Figure 4.13 is due to the diluted HNO_3 etch to enhance the image contrast. Fabrication process is shown in Figure 4.14.

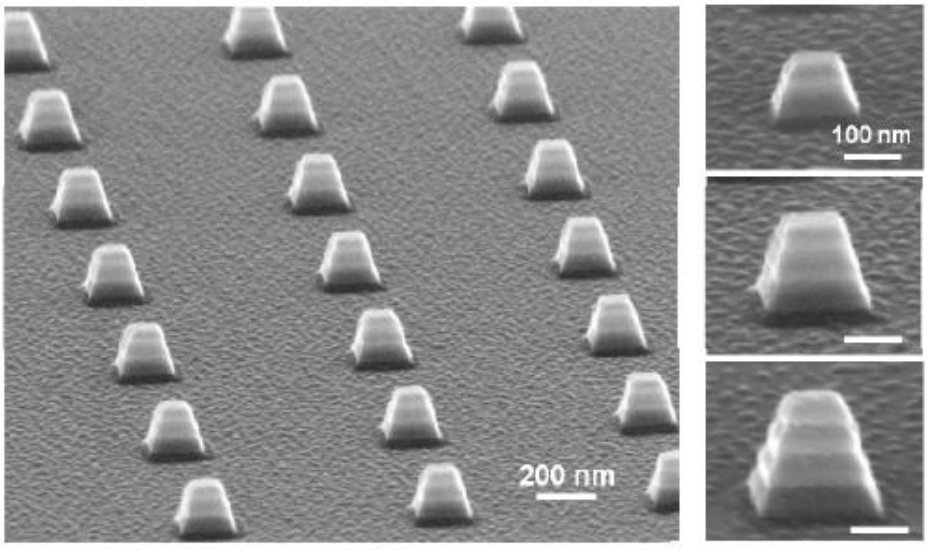

Figure 4.13. SEM image of an optical cavity array (cavity size, (170, 150) nm), with multilayer of 20nm Ag and 30nm Ge clearly visible and Magnified SEM images with different dimensions of (135, 100) nm, (170, 150) nm and (200, 200) nm, with two, three and four pairs, respectively

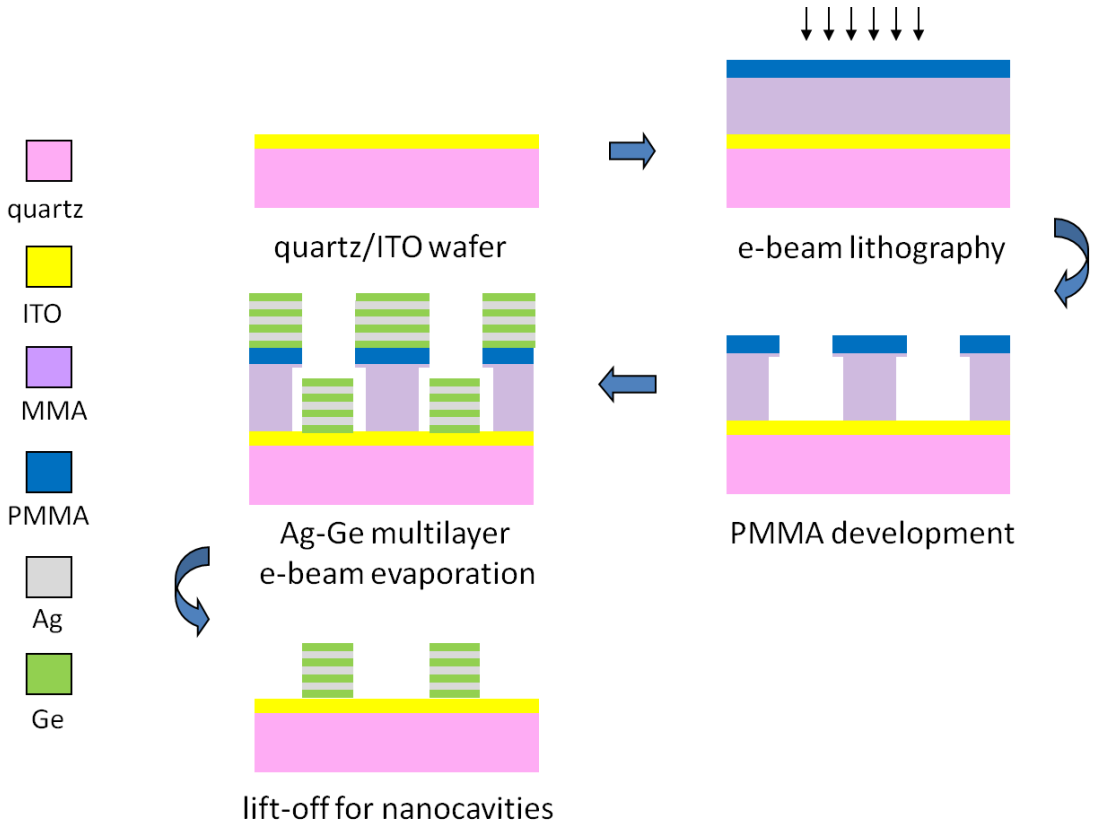

Figure 4.14. Fabrication process for metamaterial cavities. On ITO coated quartz wafer, EBL defines the template structure on bi-layer photoresist. Then, multilayer thin film stack is deposited by electron beam evaporator. Finally, the photoresist template is removed by lift-off process, and the final structure is made like ones shown in Figure 4.13.

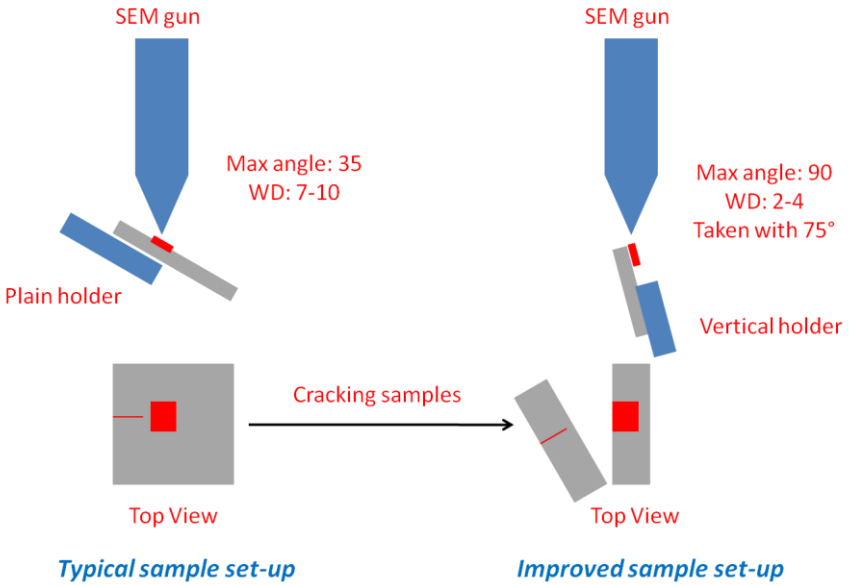

Figure 4.15. Set-up for high quality SEM showin in Figure 4.13

4.6 Optical measurement

The cavity modes were excited with a plane wave propagating along the z-direction, with x-direction polarization for the transmission measurement in Fourier-transform infrared (FTIR) spectroscopy. Figure 4.16 shows that the cavities with different sizes resonate at the same resonant frequency for the (1, 1, 1) modes. This phenomenon was observed for all three different resonance frequencies. It can be understood that, as the cavity size shrinks, both k_x and k_z scale up simultaneously along the same IFC to maintain the cavity resonant frequency. The metamaterial cavities therefore have size-dependent refractive indices, a unique feature that does not exist in conventional optical cavities where the refractive index is not strongly related to the cavity size and a larger cavity has a lower resonant frequency for a given mode order. Also, for a given cavity, the (1, 1, 2) mode has a lower resonant frequency than the (1, 1, 1) mode, thereby demonstrating the anomalous mode dispersion. When the mode order increases along the z-direction, a significant increase in k_z causes the higher-order mode to oscillate on a flatter IFC with a lower frequency (Figure 4.17). In contrast, in conventional optical cavities, the normal mode dispersion entails a higher resonating frequency for a higher-order mode in a given cavity. The measured resonating wave vectors for our indefinite cavities agree well with the calculated IFCs (Figure 4.17).

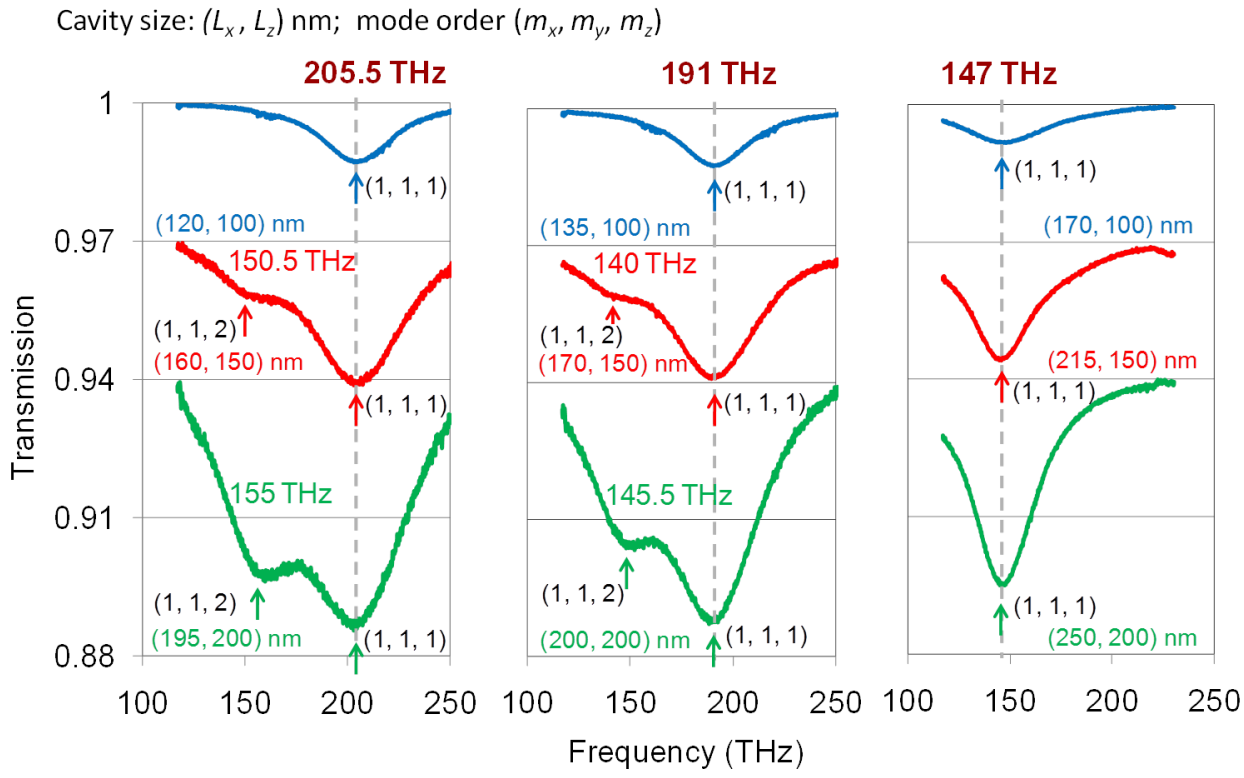

Figure 4.16. Measured FTIR transmission spectra through an indefinite optical cavity array with a 5% cavity area filling ratio for cavities of different sizes, where three panels correspond to cavities located at three different IFCs with resonant frequencies of 205.5, 191 and 147 THz.

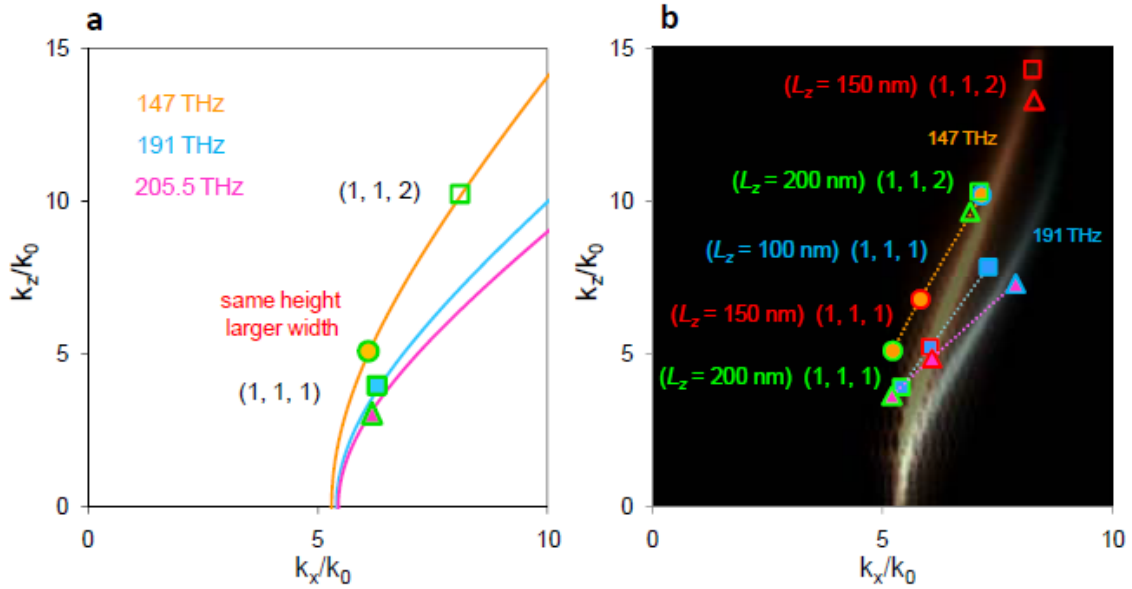

Figure 4.17. Calculated IFCs at different frequencies and resonating wave vectors of different cavity modes. (a) Hyperbolic IFCs at frequencies of 147, 191 and 205.5THz from the effective medium calculation. For cavities having the same height, a larger width gives a lower resonant frequency (the red arrow), showing the normal mode dispersion, since k_x is almost unchanged and k_z is getting larger. For the same cavity, the (1, 1, 2) mode has both larger k_x and k_z compared to the (1, 1, 1) mode, giving a lower resonant frequency (the green arrow), showing anomalous mode dispersion. (b) The measured resonating wave vectors of the (1, 1, 1) and (1, 1, 2) cavity modes shown in Figure 4.16, which match the FDTD calculated IFCs shown in the background. As illustrated with the green square markers, for cavity with size of (200, 200) nm, the (1, 1, 1) mode is located on the IFC at 191THz while the (1, 1, 2) mode is located on the IFC at 145.5THz.

By measuring the full-width at half-maximum (FWHM) of the resonance peaks in Figure 4.16, a total quality factor Q_{tot} of ~4 was obtained for all cavity modes, which is dominated by the absorption in the metal, as the relation is shown in equation (4.7)

$$\frac{1}{Q_{tot}} = \frac{1}{Q_{rad}} + \frac{1}{Q_{abs}} \tag{4.7}$$

where Q_{rad} and Q_{abs} are the quality factors from radiation and absorption, respectively. Although the resonance peaks have similar widths, the transmission depths for each cavity mode are different, which is related to the radiation coupling strength between the excitation plane wave and the cavity mode. It can be seen that the transmission depths are shallower for smaller cavities with the same mode order, and higher-order modes transmit more light (Figure 4.16). This indicates that the radiation coupling strength is strongly dependent on cavity size and mode order, which is determined by the resonating wave vector. As illustrated in Figure 4.8, for a smaller cavity, the resonating wave vector is further from the IFC of air, so radiation coupling between the cavity mode and the incident plane wave is weaker due to the increased momentum mismatch. The hyperbolic dispersion of an indefinite medium supports very large wave vectors, so the radiative loss of such cavities is strongly suppressed.

4.7 Results and discussion

4.7.1 Coupled mode theory

Based on the coupled mode theory, the schematic of the coupling between the plane wave and the metamaterial optical cavity is illustrated in Figure 4.17, which shows the relation between the amplitudes of the incoming plane wave S_{in}, the transmitted wave S_{trans}, the reflected wave S_{ref} and the cavity mode a. The rate equation for the evolution of the cavity mode is

$$\frac{da}{dt} = \left(i\omega_0 - \frac{1}{\tau_{rad,v}} - \frac{1}{\tau_{abs}} \right) a + \sqrt{\frac{1}{\tau_{rad,v}}} S_{in} \tag{4.8}$$

The incoming plane wave couples into the cavity mode and couples out to the transmitted wave vertically with the coupling rate of $1/\tau_{rad,v}$, while some photon energy is dissipated into heat with the absorption loss rate of $1/\tau_{abs}$. The transmitted wave can be expressed as

$$S_{trans} = S_{in} - \sqrt{\frac{1}{\tau_{rad,v}}} a \tag{4.9}$$

Since the total loss from the cavity mode includes both the radiation loss to free space and the absorption loss, the total quality factor Q_{tot} can be written as equation (4.7). Accordingly, the relation between the loss rate and the quality factor is

$$\frac{1}{\tau} = \frac{\omega}{2Q} \tag{4.10}$$

The on-resonance transmission *T* can be derived as

$$T = \left| \frac{S_{trans}}{S_{in}} \right|^2 = \left(\frac{Q_{tot}}{Q_{abs}} \right)^2 \tag{4.11}$$

The vertical radiation quality factor $Q_{rad,v}$ is then related to the on-resonance transmission T and the absorption quality factor Q_{abs}

$$Q_{rad,v} = \frac{\sqrt{T} \cdot Q_{abs}}{1 - \sqrt{T}} \tag{4.12}$$

Since the absorption loss dominates the total loss in the current metamaterial optical cavity and $Q_{abs} << Q_{rad,v}$, Q_{tot} is then approximately equal to Q_{abs} according to equation (4.8), and finally we have

$$Q_{rad,v} = \frac{\sqrt{T} \cdot Q_{tot}}{1 - \sqrt{T}} \tag{4.13}$$

Schematic of above derivation is shown in Figure 4.18.

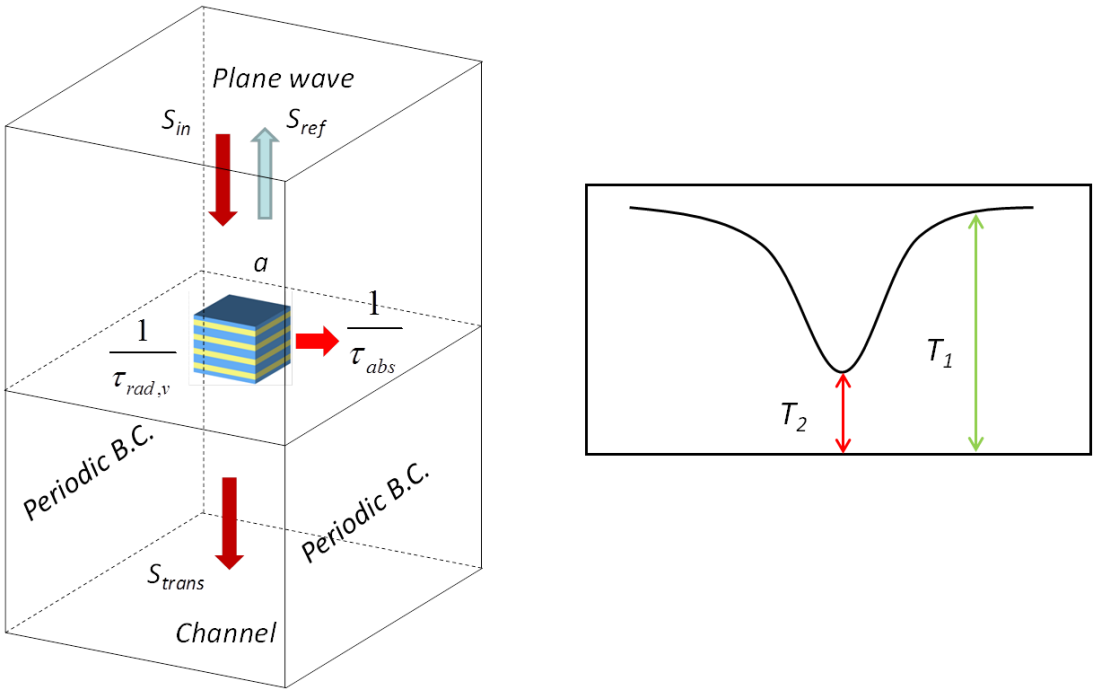

Figure 4.18. Illustration of the coupling between the plane wave and the metamaterial optical cavity based on the coupled mode theory. It shows the relation between the amplitudes of the incoming wave Sin, the transmitted wave S_{trans}, the reflected wave S_{ref} and the cavity mode a. $1/\tau_{rad,v}$ is the coupling rate between the plane wave and the cavity mode, and $1/\tau_{abs}$ is the absorption loss rate. The vertical radiation quality factor $Q_{rad,v}$ can be extracted from the on-resonance transmission T and the absorption quality factor Q_{abs}.

4.7.2 Mode volume calculation

The mode volume of the metamaterial optical cavity is calculated as

$$V_m = \frac{W_m}{\max\left[W(\vec{r})\right]} = \frac{1}{\max\left[W(\vec{r})\right]} \iiint W(\vec{r})\, d^3r \tag{4.14}$$

where W_m is the integrated electromagnetic energy over the entire space, and $W(\vec{r})$ is the local electromagnetic energy density at the position $\vec{r}$, taking into account the strongly dispersive property of silver [87],

$$W(\vec{r}) = \frac{1}{2}\left[\mathrm{Re}\left[\frac{d(\omega\varepsilon)}{d\omega}\right]\left|\vec{E}(\vec{r})\right|^2 + \mu\left|\vec{H}(\vec{r})\right|^2\right] \tag{4.14}$$

4.7.3 Effects of tilted side wall of fabricated cavities

Since the large wave vector supported in the indefinite metamaterial, the tilted side walls do not have significant effects on the optical properties of indefinite cavities, such as the quality factor, the spatial dispersion, and the mode profiles. The only major effect is that the resonant frequency will shift due to the deformed cavity geometry. Based on the FDTD simulation, Table S1 lists the resonant frequencies and radiation quality factors for both the (1, 1, 1) and (1, 1, 2) cavity modes supported by cavities having the same size of (170, 150) nm but with different tilted side wall angles of 90° and 75°. It is shown that the resonant frequencies increase when the side walls are tilted for both the cavity modes, due to the cavity size reduction. Radiation quality factor Q_{rad} does not change much for both modes since the radiation leakage from TIR from the tilted side walls is almost the same as the case from the straight side walls, although the critical angle of TIR is slightly larger at the air/indefinite-medium interface with 75° tilted angle. Cavity mode profiles are almost identical according to the field plot in Figure 4.10 and Figure 4.11 for tilted side wall angles of 90° and 75°, respectively.

Table 4.1. FDTD calculated resonant frequencies and radiation quality factors for both the (1, 1, 1) and (1, 1, 2) cavity modes supported by cavities having the same size of (170, 150) nm but with different tilted side wall angles.

Mode order	Side wall angle	Resonant frequency	Q_{rad}
(1, 1, 1)	90°	145 THz	233
	75°	191 THz	224
(1, 1, 2)	90°	110 THz	2724
	75°	140 THz	2719

4.7.4 Intrinsic material loss

The intrinsic material loss in indefinite cavities is due to the optical absorption of metallic layers, so that the total quality factor Q_{tot} is dominated by the absorption quality factor Q_{abs}. Figure 4.18 shows the FDTD calculated Q_{abs} based on the equation of $1/Q_{abs} = 1/Q_{tot} - 1/Q_{rad}$ for a single cavity, where the collision frequency of 9γ is used in the Drude model of silver. The Qabs is almost a constant (~ 4.2) independent of the wave vector, indicating it is strongly related to the intrinsic material loss rather than the cavity geometry and the mode order. In Figure 4.12, the collision frequency of 3γ is used in the Drude model of silver to calculate the transmission spectra through the cavities array, where γ is the collision frequency of bulk silver. The factor 3 is used here for considering the absorption loss from the silver film with a thickness of 20 nm ideally, which is very close to the theoretical value reported in Reference [85]. The calculated total quality factors Q_{tot} of cavity modes are around 11. However, for the fabricated cavities shown in Figure 4.16, the measured total quality factor Q_{tot} is around 4.1, which means in reality the collision frequency of the fabricated 20nm thick silver will be larger than 3γ. The FDTD simulation is then performed to fit the measured Q_{tot} in order to determine the actual collision frequency of silver. Figure 4.19 compares the FDTD calculated Q_{tot} and resonant frequency of the (1, 1, 1) mode for cavity with size of (180, 150) nm, as a function of various collision frequencies of silver. As the collision frequency increases from 3γ to 9γ, Q_{tot} reduces from 11.5 to 4.1 due to the increased absorption loss. Since the measured Q_{tot} is around 4.1, the actual collision frequency of silver is around 9γ. This value is very close to the experimental data

reported in Refefence [85] before the rapid post-annealing treatment of silver. The resonant frequency of cavity mode will only have slight shift around 168 THz as the collision frequency changes, with a variation of 1.6 THz. The cavity mode profiles will be identical for different collision frequencies. Although the total quality factor Q_{tot} is quite low due to the absorption loss from the metallic layers, indefinite cavities have ultrahigh Q_{tot}/V_m ratio up to 105 $(\lambda_0)^{-3}$, due to the deep subwavelength mode volume V_m (which can go down to 2.2×10-5 $(\lambda_0)^3$ shown in Figure 4.19). Such cavities support broadband operation with the bandwidth of several hundred nanometers due to the low Q_{tot}. The ultrahigh Q_{tot}/V_m ratio of these cavities can be used to enhance the light-matter interactions. The intrinsic material loss has been one of the major obstacles that limit the potential applications of plasmonics and metal-based metamaterials. Several approaches are currently the research focus of the field, including the rapid post-annealing treatment of silver [85], the extremely low-temperature operation of metal based optical devices [89, 90], and the gain compensated structures [91, 92, 93].

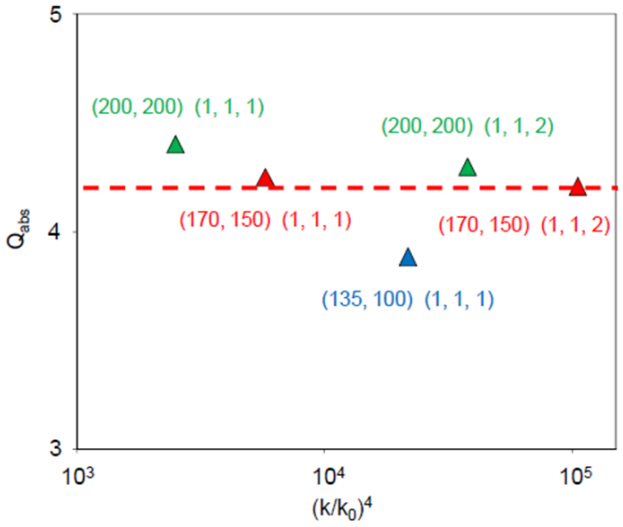

Figure 4.19. FDTD calculated Q_{abs} of the (1, 1, 1) modes and the (1, 1, 2) modes as functions of wave vector, based on the equation of $1/Q_{abs} = 1/Q_{tot} - 1/Q_{rad}$ for a single cavity. Q_{abs} is almost a constant (~ 4.2) independent of the wave vector, indicating it is strongly related to the material loss rather than the cavity geometry and the mode order. The collision frequency of 9γ is used in the Drude model of silver.

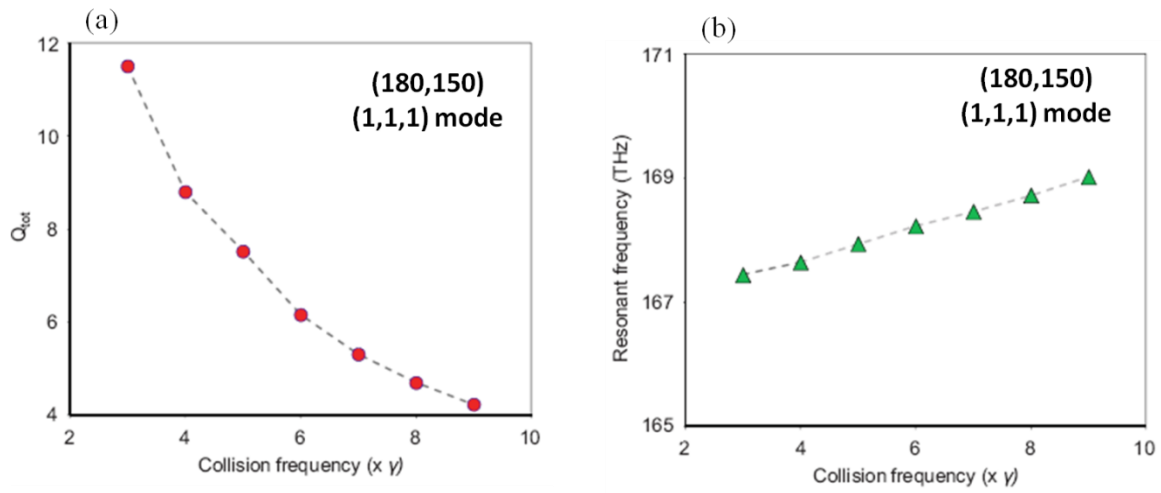

Figure 4.20. (a) FDTD calculated Q_{tot} of the (1, 1, 1) mode for cavity with size of (180, 150) nm, as a function of various collision frequencies of silver. The actual collision frequency of silver is around 9γ by fitting the measured Q_{tot}. (b) The FDTD calculated resonant frequency as a function of the collision frequency, showing a tiny change around 168 THz.

4.7.5 Vertical coupling radiation quality factor $Q_{rad,\,v}$

The ideal approach to measure the radiation quality factor of the cavity mode is to measure the electromagnetic energy decay inside the cavity without any intrinsic material loss for a single cavity. In reality, optical coupling has to be utilized to access the cavity mode and obtain its radiation ability. The averaged transmission response from the cavities array, instead of a single cavity, is measured with FTIR in our experiments in order to characterize the vertical coupling radiation quality factor $Q_{rad,v}$ between the plane wave in free space and the cavity mode. As shown in Figure 4.18, we can focus on a unit channel where the plane wave within certain cross section area couples with the cavity mode, due to the periodic boundary condition. We can look this channel as a waveguide, and the waveguide mode is the plane wave inside the channel. Using the coupled mode theory, the relation of the total quality factor Q_{tot}, the absorption quality factor Q_{abs}, and the vertical coupling radiation quality factor $Q_{rad,v}$ between the plane wave and the cavity mode can be obtained, from the measured transmission spectra through this channel. Due to the periodic boundary conditions around the channel, there is no horizontal radiation loss between each channel. It is very important to emphasize that here $Q_{rad,v}$ within the unit channel for cavities array is different from the vertical component of the radiation quality factor (Q_{rad}) of the cavity mode for a single cavity. The vertical component of the radiation quality factor of the cavity mode is the exclusive function of the single cavity and will not the function of the cavity filling ratio. Since the transmission through the channel is normalized with the plane wave inside, which is related to the cross section area of the channel, the vertical coupling radiation quality factor $Q_{rad,v}$ is a function of the cavity area filling ratio. Figure 4.21 (b) shows the FDTD calculated $Q_{rad,v}$ for cavity arrays with different cavity area filling ratios, where the cavity size is (180, 150) nm. As the cavity area filling ratio increases, the coupling strength between the plane wave inside the channel and the cavity mode gets stronger and $Q_{rad,v}$ will be reduced. With a certain cavity area filling ratio, $Q_{rad,v}$ will only strongly related to the wave vectors supported

inside cavities so that the radiation ability of different cavity modes can be compared. Figure 4.21 (a) plots the FDTD calculated $Q_{rad,v}$ for cavity arrays with cavity area filling ratios of 5% and 10% in order to compare with the experimental data in Figure 4.22 (a). It shows that the FDTD calculated results agree with the measured data very well. Although the value of $Q_{rad,v}$ for cavities array is not equal to either the radiation quality factor Q_{rad} of a single cavity or the vertical component of Q_{rad}, it reflects the vertical radiation coupling between the plane wave with a free space wave vector k_0 and the cavity mode having ultrahigh wave vector k, so that $Q_{rad,v}$ can well represent the vertical radiation loss of the individual cavity as a function of the wave vector, which has the same scaling law as Q_{rad}.

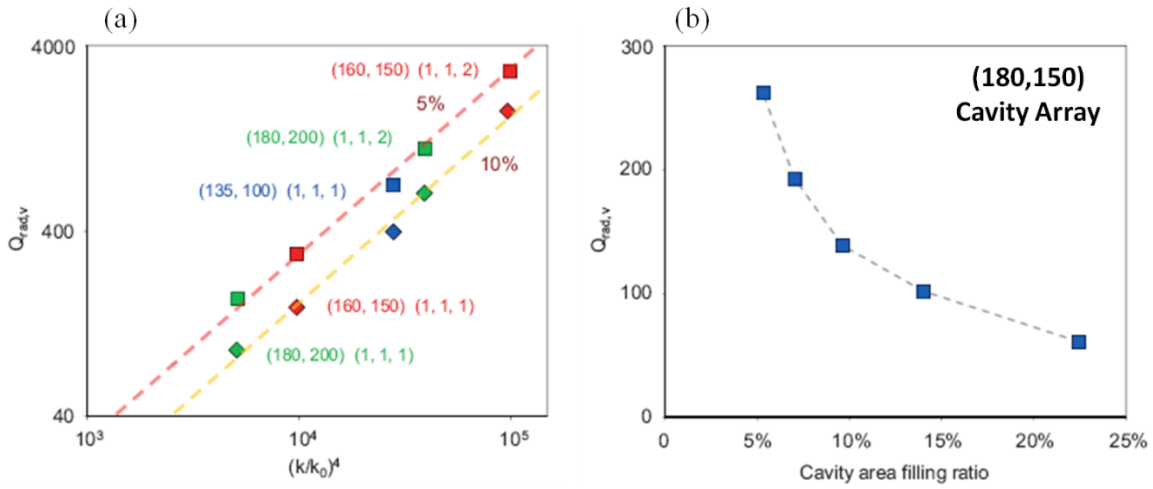

Figure 4.21. (a) FDTD calculated Qrad,v for cavity arrays with cavity area filling ratios of 5% and 10% shows the same power law of $(k/k_0)^4$. These results agree with the experimental data shown in Figure 4.21 (a) very well. The collision frequency of 9γ is used in the Drude model of silver. (b) FDTD calculated $Q_{rad,v}$ for cavity arrays with different cavity area filling ratios. The cavity has size of (180, 150) nm. As the filling ratio increases, the coupling strength between the plane wave inside the channel and the cavity mode gets stronger and $Q_{rad,v}$ will be reduced. The collision frequency of 9γ is used in the Drude model of silver.

To measure the Q_{rad} of the cavity modes, the absorption loss of the metal has to be isolated. We used coupled mode theory [80, 81] to retrieve the vertical coupling radiation quality factors $Q_{rad,v}$ between the plane wave and the cavity modes within a unit waveguide channel based on the measured transmission spectra from the cavity array.We found a universal fourth power law between $Q_{rad,v}$ and k: that is, $Q_{rad,v} \approx (k/k_0)^4$ or n_{eff}^4, for all cavities of different height, width, mode order and resonant frequency (Figure 4.22 (a)). Because the wave vector is proportional to the mode order divided by the cavity size, a smaller cavity or higher-mode order has a higher $Q_{rad,v}$ arising from the larger momentum mismatch. Although the experiment measured $Q_{rad,v}$, the FDTD calculation shows that the total radiation quality factor Qrad also follows the fourth power law, giving $Q_{rad} \approx (k/k_0)^4$ (Figure 4.22 (b)). Such a universal scaling law can be understood by the fact that Q_{rad} is proportional to n_{eff}/a_{rad}, where a_{rad} is the radiation loss of the cavity mode due to TIR. The radiated power can be represented as the integral of the k-space distribution of the cavity mode over the light cone of air in three dimensions, so that arad is proportional to k^{-3} [82,

83]. Because neff is proportional to k, Q_{rad} therefore increases as the fourth power of k (Figure 4.23). This unique behaviour of Q_{rad} in the indefinite cavity is very different from that in conventional dielectric optical cavities with dimensions on a scale larger than the wavelength, such as in microspheres and microdisks, where the TIR induced Qrad decreases when the cavity becomes smaller due to the larger surface curvature leading to increased radiation leakage into the light cone of air. The indefinite cavities also allow an unnaturally high refractive index, and a maximum value of 17.4 is obtained for the (1, 1, 2) modes shown in Figure 4.22 (a).

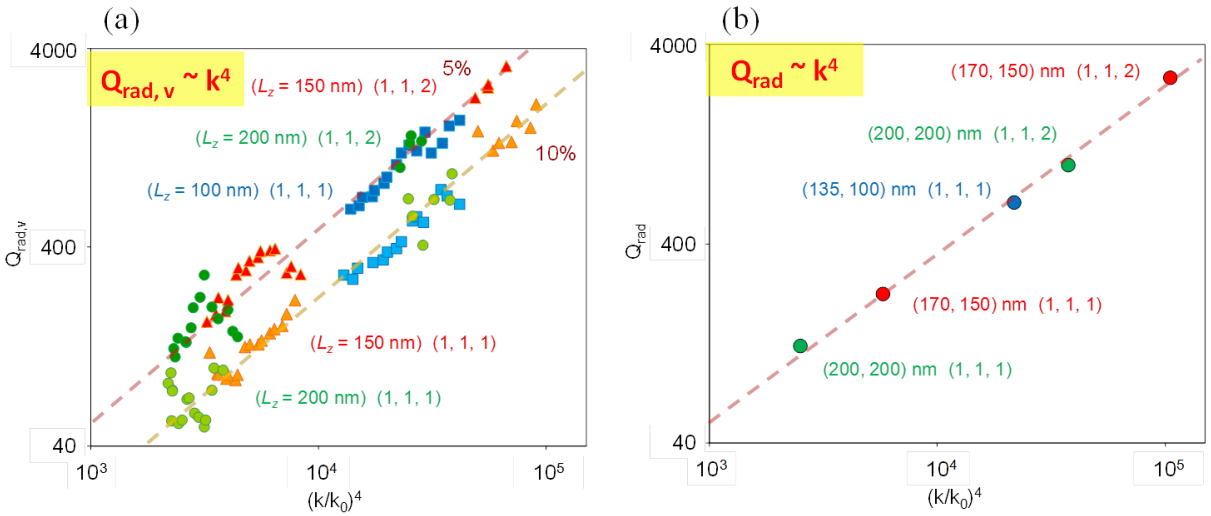

Figure 4.22. Radiation quality factor as a function of the resonating wave vector of a cavity mode. (a) The retrieved vertical radiation quality factor $Q_{rad,v}$ scales as $(k/k_0)^4$ or $n_{eff}{}^4$, a universal fourth power law, for cavities with different dimensions, resonance frequencies and mode orders. The cavity sizes investigated include (~110-185,100) nm, (~140-215,150) nm and (~185-255,200) nm for the (1,1,1) mode, and (~140-170,150) nm and (~185-210,200) nm for the (1,1,2) mode. Cavity area filling ratios of 5% and 10% are considered. (b) FDTD-calculated total radiation quality factor Q_{rad} of a single cavity shows the same power law. The dashed lines are fitting lines for the colored dots.

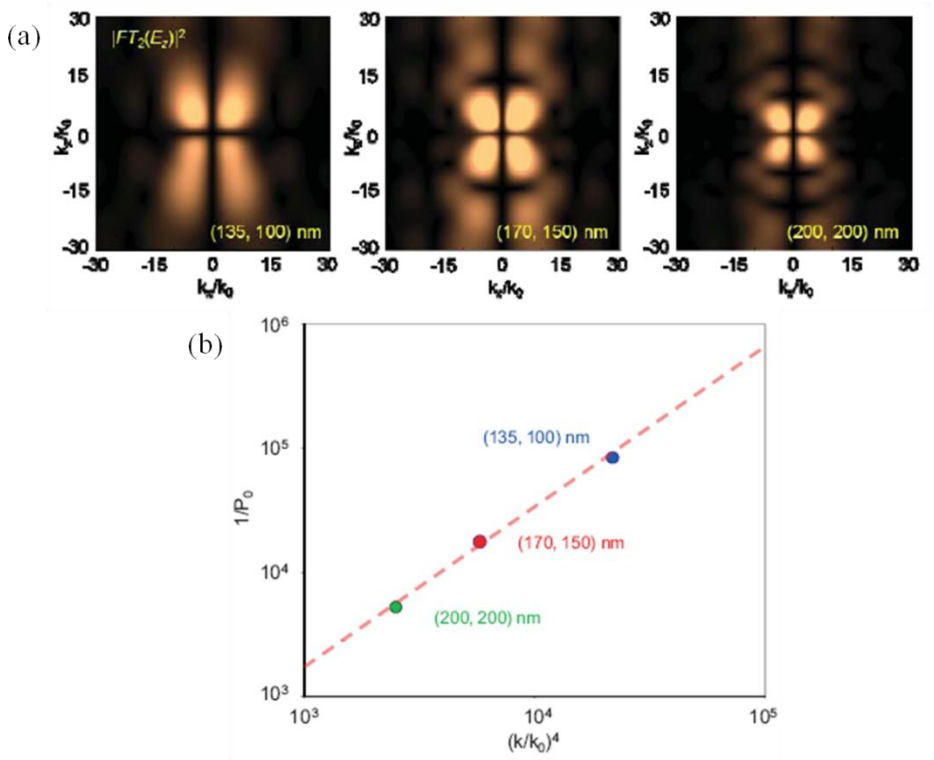

Figure 4.23. k-space analysis of cavity modes. (a) 2D k-space distribution of the electric field E_z component $|FT_2(E_z)|^2$ of the (1, 1, 1) modes in three different cavities at the same resonant frequency 191 THz as shown in Figure 4.11. (b). The radiative power of the cavity mode P_0 as a function of to $(k/k_0)^4$, where P0 is obtained from the integration of $|FT2(E_z)|^2$ within the light cone ($k_{//} \leq k_0$). It shows that the radiation quality factor Q_{rad} is proportional to $(k/k_0)^4$.

4.8 Summary

In this chapter, I demonstrated that 3D nanoscale optical cavities made of hyperbolic metamaterials have unprecedented anomalous scaling laws, which are drastically different from the conventional cavities made of natural materials. In contrast to conventional cavities whose sizes are limited to wavelength scale, indefinite cavities can be scaled down into extremely deep subwavelength sizes at the exact same resonant frequency, due to their size-dependent effective refractive indices. As cavity size goes down, the radiation quality factor increases dramatically, following the fourth power scaling law of the resonating wave vector resulted from the hyperbolic dispersion of indefinite medium. These unique properties of indefinitecavities will significantly increase the photon density of states and therefore enhance light-matter interactions. Such indefinite cavities open new possibilities for nanophotonic applications, in cavity quantum electrodynamics, optical nonlinearities, optomechanics, biosensing and optical communication. Also, this highly tunable refractive index metamaterials array will offer an opportunity achieving a variety of metasurface applications controlling light more exotically and actively with large scale metamaterials manufacturing.

Chapter 5

Chiral metamaterials for photo-induced negative refractive index switching

5.1 Introduction to chirality and chiral metamaterials

Chirality, which refers to structures lacking any mirror symmetry planes, is ubiquitous in nature, ranging from molecules and polymers to crystals. It is of great importance in biological and medical sciences as most biomolecules—the building blocks of life such as DNA—are chiral. Switching the handedness of chiral molecules under external stimuli has been found in various natural materials, such as organic molecules, sol-gel and even solid-state systems [94, 95, 96, 97, 98, 99]. It is also particularly important in the study of stereochemistry and biology, as molecules with the same constituent atoms but different spatial configurations can result in significantly different physiological responses. Chirality of natural materials can be switched structurally by various means, such as photoexcitation [94, 95, 96, 97], electron tunneling [100], application of electric fields [101] and temperature control [102]. Photo-induced chirality switching is of particular interest because of the ease of addressability. The underlying mechanism of chirality switching in organic molecules or polymers is a molecular structural change induced by an external stimulus, as illustrated in Figure 5.1. Examples are the photo-induced switching through the *trans-cis* isomerization of azobenzene and its derivatives [103, 104, 105]. The structurally induced chirality switching modifies the optical responses of molecules where the circular dichroism (CD), or the relative absorption between left-handed (LH) and right-handed (RH) circularly polarized waves, is reversed (Fig. 1). As chiral molecules interact differently with electromagnetic waves of LH and RH circular polarizations, chirality switching is of great significance in controlling the polarization states. However, the optical activity in natural materials is very weak, and therefore the effect of chirality switching is not conspicuous. Metamaterials are a new class of custom-designed composites with deep subwavelength building blocks, called metamolecules. Recent progress in metamaterials has led to the realization of gigantic optical activity that is several orders of magnitude stronger than that of natural materials [106, 107, 108, 109]. However, the handedness of those chiral metamolecules was fixed once fabricated and could not be reconfigured in real-time. The concept of stereochemistry has been recently introduced to metamaterials; the change in the spatial configuration in metamolecules induces dramatic change in their optical properties [110, 111]. A straight translation of chirality switching from organic molecules to metamolecules would be a structural reconfiguration of the metamolecule in response to an external stimulus. However, this would require a dynamically tunable mechanical system that entails great manufacturing complexity. Although mechanically tunable planar metamaterials have been demonstrated [112, 113, 114], the structural tuning or twisting of three-dimensional complex chiral metamolecules still faces significant challenges, not to mention the slow switching speed that is generally intrinsic to mechanical systems.

In this chapter, I will show that, through designing a delicate artificial chiral metamolecule incorporated with a photoactive medium, it is possible to transfer the concept of ‘handedness

switching' from organic chemistry to metamaterials without introducing any structural change, in stark contrast to the case of organic chiral molecules. We design optically switchable chiral terahertz metamaterials and experimentally observe handedness switching in the forms of reversed CD and reversed optical rotatory dispersion (ORD). It should be noted that the chirality (handedness) switching is a different process from the optically induced chirality in metamaterials previously demonstrated, where the chirality of a metamaterial was merely switched between on and off, but not reversed [115]. Benefitting from the strong switching effect in comparison to natural materials, the handedness-switching metamaterials may find important applications in terahertz technologies, ranging from vibrational CD for identification of the chirality and structures of organic molecules, to the precise non-contact Hall measurement.

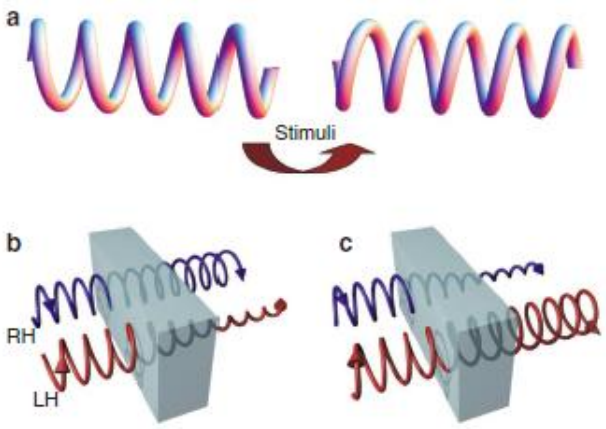

Figure 5.1. The general principle of chirality switching in natural materials. (a) Schematic of a chiral molecule that lacks mirror symmetry in all directions. Under an external stimulus such as photoexcitation, temperature change or electric field, the chiral molecule undergoes a structural change to its mirror image, that is, the chirality is switched. (b) A material composed of the chiral molecules absorbs light more strongly for one circular polarization than the other. (c) After chirality switching, the chiral material reverses its responses to the two circular polarizations.

5.2 Design of switchable chiral metamaterials

There are two pads in a unit structure to achieve switching effect: One is between pads and the other is middle of metal strip. As several literatures showed before, since the electric and magnetic dipoles share the same structural resonance, the excitation of one dipole would inevitably lead to the excitation of the other. Because the angle between directions of the two dipoles is small (~30^{o}), a strong chiral behavior is expected for this design. Under the condition without a external light, the left handed structure and the right handed structure are available, but the right handed structure will have different resonance frequency because the length of the gold strip with Si pad is shorter than the other so that the strength of electric dipole will be different as Figure 5.2 (a).

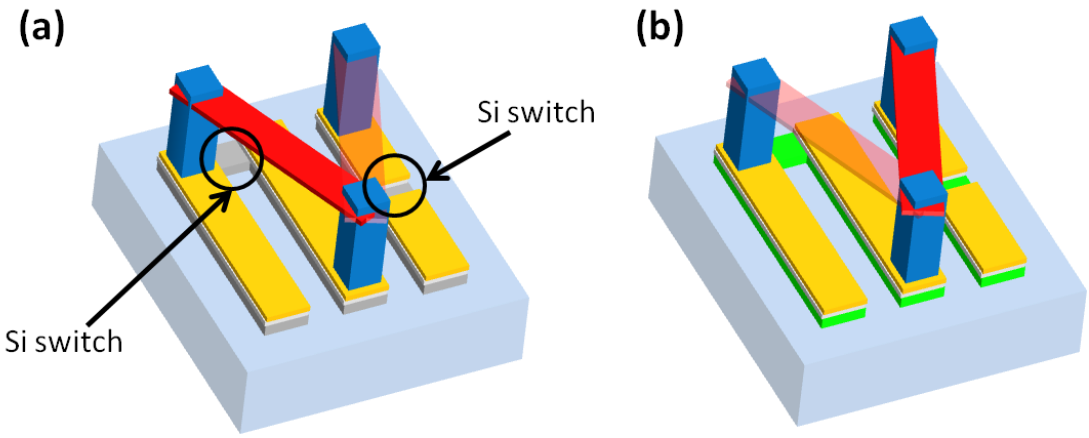

Figure 5.2. Schematic of photo-induced switching design. (a) without light (b) with light

On the contrary, when Si pads are activated by the external light, left handed structure is not working any longer because of shortage between two metal strips and right handed structure will happen since the metal strip will be connected electrically by electro-conductive Si pad as Figure 5.2 (b). In addition, the right handed structure will have the resonance frequency shifting to that of the left handed structure without the external light because the effective length of gold strip will be same the the other strip. Therefore, by controlling the external beam, two switching effects-shifting and attenuating resonances- are expected. Based on this schematic, the final design for chiral switching device is made as shown in Figure 5.3.

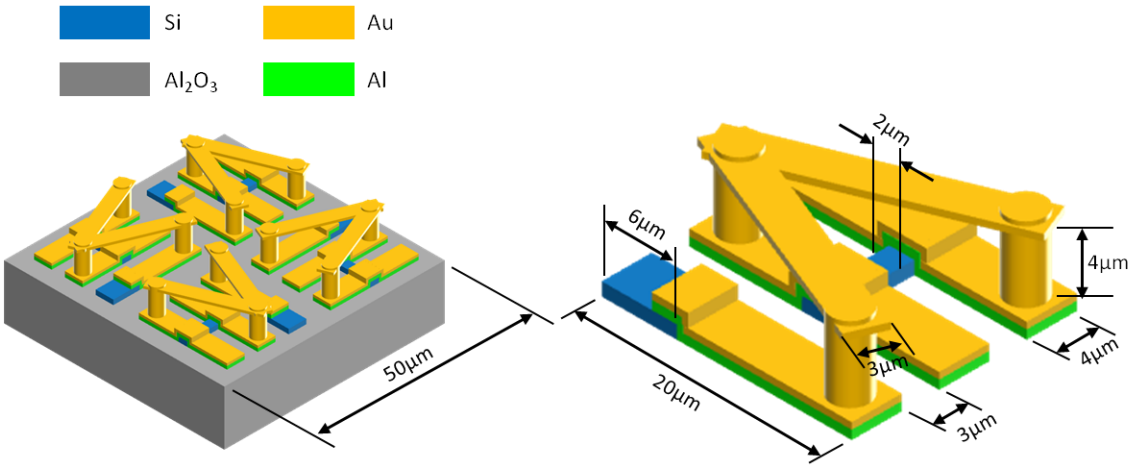

Figure 5.3. Final design of chiral switching metamaterials. Schematic of the chirality switching metamaterial. The unit cell consists of four chiral resonators with fourfold rotational symmetry. The key geometrical parameters are labeled in the figure.

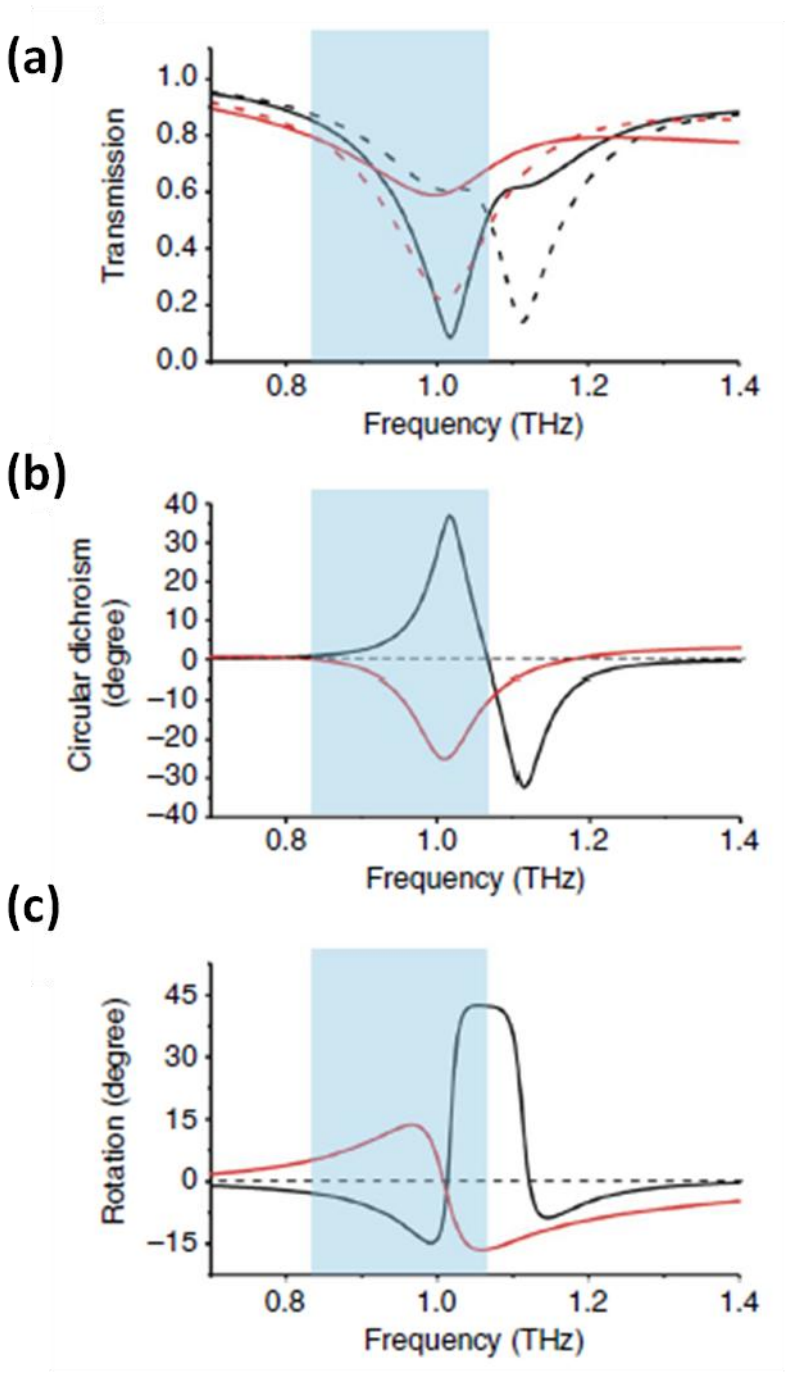

Figure 5.4. Theoretical calculations on chiral switching metamaterials. (a) The transmission spectra of left-handed (solid) and right-handed (dashed) circular polarizations, without (black) and with (red) photoexcitation. The shaded region represents the frequency range where the relative transmission amplitude between LH and RH polarization is reversed. (b) The ellipticity calculated from the transmission spectra without (black solid) and with photoexcitation (red solid). In the shaded area the sign of circular dichroism is flipped. (c) The optical rotatory dispersion (ORD) without (black solid) and with optical pumping (red solid). These numerical results show good agreement with the experimental observations.

5.3 Numerical studies of switchable chiral metamaterials

We have performed full-wave simulations to validate the above chirality switching metamaterials using CST Microwave Studio. Figure 3a shows the schematics of the unit cell of the metamaterial, which consists of four chiral resonators arranged with four-fold rotation symmetry. In the simulation, we have assumed a photo-conductivity of 5×10^4 Scm^{-1} for the optically irradiated silicon [118]. As shown in Figure 5.4 (a), in the absence of photo-excitation, the transmission spectra of the LH (black solid curve) and RH (black dashed curve) polarizations exhibit a strong resonance feature, with a transmission dip < 0.2, at 1.01 and 1.11 THz, respectively. These two resonances are consistent with the experimental results shown in Fig. 2. With photo-excitation, the resonance for the LH polarization is dramatically weakened, and the resonance for the RH polarization is shifted to a lower frequency around 1.005 THz, that is, closely aligned with that for the LH polarization without photo-excitation, but slightly broadened and less pronounced because of the extra ohmic loss introduced by the optically doped silicon pad. The calculated CD and ORD spectra are shown in Figure 5.4 (b) and (c). Reversed CD and ORD are simultaneously obtained in a broad frequency range from 0.84 to 1.07 THz, as marked by the shaded region. The simulation results are in reasonably good agreement with the experimental observations.

5.4 Fabrication of switchable chiral metamaterials

Large scale (2cm by 2cm) chiral metamaterials have been fabricated using standard semiconductor processing technologies of multi-step photolithography with overloay. The fabrication starts with a silicon-on-sapphire wafer. Silicon layer (600-nm thick) is patterned by photo-lithography (MA6, Karl Suss) and dry etched (PK-12 RIE, Plasma-Therm) to define the silicon pads (Figure 5.5 (a)). Aluminium (Al) is sputtered (300 nm; Auto 306, Edwards) onto the sample as an electrode for the subsequent electroplating process. On top of Al-covered silicon pads, 300-nm-thick gold pads are fabricated by photo-lithography, followed by electron beam evaporation (Solution, CHA Industries) and lift-off process (Figure 5.5 (b)). Five-micrometre-thick SU-8 (SU-8 3000, Microchem) is then coated and holes are patterned in the SU8 layer by photo-lithography and dry etching. Low current electroplating is performed to grow gold pillars in the holes (Figure 5.5 (c)). Gold bridges connecting the gold pillars are subsequently fabricated by photo-lithography and lift-off process (Figure 5.5 (d)). Finally, SU-8 and Al are removed by oxygen plasma etching and Al etchant (Type A, Transene Company), respectively, leading to the final structure shown in Figure 5.6 (a) and (b) of SEM images. We note that the metamaterial design and fabrication process can be easily transferred to sub-micron scale by replacing optical lithography with electron beam lithography. Indeed, by using Ebeam lithography and layer-by-layer fabrication, a three-dimensional magnetic metamaterial has been recently realized which operates at the infrared frequencies. This will be discussed in later chapter for nanofabrication.

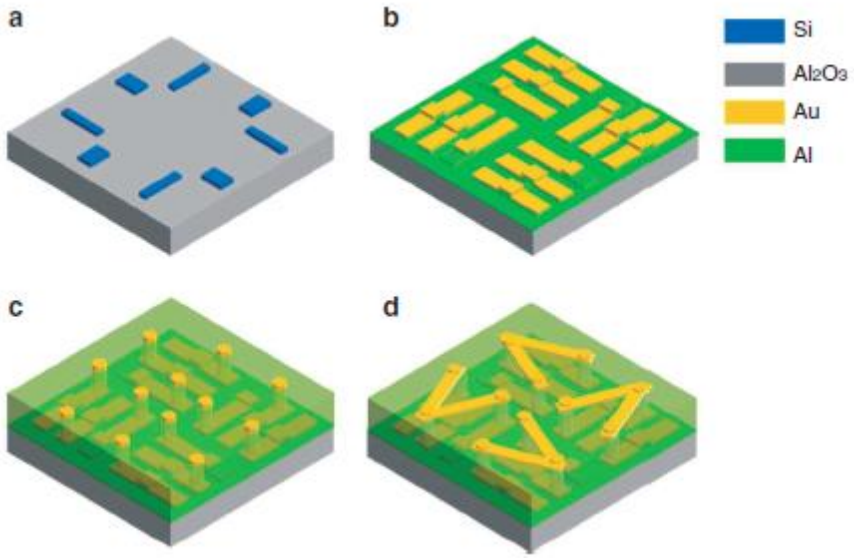

Figure 5.5. Flowchart of the fabrication of the handedness switching metamaterials. (a) Patterning of silicon pads (blue) on top of the Al_2O_3 substrate (grey) by photo-lithography and reactive ion etching. (b) Fabrication of gold pads on top of Al-coated silicon pads by a second photo-lithography followed by electron beam evaporation and lift-off process. (c) Coating of spin-on-glass and SU-8 on the wafer, followed by patterning of holes in the SU-8 by using photo-lithography and dry etching. Then, gold columns are created in the holes by electroplating. (d) Fabrication of gold bridges that connect the gold pillars by another photo-lithography process.

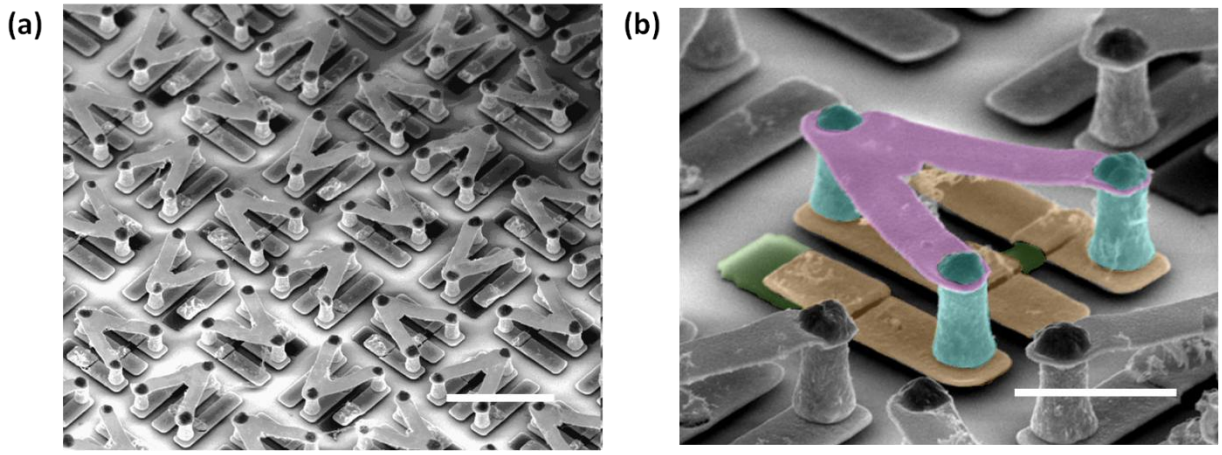

Figure 5.6. Scanning electron microscopy images of the fabricated metamaterial. The period of the metamaterial is 50μm, which is far less than the wavelength of the terahertz waves. Scale bar in (a), 25μm. In (b), the purple, blue and yellow colours represent the gold structures at different layers and the two silicon pads are shown in green. Scale bar, 10μm.

5.5 Optical measurement

The terahertz chiral metamolecules are fabricated on top of a silicon-on-sapphire (SOS) substrate. As shown in Figure 5.6 (a) and (b), the structures are arranged in a fourfold rotational symmetry, such that the eigen-modes of the light propagating along normal incidence are circularly polarized. The unit cell has a lateral dimension of 50μm, which is much less than the resonant wavelength of a few hundred micrometres in the terahertz frequency range, qualifying the chiral artificial structure as a metamaterial. Under strong optical illumination with photon energy greater than the bandgap of silicon, the excitation of photo-carriers turns the incorporated silicon pads from insulating to highly conducting state, switching optoelectronically the electromagnetic chirality. Similar approaches of incorporating semiconductors into sub-wavelength resonators have been used to actively manipulate the electromagnetic resonances of metamaterials by photo-excitation or electric bias [116, 117, 118, 119].

The chirality switching in the above terahertz metamaterials was experimentally demonstrated through measurements using an optical-pump terahertz-probe (OPTP) spectroscopy system. The OPTP system provides 50fs laser pulses with a centre wavelength of 800nm and a repetition rate of 1 kHz to optically excite charge carriers in the silicon pads. Figure 5.8 (a) shows the transmission spectra for the two circularly polarized terahertz waves. Without photo-excitation, the metamaterial strongly interacts with both LH and RH circular polarizations, but at different frequencies. This is demonstrated by the transmission dips at frequencies of 1.09 and 1.19 THz in the transmission spectra for LH (black solid) and RH (black dashed) circularly polarized waves, respectively. When illuminated by near-infrared laser pulses with fluence of about 1 $mJcm^{-2}$, the resonance for LH polarization disappears and leaves a featureless transmission spectrum (red solid). Meanwhile, we observed a red-shifted resonance for RH polarization (red dashed) from 1.19 to 1.05 THz. As a result, the relative transmission amplitudes between the two circular polarizations are reversed in the frequency range between 0.9 and 1.14 THz, as marked by the shaded region. Within this frequency range, the RH polarization, which initially exhibited a higher transmission, yields a lower transmission than that of LH polarization with photo-excitation.

CD and ORD are the two most commonly used techniques for characterizing the optical activity of chiral materials. CD refers to the difference between the transmission spectra of two circular polarizations, and therefore it is related to the ellipticity of the transmitted beam for a linearly polarized incident beam, and it can be calculated by $\theta = \tan^{-1}[(E_R - E_L)/(E_R + E_L)]$. Here E_R(L) is the transmission amplitude for right (left)-handed circular polarizations. In contrast, ORD measures the polarization rotation angle arising from the transmission-phase difference between the two circular polarizations. As shown in Figure 5.8 (b) and (c), within the shaded regions, both the signs of CD and ORD are indeed flipped. Interestingly, the ORD shows opposite switching behaviors at two frequency bands, from negative to positive between 0.9 and 1.05 THz, and from positive to negative between 1.05 and 1.19 THz. For an incident beam linearly polarized in the vertical direction, the representative polarization states of the transmitted wave are shown in Figure 5.8 (d) and (e) for two frequencies at 1.0 and 1.1 THz. At both frequencies, the polarization states of the transmitted wave are elliptical rotating clockwise when there is no photo-excitation (black). Under photo-excitation, the rotation is reversed to anticlockwise (red), and meanwhile, the polarization of the transmitted wave, that is, the orientation of the long axis of the polarization ellipses, is flipped from the left side of vertical

axis (-3.6°) to the right side (5.7°) at 1.0 THz, and from the right side (13.8°) to the left side (-3.6°) at 1.1 THz. The flipped ORD, together with reversed CD, serve as direct evidences that the metamaterial exhibits a genuine chirality switching behavior. The chirality switching effect of the demonstrated metamaterial is exceedingly strong, exhibiting a flipping of rotation angle in excess of 10° for a monolayer of metamolecules. Meanwhile, the switching is transient, and the sample will be restored to its original chiral state within milliseconds, determined by the lifetime of the photo-carriers in silicon. This relaxation time can be reduced by using photoactive materials with a shorter carrier lifetime.

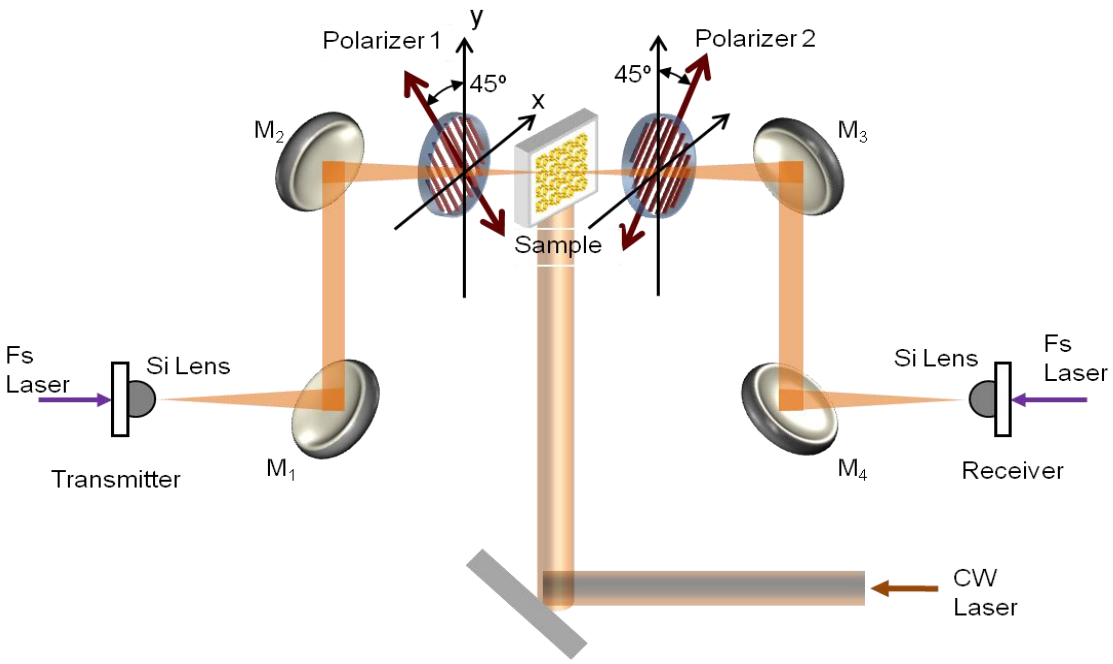

Figure 5.7. The time domain terahertz spectroscopy and pumped laser setup to characterize the transmissions of the chiral metamaterials. The photoconductive switch-based THz-TDS system consists of four paraboloidal mirrors arranged in an 8F confocal geometry, enabling excellent terahertz beam coupling between the transmitter and receiver and compressing the beam to a frequency independent beam waist with a diameter of 3.5mm as well. The THz-TDS system has a usable bandwidth of 0.1-4.5 THz (3 mm-67μm) and a signal to noise ratio over 4 orders of magnitude.

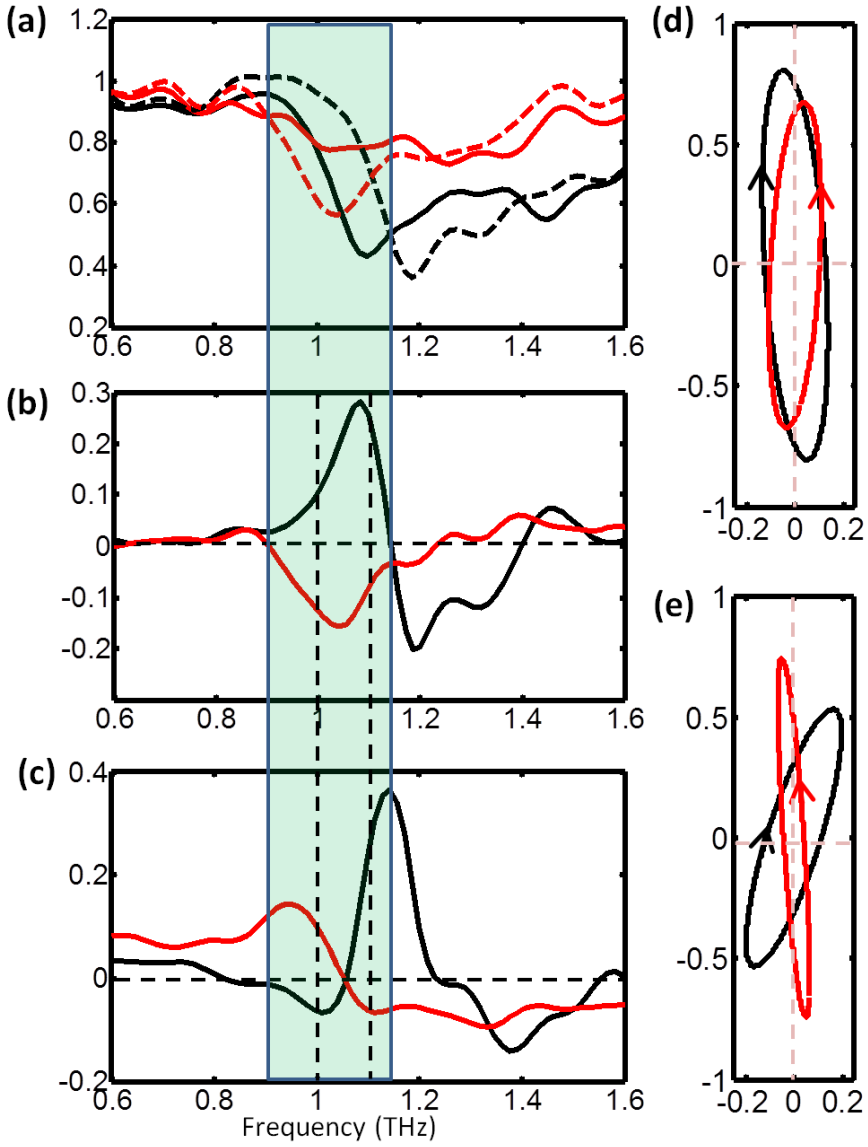

Figure 5.8. Experimental demonstration of chiral switching metamaterials. (a) The measured transmission spectra of LH (solid) and RH (dashed) circular polarizations, without (black) and with (red) photoexcitation. The shaded region represents the frequency range where the relative transmission amplitude between LH and RH polarization is reversed. (b) The CD spectrum (that is, ellipticity) and (c) the ORD derived from the measured transmission amplitude and phase spectra, without (black) and with (red) photoexcitation. In the shaded area, both the signs of CD and ORD are flipped, indicating the switching of handedness of the metamolecules. (d, e) The polarization states without (black) and with (red) photoexcitation for a linearly and vertically polarized incident terahertz beam transmitting through the chiral switching metamaterial at 1.0 and 1.1 THz, respectively. These two frequencies are also marked on the CD, and ORD spectra. At both frequencies, the polarization states turn from elliptical clockwise to elliptical anticlockwise under photoexcitation. Meanwhile, the major axis of the polarization ellipse is flipped from left to right at 1.0 THz, and from right to left at 1.1 THz.

5.6 Result and discussion

5.6.1 Optical characterization

We characterized the switchable chiral metamaterial using OPTP spectroscopy. The transmission of the linearly polarized terahertz pulses through the chiral metamaterial was measured in the time domain, with and without photo-excitation. Photo-excitation used near-infrared (~800 nm) laser pulses (50 fs) with a repetition rate of 1 kHz that illuminated the metamaterial sample a few picoseconds before the arrival of the terahertz pulses. The pump laser was focused down to a spot ~5 mm in diameter on the surface of the chiral sample, exciting electron-hole pairs across the 1.12 eV band gap in all the silicon islands. To obtain the transmission coefficients of circularly polarized waves, that is, T_{++}, T_{-+}, T_{+-} and T_{--}, we measured four linear copolarization and cross-polarization transmission coefficients, T_{xx}, T_{yx}, T_{xy} and T_{yy}. Transmission coefficients of circularly polarized waves were then obtained from the linear measurements using the following equation:

$$\begin{pmatrix} T_{++} & T_{+-} \\ T_{-+} & T_{--} \end{pmatrix} = \frac{1}{2}\begin{pmatrix} \left(T_{xx}+T_{yy}\right)+i\left(T_{xy}-T_{yx}\right) & \left(T_{xx}-T_{yy}\right)-i\left(T_{xy}+T_{yx}\right) \\ \left(T_{xx}-T_{yy}\right)+i\left(T_{xy}+T_{yx}\right) & \left(T_{xx}+T_{yy}\right)-i\left(T_{xy}-T_{yx}\right) \end{pmatrix} \tag{5.1}$$

where the first and second subscripts refer to the incident and transmitted wave, + and − refer to the RH and LH circularly polarized waves, and *x* and *y* refer to the two linearly polarized waves with the electric field polarized along two orthogonal directions.

5.6.2 Discussion about the measurement result

The underlying mechanism responsible for the chirality switching in the terahertz metamaterial is illustrated schematically in Figure 5.9. We start from a chiral metamaterial design that has recently led to the demonstration of chirality-induced negative refractive index14. As shown by the equivalent inductor-capacitor (LC) circuit of the metamolecule in Figure 5.9 (a), the metal loops function as inductors and the gap between the metal strips as capacitors of capacitance *C*. A single meta-atom exhibits a strong chirality at the LC resonance frequency, and consequently a positive or negative peak in CD spectrum depending on the chirality of the structure (Figure 5.9 (a)). When two chiral meta-atoms of the same shape but opposite chirality are assembled to form a metamolecule, the mirror symmetry is preserved, resulting in vanishing of optical activity. From a different point of view, the optical activity arising from these two meta-atoms of opposite chirality cancels out each other. We next introduce a silicon pad (gray) to each chiral meta-atom in the metamolecule, but at different locations, as shown in Figure 5.9 (b). In one chiral atom (Meta-A), a silicon pad bridges the two base metal stripes, and in the other atom (Meta-B), a silicon pad replaces part of a base metal strip. The functions of silicon pads are twofold: they serve to break the mirror symmetry and induce chirality for the combined metamolecule, and function as optoelectronic switches to flip the chirality of the metamolecule under strong photo-excitation. For Meta-A, the insertion of the silicon bridge has very little effect on the resonance, as silicon has only slightly higher permittivity (11.7) than the sapphire substrate (10.5). Whereas the incorporation of silicon pad in Meta-B introduces a significant reduction of the capacitance of the equivalent LC circuit ($C' < C$) due to the shortening of the

metal strip, and therefore shifts the resonance towards a higher frequency. The combined structure—the metamolecule—exhibits a representative CD spectrum in Figure 5.9 (b), where at the original resonance frequency ω_0, the electromagnetic response of the metamolecule is dominated by Meta-A, as the resonance of Meta-B is shifted to a higher frequency. This explains the experiment observation shown in Figure 5.8 (b) (black curve). Under strong photoexcitation using near-infrared laser pulses with photon energy above the bandgap of silicon, the generation of high concentration of free charge carriers turns the originally nearly intrinsic silicon pads into conductors (denoted by the blue areas in Figure 5.9 (c)). As shown by the equivalent circuit, this leads to an increase in the capacitance from *C′* to *C*, and consequently a red-shifting of resonance frequency of Meta-B to ω0. Meanwhile, the equivalent LC circuit for Meta-A is shortened due to photoexcitation. As a result, the CD is reversed, shown in Figure 5.9 (c), as compared with the case without photoexcitation in Figure 5.9 (b), which is in good agreement with the experimental observation of CD switching shown in Figure 5.8 (b). Here, we have proposed a general scheme to design active metamaterials, which can be switched between two opposite electromagnetic properties (in this case, left and right handedness). This scheme relies on the combination of two meta-atoms with opposite properties, one is functional but the other is inactive within the frequency range of interest. With suitable design, the two meta-atoms respond oppositely to an external stimulus, that is, the inactive one becoming functional and vice versa. This general design principle is not limited to handedness switching; it can also be applied to realize dynamic reversing of other electromagnetic functionalities.

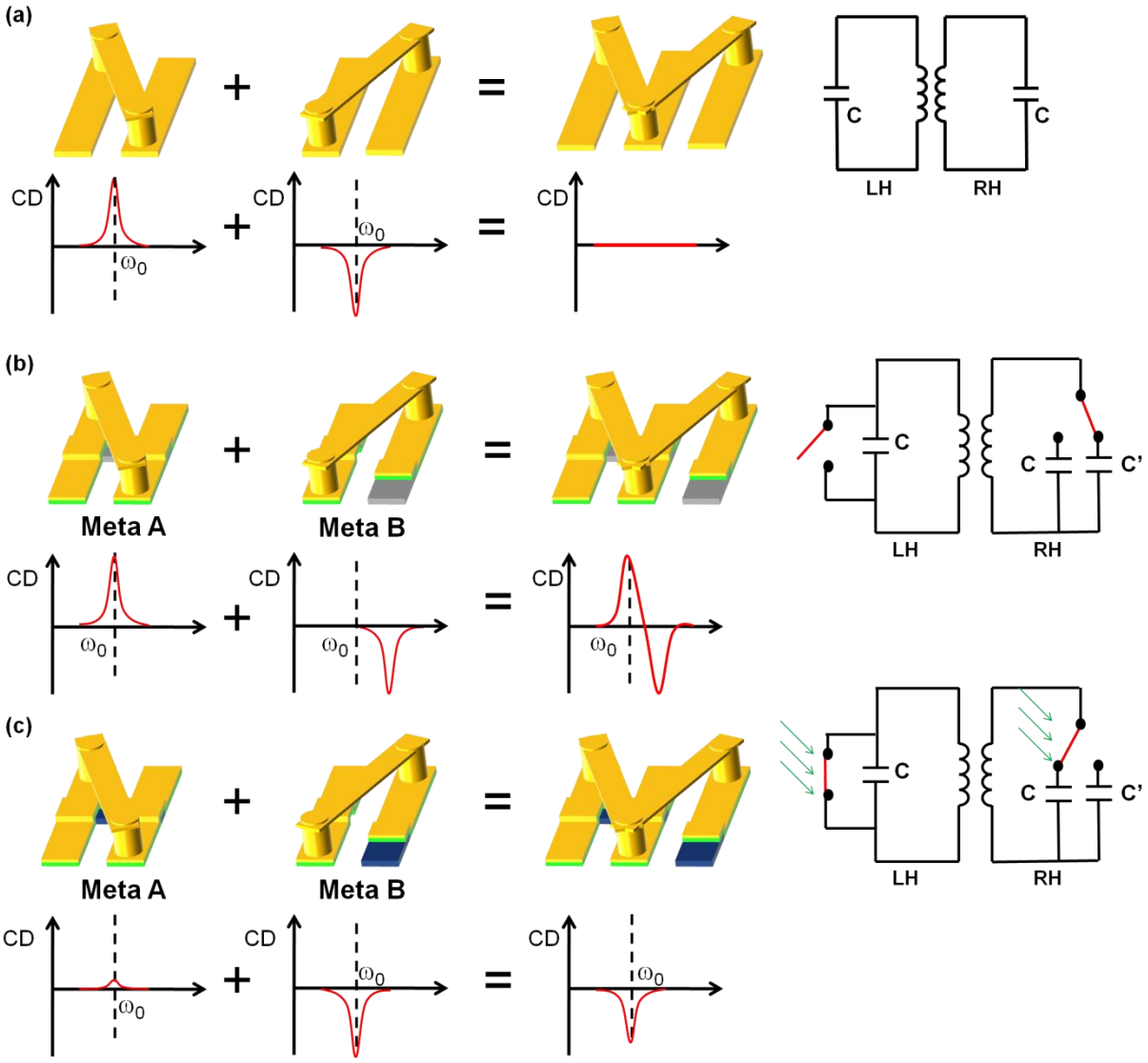

Figure 5.9. Schematic design of chiral switching metamaterials illustrating the underlying mechanism. (a) A metamolecule consisting of two meta-atoms of opposite chirality. Each meta-atom is a three-dimensional gold split-ring resonator with its loop tilted relative to the gap, leading to the coupling between the electric and magnetic responses, and consequently, a strong chirality and large CD at its resonance frequency. When combined into a metamolecule, the optical activity arising from the two meta-atoms cancels each other out, resulting in a vanishing circular dichroism spectrum. The metamolecule can be represented by an equivalent circuit consisting of two LC resonators. (b) Silicon pads (grey) are incorporated to the metamolecule. The mirror symmetry is broken, and the metamolecule exhibits chirality at resonance frequencies. The silicon pads also function as the optoelectronic switches in the equivalent circuit. (c) With photoexcitation, photocarriers are generated in the silicon pads, leading to a switching of chirality in the form of reversed circular dichroism.

5.7 Summary

Switching the handedness, or the chirality, of a molecule is of great importance in chemistry and biology, as molecules of different handedness exhibit dramatically different physiological properties and pharmacological effects. Here we experimentally demonstrate handedness switching in metamaterials, a new class of custom-designed composites with deep subwavelength building blocks, in response to external optical stimuli. The metamolecule monolayer flips the ellipticity and rotates the polarization angle of light in excess of 10° under optical excitation, a much stronger electromagnetic effect than that of naturally available molecules. Furthermore, the experimentally demonstrated optical switching effect does not require a structural reconfiguration, which is typically involved in molecular chirality switching and is inherently slow. The handedness switching in chiral metamolecules allows electromagnetic control of the polarization of light and will find important applications in manipulation of terahertz waves, such as dynamically tunable terahertz circular polarizers and polarization modulators for terahertz radiations.

Chapter 6

Metamaterials and plasmonics applications

6.1 Metasurface for strong photonic spin hall effect observation

6.1.1 Introduction to spin hall effect and metasurface

The relativistic spin-orbit coupling of electrons results in intrinsic spin precessions and, therefore, spin polarization–dependent transverse currents, leading to the observation of the spin Hall effect (SHE) and the emerging field of spintronics [120, 121, 122]. The coupling between an electron's spin degree of freedom and its orbital motion is similar to the coupling of the transverse electric andmagnetic components of a propagating electromagnetic field [123]. To conserve total angular momentum, an inhomogeneity of material's index of refraction can cause momentum transfer between the orbital and the spin angular momentum of light along its propagation trajectory, resulting in transverse splitting in polarizations. Such a photonic spin Hall effect (PSHE) was recently proposed theoretically to describe the spin-orbit interaction, the geometric phase, and the precession of polarization in weakly inhomogeneous media, as well as the interfaces between homogenous media [124, 125]. However, the experimental observation of the SHE of light is challenging, because the amount of momentum that a photon carries and the spin-orbit interaction between the photon and its medium are exceedingly small. The exploration of such a weak process relies on the accumulation of the effect through many multiple reflections [126] or ultrasensitive quantum weak measurements with pre- and postselections of spin states [127, 128]. Moreover, the present theory of PSHE assumes the conservation of total angular momentum over the entire beam [124, 125, 126, 127, 128], which may not hold, especially when tailored wavelength-scale photonic structures are introduced. In thiswork, we demonstrate experimentally the strong interactions between the spin and the orbital angular momentum of light in a thin metasurface—a two-dimensional (2D) electromagnetic nanostructure with designed in-plane phase retardation at the wavelength scale. In such an optically thin material, the resonance-induced anomalous "skew scattering" of light destroys the axial symmetry of the system that enables us to observe a giant PSHE, even at the normal incidence. In contrast, for interfaces between two homogeneous media, the spin-orbit coupling does not exist at normal incidence [124, 125, 126, 127, 128].

Metamaterial made of sub-wavelength composites has electromagnetic responses that largely originate from the designed structures rather than the constituent materials, leading to extraordinary properties including negative index of refraction [5, 6], superlens [13], and optical invisibilities [19, 25]. As 2D metamaterials, metasurfaces have shown intriguing abilities in manifesting electromagnetic waves [129, 130]. Recently, anomalous reflection and refraction at a metasurface has been reported [131, 132), and a variety of applications, such as flat lenses, have been explored [133, 134, 135, 136]. However, the general approach toward metasurfaces neglects the spin degree of freedom of light, which can be substantial in these materials. We show here that the rapidly varying in-plane phase retardation that is dependent on position along the metasurface introduces strong spin-orbit interactions, departing the light trajectory (S) from

what is depicted by Fermat principles, $S = S_{Fermat} + S_{SO}$ (where S_{SO} is a correction to the light trajectory raised from the metasurface-induced spin-orbit interaction).

6.1.2 Theoretical studies of spin hall effect at metasurface

The PSHE or the spin-orbit interaction arises from the noncolinear momentumand velocity (the change of trajectory) of light. When light is propagating along a curved trajectory (Figure 7.1 (a)), the time-varyingmomentum along the light path must introduce a geometric polarization rotation tomaintain the polarization transverse to its new propagation direction [137], $\dot{\hat{\boldsymbol{e}}} = -\boldsymbol{k}\left(\hat{\boldsymbol{e}}\cdot\dot{\boldsymbol{k}}\right)/k^2$. Here, $\dot{\hat{\boldsymbol{e}}}$ and $\boldsymbol{k}$ are the polarization vector and the wave vector, respectively, $\dot{\boldsymbol{k}}$ is the change of the propagation direction, and $\boldsymbol{k}$ is the amplitude of the wave vector. The rotation of the polarization depends on the helicity of light and may be considered as circular birefringence with a pure geometric origin [137, 138, 139]. As the back-action from geometric polarization rotations, the spin-orbit interaction also changes the propagation path of light, as we will show in later sections, resulting in a helicity-dependent transverse displacement for light; i.e., photonic SHE.

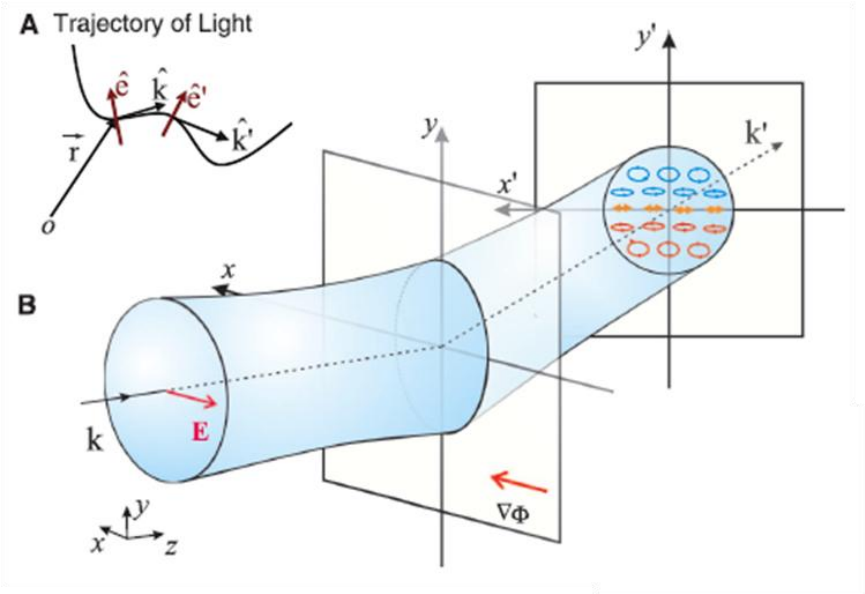

Figure 6.1. (a) Schematic of the PSHE. The spin-orbit interaction originates from the transverse nature of light. When light is propagating along a curved trajectory, the transversality of electromagnetic waves requires a rotation in polarization. (b) Transverse polarization splitting induced by a metasurface with a strong gradient of phase retardation along the x direction. The rapid phase retardation refracts light in a skewing direction and results in the PSHE. The strong spin-orbit interaction within the optically thin material leads to the accumulation of circular components of the beam in the transverse directions (y′ directions) of the beam, even when the incident angle is normal to the surface.

For an ordinary interface between two homogeneous media, when a Gaussian beam impinges onto the interface at normal incidence, the axial symmetry normal to the surface eliminates the spin-orbit coupling, and the total angular momentum of the entire beam is conserved. However, by designing a metasurface with a rapid gradient of phase discontinuity ∇F along the interface in the x direction (Figure 7.1 (b)), we introduce a strong spin-orbit coupling when the light is refracted off the interface. The rapid, wavelength-scale phase retardation can be incorporated in the optical path by suitable design of the interface [131, 132, 140]. Such a position-dependent phase discontinuity removes the axial symmetry of the interface and, therefore, allows us to observe the PSHE, even at the normal incident angle. Figure 1B schematically depicts the PSHE for the light beam that is refracted off a metasurface with rapid in-plane phase retardation. The momentum conservation at the metasurface now must take into account that the position-dependent phase retardation and the induced effective circular birefringence are determined by the gradient of the in-plane phase change or the curvature of the ray trajectory, $\left(\dot{\boldsymbol{k}}\times\boldsymbol{k}\right)/k^2$ (126), where $\dot{\boldsymbol{k}}$ depends on the rapid phase change. For a linearly polarized incidence, light of opposite helicities will be accumulated at the opposite edges of an anomalously refracted beam in the transverse direction (Figure 7.1 (b)). The faster the in-plane phase changes, the stronger the effect becomes. Because both the local phase response and its gradient are tailored through metamaterial design, the optical spin-orbit interaction from the metasurface is strong, broadband, and widely tunable.

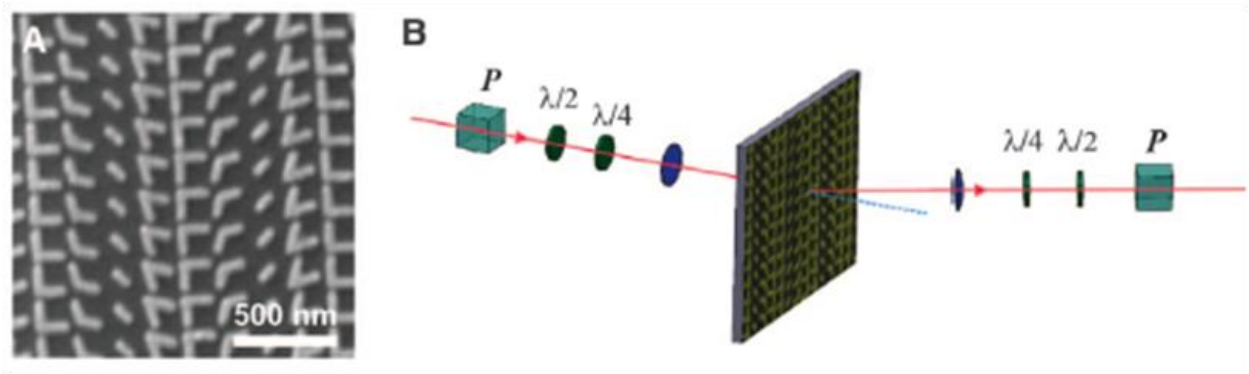

Figure 6.2. (a) Scanning electron microscope image of a metasurface with a rapid phase gradient in the horizontal (x) direction. The period of the constituent V-shaped antenna is 180nm. Eight antennas with different lengths, orientations, and spanning angles were chosen for a linear phase retardation, ranging from 0 to 2p with p/4 intervals. Scale bar, 500nm. (b) Light from a broadband source was focused onto the sample with a lens (focal length f = 50mm). The polarization can be adjusted in both the x and y directions with a half-wave plate. The regularly and anomalously refracted far-field transmission through the metasurface was collected using a lens (f = 50 mm) and imaged on an InGaAs camera. The polarization state of the transmission is resolved by using an achromatic quarter-wave plate (l/4), a half-wave plate (l/2), and a polarizer with a high extinction ratio. P, polarizer.

6.1.3 Experiment for photonic spin hall effect at metasurface

To experimentally observe the strong PSHE at the metasurfaces, we used a polarization-resolved detection setup (Figure 7.2), which allows precise measurement of Stokes parameters of the refracted beam, providing the spin-state information of the light in the far field. A supercontinuum light source is used for broadband measurement, and the beam is focused onto the sample with a spot size of ~50mm. Our metasurfaces consist of V-shaped gold antennas. By changing the length and orientation of the arms of the V-shaped structures, the sub-wavelength antennas at resonance introduce tunable phase retardations between the incident and the forward-propagating fields. For linear phase retardation along the x direction, we chose eight antennas with optimized geometry parameters. We measured samples with different phase gradients; a scanning electron microscope image of the antenna array with a phase gradient of 4.4 rad/mm is shown in Figure 7.2 (a) as one example. We used a lens of 50-mm focal length to collect the anomalously refracted far-field transmission through the metasurface, and we imaged this transmission on an InGaAs camera. The polarization of the incidence is linear and can be adjusted in either the x or y directions with a half-wave plate. The polarization states of the anomalously and the regularly refracted beams are resolved at the far field using an achromatic quarter-wave plate, a half-wave plate, and a polarizer with an extinction ratio greater than 105 for all wavelengths of interest.

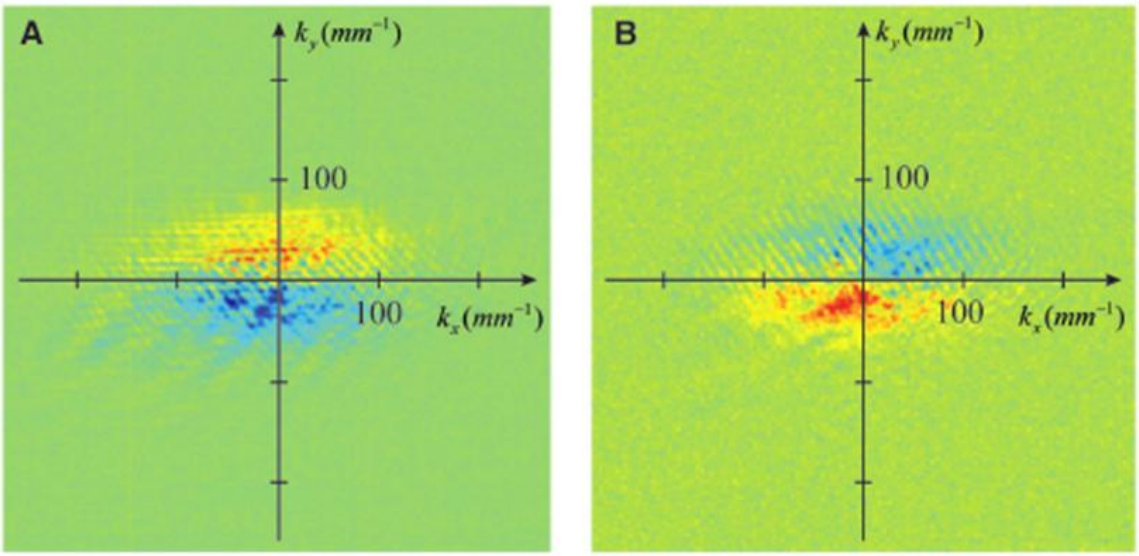

Figure 6.3. (a) Observation of a giant SHE: the helicity of the anomalously refracted beam. The incidence is from the silicon side onto the metasurface and is polarized along the x direction along the phase gradient. The incidence angle is at surface normal. Red and blue represent the right and left circular polarizations, respectively. (b) Helicity of the refracted beam with incidence polarized along the y direction.

6.1.4 Result and discussion

Because the polarization state of light is unambiguously determined by the Stokes vector $\vec{S}$ on a unit Poincaré sphere, the evolution of the polarization due to spin-orbit interaction is well described by the precession of the Stokes vector on a Poincaré sphere. The helicity or the handedness of light is given by the circular Stokes S_z parameter (circular polarization) $S_z = \frac{I_{\sigma^+} - I_{\sigma^-}}{I_{\sigma^+} + I_{\sigma^-}}$, where I_{σ^+} and I_{σ^-} are the intensities of the anomalous refraction with circular polarization basis, which were imaged successively using the camera. The coordinates of the image represent the in-plane wave vectors of the refracted beams. The right circular s+ and left circular s– polarizations are discriminated by setting appropriately the angle of the wave plates and polarization analyzer. Using the polarization-resolved detection, we calculated the circular Stokes parameter of the anomalously refracted beam from measurements for each pixel; this is shown in Figure 7.3 (a) for x-polarized incidence. The in-plane wave vector dependence of the circular Stokes parameters shows a maximal value of ~0.1 located at $\pm\pi/2$, and the sign of S_z is reversed between $+\pi/2$ and $-\pi/2$, showing a transverse motion of the polarization. Whereas the incident angle is kept at zero throughout the experiment, the phase gradient along the interface removes the axial symmetry of the optical system and enables the direct observation of the PSHE for the anomalously refracted beams with different circularly polarized light. Figure 7.3 (b) shows the PSHE effect for y-polarized incidence: The helicity of the refracted beam is clearly inverted due to the 90° phase rotation of the incidence. As the transverse spin current is solely determined by the longitudinal components of electromagnetic fields, such a distinct PSHE can only be observed in the anomalously refracted beam. As a control experiment, the spin-orbit coupling vanishes for the regularly transmitted beam, which exits the metasurface in the direction of the surface normal.

The photonic spin-orbit interaction in a curved light path not only manifests a helicity-dependent circular birefringence but also influences the trajectory of light. This effect resembles the Imbert-Fedorov shifts in the case of total internal reflections [141] and the recently observed optical Magnus effect at the near field [142, 143]. When considering spin-orbit coupling, the ordinary Fermat principle based on ray optics is not sufficient in predicting the light trajectory; therefore, a helicity-dependent transverse motion of light emerges from the additional geometric phases due to spin-orbit interaction. For the incident light with a pure spin state (circularly polarized), a transverse motion of the beam's center of mass is thus expected. Such a transverse motion occurs in real space and can be directly measured. Replacing the polarization optics shown in Figure 7.2 (b) with a variable liquid-crystal phase retarder, we measured the spin-dependent motion of photons (the relative displacement between the anomalously refracted I_{σ^+} and I_{σ^-}) by an InGaAs quadrant detector with polarized incident beam periodically modulated in either left- (s+) or right-handed (s–) polarization states. Throughout the experiment, the incidence angle was kept at normal incidence to the sample. The tailored in-plane phase gradient induces anomalous transmission at different refracting angles determined by the gradient. Figure 7.4 (a) shows the refraction angle at different incident wavelengths for multiple samples with different phase gradients. The anomalous refraction angle approaches 90° when the incident wavelength approaches eight times the period of the V-shaped antennas. In Figure 7.4 (b), the transverse motions of the beams are shown at the normal incident for wavelengths over hundreds

of nanometers in bandwidth. The feedback from the polarization clearly deviates the trajectory from that given by the ordinary Fermat Principle. The strong spin-orbit interactions induced by the resonant V-shaped antenna array enable the observation of the transverse displacement, which increases rapidly as the anomalous refraction angle approaches 90°. Current PSHE theory assumes the conserved momentum solely over the Gaussian wave packet. However, the rapid phase gradient along the metasurface supplies additional momentum, making such a theoretical treatment incomplete. A new apparatus for analytical analysis should be developed to account for such a rapid phase gradient along the surface. By considering the energy transport at the interface, however, the polarization-dependent transverse motion of light can be analyzed by integrating the Poynting vectors (including the evanescent fields) over the half-space of the exiting medium (see the supplementary materials). The strong photonic SHE at a metasurface with a designed phase discontinuity over the wavelength scale enables the observation of transverse motions of circularly polarized light. The anomalous skew scattering of light simultaneously breaks the rotational symmetry in the polarization space and the axial symmetry along its trajectory, giving rise to a broadband PSHE, even at the normal incidence. The generation and manipulation of strong spin-orbit interaction of light with tailored nanomaterials provide a new degree of freedom in information transfer between spin and orbital angular momentum of photons.

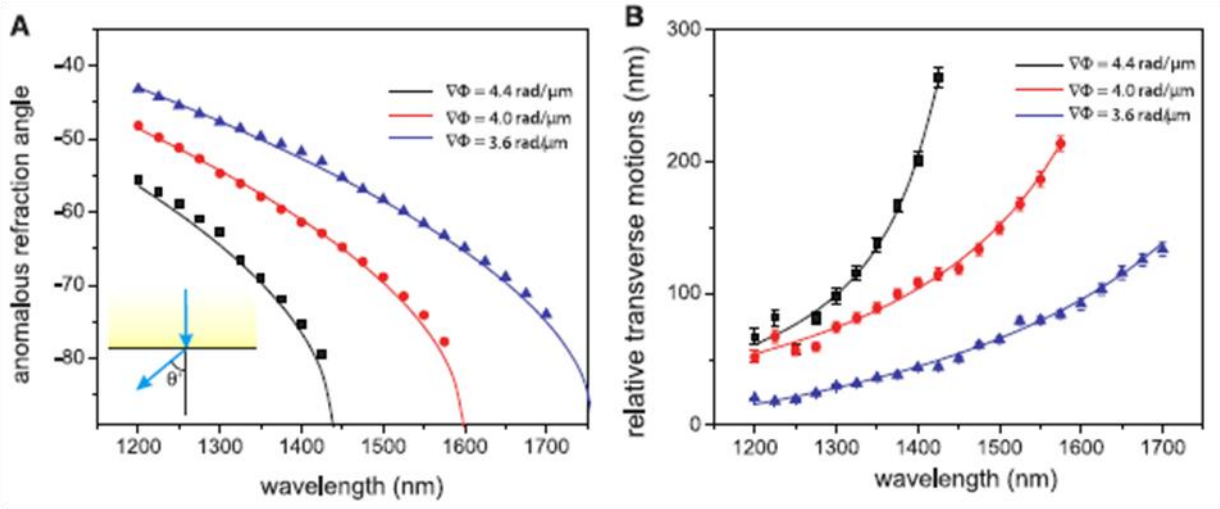

Figure 6.4. (a)Wavelength dependence of the refraction angles when excitation is normally incident onto the metasurface. The measurement was conducted for three samples with different phase gradients of 3.6, 4.0, and 4.4 rad/mm. Themeasured refraction angles agree well with the theoretical predictions (solid curves). The angles are the same for both the left and right circularly polarized light. (Inset) Schematic depiction of the light trajectory for the anomalous refraction for the surface normal incidence. (b) Transverse motion (data points with error bars) between anomalously refracted light beams with right and left circular polarizations, showing a PSHE effect over a broad range of wavelengths. Solid curves are a guide for the eyes. The measurement was performed for three metasurfaces with different phase gradients. The incidence was kept at surface normal but was periodically modulated between the left and right circular polarizations. Any transverse motion of the weight center of the beam was detected by a position-sensitive detector.

6.1.5 Analysis for photonic spin hall effect

One can quantitatively evaluate the PSHE shift at metasurfaces by considering the total energy transport at the interfaces. Any transverse motion of light is captured by the transverse components of Poynting vectors. Integrating the Poynting vectors (including the evanescent fields) over the full half-space above the metasurface allows us to evaluate the overall transverse displacement for a transmitted beam with finite size [144],

$$\Delta = \frac{1}{S_z}\int_0^\infty S_y(z)dz \tag{7.1}$$

Here S_y denotes the Poynting vector component that is perpendicular to the plane of incidence (*i.e.*, along transverse *y*-direction in Figure 7.1). S_z is the *z* (surface normal) component of the Poynting vector of the transmitted beam at the interface ($z = 0$). The procedure is general and applicable to both transmitted and reflected fields. A similar approach has been employed by Renard to analyze the Göös-Hänchen effect a longitudinal beam displacement occurs at Total Internal Reflection, by integrating the longitudinal components of Poynting vector $\delta_{GH} = \frac{1}{S_z}\int_0^\infty S_x(z)dz$ (30). To evaluate the effect numerically we use the rigorous Fourier modal method for solving the Poynting vectors of the transmitted fields [145]. Figure 7.5 show the numerically integrated PSHE shifts for a metasurface with a phase gradient of 4.4 rad/μm. The incident polarization is circular and the result agrees well with the experiments. The finite sized Gaussian beam is simulated by the superposition of a set of plane waves (11×11 plane waves) spanning in both polar and azimuthal directions,

$$E(r) = \int_{-\infty}^{\infty} e(k)E_0 \exp\left[-\frac{k_{//}^2}{\sigma_k^2}\right] e^{-ik\cdot r}dr^3 \tag{7.2}$$

Here ($\boldsymbol{k}$) is the electrical field vector of each individual plane wave, and E_0 is the amplitude of the incident Gaussian wavepacket. $k_{||}$ is the transverse components of the wave vector $\boldsymbol{k}$. σ_k measures the angular spectral width of the beam and a 4-degree spectral width is chosen for the calculations shown in Figure 7.5. For each individual plane wave, sufficiently large numbers of Fourier orders (21×21) were retained in the simulation to ensure the convergence.

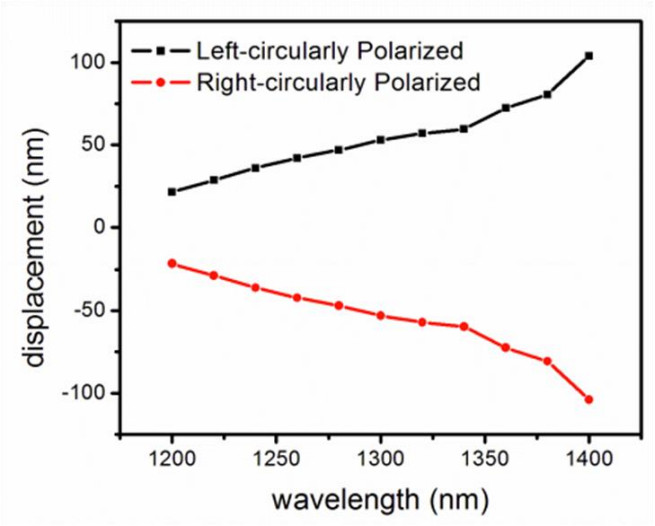

Figure 6.5. PSHE of circularly polarized light for a metasurface with a phase gradient of 4.4rad/μm

6.1.6 Summary

The spin Hall effect (SHE) of light is very weak because of the extremely small photon momentum and spin-orbit interaction. Here, we reported a strong photonic SHE resulting in a measured large splitting of polarized light at metasurfaces [146]. The rapidly varying phase discontinuities along a metasurface, breaking the axial symmetry of the system, enable the direct observation of large transverse motion of circularly polarized light, even at normal incidence. The strong spin-orbit interaction deviates the polarized light from the trajectory prescribed by the ordinary Fermat principle. Such a strong and broadband photonic SHE may provide a route for exploiting the spin and orbit angular momentum of light for information processing and communication.

6.2 Plasmonics assisted flying head nanolithography

6.2.1 Introduction to nanolithography beyond diffraction limit

Optical imaging and photolithography promise broad applications in nano-electronics, metrologies, and single-molecule biology. Light diffraction however sets a fundamental limit on optical resolution, and it poses a critical challenge to the down-scaling of nano-scale manufacturing. Surface plasmons have been used to circumvent the diffraction limit as they have shorter wavelengths. However, this approach has a trade-off between resolution and energy efficiency that arises from the substantial momentum mismatch. Here we report a novel multi-stage scheme that is capable of efficiently compressing the optical energy at deep sub-wavelength scales through the progressive coupling of propagating surface plasmons (PSPs) and localized surface plasmons (LSPs). Combining this with airbearing surface technology, we demonstrate a plasmonic lithography with 22nm half-pitch resolution at scanning speeds up to 10m/s. This low-cost scheme has the potential of higher throughput than current photolithography, and it opens a new approach towards the next generation semiconductor manufacturing. Creating super-fine nano-scale patterns with high throughput is essential for high-speed computing, data storage and broader applications for nano-manufacturing. Photolithography has been the most successful process for continuing the scaling down of semiconductor devices as predicted by Moore's law [147, 148]. However, due to the diffractive nature of light, it becomes increasingly costly and difficult for the current optical lithography to continue the reduction of node size. For example, the state-of-the-art optical immersion tool cost for dedicated double- and multiple- patterning techniques is exceeding $50M per tool. And the process complexity now makes the mask set cost over 5 million US dollars because of the large amount of data required to write these masks and the difficulties in implementing the necessary optical proximity correction [149]. Because of the ever-increasing complexity and cost of the mask-based lithography, maskless schemes are emerging as a viable approach by eliminating the need for masks to reduce cost and design cycle [150]. However, the low throughput of most maskless methods due to the serial and slow scanning nature remains the bottleneck. Although multi-axial electron-beam lithography has been proposed to increase throughput by using multiple beams in a parallel manner, there are difficulties in simultaneously regulating the multiple beam sizes and positions because of the thermal drift and electrical charge Coulomb interactions, which result in significant lens aberration [151, 152, 153, 154, 155, 156, 157]. Another optical maskless approach is to use assisting light beams to control the resist kinetics to achieve subdiffraction features [158, 159, 160]. It provides a low-cost alternative, however the achievable feature size is still greatly affected by the spatial regulation capability of the far field optics. Amajor improvement inmaskless lithography is thus critical in order to satisfy the demands inmass production for the semiconductor industry.Working at optical near-field is another approach to overcome the resolution limitation of conventional photolithography techniques, but it still faces key obstacles such as energy throughput and working distance control for high volume manufacturing [161, 162, 163, 164, 165, 166]. To overcome those limitations, the plasmonic nanolithography (PNL) technique has been explored for high-speed maskless nearfield nano-patterning using a plasmonic lens (PL) [167]. Despite the promising potential of PNL, important issues such as the trade-off between spatial confinement and inherit loss of surface plasmons (SPs), and therefore the throughput, are yet to be solved before this approach becomes practically viable. A fundamentally new optical scheme in realizing efficient optical confinement at deep sub-wavelength scale is needed.

PSP and LSP have been used in high resolution optical imaging, light delivery and lithography beyond the diffraction limit [13, 14, 30, 69, 168, 169, 170, 171, 172, 173, 174, 175, 176, 177, 178, 179, 180, 181, 182, 183]. Typical PSP is suitable for optical wave guiding applications, however, its poor spatial confinement makes it difficult to further scale-down the resolution [184, 185, 186, 187]. On the other hand, LSP can achieve deep sub-wavelength optical confinement, but it does not provide enough energy throughput due to accessing the same features at 1/16 of the excitation wavelength through a progressive multi-stage focusing scheme. (b) Designs of plasmonic lens (PL) structures and simulation results. Two cases of PL designs are shown here for comparison, including: case I (left), a PL consisting of two ring grooves and a centered 40nm diameter circular aperture working with PSP; case II (right), a multi-stage plasmonic lens (MPL) consisting of two ring grating slits with the dumbbell-shaped aperture and an additional outer ring reflector (RR) slit working with both PSP and localized surface plasmon (LSP). Both of them are made of a 60nm Cr thin film and optimized for illumination at 355nm wavelength with linear polarization along the x-axis. Both scale bars are 500nm. (c) The simulated light intensity profiles at the plane 10nm away from the lens along the x-axis which are normalized to the incident light. At the deep sub-wavelength region, the PSP itself is incapable of sustaining high transmission through the circular aperture, but the LSP greatly helps to improve the center transmission by several orders. (d) Temperature profiles in the thermal type resist layer under MPL heating. Two different time durations of laser pulse of 10 ps (red) and 10ns (blue), respectively, have been used in the numerical study. By properly controlling the laser power level and pulse duration, we can further improve the feature size down to 22nm. The ps-pulsed laser has great advantages over the modulated continuous-wave laser in terms of pattern size and contrast.

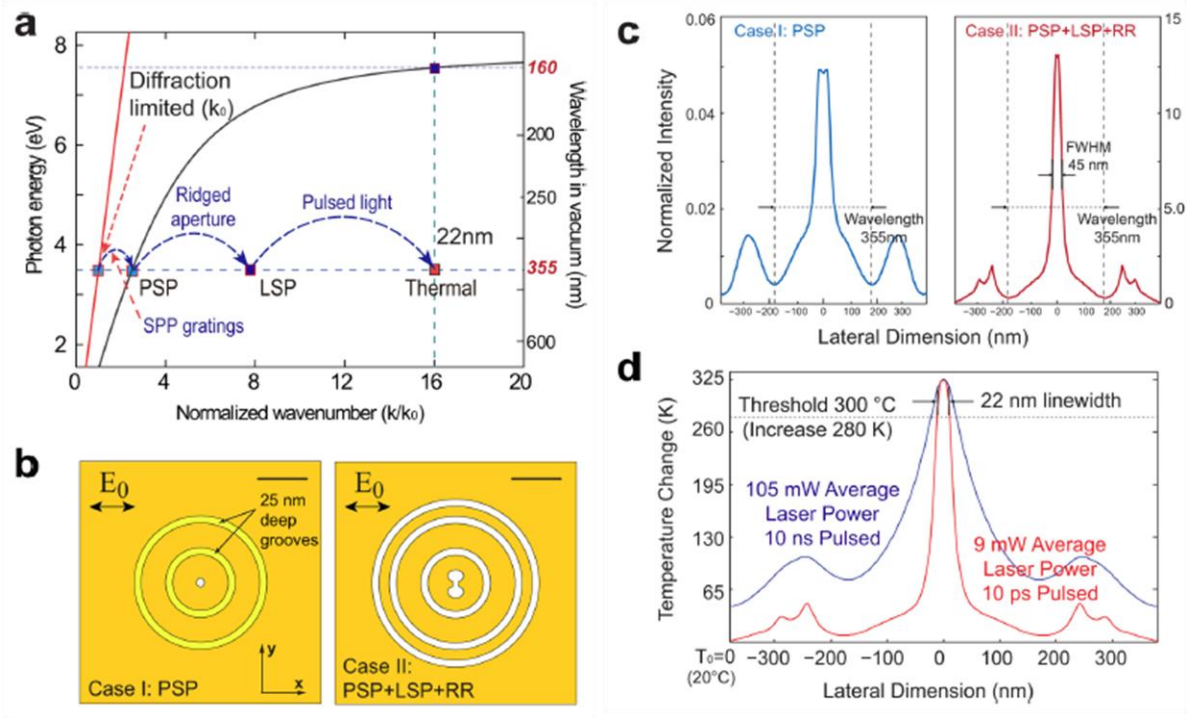

Figure 6.6. Progressive multi-stage focusing scheme efficiently squeezes light to the deep sub-wavelength scale. (a) The accessible wavenumber range (red line) for conventional optics is limited to k0 by diffraction. The dispersive nature of the propagating surface plasmon (PSP) allows accessing a broader range of wavenumbers (black solid line), however a very short excitation wavelength (160nm) is still required to resolve 22nm features with high intrinsic loss. Our multi-stage approach allowsmodes efficiently for imaging, sensing, energy conversion and storage [185, 189, 190, 191, 192]. Here we report a new nano- focusing scheme based on a multi-stage plasmonic lens (MPL) design on an air bearing surface (ABS) utilizing both PSP and LSP. Through this progressive focusing scheme, as illustrated in (a), that combines PSP focusing, LSP conversion and nano-scale thermal management on the photoresist, we are able to efficiently squeeze light into the deep sub-wavelength scale and achieve nanolithography with 22nm resolution using a 355nm pulsed laser source. In comparison with the state-of-art immersion photolithography, our plasmonic lithography system costs orders of magnitude less than the current lithography tool.

6.2.2 Design and numerical studies of plasmonic lens

The key MPL design to achieve the high resolution with the required throughput consists of a dumbbell-shaped aperture, a set of ring couplers (two inner rings) and a ring reflector (the outer ring), fabricated on a metallic thin film. As schematically illustrated in Figure 6.6 (a), the PSPs are excited and propagate towards the center of MPL by using a circular shape grating, where they are further efficiently converted into deep subwavelength LSPs through the dumbbellshaped aperture, thereby achieving an optical confinement of less than 50 nanometers. In comparison to the extremely low optical transmission through the deep-subwavelength holes, a MPL can provide 5-10 orders of magnitude higher optical transmission in the same area which ensures that

the focused light spot has enough energy for writing patterns at an extremely fast scanning speed [193, 194]. Through electromagnetic simulation we compared two plasmonic structure designs working at the excitation wavelength of 355nm with their corresponding light intensity normalized by the incident light intensity (CST Microwave Studio). In Figure 6.6 (b), case I shows an example of PSP-based PL with a 40nm diameter circular aperture at its center [153, 170]. By guiding the PSP energy towards the center it is capable of producing orders of magnitude higher transmission through the same size hole. However, it can be seen that the net transmission through a PSP-based PL decreases rapidly when the center hole size further reduces into the deep sub-wavelength region. Case II shows our new MPL design where the center hole is replaced by a dumbbell-shaped aperture in order to convert PSP into LSP to enhance the confinement and intensity at the focal point [195, 196, 197, 198]. The performance of the MPL is further improved by adding a third ring placed at a half-wave length position of the circular grating so that it acts as a reflector for the outward propagating PSP waves due to deconstructive interference. The central focal spot by the MPL has a peak intensity of 13.1 times the incidence light with a 45nm FWHM spot size. The ring gratings are etched all the way through the metal film thereby causing the side lobes with a maximum intensity of 2.0 times of incidence, corresponding to a contrast ratio of 6.5 to the focal spot intensity, which is well under the exposure threshold for our current maskless lithography purpose. The contrast ratio can be further enhanced to 70 or more by replacing the grating slits with shallow blind grooves similar as those used in case I (Figure 6.11). High throughput writing requires using a large number of lens array at high speed, which calls for efficient PSP energy utilization for each lens. We designed the MPL with a diameter of about 1 mm with a Cr metal layer because its superb mechanical properties can prevent lens damage when the lens flies within a few nanometers above the substrate at high speeds of several meters per second. Replacing Cr with other metals, such as aluminum with a better mechanical lens protection can further improve the peak intensity by a few times (Figure 6.7).

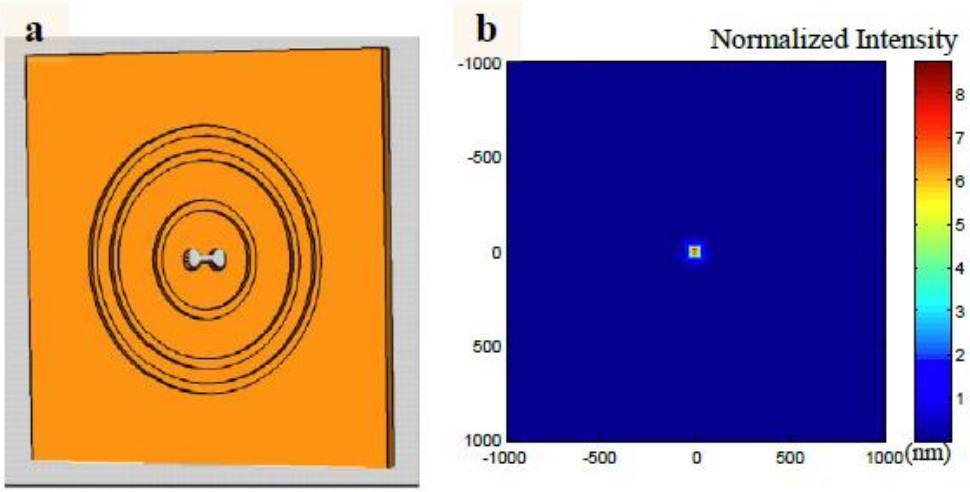

Figure 6.7. The contrast of the MPL focus can be enhanced by replacing the etched-through rings with shallow blind grooves from the incident side, showing (a) the perspective view of the MPL

with shallow blind grooves, and (b) the side lope transmissions have be attenuated by more than one order of magnitude and the contrast ratio is enhanced to 70.

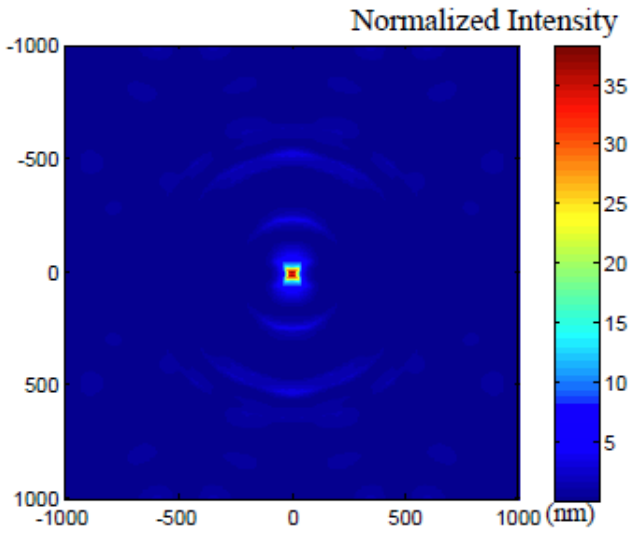

Figure 6.8. When replacing Cr with Al, the focus spot intensity can be further improved by a few times higher than that of Figure 6.11(c).

6.2.3 Fabrication of metamaterial and plasmonic nanolithography system

The sapphire ABS was fabricated using micro-fabrication techniques as the fabrication procedures shown in Figure 6.9. First, the ABS pad recess was fabricated using a commercially available lithography setup (Karl Suss MA6 Mask Aligner) to make a resist pattern and a subsequent Aluminum RIE etcher to etch sapphire substrate. Subsequently, the ABS base recess was fabricated using a chromium etch mask due to the required large etching depth (~2.4um). The base pattern was lithographically transferred onto photoresist on top of 4.5um thick Cr film deposited on sapphire sample. Wet etching using CR-7 etcher was used to etch chromium as the etch mask, then, the pad recess was fabricated using Aluminum RIE etcher to etch sapphire sample. Figure 6.9 shows the image of the fabricated ABS after the etching process. After dicing the ABS using an automatic dicing saw, an 80-nm chromium film and a 15nm diamond-like-coating protective layer were sputtered on the ABS using a sputtering machine (Edwards Auto 306 DC and RF Sputter Coater). The chromium film was employed due to its hardness. After that a plasmonic lens or an array of plasmonic lenses was fabricated using focused ion beam milling (FIB, FEI Strata 201XP). The film on ABS is prepared as follows. First the 80nm thick Cr film, following by a transition layer of a few-nanometer thick chromium-carbide and a 12nm thick diamond like carbon (DLC) film were deposited on the sapphire slider using sputtering machine. In order to improve the adhesion of the DLC to Cr film, the thin transition layer of chromium-carbide film is employed by co-sputtering of Cr and C simultaneously.

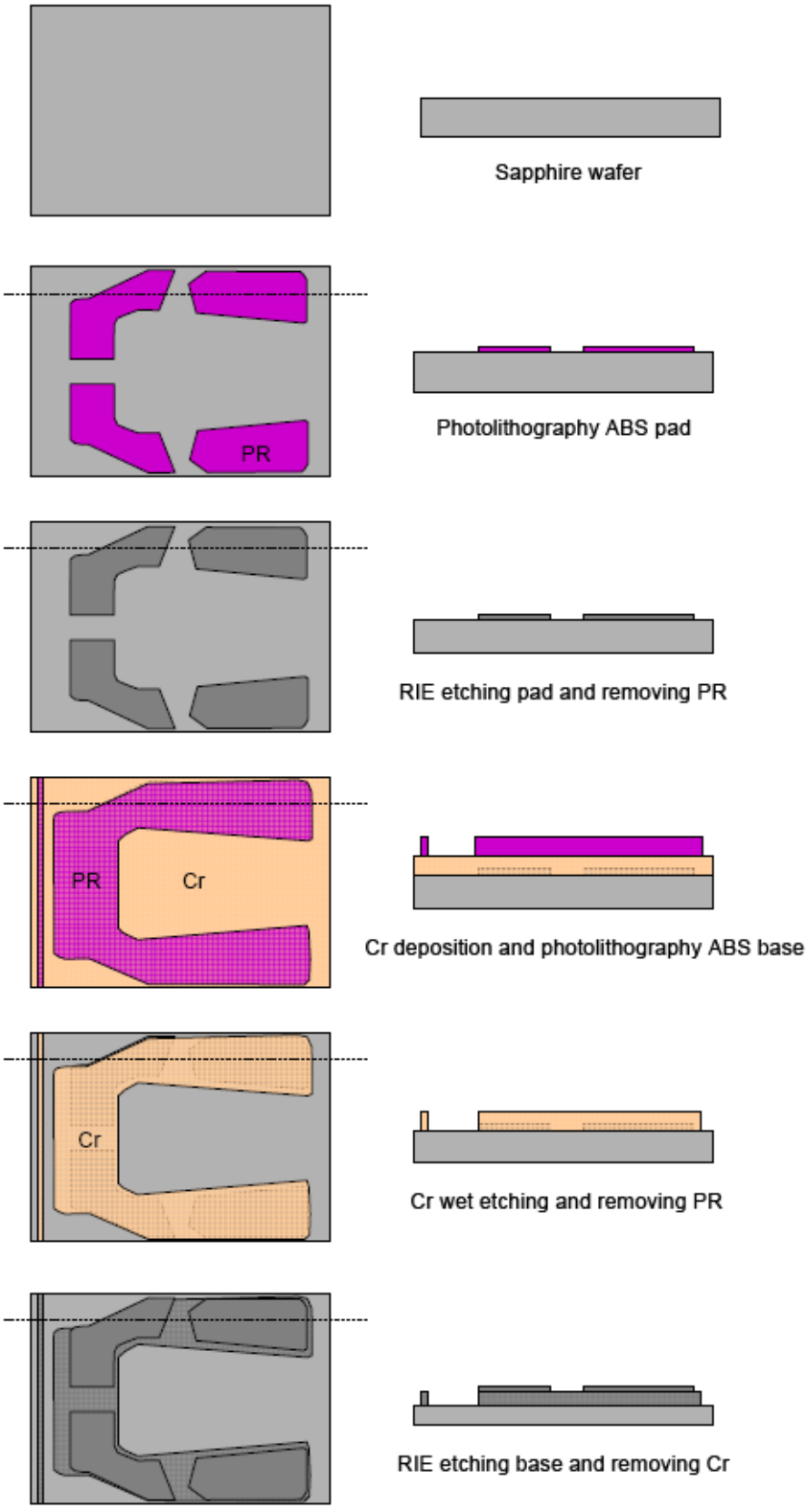

Figure 6.9. Air bearing slider fabrication process

6.2.4 Flying head lithography system set-up

Instead of continuous-wave laser we use a pulsed laser with a thermal resist to achieve the high resolution and patterning throughput by lowering the required operating laser power level and controlling the heat diffusion at the nanoscale. Figure 6.6 (d) shows the simulated temperature profiles in the thermal resist layer under heating from the optical field of focused plasmons from MPL under two different laser pulses. With 10 ps-pulses, we can further improve the feature size down to 22nm (about half of the optical spot of 45 nm focused by the MPL) and reduce the required laser average power from 105mW to merely 9mW by utilizing the nonlinear and time dependent response of thermal resist [199, 200]. The high-speed plasmonic writing involves the competition of optical absorption at the nanoscale, heat accumulation and thermal diffusion. The energy deposited into the nanoscale resist volume can rapidly diffuse into the neighboring region within a nanosecond, which enlarges the exposed features, increases the required laser power, and causes pattern distortion. Therefore, the pulsed laser has great advantages over the continuous-wave laser for ensuring the good thermal confinement in the resist layer. Application of the pulsed laser also allows the employment of a PL array for parallel patterning. Using advanced ABS techniques, we can fly a scanning device of a few millimeters that carries arrays of MPLs (up to 16,000) at sub-10nm above a resist surface with a speed of 4-14 m/s (Figure 6.12). We experimentally demonstrated high throughput direct writing at 22nm half pitch and the parallel patterning. The ABS technique used for the scanning gap control is a self-positioning method which can maintain a consistent nano-scale gap during high speed scanning. The air flow created by the relative motion between the rotating substrate and the ABS generates an aerodynamic lift force, which is balanced by the force supplied by a spring suspension. Due to the high air bearing stiffness and small actuation mass, the flying head can follow the substrate profile and maintain a consistent flying height of 5-20nm with sub 1-nm variation. The ABS was designed using an in-house developed air bearing simulators [201] and fabricated at the bottom of the transparent flying head made of sapphire using micro-fabrication. With careful ABS design, it is possible to achieve a consistent working gap at a wide range of substrate rotation speeds and radial positions, and therefore eliminate the need for a high bandwidth feedback control loop, one of the major technical barriers for high speed patterning using AFM-type scanning probes. In our work, the working gap is 10nm over the velocity range from 4 to 14m/s with a sub-1nm variation. The pitch and roll angles of the flying head are kept consistent at 40mrad and sub-1 mrad, respectively. The array of MPL (SEM image shown in Figure 6.11 (a) and (b)) was later fabricated by focused ion beam milling on a 60nm thick chromium (Cr) film coated on the ABS. Figure 6.11 (c) shows the field intensity distribution at the plane 10nm distance away from the lens and has been normalized to the incident light intensity. As schematically shown in Figure 6.11 (d), each of the MPLs can be controlled using independent laser beam in order to enable high-throughput parallel writing.

In the nanolithography experiments, detailed experimental set-up is shown in Figure 6.10. A spindle was used to rotate the substrate with the resist at 2,500rpm corresponding to a linear speed of 4-14 m/s at different radii, and a ps-pulsed UV laser (Vanguard, Spectra-Physics, 355 nm wavelength) was used as the exposure light. Through a single UV objective, a few individually modulated laser pulse trains were first focused down to separated spots with diameter of several micrometers to illuminate the area of the designated MPL structure on the ABS surface. Then, each of the MPLs further focuses the pre-focused light spot to a nanoscale spot for patterning the resist layer. The information of the relative position between the flying

head and substrate is provided by the spindle encoder (angular) and a linear nanostage (radial), which feeds to a home-made pattern generator to pick the laser pulse for exposure through an optical modulator. During the test, an interferometry setup and an acoustic emission sensing module were installed to monitor the real-time motion of the flying head during the lithography process. The resist used in our test is $(TeO_2)_xTe_yPd_z$ [x~80% wt., y~10% wt., z~10%wt.], an inorganic thermal type developed on the basis of the Te-TeOx resist. Pd is added to the Te-TeO_x in order to enhance the exposure uniformities and resist resolution by forming finer crystalline grains during phase transition, and its thermal stability is also beneficially improved. This inorganic resist is employed also because of its good mechanical properties for tribological issues, and good sensitivity for high-resolution. After the PNL experiment, the exposed patterns were developed in diluted KOH solution and then examined by AFM.

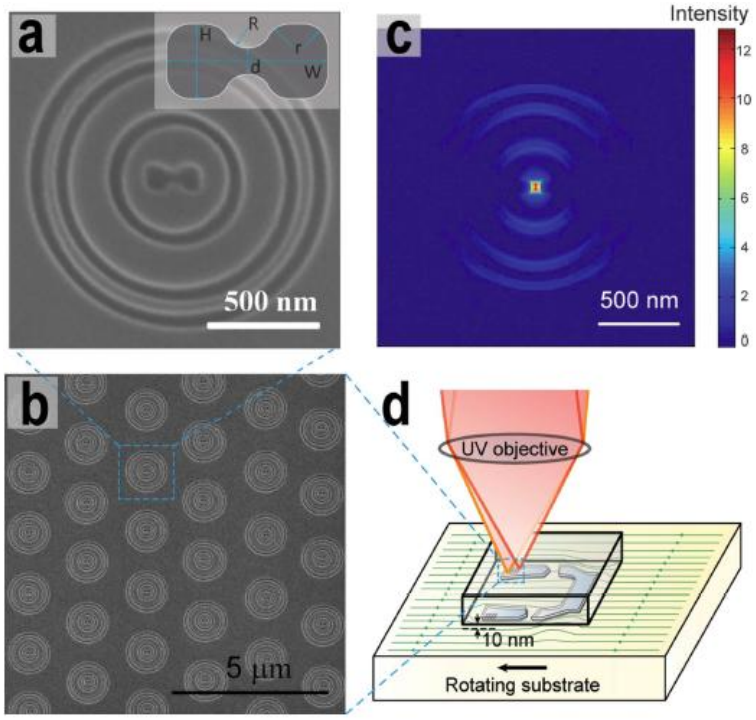

Figure 6.10. MPL array and plasmonic flying head enable high-throughput maskless plasmonic nanolithography (PNL) by focusing the ultraviolet laser energy into nano-scale spots onto the high speed spinning substrate. (a) The SEM picture of a multistage plasmonic lens (MPL) consisting of a dumbbell-shaped aperture, a set of ring couplers (two inner rings) and a ring reflector (the outer ring), fabricated on a metallic thin film in 60nm thick Cr film. The parameters of the centre aperture are shown in the insert, where W5240 nm, H598 nm, R535 nm, r540 nm, and d526nm. The radii of the three rings are 240, 480, and 600nm. And the width of the rings is 50nm. (b) SEM image of hexagonally packed MPL array. (c) The field intensity distribution at the plane 10nm distance away from the MPL surface normalized to the incident intensity of 355nm wavelength light. The half-circular shaped side lopes in the intensity profile are the direct transmissions through the three rings and their intensities are far below the exposure threshold of the resist. (d) Advanced air bearing surface (ABS) is used to maintain the gap between the lenses and the substrate at 10nm at a linear scanning speed of 10 m/s.

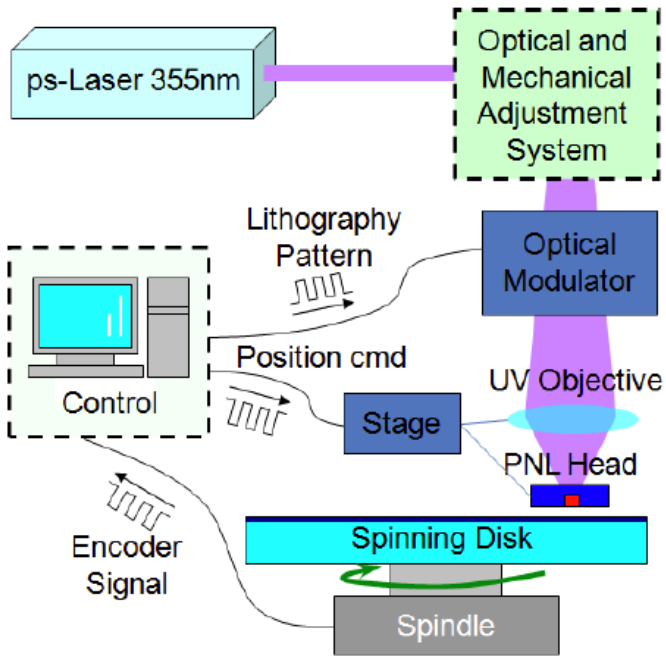

Figure 6.11. Plasmonic nanolithography (PNL) experiments layout. A control system is used during patterning process to modulate the incident beam based on the relative position between the PNL head and the spinning substrate.

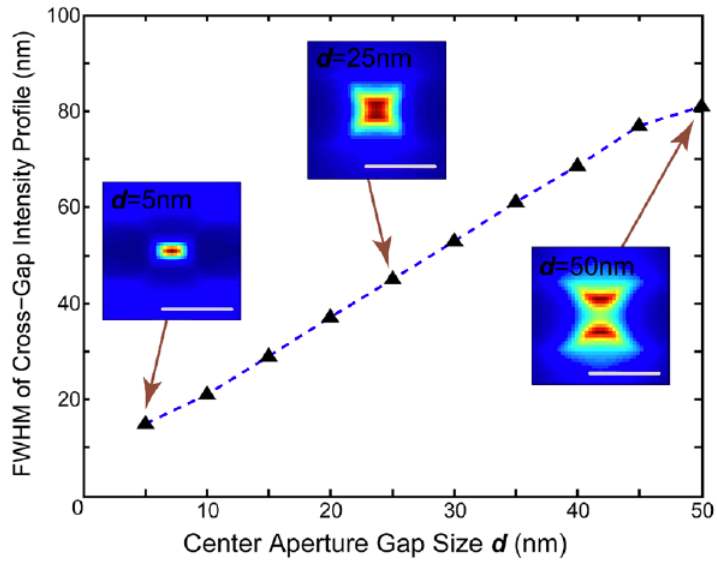

Figure 6.12. MPL's field confinement is a function of the gap size of the center aperture (gap size *d* in the insert of Fig. 2a). The FWHM of the intensity profile almost linearly increases from 15nm to 81nm at the gap range of from 5nm to 50nm. As the gap further increases beyond 50nm, the focal spot eventually splits into two separate focal spots. Therefore, a reasonably smaller gap size is preferable for generating finer feature. All scale bars are 100nm.

6.2.5 Plasmonic flying head lithography result and discussion

Figures 6.13 (a) and (b) show the AFM image of closely patterned dots with 22nm half-pitch resolution by PNL with the cross-sectional scan (Figure 6.13 (c)). The results are in agreement with the experimental conditions (substrate velocity at 7m/s and the laser pulse repetition rate at 160 MHz), and each dot is generated by a single laser pulse. Similar to other maskless approaches, writing at a higher laser power or higher pattern spatial frequency allows the dots to merge into continuous lines with different widths. The result is shown in Figure 6.14 where two MPLs in the lens array independently write on the thermal resist in parallel. To obtain 50nm wide solid lines, the MPL1 was excited with a laser power twice that used for Figure 6.13, and the MPL2 simultaneously used a ramping laser power varying from 2 to 4 times. It is shown that the exposure feature size can be controlled by regulating the laser power during the pattern writing. It should also be noted that the pattern definition can be greatly improved by the optimization of the resist exposure threshold and post-development conditions.

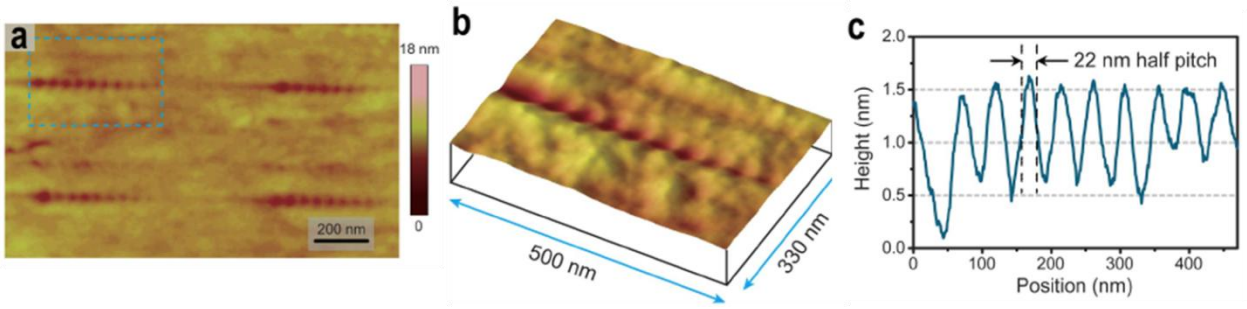

Figure 6.13. AFM image of closely packed dots at 22nm half-pitch on the thermal resist. (a) AFM image of four trains of dot lines. (b) 3D topography of the boxed dot line in Figure (a). (c) cross-sectional profile of the dot line in Figure (b).

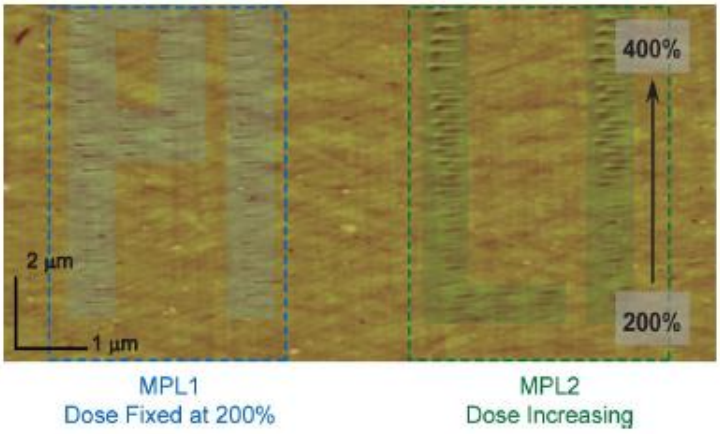

Figure 6.14. AFM image of a PNL parallel writing result on the thermal resist. Two of MPLs in an array were used to simultaneously write independent patterns, capital letters “PI” and “LI”, respectively. MPL1 used a fixed laser power at 2 times that used in generating the result in Fig. 3, and MPL2 used an increasing power varying from 2 to 4 times. As the laser power level further increases, the side lobe patterns from the MPL start to show on the resist layer.

6.2.6 Summary

In this chapter, we have demonstrated a high speed plasmonic nanolithography with 22 nm half-pitch resolution. This is achieved by employing multi-stage plasmon focusing through relatively low-loss propagating surface plasmons focusing and later conversion to localized plasmons. This allows the highly efficient transmission and focusing of near-field spot which is the key to improving the throughput, for a given laser power, by increasing the scanning speed and/or by employing a great number of MPLs and flying heads for parallel patterning. In principle, this scheme allows a single flying head to carry up to 16,000MPLs, which can pattern a 12inch wafer in minutes. This is comparable to conventional production-level photolithography but at a much higher resolution of 22nm half-pitch size. This new scheme enables a low cost, high-throughput maskless nano-scale fabrication with a few orders of magnitude higher throughput than conventional maskless approaches. It may allow continuously scaling to smaller node size beyond 22nm by utilizing shorter SPs wavelength and guiding mechanisms, and it opens up a promising route towards the next generation lithography for semiconductor manufacturing [189]. In addition, it also holds a great potential in the next generation magnetic data storage, known as heat assisted magnetic recording (HAMR) and Bit-PatternedMedia (BPM), to achieve two orders higher capacities in the future [202].

Chapter 7

Nanofabrication techniques for metamaterials and plasmonics

7.1 Photolithography overlay for microscale 3D metamaterials

Photolithography is one of common patterning methods to define the structures in microscale science and engineering. I would like to show an example to describe general photolithography process with switchable chiral metamaterials device for photo-induced negative refractive index switching we dealt in chapter 5. The device has full 3D structures made by photolithography overlay, electroplating, lift-off, wet & dry etching and so on.

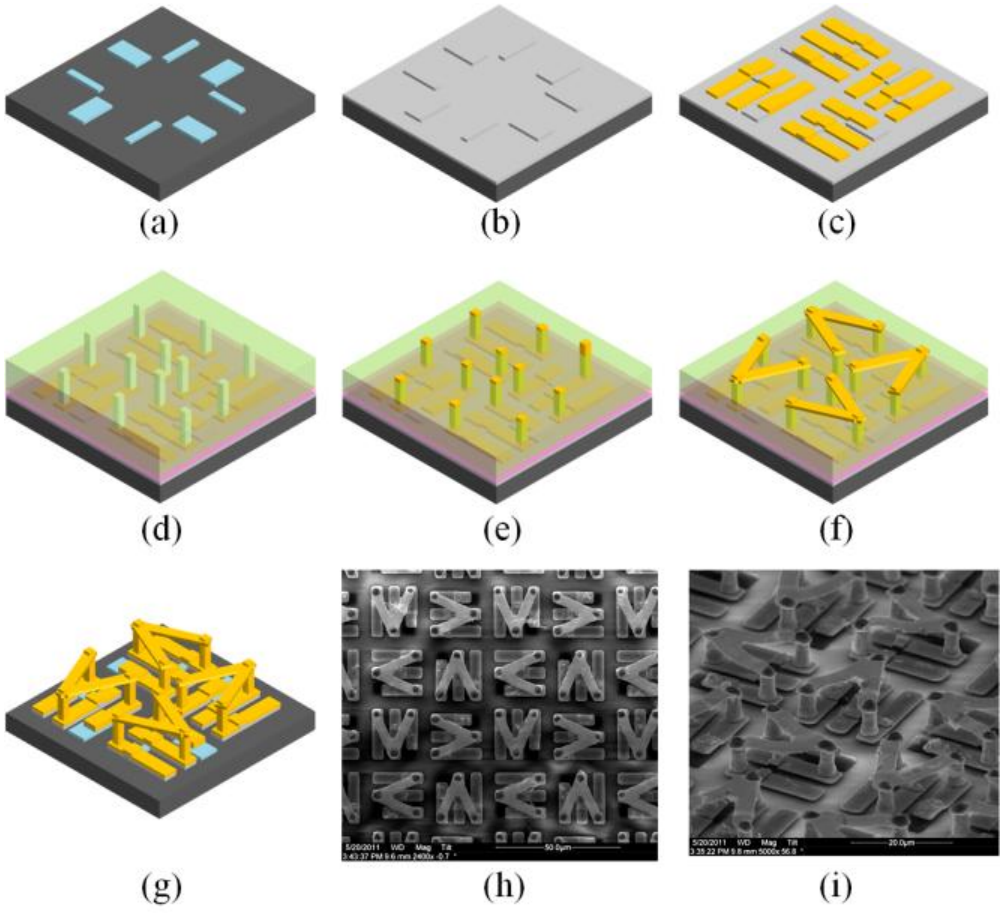

Figure 7.1. Fabrication flow and final SEM pictures

7.1.1 Substrate cleaning

The switchable chiral metamaterial device starts with Silicon on Sapphire (SOS) wafer whose thickness of Si is 0.6um. Initially, the substrate is cleaned to remove organic, metallic, and oxidized contaminants with piranha cleaning at 120℃ for 10min. Rinse with DI water and 5:1 buffered oxide etchant (BOE) for 1min are followed to remove a native oxide layer. The water rinse treats it again and spin dry step is the final step of the substrate preparation as Figure 7.2.

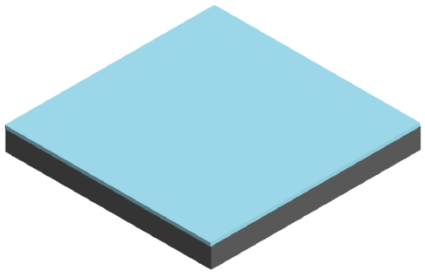

Figure 7.2. SOS substrate

7.1.2 Definition of Si pads

Si pad plays a role of a switch to turn on and off negative index by external pumped laser. To define this pad, OCG825 g-line photoresist is spun on the substrate and baked at 90℃ for 90sec. Karl-Suss MA6 mask aligner exposes UV light with vacuum contact mode for 50mJ/cm^2 of g-line and the UV exposed area is developed by the developer OCG 934 for 60sec. Si is etched by Reactive Ion Etcher (RIE, PTHERM) with the gases of SF_6 60sccm and O_2 6sccm, the power of 100W for 90sec. The mask photoresist will be removed by photoresist remover, PRS-3000 for 10min. Finally, piranha and DI water cleaning are followed for cleaning as Figure 7.3.

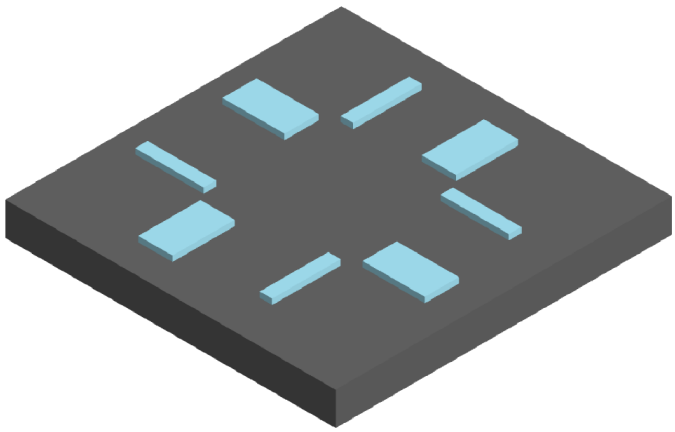

Figure 7.3. Definition of Si pads

7.1.3 Deposition of electrode

Electroplating will be used to make Au pillars afterwards, and it needs an electrode layer on the substrate. Aluminum (Al) layer is deposited on the substrate by a sputter which can give good step coverage on Si pads. Sputtering conditions are Ar 30sccm, power of 100W, and time 60min for conformal deposition to make 400nm of total thickness as Figure 7.4.

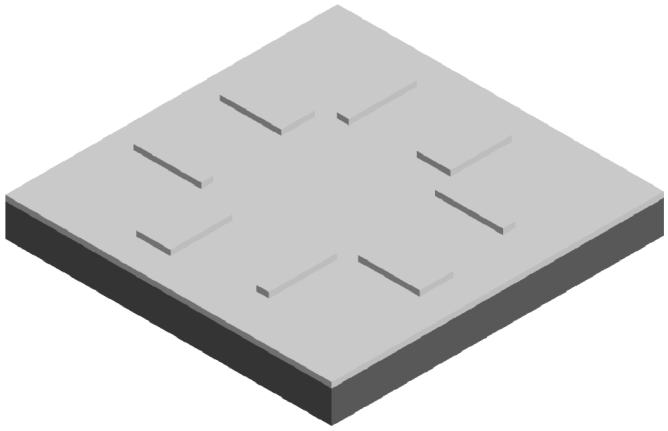

Figure 7.4. Deposition of electrode

7.1.4 Definition of Au pads

300nm of Au pads will be defined on the Si pads as Figure 7.5. LOR 10A is spun on the substrate and baked at 170℃ for 5min. Rohm and Haas S1818 positive resist is spun on the surface and baked at 110℃ for 2min. Karl-Suss MA6 mask aligner exposes UV light with vacuum contact mode for 120mJ/cm^2 of g-line and the UV exposed area is developed by the developer MF-26A for 110sec and rinsed by DI water. 10nm Cr and 300nm Au are deposited by electron beam evaporator. PRS-3000 is used for lift-off at 70℃ for several hours.

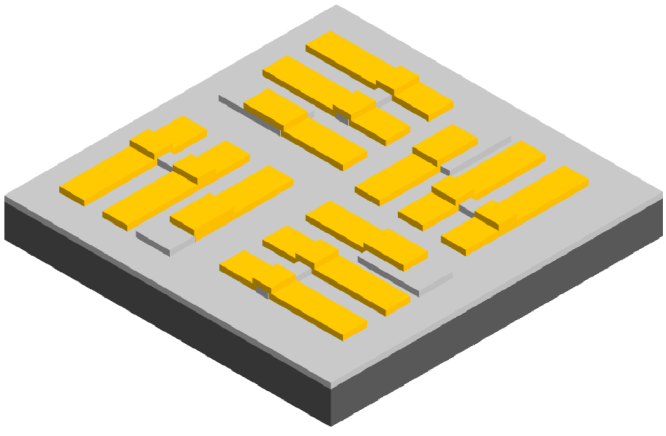

Figure 7.5. Definition of Au pads

7.1.5 Definition of contacts

Electroplating solution attacks Al electrode layer, so the electrode layer should be protected during electroplating process. Spin on glass (SOG, Futurex IC1-200) is spun on the substrate with 2500rpm and baked at 170℃ for 15min. After SOG process, normal UV lithography is followed to define contact for the Au pillars (Figure 7.6).

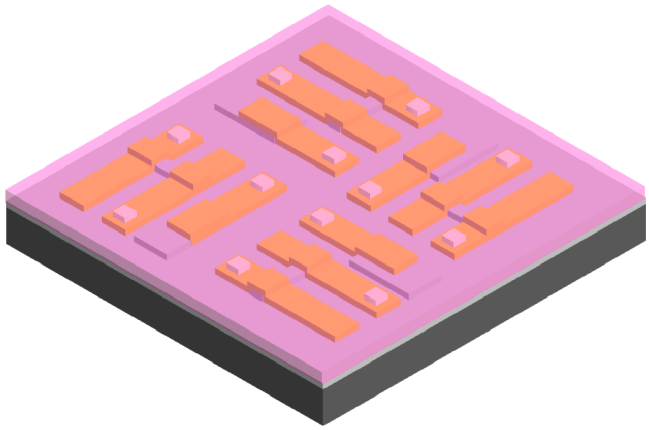

Figure 7.6. Definition of contacts

7.1.6 Definition of SU-8 mold

5um of SU-8 is spun on the substrate to make a mold for electroplating. SU-8 3005 is used with 3000rpm and baked at 95℃ for 5min. Karl-Suss MA6 mask aligner exposes UV light with vacuum contact mode for 50mJ/cm^2 of i-line and the UV exposed area is developed by the developer SU-8 developer for 60sec and rinsed by IPA. The hard bake step is following with 190℃ for 15min. Oxygen plasma etching is following to remove residual of SU-8 on the surface.

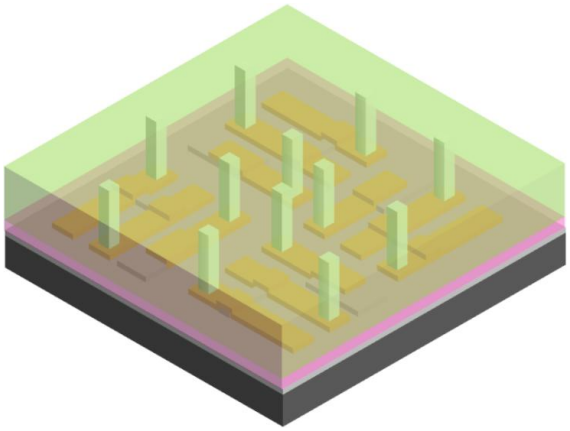

Figure 7.7. Definition of SU-8 mold

7.1.7 Electroplating

Au pillars are grown by electroplating process. The electroplating solution uses Trensene Pure Gold SG-10 for 60℃. Generally, since the lower electric current gives better surface quality of Au, 1mA of electric current is used for 45 minutes. DI water rinse is the post of the electroplating process. It is shown in Figure 7.8.

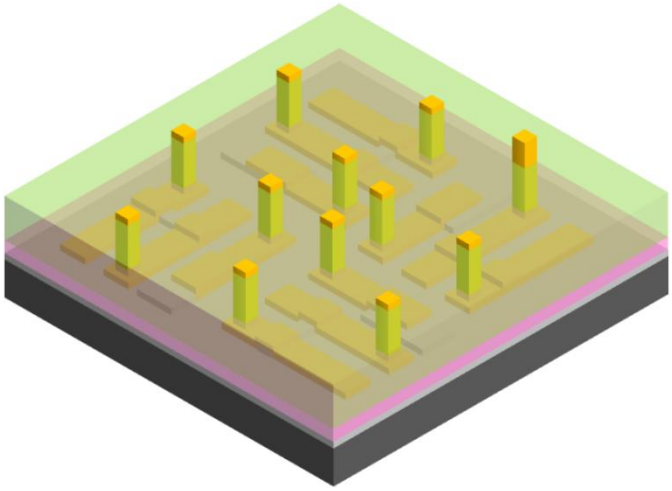

Figure 7.8. Electroplating of pillars

7.1.8 Definition of Au Bridge

To connect the pillars V-shape of 300nm thick Au bridges will be defined on top as Figure 7.8. Same process in Figure 7.4 (Au pad definition) is repeated.

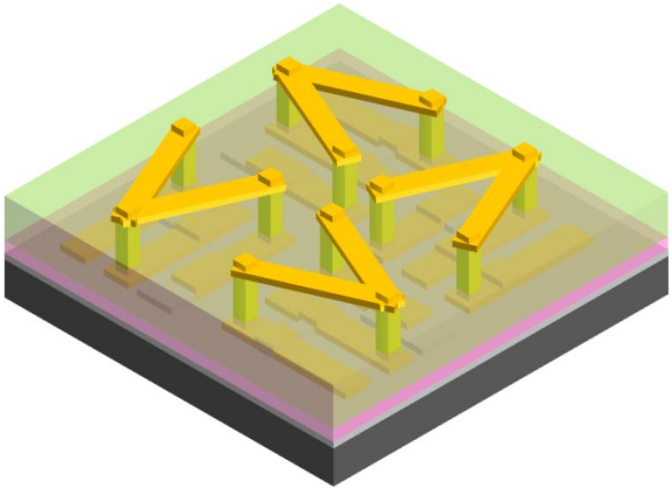

Figure 7.9. Definition of Au bridges

7.1.9 Post electroplating and dicing

Although Cr is deposited while making Au bridges to enhance adhesion between pillars and bridges, additional process for enhancing adhesion may be needed because the structure will be released into the air. The electroplating solution uses Trensene Pure Gold SG-10 for 60℃. 1mA of electric current is used for 5 minutes. DI water rinse is the post of the electroplating process. Dicing process is following to cut dies of 16.5mm x 16.5mm. Since sapphire is hard material, the speed of cut is set to the lowest value, 0.4mm/sec, and the depth of the cut is shallow, 200um at once. Each cut lane needs at least twice of cut to minimize chipping and damaging to the dies.

7.1.10 Release of structures

The release steps are composed of removing SU-8, SOG, and aluminum in order. Oxygen plasma etch is used to etch SU-8 with 300W for 25min. This dry etch method can minimize the damage of the structures rather than wet process like piranha treatment. SOG can be removed by dipping into BOE 5:1 for 6min and aluminum for electrode can be removed by dipping into Al etchant for 8min at room temperature. DI water rinse is following and IPA is the final rinse solution to minimize the damage of the structure for low surface tension liquid and the final structure is shown in Figure 7.9.

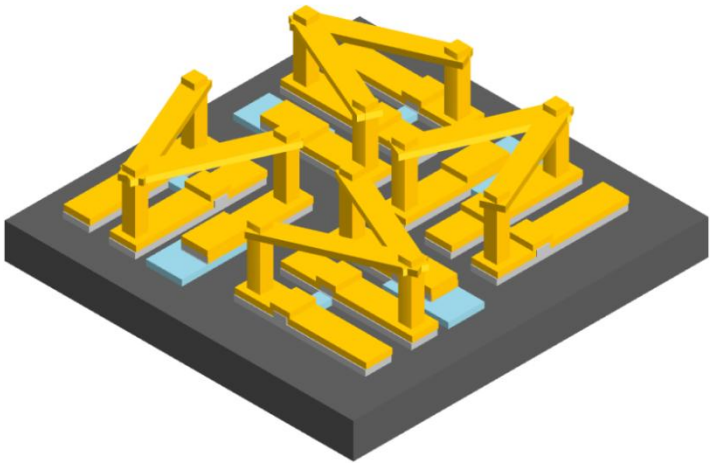

Figure 7.10. Release of the structure

7.1.11 Summary

In this chapter, I described a way making a microscale metamaterial device with photolithography. Even though most of metamaterials need smaller feature in nanoscale, microfabrication techniques are still important to make microsize and large area metamaterial devices in terahertz and higher frequencies. Electron beam evaporation, lift-off process, etching techniques are still used for nanofabrication which will be described in next chapter.

7.2 Electron beam lithography overlay for nanoscale 3D metamaterials

Electron beam lithography (EBL) is the most essential technique in nanoscale science and engineering as providing nanometer scale very high resolution and flexible design methodology with direct writing capability despite several disadvantages such as slow writing speed and difficulty in overlay process. Especially due to overlay limitation, it's very difficult to fabricate nanostructures including metamaterial and plamonic structures, and this is one of the biggest obstacle to achieve more practical devices such as 3D, isotropic and bulk materials and devices. In this chapter, I would like to show my effort to achieve highly reproducible and precise overlay methods with super accurate aligning control. With this technique, advanced metamaterials structures and further metadevices can be made easily and integrated with conventional nanofabrication & microfabrication techniques.

7.2.1 Principle of EBL overlay and strategy for alignment marks

For the overlay alignment, at least two alignment marks are needed and their positions could affect the alignment accuracy. To minimize the align error in both lateral directions, cross type alighment mark like Figure 7.11 is designed. In addition it turns out the longer distance gives better accuracy due to angled tilting error correction of EBL system. Alignmark is designed like Figure 7.12 and alignment measuring ruler is designed like Figure 7.13. Later this alignmark is patterned on the substrate, and then aligned with virtual alignmark (cross shape in Figure 7.11) during EBL process.

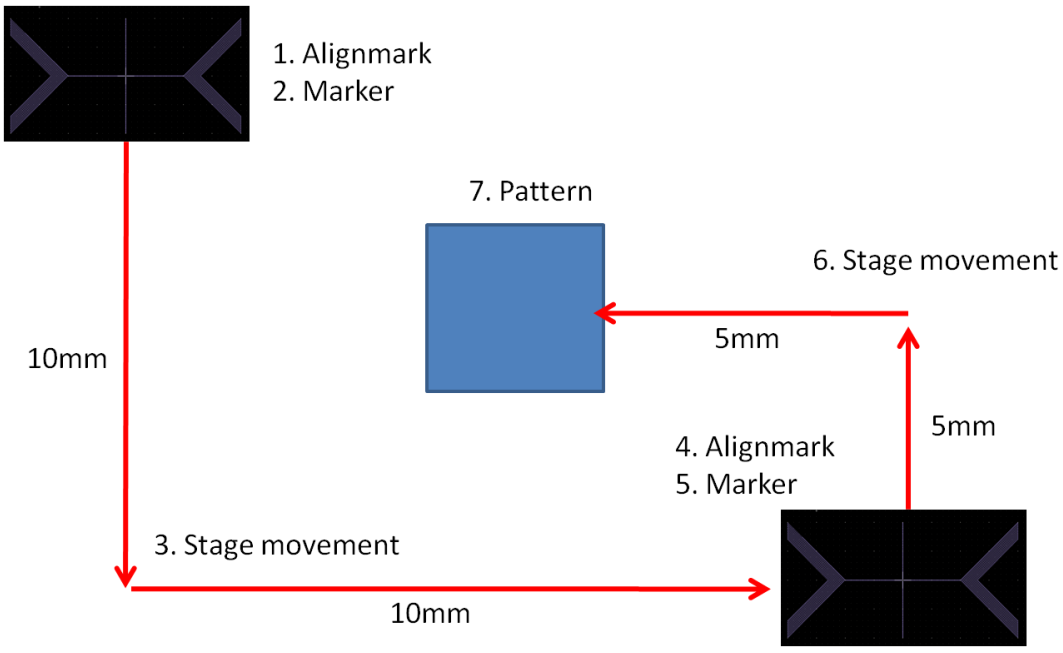

Figure 7.11. EBL writing sequence and the locations of alignment marks. Cross shapes are alignmarks and center rectangular area is patterns to be exposed and aligned.

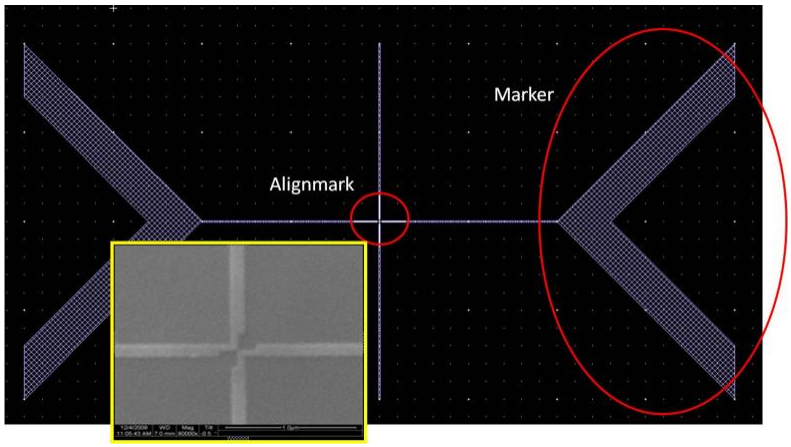

Figure 7.12. Alignmark patterned in substrate during first layer EBL process

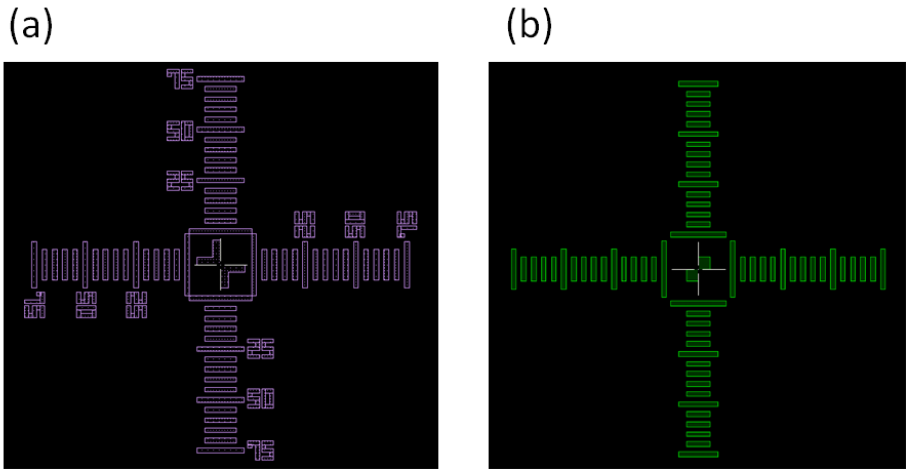

Figure 7.13. Alignment error measuring pattern

The alignment test pattern is composed of 1st and 2nd layers as Figure 7.13 (a) and (b), respectively, and they play a role of calipers that is composed of intentionally shifted bars. To measure the mis-alignment, the matched bars are found for x and y direction and the mis-alignment can be read from the matched bars. For example, from Figure 7.14, the matched bars are located on +70nm position of x direction, and -65nm position of y direction. At least 500 experiments were repeated to measure average alignment error shown in Table 7.1.

Table 7.1. Average alignment error

	X:10mm Y:10mm
σ_x	4.7nm
σ_y	4.6nm

Figure 7.14 and 7.15 shows a mis-aligned and good-aligned ruler, respectively. In the case of Figure 7.15, alignment error is below 5nm which is also mentioned in Table 7.1, and this value is consistently repeated through entire projects except some certain cases of machine malfunctionings.

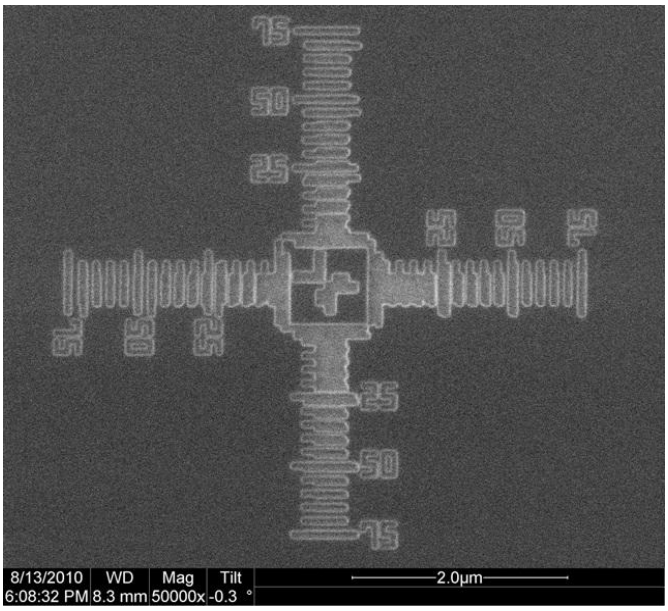

Figure 7.14. Result of misaligned overlay

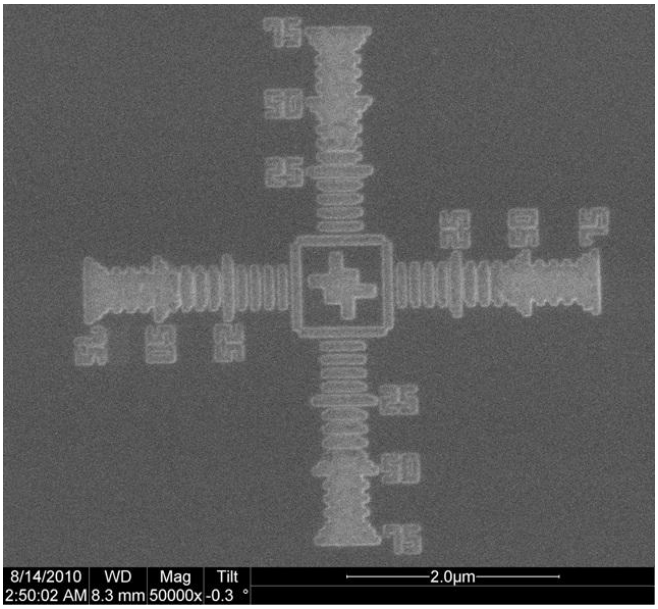

Figure 7.15. Result of well-aligned overlay

7.2.2 Examples of metamaterials structures by high precision EBL overlay

EBL overlay allows several types of new fabrication flexibility for nanometer scale metamaterial structures. A type of chiral metamaterial [Shuang, PRL] is fabricated in micrometer scale working in terahertz frequency range. If we want the chirality to work in optical frequencies or visible frequencies, we have to make much smaller structure in nanometer dimension which is available with neither conventional microfabrication technology nor non-overlay EBL. Figure 7.17 is a nanometer dimension chiral metamaterial which is scaled down to the factor of 40 by EBL overlay techniques (Figure 7.16). Even though the overlay process is very difficult to achieve and not as conventional as the one of photolithography, this well prepared result shows the possibility of the 3D metamaterial structures would be possible to be made for optical frequencies and visible frequencies applications.

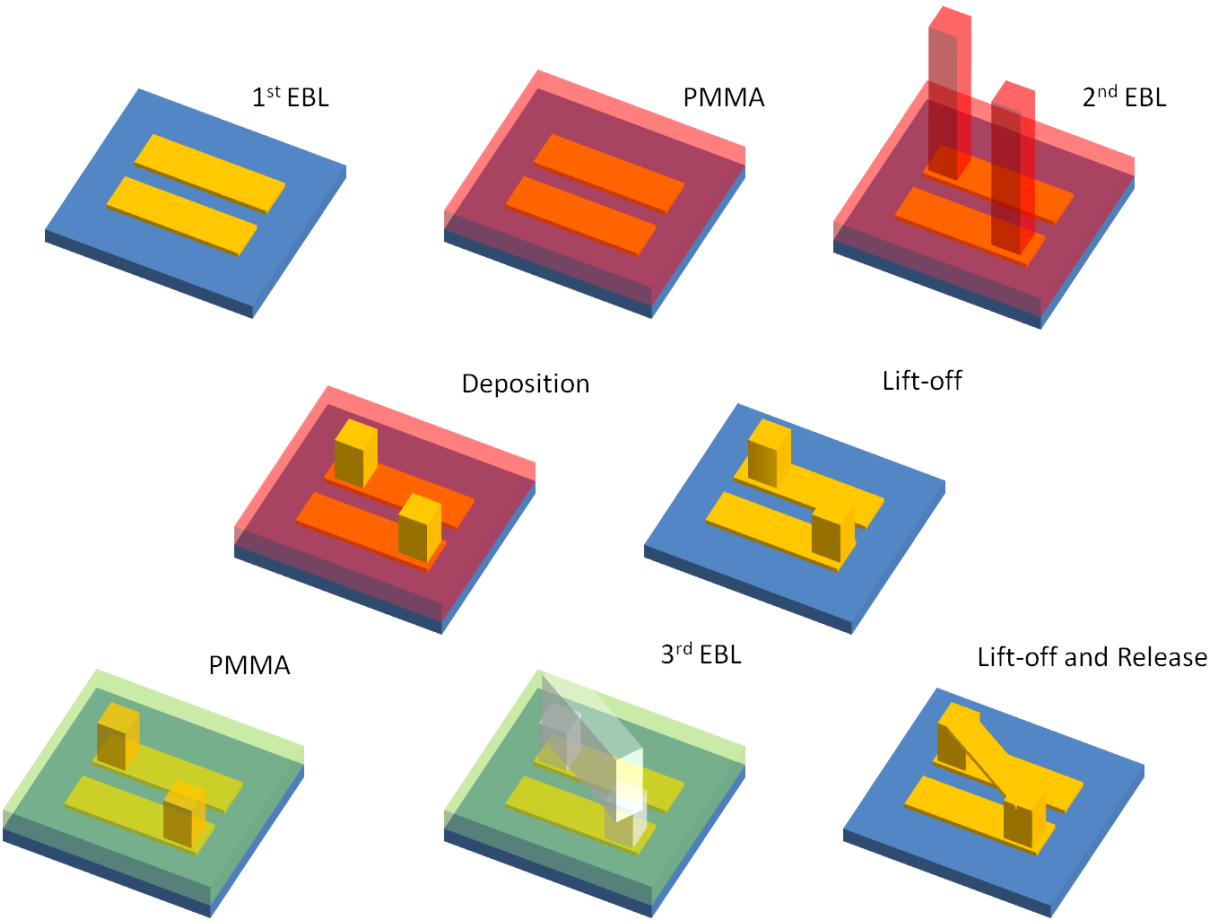

Figure 7.16. Fabrication process of three times EBL overlay for nanoscale chiral metamaterials

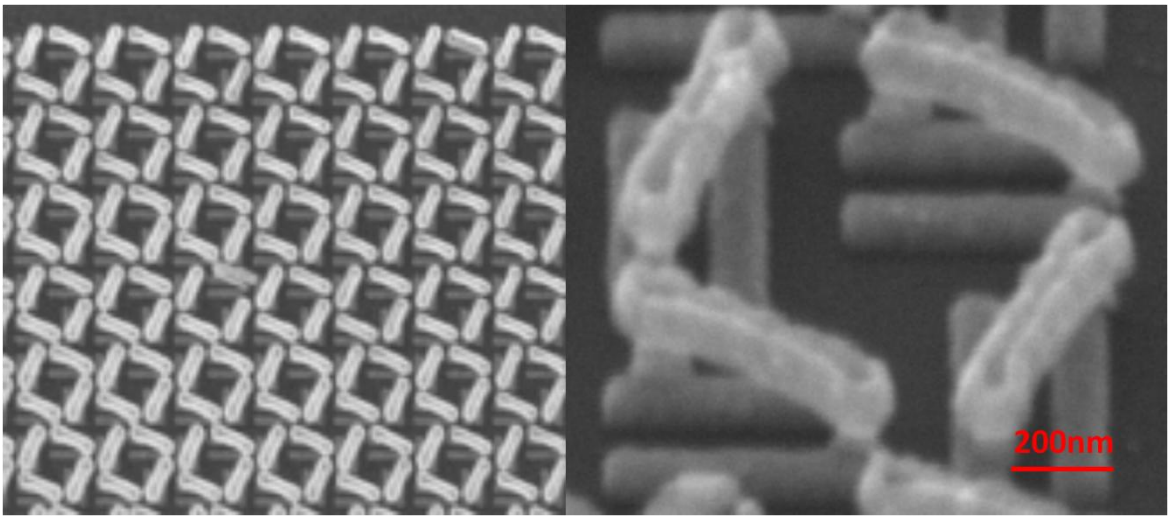

Figure 7.17. The result of chiral metamaterials whose size is scaled down to the factor of 40

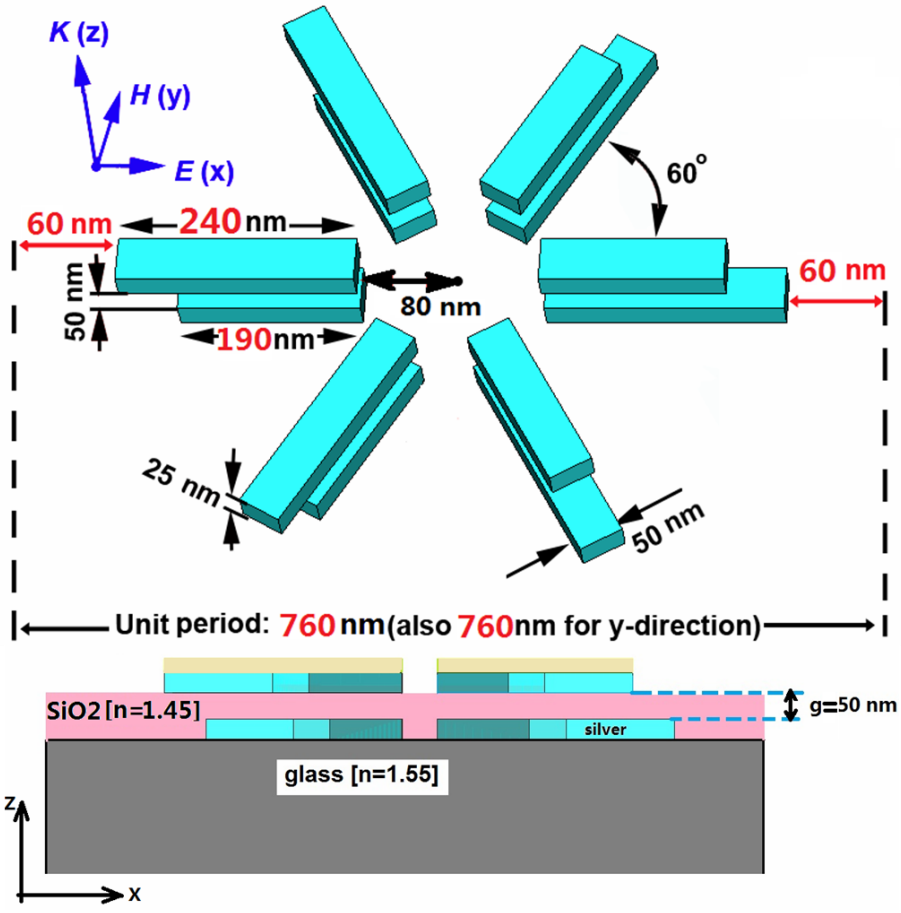

Figure 7.18. Design of 3D toroidal metamaterials

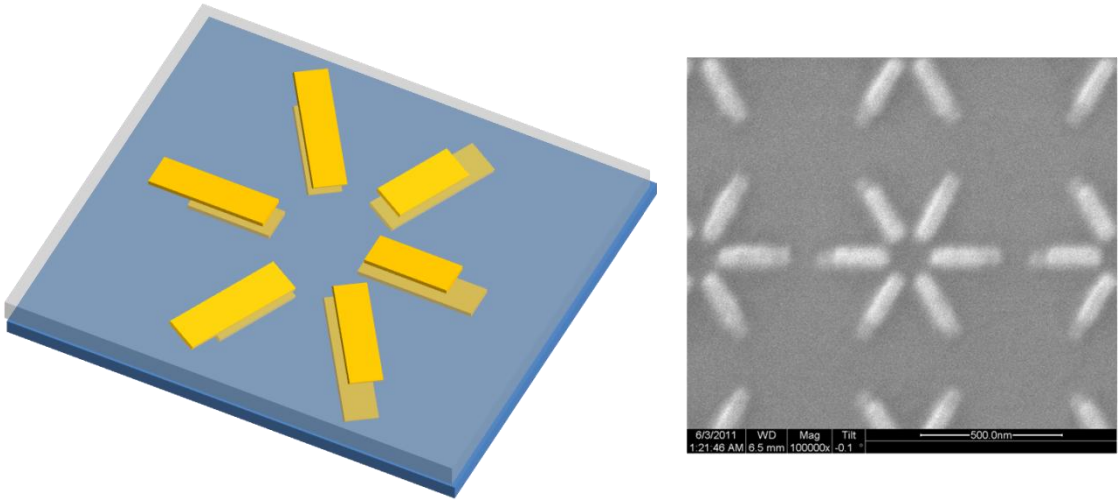

Figure 7.19. 3D view of toroidal metamaterials and the fabrication result with two times EBL overlay with SiO_2 interlayer between two EBL patterns

Figure 7.18 and 7.19 shows another type of applications using EBL overlay. The first EBL pattern (toroidal pattern at the bottom) and the second EBL pattern (toroidal pattern on the top) are separated by 50nm SiO_2 thin film layer. The interlayer coating and 2nd EBL structure are following by the 1st EBL structure subsequently. In this type of overlay technique, we can stack the multiple layers of EBL patterns with separation layer between each of them. Each EBL layer is not connected to each other, and they can make three dimensional and bulk type of metamaterial structures. Figure 7.19 shows another example of two steps EBL overlay to demonstrate optical isolator metamaterial having directional transmission. Like the case of Figure 7.19, the first patterns are generated by EBL and lift-off process, and interlayer of SiO_2 is deposited. Then, the second patterns are made by EBL overlay to align with the first layer.

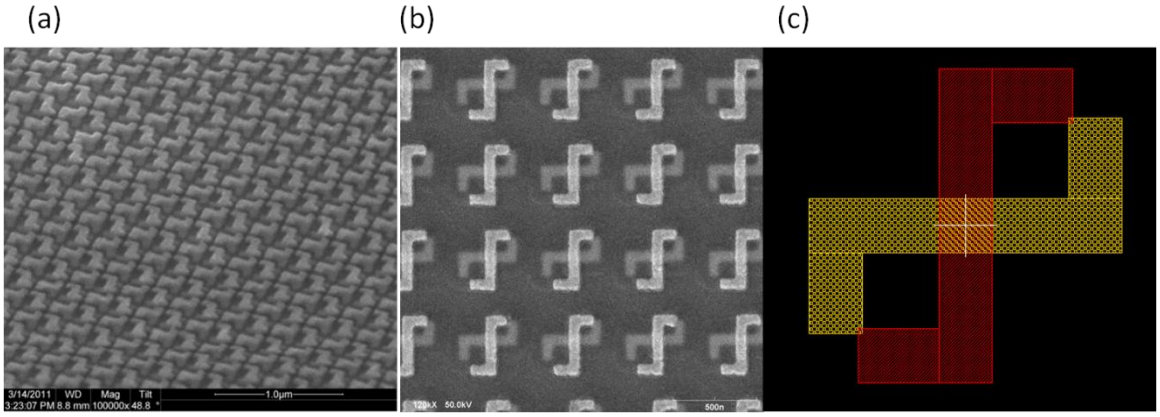

Figure 7.20. Optical isolator made by two times EBL overlay

Figure 7.21 and 7.22 show the new type of applications making isotropic negative refractive index metamaterials which are only available by very accurate multisteps EBL overlay process.

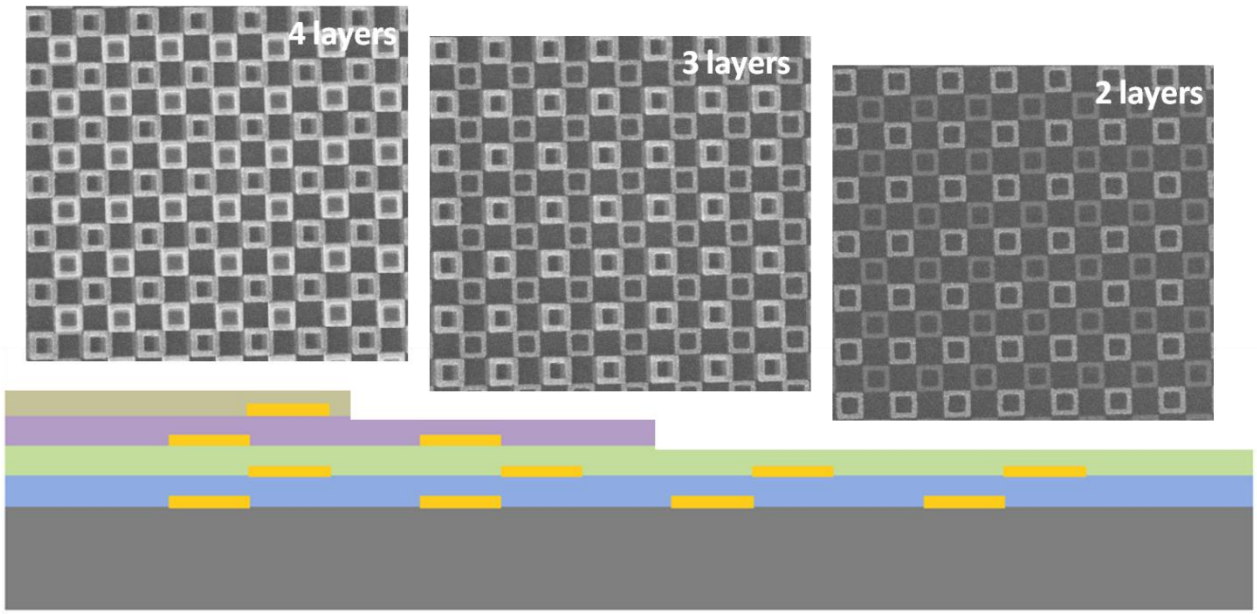

Figure 7.21. Four times EBL overlay process of stacked ring structure for isotropic negative refractive index metamaterial

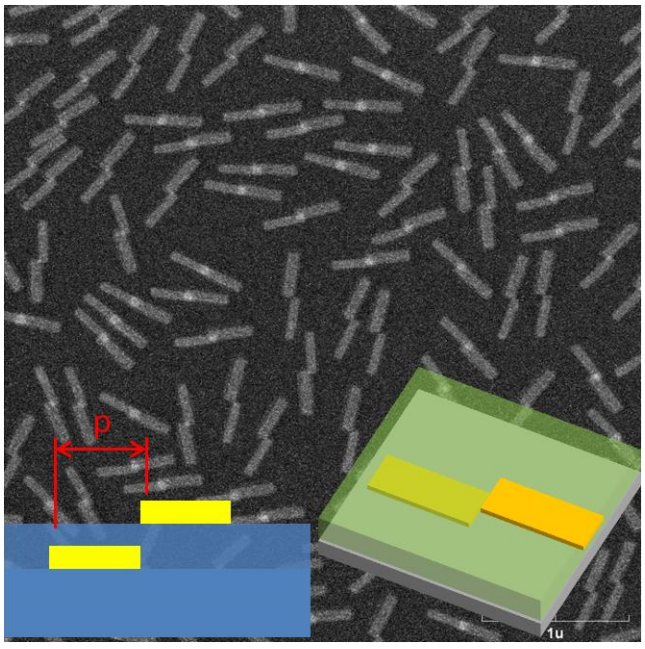

Figure 7.22. Two times EBL overlay process of stacked random bar structure for isotropic negative refractive index metamaterial

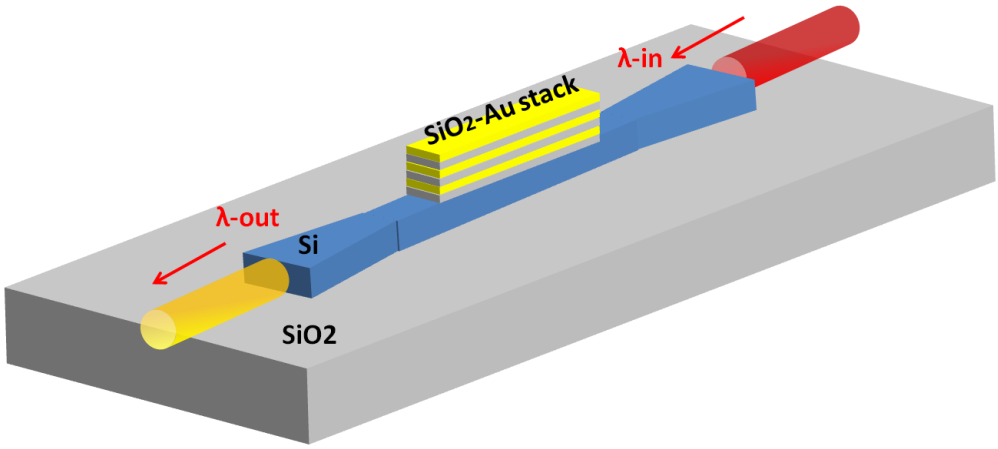

Figure 7.23. Design of hyperbolic metamaterial stacked SOI waveguide (2 EBLs)

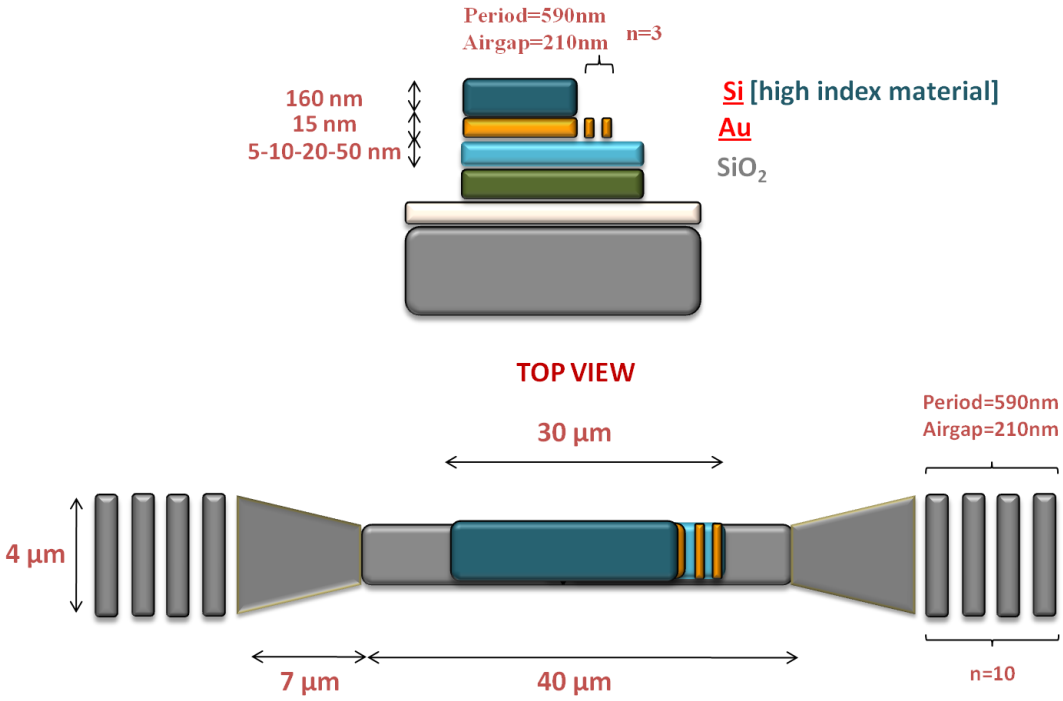

Figure 7.24. Design of SOI waveguide with three times EBL overlay (4 EBLs)

Figure 7.23 and 7.24 shows another application where a hyperbolic metamaterial of gold and silicon oxide multilayer is integrated into the silicon-on-insulator (SOI) waveguide. In this case, the first EBL patterning is achieved to define the waveguide structure on SOI substrate, and then the second (Figure 7.23) and the third & the fourth (Figure 7.24) EBLs are executed to define the hyperbolic metamaterial template, respectively. Finally, hyperbolic metamaterial is deposited by electron beam evaporation to fill the template on the top of SOI wafer. The fabricated devices of Figure 7.23 and 7.24 are shown in Figure 7.24 (a) and (b), respectively.

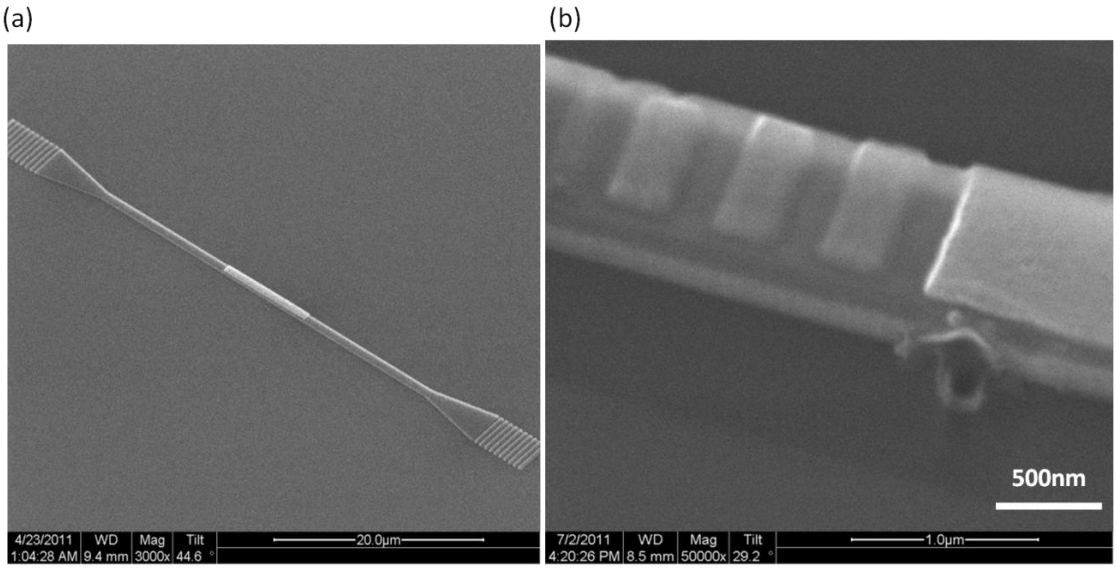

Figure 7.25. Fabrication of hyperbolic metamaterial stacked SOI waveguides. (a) SEM picture of fabricated waveguide in Figure 7.23 (b) SEM picture of fabricated waveguide in Figure 7.24

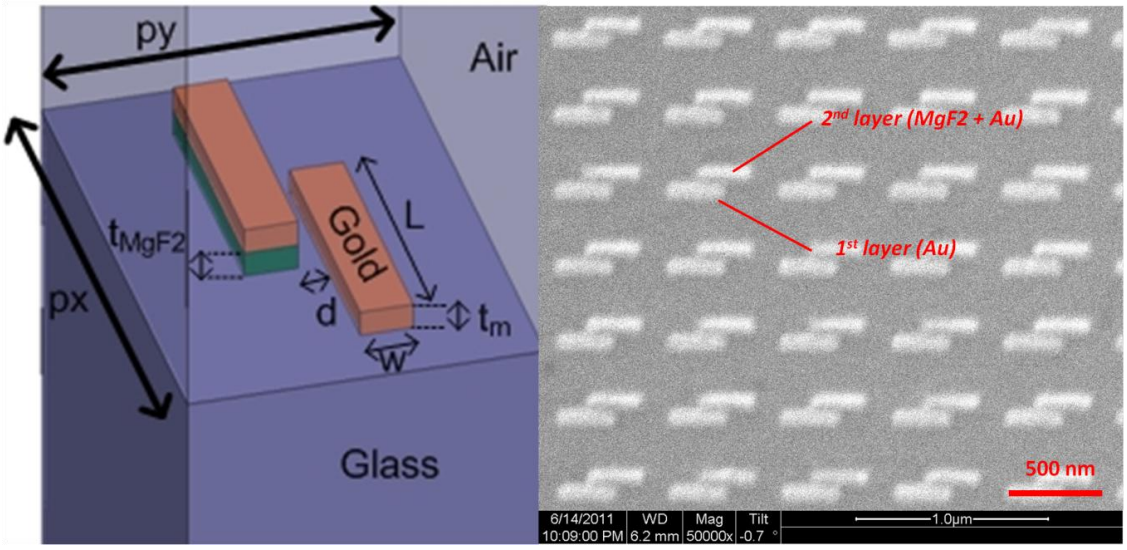

Figure 7.26. Design and fabrication of asymmetric bars structure with two different heights

The final approach is fabricating two or more different heights and materials structure fabrication. Due to the nature of EBL and lift-off process, a single height structure and a single type of material can be defined per EBL process. Therefore, fabricating two structures with different heights or different materials are not possible with single EBL process. However, introducing with EBL overlay process it becomes possible as shown in Figure 7.26, 7.27 and 7.28. Very precise EBL aligning related metamaterials and plasmonics works are shown in several literatures [110, 177, 205, 206, 207].

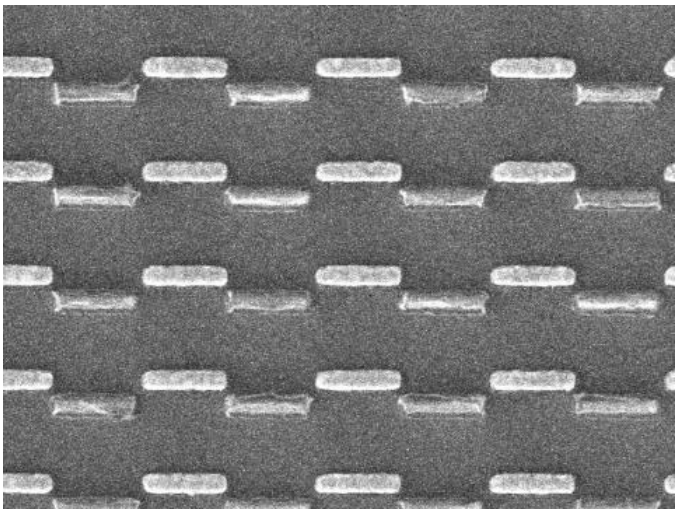

Figure 7.27. Detailed view of asymmetric bars structure with two different heights

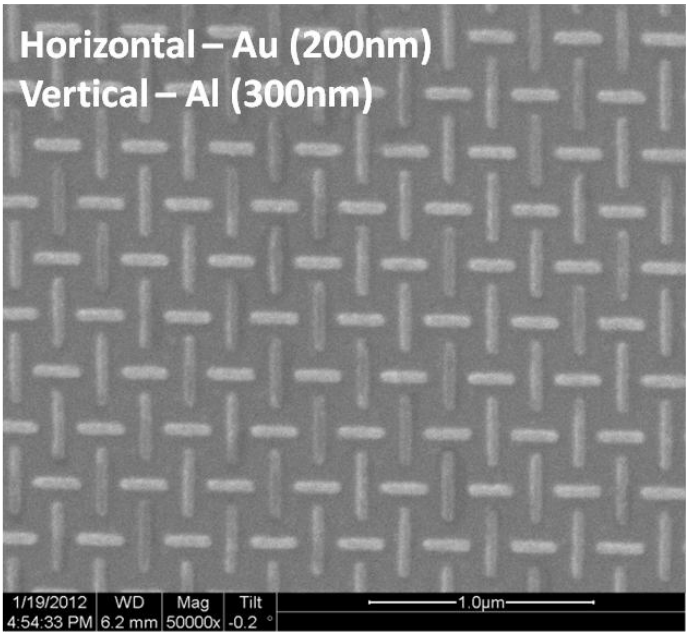

Figure 7.28. Design and fabrication of plasmonic bars structure with two different materials

7.2.3 Summary

In summary, EBL overlay process with highly precise align error allows several new types of metamaterial and plamonic structures, especially for 3D structures, CMOS compatible integrated devices, multiple materials and height combination in a single device and so on. This will offer a new platform and methodology toward three dimensional, bulk and isotropic metamaterial and plasmonic structures for more practical devices.

7.3 High resolution lift-off

7.3.1 Cold development

In EBL process, lift-off process is a subsequent process to define patterns because this process can make patterns with variety of material. When electron beam exposes to PMMA resist, it causes scission of the polymer chains to make low molecular weight segments and the exposed will be washed by developer (MIBK:IPA=1:3 solution, Microchem). While exposing of electron beam, scattered electron beam from the substrate also cuts the polymer chain from the bottom side and it results in negative angle of the developed area. However, when the resist is in developing, the corner of top surface of the resist also will be developed and it makes positive angle of resist. This positive angle of resist causes that material will be deposited on the side wall and it results in poor pattern definition as Figure 7.29 (a). However, instead of using room temperature developer, if cold developer is used for developing process, the resist is cooled, the higher molecular weight chain segments freeze-out more rapidly than the lower molecular weight segments that would be found in the exposed region. Therefore, the lower molecular weight region, the bottom of a resist, will be developed faster than the higher molecular weight region, the top of a resist [203]. This process helps the vertical angle make negative to prevent side wall deposition and the fine patterns can be obtained as Figure 7.29 (b). This sharper and angled PMMA structure allows cleaner lift-off process due to minimized side-wall interaction. Lift-offed metamaterials structures such as metamaterial optical cavities in the chapter 4 in this dissertation are all made by the cold development otherwise there is noted.

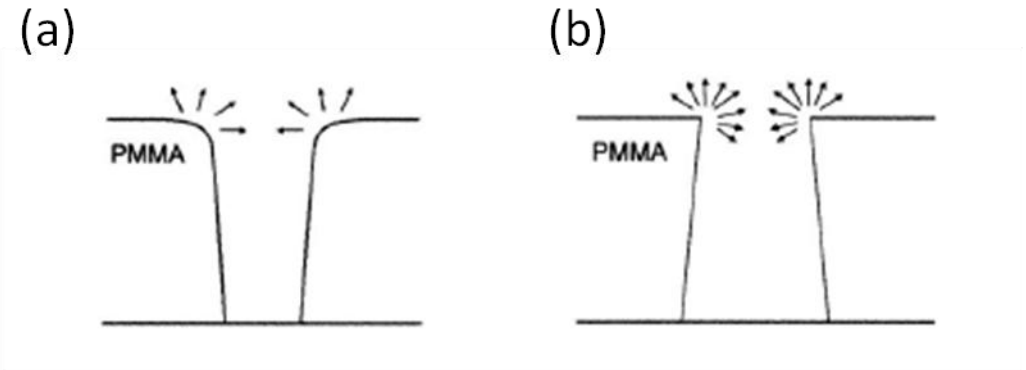

Figure 7.29. The effect of the developing temperature. (a) Room temperature (25℃) (b) Low temperature (4℃)

To compare both schemes above, several test patterns are made with EBL and gold lift-off in PMMA A3. The temperature of a developer is 4℃ and the development time is 3 times longer

than the case of the room temperature (RT). Figure 7.30

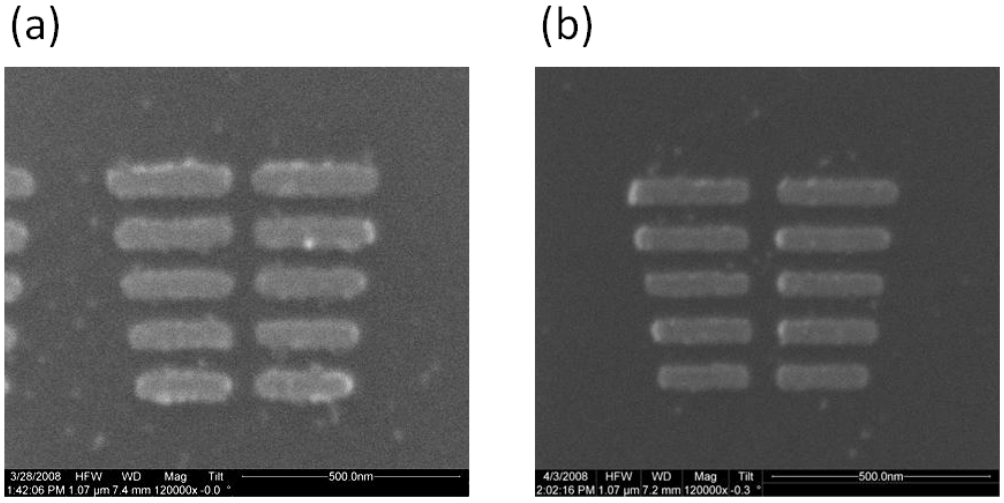

Figure 7.30. (a) shows the sample developed by room temperature and Figure 7.30 (b) shows the sample developed by cold temperature. The RT sample represents poor line sharpness and corner roundness and, finally, the dimension of the pattern is hard to match to the original design. However, the cold developed case represents much better pattern quality and this process is very effective to the EBL lift-off process.

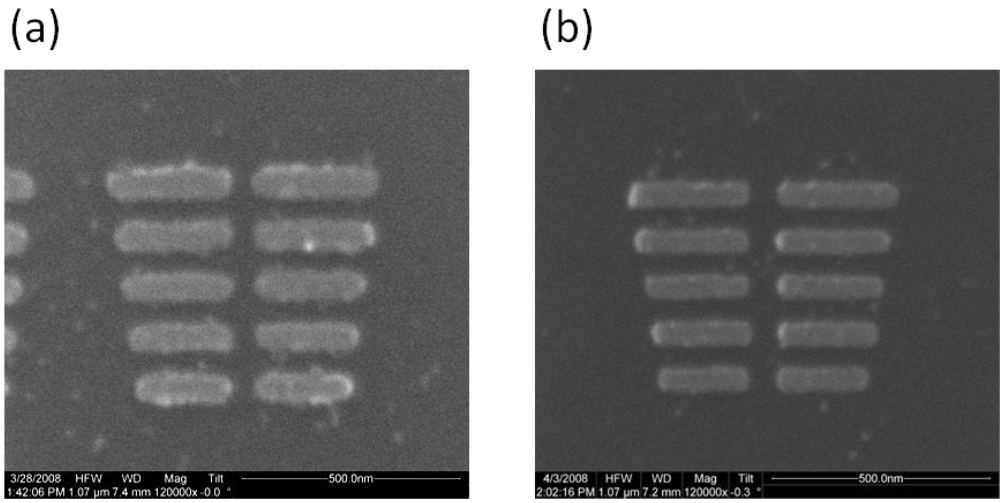

Figure 7.30. The comparison of the temperature of developer (a) RT (25℃) (b) Cold (4℃)

The other plasmonic antenna structures are shown at Figure 7.31 as examples of improved quality of EBL and lift-off process very much.

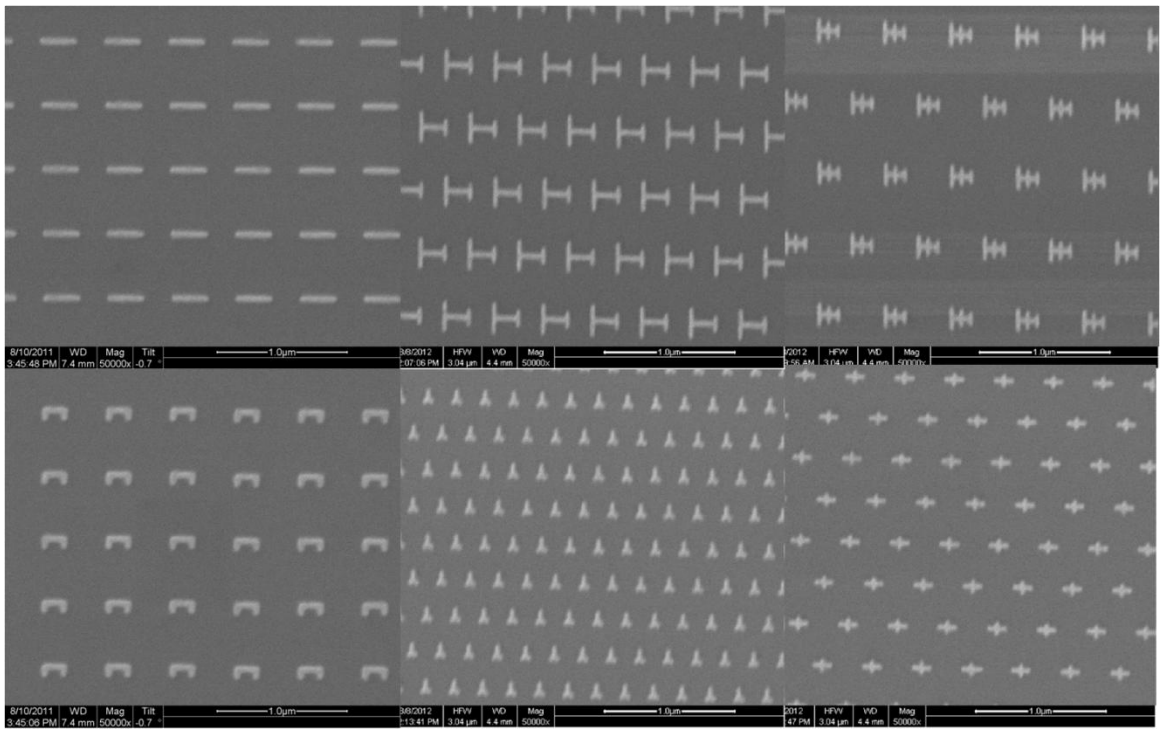

Figure 7.31. Examples of the structure made by cold development process. Plasmonic and metamaterial structures such as nanowires, phonon bars, split ring resonators array are shown.

7.3.2 Bi-layer MMA-PMMA resists process

The cold development process can make negative angle of side wall in photoresist to make fine features, but if the temperature goes up in the middle of development process or the temperature is not enough low, the vertical profile can make bad effect to have positive side wall. The bi-layer MMA-PMMA process uses two types of resists, MMA and PMMA, and they have different sensitivity of electron beam. MMA is much more sensitive than PMMA so that the developed pattern in MMA with same electron beam doses will be bigger than the pattern in PMMA. Therefore, if MMA layer is below PMMA layer, the vertical profile will have 2 steps and the bottom step in MMA region will be wider than PMMA region. The schematic process of single layer and bi-layer process are shown in Figure 7.32 and 7.33, respectively. Usually,

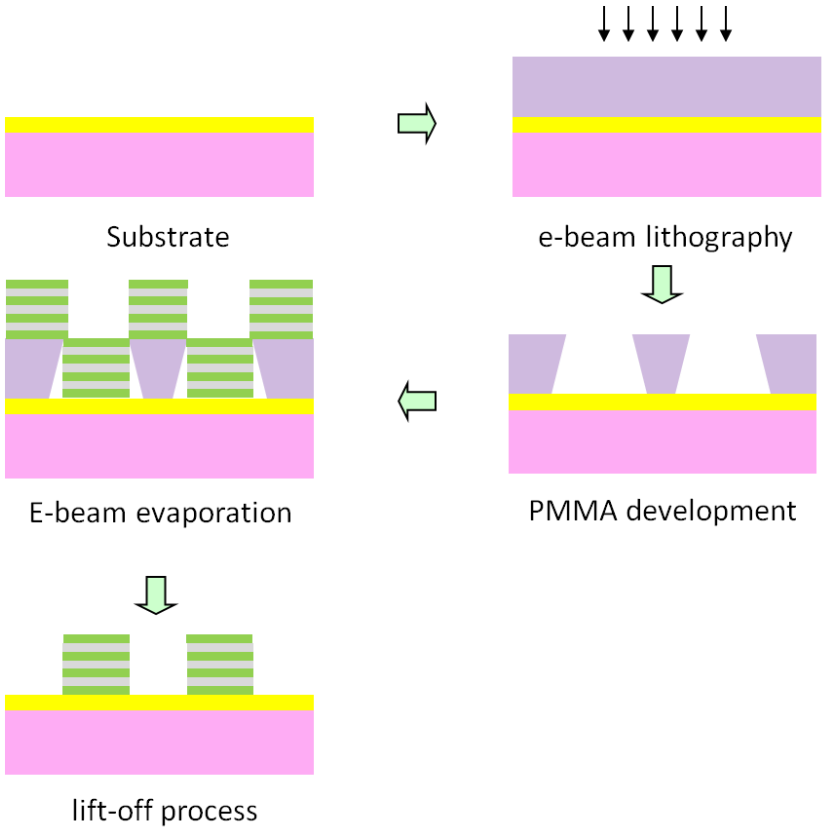

Figure 7.32. Single layer lift-off process with PMMA

For the bi-layer lift-off process, firstly, MMA and PMMA are spun on the substrate in order, and electron beam is exposed on the top surface. Because of different sensitivity to electron beam, the width of patterns in MMA will be wider than in PMMA, and it prevents material deposited on the side wall. Unless there is special comment, I used three times higher MMA layer than the final structure for better quality lift-off process. Finally, the patterns are obtained and a very fine pattern without any residue can be obtained as Figure 7.33 (b) comparing to the Figure 7.33(a) by single layer process.

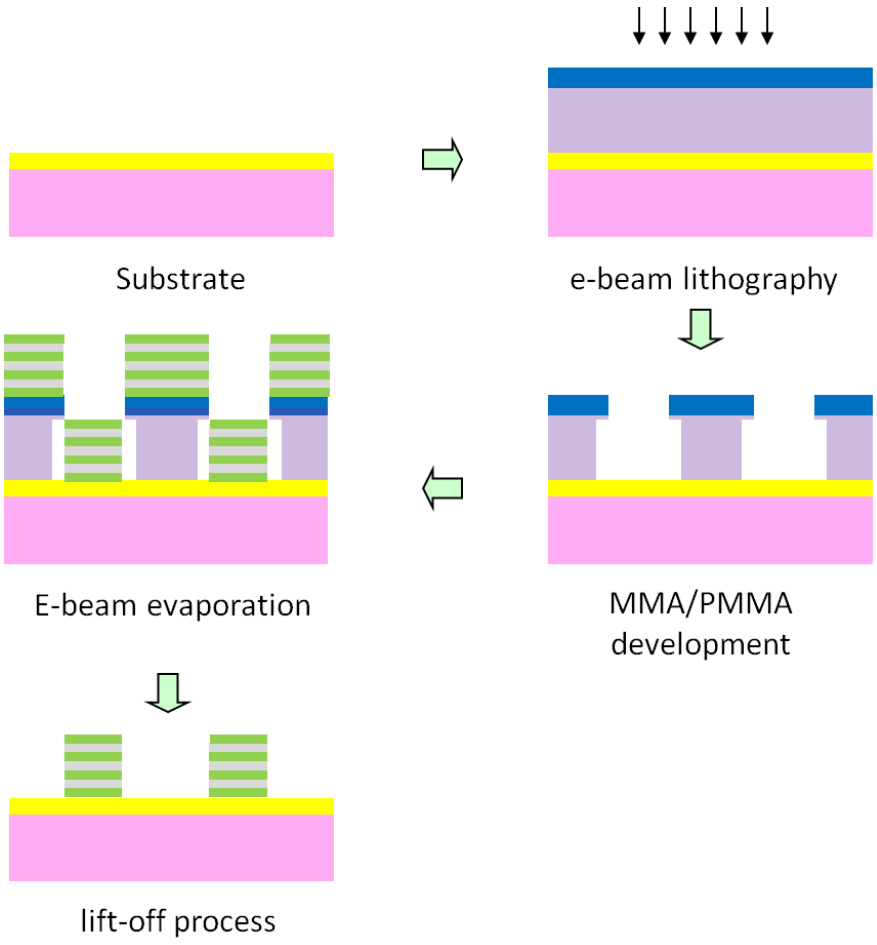

Figure 7.33. Bi-layer lift-off process with MMA/PMMA

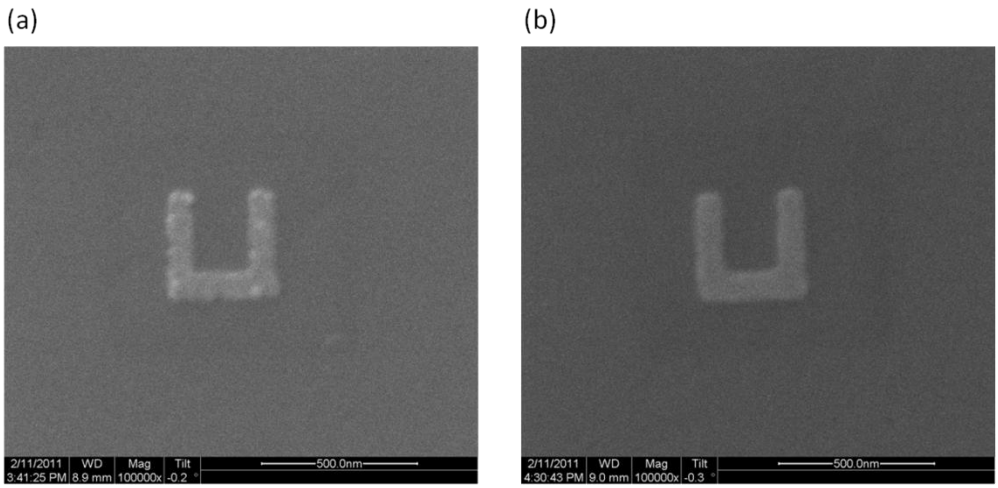

Figure 7.34. Example of bi-layer MMA-PMMA process (a) Split ring resonator with single layer lift-off process (b) Split ring resonator with bi-layer lift-off process

7.3.3 Summary

In this chapter, I discussed several creative methods to improve the quality of metal and dielectric nanostructures based on nanofabrication techniques such EBL and lift-off process for metamaterials and plasmonics research. As well as high resolution is important, the clean profiles of structure such as surface roughness and sidewall are also important to show proper optical properties for the purpose of metamaterials and plasmonics. The methods discussed in this chapter are one of the efforts to compensate the lack of proper techniques for the fast development of nanofabrication tools.

7.4 Controllable single quantum dot lithography

Quantum dots (QDs) are one of the most interesting components in nanoscience and nanotechnology. For its very efficient single emitter property, it is considered as a future emitting source which could be widely used for semiconductor, display and laser technology. However, current problem is controlling the number and position of QDs. To integrate QDs into nanodevices such as nanophotonic and nanoelectronic devices, we have to control the exact number of QDs to be located on the devices and the precisely aligned location on the devices. The more QDs are located in a position, the more chance they could be aggregated to each other. Also, if QDs are positioned in unwanted locations, it will prevent high performance of the devices. Therefore, in this chapter, I will show very precise and accurate position control with single QD as a future lithography technique of QDs and further nanoparticles. It will be hugely impactful for several research, especially for integrating QDs with metamaterials and plasmonics devices to enhance their performance.

7.4.1 Direct lift-off method

Direct lift-off method is dealing QDs like normal materials for lift-off process. After making templates structures in photoresist, depositing QDs (actually spreading out QDs on the substrate) is followed. Finally, once we remove photoresist by acetone or other solvents, only QDs structure remains on the substrate. The merit of this process is very easy integration with EBL process. EBL process is very standard process to define the nanostructures as we discussed previous chapters, and EBL overlay allows very precise control of structure positioning on the existing structure. Therefore, QDs are also possible to be positioned on the designated location of the existing devices. The drawback of this process is very difficult to control the number of QDs. Generally, putting single QD is meaningful for many research directions, but in this case many QDs are being aggregated during spreading and soaking processes. Therefore, only with very precise concentration control, it would show more promising for QDs lithography. Figure 7.35 shows the process flow. It is very similar to the normal lift-off process. As like normal lift-off process is done with thin film deposition in polymer template, this method also use polymer as a template to define the nanostructure of QDs. Finally polymer is removed to release the QDs only nanostructures on the substrate. Figure7.36 and 7.37 are the results from two different QDs depositing method, one is Electrical deposition and the other is alternative charged QDs deposition. Figure 7.37 shows more uniform distribution though both didn’t show single QD.

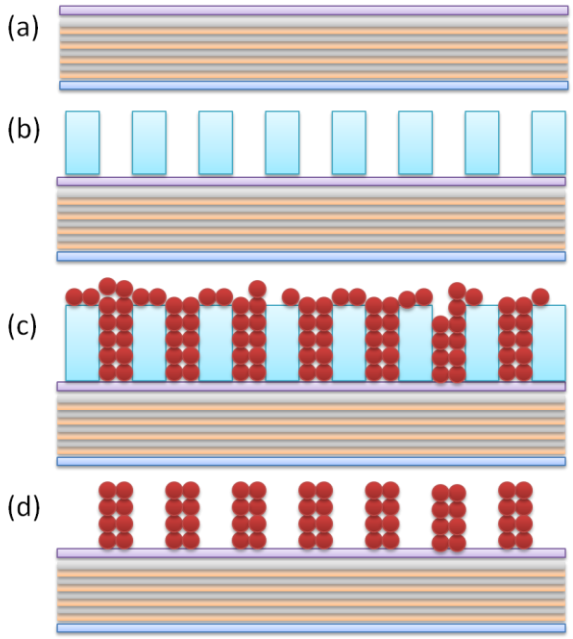

Figure 7.35. Direct QDs lift-off process flow. (a) Substrate preparation. (b) EBL process defines template. (c) QDs are spread out and soaked for a while. This stage is compatible to deposit thin film in normal lift-off process. (d) Photoresist is removed, thus the QDs structure only remains.

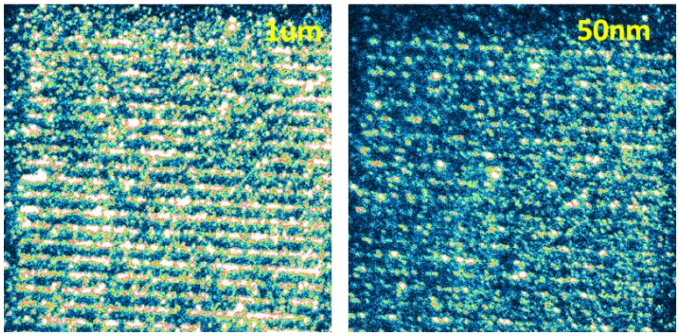

Figure 7.36. Result of direct QDs lift-off process with electrical deposition of QDs

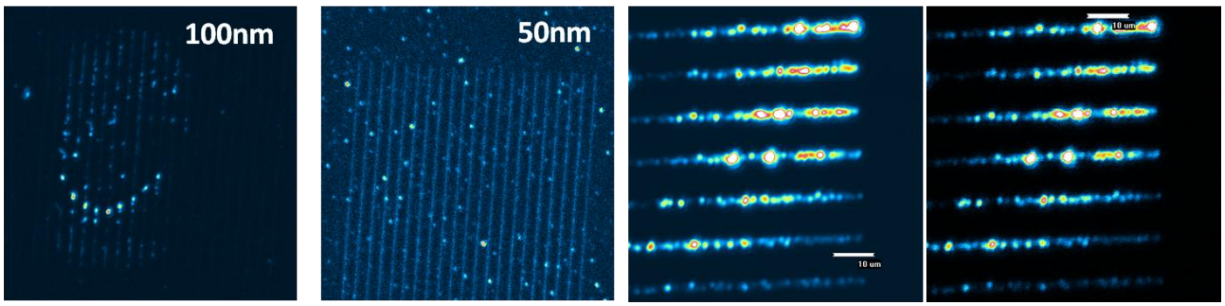

Figure 7.37. Result of direct QDs lift-off process with alternatively charged QDs deposition

7.4.2 Direct EBL on QDs doped photoresist method

Second method is direct EBL writing on QDs doped photoresist. In this case we mix QDs into liquid type of PMMA or power type of PMMA with toluene solvent. With careful control of concentration, we expect QDs are distributed in the entire PMMA uniformly. However, controlling uniformity is difficult to achieve. Instead, relatively easy patterning through normal EBL process allowed very flexible design process due to EBL's direct exposure on the QDs doped PMMA. Figure 7.38 describes fabrication flow of direct EBL writing on QDs doped PMMA. It allows easy fabrication method, but concentration control for single QD was very difficult. Figure 7.39 shows an example made by this method.

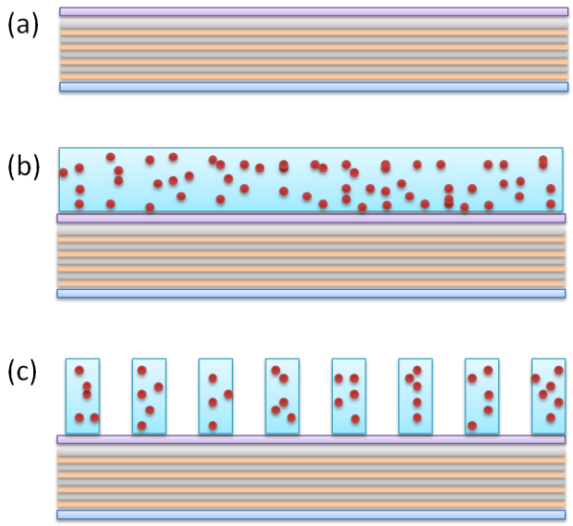

Figure 7.38. Direct EBL on QDs doped PMMA process flow. (a) Substrate preparation. (b) QDs doped PMMA is spin coated on the substrate. (c) EBL exposes the PMMA for designed structure.

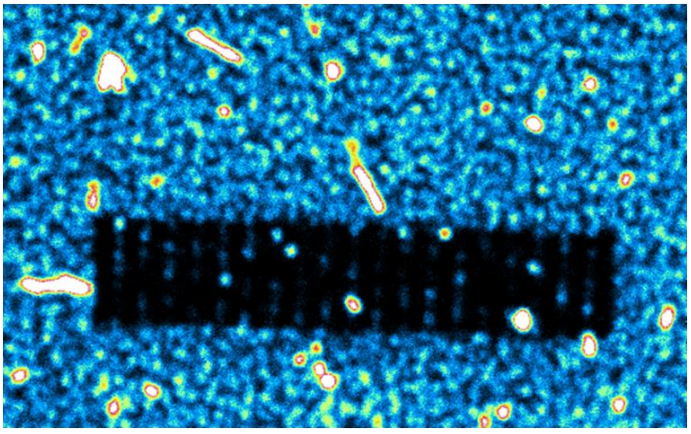

Figure 7.39. Result of direct EBL on QDs doped PMMA. In the center area, 50nm wide line array is well defied with QDs relatively uniformly. However, there is no clue it is single QD.

7.4.3 Functionalized gold-QD binding method

To overcome previous two methods, I needed more controllable and repeatable method locating QDs onto the exact position as well as sorting a single QD, not multiple aggregated QDs. The method discussed in this chapter offers exact positioning with EBL overlay technique discussed in previous chapter and single QD sorting by chemical functionalization.

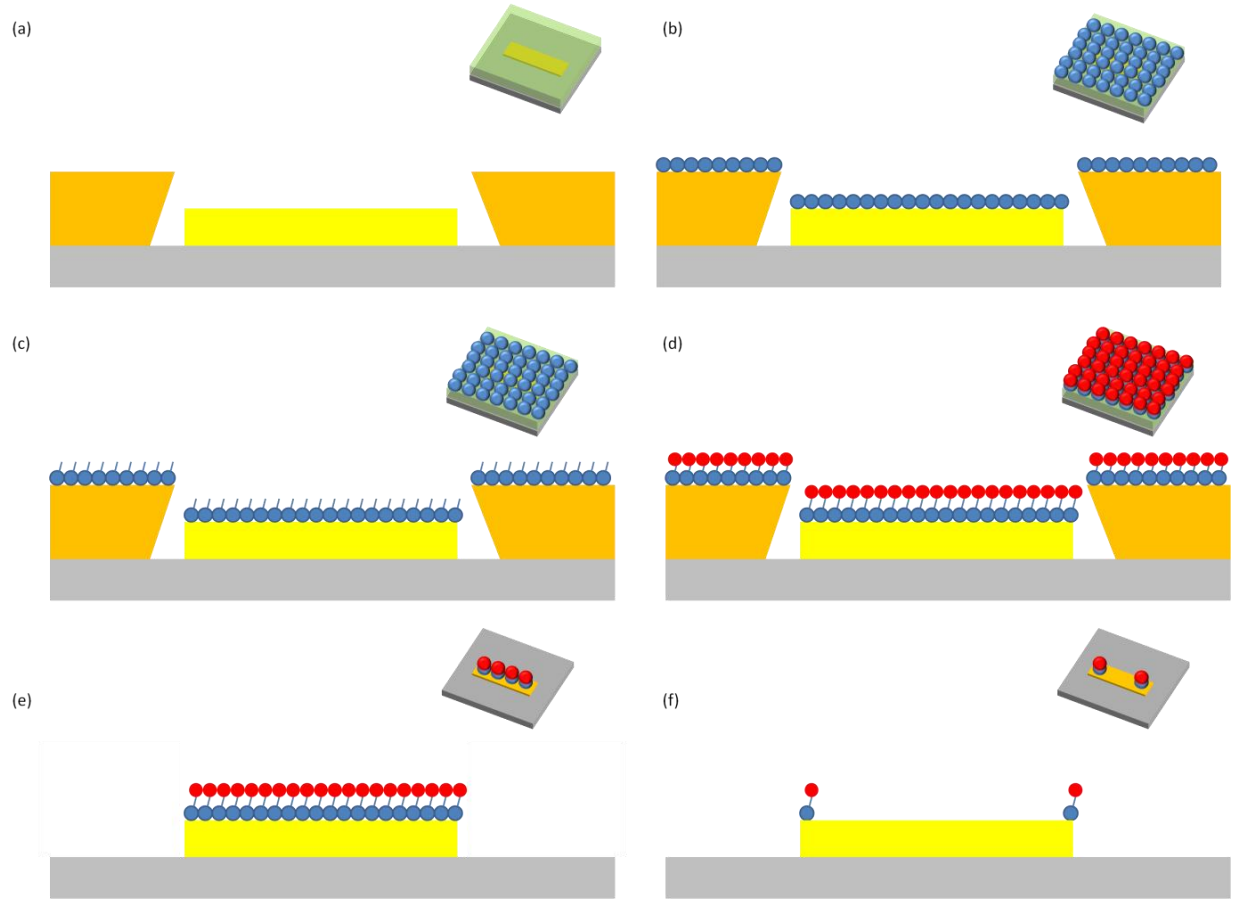

Figure 7.40. Fabrication process of single QD binding with functionalization on gold. (a) Normal EBL process and gold deposition (b) MUA treatment (c) EDC coupling treatment (d) QDs binding to EDC coupled MUA (e) The final structure of single QDs coupled gold bar (1 EBL) (f) The final structure of selectively postioned single QDs coupled gold bar (2 EBLs)

In order to achieve this precise single QD lithography, I used EBL overlay process twice together with selective chemical functionalization of predefined areas by EBL. I used core-shell (CdSeTe/ZnS) quantum dots with a polymer coating (Invitrogen, QD amine-800 ITK). Normal EBL process defines the structures on an ITO coated glass substrate, formed by subsequent electron beam evaporation of 2nm Cr and 30nm Au layer. If the entire gold structure needs single QDs deposition on top, QD method is followed. (Figure) If the selective area of gold structure needs single QDs, lift-off is first executed and second EBL process is followed to

define the area where QDs will connected only. For chemistry part, the sample is soaked in mercapto-undecanoic acid (MUA) diluted with ethanol (50ml x 5mM x 10^-6mol/ml x 207g =50mg MUA in 50ml 200 proof ethanol) for 48 hours. At this moment, no pH adjustment is necessary. Then, activation process with carbodiimide (EDC) for amine type QDs binding is followed. EDC is prepared with one capsule (40mg) in 1ml buffer (MES pH 5.2) and the MUA treated sample is soaked in EDC solution for 30mins, and then cleaned with buffer solution (pH<7.5). Quantum dot is carefully diluted in PBS solution (pH 7-7.5) to optimize the number of QDs which prevents aggregation of QDs, this gives single QDs binding. 2ul QDs is diluted 4ml and 8ml PBS with sonication for uniformity. Finally, while QDs solution soaks the sample, QDs are covalently bound to the MUA functionalized regions. After some minutes, the remaining resist is removed by a standard lift-off protocol. As a result, I could estimate that the distance between the outer surface of the QD shell and the metal is around 6 nm, sufficient to avoid luminescence quenching and to provide efficient coupling.

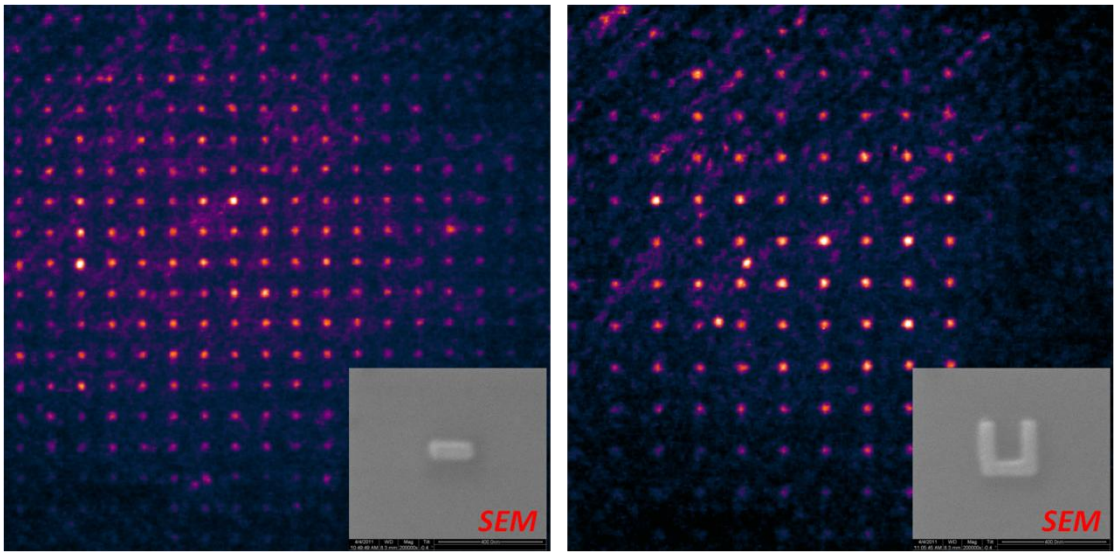

Figure 7.41. SEM images of QDs lithography. (a) Single QDs on bar array (b) Single QDs on split ring resonator (SRR) array

Figure 7.41 is the result of fabricated samples. 7.41 (a) is single gold bar array with 1.5um pitch between each bar. 7.41 (b) is single SRR array with 2um pitch. Both samples show uniformly bright structure comparing background on the quartz substrate. Even though some residues of QDs are shown on the substrate, the contrast between the substrate and the structure is very high. To check the quality and the performance whether they are single QDs or aggregated multiple QDs, optical measurement and characterization are followed. 532nm laser in 30mW is used for pumping the structure and 100x 1.4NA oil immersion objective is used for capturing images. Radiation patterns are obtained as shown in Figure 7.42 and 7.42. Bar array has 58% contrast ratio which confirms the single QDs quality to emit the light along dipole direction. SRR array has 80% contrast ratio to confirm the quadruple structure.

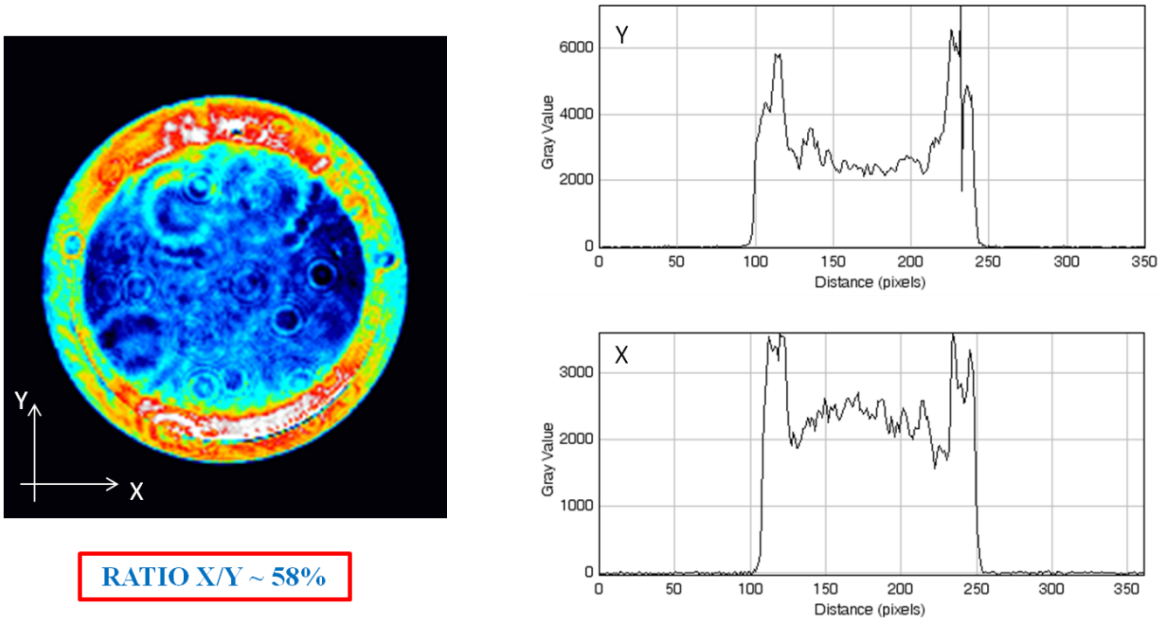

Figure 7.42. Measurement result of single gold bar array with single QDs

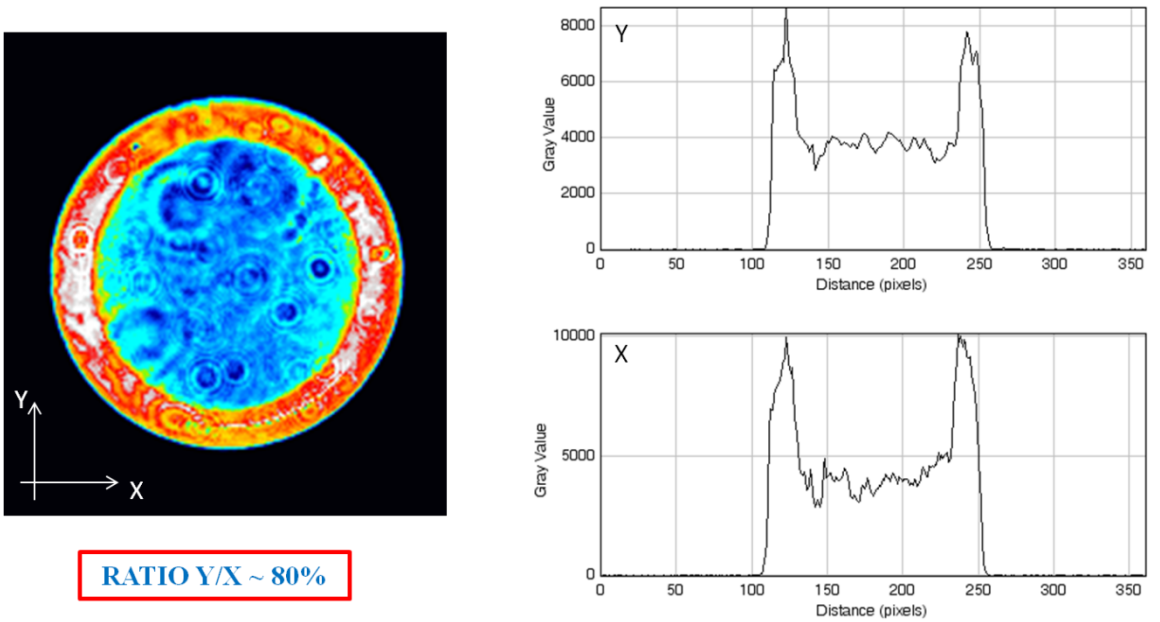

Figure 7.43. Measurement result of single gold SRR array with single QDs

In summary, controllable QDs positioning as a lithographic method and confirmable single QD sorting techniques is shown in this chapter. This technique will integrate current metamaterials and plasmonic structures to enhance emitting performance and other practical applications such as display and light source technology [207, 208].

Chapter 8

Conclusion

As nanoscience and nanotechnology have developed significantly for the last several decades, controlling and manipulating light beyond the diffraction limit cannot be over-emphasized in the field of optics and photonics. Also, achieving smaller devices with faster performance has been a key area in electronics and computer science. The invention of metamaterials has greatly supported the realization of dreams and science fiction with unprecedented phenomena such as negative refraction of light and invisibility cloaking.

This dissertation focuses on efforts to control and manipulate light beyond the diffraction limit based on developing novel multi-functional nanoscale materials and devices using the concept of metamaterials. These materials show extraordinary optical properties such as unbounded wavevector access for propagating and confining sub-diffraction light very efficiently, switchable negative refractive index and high-resolution/high-throughput nanolithography. Based on the development of such materials and devices, I made a significant effort to control and manipulate the light beyond diffraction limit.

After a brief introduction of materials science, the fundamentals of metamaterials, plasmonics, and basic electromagnetism including dispersion relations, permittivity and permeability, and Snell's law are presented in the first chapter. In chapter 2-4, I discussed the fundamental physics of hyperbolic metamaterials and applications. with a very strongly anisotropic and controllable dispersion relation, unique applications are introduced in each chapter. Chapter 2 showed theoretical studies of hyperbolic metamaterials, which are essential to understanding hyperbolic dispersion and allowing further design of metamaterial devices. Chapter 3 focused on the experimental demonstration of spherical hyperlens for two dimensional real-time super-resolution imaging beyond the diffraction limit at visible frequencies. Chapter 4 presented another hyperbolic metamaterial application of an optical cavity which is scaled down to far smaller than the diffraction limit and achieved confinement of light into truly nanometer dimensions. Chapter 5 and chapter 6 covered different types of metamaterials, including fundamentals and applications. In chapter 5, a novel switching device of negative refractive index by light is demonstrated experimentally. Chapter 6 discussed not only a new metamaterial application called a metasurface, which allows unprecedented properties such as strong spin hall effect observation, but also plasmonic and metamaterial assisted super-resolution flying head nanolithography for overcoming current resolution and throughput limitations of lithography. Chapter 7 is dedicated to the nanoscale fabrication techniques. The details of the fabrication processes of the devices described in this thesis and the details of recipes are provided. Also, useful nanofabrication techniques are introduced for metamaterials and plasmonics research.

In spite of great development of science and technology, there are still many undiscovered things waiting to be unveiled. Obviously, the more we discover new things, the more new possibilities are revealed. I am very pleased to be a part of discovering exciting science and technology, and I am confident that I will be the heart of further advances in science and technology that will contribute to the world.

Bibliography

1. R. Hummel, *Understanding Materials Science*, Springer, (2004)

2. V. G. Veselago, "The electrodynamics of substances with simultaneously negative values of eta and mu", *Soviet Physics - Uspekhi|Uspekhi Fizicheskii Nauk|Soviet Physics - Uspekhi*, **517** (1967)

3. V. Lindell *et al.*, "BW media-media with negative parameters, capable of supporting backward waves", *Microwave and Optical Technology Lett.* **31** (2), 129 (2001)

4. Ashwin K. Iyer and George V. Eleftheriades, (Wiley Interscience, 2005)

5. J. B. Pendry, "Negative refraction makes a perfect lens", *Phys. Rev. Lett.* **85**, 3966 (2000)

6. R. A. Shelby *et al.*, "Experimental verification of a negative index of refraction", *Science* **292**, 77 (2001)

7. D. R. Smith *et al.*, "Metamaterials and negative refractive index", *Science* **305**, 788 (2004)

8. M. Choi *et al.*, "A terahertz metamaterial with unnaturally high refractive index", *Nature* **470**, 369 (2011)

9. M. Silveirinha *et al.*, "Design of matched zero-index metamaterials using nonmagnetic inclusions in epsilon-near-zero-media", *Phys. Rev. B* **75**, 075119 (2007)

10. S. Kocaman *et al.*, "Zero phase delay in engative-refractive-index photonic crystal superlattices", *Nature Photon.* **5**, 499 (2011)

11. E. Abbe, "Beiträge zur theorie des mikroskops und der mikroskopischen wahrnehmung", *Arch. Mikroskop.* Anat. **9**, 413 (1873)

12. M. Born and E. Wolf, E. *Principles of Optics* 4th edn. (Pergamon, 1970)

13. N. Fang, H. Lee, C. Sun and X. Zhang, "Sub-diffraction-limited optical imaging with a silver superlens", *Science* **308**, 534 (2005)

14. Z. Liu *et al.*, "Far-field optical hyperlens magnifying sub-diffraction-limited objects", *Science* **315**, 1686 (2007)

15. J. Pendry *et al.*, "Magnetism from conductors and enhanced nonlinear phenomena", *Microwave Theory and Techniques, IEEE Transactions*, **47**, 2075 (1999)

16. T. J. Yen, W.J. Padilla, N. Fang, D.C. Vier, D.R. Smith, J.B. Pendry, D.N. Basov, and X. Zhang, "Terahertz Magnetic Response from Artificial Materials", *Science*, **303**, 1494 (2004)

17. S. Linden, C. Enkrich, M. Wegener, J. Zhou, T. Koschny, and C.M. Soukoulis, "Magnetic Response of Metamaterials at 100 Terahertz", *Science*, **306**, 1351 (2004)

18. J. B. Pendry, A. J. Holden, W. J. Stewart, and I. Youngs, "Extremely Low Frequency Plasmons in Metallic Mesostructures," *Phys. Rev. Lett.*, **76**, 4773 (1996)

19. J. B. Pendry, D. Schurig, and D. R. Smith, "Controlling Electromagnetic Fields", *Science*, **312**, 1780 (2006)

20. U. Leonhardt, "Optical Conformal Mapping", *Science*, **312**, 1777 (2006)

21. D. Schurig, J. J. Mock, B.J. Justice, S.A. Cummer, J.B. Pendry, A.F. Starr, and D.R. Smith, "Metamaterial Electromagnetic Cloak at Microwave Frequencies," *Science*, **314**, 977 (2006)

22. W. Cai, U.K. Chettiar, A.V. Kildishev, and V.M. Shalaev, "Optical cloaking with metamaterials", *Nature Photon.*, **1**, 224 (2007)

23. J. Li and J.B. Pendry, "Hiding under the Carpet: A New Strategy for Cloaking", *Phys. Rev. Lett.*, **101**, 203901 (2008)

24. R. Liu, C. Ji, J.J. Mock, J.Y. Chin, T.J. Cui, and D.R. Smith, "Broadband Ground-Plane Cloak", *Science*, **323**, 366 (2009)

25. J. Valentine, J. Li, T. Zentgraf, G. Bartal, and X. Zhang, "An optical cloak made of dielectrics", *Nature Mater.*, **8**, 568 (2009)

26. J. C. Halimeh, T. Ergin, J. Mueller, N. Stenger, and M. Wegener, "Photorealistic images of carpet cloaks", *Optics Express*, **17**, 19328 (2009)

27. T. Ergin, N. Stenger, P. Brenner, J.B. Pendry, and M. Wegener, "Three-Dimensional Invisibility Cloak at Optical Wavelengths", *Science*, **328**, 337 (2010)

28. R. D. Piner, J. Zhu, F. Xu et al., ""Dip-pen" nanolithography", *Science* **283,** 661 (1999)

29. Z. Hua, S. W. Chung, and C. A. Mirkin, "Fabrication of sub-50-nm solid-state nanostructures on the basis of dip-pen nanolithography", *Nano Lett.* **3**, 43 (2003)

30. T. W. Ebbesen, H. J. Lezec, H. F. Ghaemi et al., "Extraordinary optical transmission through sub-wavelength hole arrays", *Nature* **391**, 667 (1998)

31. T. Thio, H. F. Ghaemi, H. J. Lezec et al., "Surface-plasmon-enhanced transmission through hole arrays in Cr films", *J. Opt. Soc. Am. B* **16** , 1743 (1999)

32. A. Krishnan, T. Thio, T. J. Kima et al., "Evanescently coupled resonance in surface plasmon enhanced transmission", *Opt. Commun.***200**, 1 (2001)

33. A. Dogariu, A. Nahata, R. A. Linke et al., "Optical pulse propagation through metallic nano-apertures", *Appl. Phys. B-Lasers and Optics* **74**, S69 (2002)

34. L. Salomon, F. Grillot, A. V. Zayats et al., "Near-field distribution of optical transmission of periodic subwavelength holes in a metal film", *Phys. Rev. Lett.* **86**, 1110 (2001)

35. B. Pettinger, B. Ren, G. Picardi et al., "Nanoscale probing of adsorbed species by tip-enhanced Raman spectroscopy", *Phys. Rev. Lett.* **92**, 096101/1 (2004)

36. A. J. Haes and R. P. Van Duyne, "A unified view of propagating and localized surface plasmon resonance biosensors", *Anal. Bioanal. Chem.* **379**, 920 (2004)

37. J. M. Brockman, B. P. Nelson, and R. M. Corn, "Surface plasmon resonance imaging measurements of ultrathin organic films", *Annu. Rev. Phys. Chem.* **51**, 41 (2000)

38. D. R. Smith and D. Schurig, "Electromagnetic wave propagation in media with indefinite permittivity and permeability tensors", *Phys. Rev. Lett.* **90**, 077405 (2003)

39. J. Yao et al., "Optical negative refraction in bulk metamaterials of nanowires", *Science*, **321**, 930 (2008)

40. Y. Liu, G. Bartal, and X. Zhang, "All-angle negative refraction and imaging in a bulk medium made of metallic nanowires in the visible region", *Opt. Express*, **16**, 15439 (2008)

41. V. A. Podolskiy and E.E. Narimanov, "Strongly anisotropic waveguide as a nonmagnetic left-handed system", *Phys. Rev. B*, **71**, 201101 (2005)

42. W. Cai. *Optical Metamaterials: Fundamentals and Applications*, Springer (2009)

43. W. R. Tinga, W. A. G. Voss, D. F. Blossey, "Generalized approach to multiphase dielectric mixture theory", *J. Appl. Phys.* **44**, 3897 (1973)

44. K. H. A. Lau, L. Tan, K. Tamada, M. S. Sander, and W. Knoll, "Highly sensitive detection of processes occurring inside nanoporous anodic alumina templates: a waveguide optical study," *J. Phys. Chem. B*, **108**, 10812 (2004)

45. G. L. Hornyak, C. J. Patrissi, and C. R. Martin, "Fabrication, characterization, and optical properties ofgold nanoparticle/porous alumina composites: the nonscattering Maxwell−Garnett limit," *J. Phys. Chem. B*, **101**, 1548 (1997)

46. P. B. Johnson and R. W. Christy, "Optical constants of the noble metals," *Phys. Rev. B*, **6**, 4370 (1972)

47. Z. Jacob, *et al.*, "Optical hyperlens: far-field imaging beyond the diffraction limit", *Opt. Express* **14**, 8247 (2006)

48. Salandrino and N. Engheta, “Far-field subdiffraction optical microscopy using metamaterial crystals: theory and simulations”, *Phys. Rev. B* **74**, 075103 (2006)

49. G. V. Naik *et al.*, “Demonstration of Al:ZnO as a plasmonic component for near-infrared metamaterials”, *Proc. Natl. Acad. Sci. USA*, **109**, 8834 (2012)

50. A. V. Kildishev, A. Boltasseva and V. M. Shalaev, “Plana photonics with metasurface”, *Science*, **339**, 1289 (2013)

51. R. Hillenbrand and F. Keilmann, “Optical oscillation modes of plasmon particles observed in direct space by phase-contrast near-field microscopy”, *Appl. Phys. B* **73**, 239 (2001)

52. T. Taubner *et al.*, “Near-field microscopy through a SiC superlens”, *Science* **313**, 1595 (2006)

53. H. Lee *et al.*, “Development of optical hyperlens for imaging below the diffraction limit”, *Opt. Express* **15**, 15886 (2007)

54. A. V. Kildishev and E. E. Narimanov, “Impedance-matched hyperlens”, *Opt. Lett.* **32**, 3432 (2007)

55. Y. Xiong, Z. Liu and X. Zhang, “A simple design of flat hyperlens for lithography and imaging with half-pitch resolution down to 20 nm”, *Appl. Phys. Lett.* **94**, 203108 (2009)

56. W. Wang *et al.*, “Far-field imaging device: planar hyperlens with magnification using multi-layer metamaterial”, *Opt. Express* **16**, 21142 (2008)

57. M. Tsang and D. Psaltis, “Magnifying perfect lens and superlens design by coordinate transformation”, *Phys. Rev. B* **77**, 035122 (2008)

58. A. V. Kildishev *et al.*, “Materializing a binary hyperlens design”, *Appl. Phys. Lett.* **94**, 071102 (2009)

59. J. Li *et al.*, “Experimental demonstration of an acoustic magnifying hyperlens”, *Nature Mater.* **8**, 931 (2009)

60. S. Schwaiger *et al.*, “Rolled-up three-dimensional metamaterials with a tunable plasma frequency in thevisible regime”, *Phys. Rev. Lett.* **102**, 163903 (2009)

61. A. V. Kildishev and V. M. Shalaev, “Engineering space for light via transformation optics”, *Opt. Lett.* **33**, 43 (2008)

62. S. Han *et al.*, “Ray Optics at a Deep-Subwavelength Scale: A Transformation Optics Approach”, *Nano Lett.* **8**, 4243 (2008)

63. E. J. Smith, Z. Liu, Y. F. Mei, O.G. Schmidt, “System investigation of a rolled-up metamaterial optical hyperlens structure”, *Appl. Phys. Lett.* **95**, 083104 (2009)

64. H. Changkwon, *Thin film optics*, Techmedia (2009)

65. J. Rho *et al.*, "Spherical hyperlens for two-dimensional sub-diffractional imaging at visible frequencues", *Nature Commun.*, **1**, 143 (2010)

66. J. Valentine, *et al*. "Three-dimensional optical metamaterial with a negative refractive index", *Nature* **455**, 376 (2008)

67. S. M. Mansfield, and G. S. Kino, "Solid immersion microscope",. *Appl. Phys. Lett.* **57**, 2615 (1990)

68. Z. Shi *et al.* "Slow-Light Fourier Transform Interferometer", *Phys. Rev. Lett.* **99**, 240801 (2007)

69. T. Zentgraf *et al.*, "Plasmonic Luneburg and Eaton lenses", *Nature Nanotechnol.* **6**, 151 (2011)

70. S. M. Spillane, T. J. Kippenberg, and K. J. Vahala, "Ultralow-threshold Raman laser using a spherical dielectric microcavity", *Nature* **415**, 621 (2002)

71. D. K. Armani, T. J. Kippenberg, S. M. Spillane, K. J. Vahala, "Ultra-high-*Q* toroid microcavity on a chip", *Nature* **421**, 925 (2003)

72. Y. Akahane, T. Asano, B. S. Song, & S. Noda, "High-*Q* photonic nanocavity in a two-dimensional photonic crystal", *Nature* **425**, 944 (2003)

73. K. J. Vahala, "Optical microcavities". *Nature* **424**, 839 (2003)

74. M. Soljacic, and J. D. Joannopoulos, "Enhancement of nonlinear effects using photonic crystals", *Nature Mater.* **3**, 211 (2004)

75. T. Yoshie, *et al.* "Vacuum Rabi splitting with a single quantum dot in a photonic crystal nanocavity", *Nature* **432**, 200-203 (2004)

76. T. J. Kippenberg and K. J. Vahala, "Cavity optomechanics: back-action at the mesoscale", *Science* **321**, 1172-1176 (2008)

77. J. T. Shen, P. B. Catrysse, and S. Fan, "Mechanism for designing metallic metamaterials with a high index of refraction", *Phys. Rev. Lett.* **94**, 197401 (2005)

78. J. Shin, J. T. Shen, and S. Fan, "Three-dimensional metamaterials with an ultrahigh effective refractive index over a broad bandwidth", *Phys. Rev. Lett.* **102**, 093903 (2009)

79. J. Yao *et al.*, "Three-dimensional nanometer scale optical cavities of indefinite medium" *Proc. Natl. Acad. Sci. USA.* **108**, 11327 (2011)

80. C. Manalatou, *et al.*, "Coupling of modes analysis of resonant channel add-drop filters", *IEEE J. Quantum Electron.* **35**, 1322 (1999)

81. Y. Akahane, YT. Asano, B. S. Song, S. Noda, "Fine-tuned high-Q photonic-crystal nanocavity", *Opt. Express* **13**, 1202 (2005).

82. D. Englund, I. Fushman, and J. Vuckovic, "General recipe for designing photonic crystal cavities", *Opt. Express* **13**, 5961 (2005)

83. H. A. Wheeler, "Fundamental limitations of small antennas", *Proc. IRE* **35**, 1479 (1947)

84. N. P. Kobayashi, M. S. Islam, W. Wu, P. Chaturvedi, N. X. Fang, S. Y. Wang, and R. S. Williams, "Ultrasmooth Silver Thin Films Deposited with a Germanium Nucleation Layer", *Nano Lett.* **9,** 178 (2009)

85. W. Chen, M. D. Thoreson, S. Ishii, A. V. Kildishev, and V. M. Shalaev, "Ultra-thin ultra-smooth and low-loss silver films on a germanium wetting layer", *Opt. Express* **18**, 5124-5134 (2010).

86. A. Sihvola, "Electromagnetic Mixing Formulas and Applications", *Institution of Electrical Engineers* (1999)

87. C. A. Foss, G. L. Hornyak, J. A. Stockert, and C. R. Martin, "Template synthesized nanoscopic gold particles: optical spectra and the effects of particle size and shape", *J. Phys. Chem.* **98**, 2963 (1994)

88. B. Min *et al.*, "High-Q Surface-Plasmon-Polariton Whispering-Gallery Microcavity", *Nature 457*, 455 (2009)

89. M. T. Hill, *et al.* "Lasing in metallic-coated nanocavities", *Nature Photon*. **1**, 589 (2007)

90. Y. Y. Gong and J. Vuckovic, "Design of plasmon cavities for solid-state cavity quantumelectrodynamics applications", *J. Appl. Phys. Lett.* **90**, 033113 (2007)

91. M. A. Noginov, *et. al.*, "Demonstration of a spaser-based nanolaser", *Nature* **460**, 1110 (2009)

92. S. Xiao, V. P. Drachev, A. V. Kildishev, X. Ni, U. K. Chettiar, H.-K. Yuan & V. M. Shalaev, "Lossfree and active optical negative-index metamaterials", *Nature* **466**, 735 (2010).

93. I. De Leon and P. Berini, "Amplification of long-range surface plasmons by a dipolar gain medium", *Nature Photon.* **4**, 382 (2010)

94. K. Murata *et al.* "Thermal and light control of the sol-gel phase transition in cholesterol-based organic gels. Novel helical aggregation modes as detected by circular dichroism and electron microscopic observation", *J. Am. Chem. Soc.* **116,** 6664 (1994)

95. N. Koumura, R. W. J. Zijlstra, R. A. van Delden, N. Harada and B. L. Feringa, "Light-driven monodirectional molecular rotor", *Nature* **401,** 152 (1999)

96. J. J. D. de Jong *et al.,* "Reversible optical transcription of supramolecular chirality into molecular chirality", *Science* **304,** 278 (2004)

97. K. Ikeda *et al.,* "Photo-induced chirality switching in a cobaloxime complex crystal", *J. Chem. Phys.* **122,** 141103 (2005)

98. B. L. Feringa, *Molecular Switches* (Wiley-VCH, 2001)

99. N. P. M. Huck, W. F. Jager, B. de Lange, and B. L. Feringa, "Dynamic control and amplification of molecular chirality by circular polarized light", *Science* **273,** 1686 (1996)

100. V. Simic-Milosevic, J. Meyer and K. Morgenstern, "Chirality change of chloronitrobenzene on Au(111) induced by inelastic electron tunneling", *Angew. Chem. Int. Ed.* **48,** 4061 (2009)

101. R. A. Reddy *et al.* "Field-induced switching of chirality in undulated ferroelectric and antiferroelectric SmCP phases formed by Bent-Core mesogens", *Angew. Chem. Int. Ed.* **44,** 774 (2005)

102. T. Hasegawa *et al.* "Temperature-driven switching of helical chirality of poly[(4-carboxyphenyl)acetylene] induced by a single amidine enantiomer and memory of the diastereomeric macromolecular helicity", *Macromolecules* **39,** 482 (2006)

103. S. Kucharski, R. Janik, H. Motschmann and C. Radge, "*Trans-cis* isomerisation of azobenzene amphiphiles containing a sulfonyl group", *New J. Chem.* **23,** 765 (1999)

104. R. Siewertsen *et al.* "Highly efficient reversible *Z-E* photoisomerization of a bridged azobenzene with visible light through resolved S1(nπ*) absorption Bands", *J. Am. Chem. Soc.* **131,** 15594 (2009)

105. H. Rau, "Spectroscopic properties of organic AZO-compounds", *Angew. Chem. Int. Ed. Engl.* **12,** 224 (1973)

106. A. V. Rogacheva *et al.*, "Giant gyrotropy due to electromagnetic-field coupling in a bilayered chiral structure", *Phys. Rev. Lett.* **97,** 177401 (2007)

107. S. Zhang *et al.* "Negative refractive index in chiral metamaterials", *Phys. Rev. Lett.* **102,** 023901 (2009)

108. E. Plum *et al.* "Metamaterial with negative index due to chirality", *Phys. Rev. B* **79,** 035407 (2009)

109. J. K. Gansel *et al.* "Gold helix photonic metamaterial as broadband circular polarizer", *Science* **325,** 1513 (2009)

110. N. Liu, H. Liu, S. Zhu and H. Giessen, "Stereometamaterials", *Nature Photon.* **3,** 157 (2009)

111. H. Liu *et al.* "Lagrange model for the chiral optical properties of plasmonic stereometamaterials", *Phys. Rev. B* **81,** 241403(R) (2010)

112. H. Tao *et al.* "Reconfigurable terahertz metamaterials", *Phys. Rev. Lett.* **103,** 147401 (2009)

113. I. M. Pryce, K. Aydin, Y. A. Kelaita, R. M. Briggs and H. A. Atwater, "Highly strained compliant optical metamaterials with large frequency tenability", *Nano Lett.* **10,** 4222 (2010)

114. J. Y. Ou, E. Plum, L. Jiang and N. I. Zheludev, "Reconfigurable photonic metamaterials", *Nano Lett.* **11,** 2142 (2011)

115. N. Kanda, K. Konishi and M. Kuwata-Gonokami, "Light-induced terahertz optical activity", *Opt. Lett.* **34,** 3000 (2009)

116. W. Padilla, A. Taylor, C. Highstrete, M. Lee and R. Averitt, "Dynamical electric and magnetic metamaterial response at terahertz frequencies", *Phys. Rev. Lett.* **96,** 107401 (2006)

117. H. T. Chen *et al.* "Active terahertz metamaterial devices", *Nature* **444,** 597 (2006)

118. H. T. Chen *et al.* "Experimental demonstration of frequency-agile terahertz metamaterials", *Nature Photon.* **2,** 295 (2008)

119. T. Driscoll, *et al.* "Memory metamaterials", *Science* **325,** 1518 (2009)

120. E. Hirsch, "Spin Hall effect", *Phys. Rev. Lett.* **83**, 1834 (1999)

121. S. A. Wolf *et al*., "Spintronics: A spin-based electronics vision for the future", *Science* **294**, 1488 (2001)

122. T. Jungwirth, J. Wunderlich, K. Olejník, "Spin Hall effect devices", *Nature Mater.* **11**, 382 (2012)

123. B. A. Bernevig, X. W. Yu, S. C. Zhang, "Maxwell equation for coupled spin-charge wave propagation", *Phys. Rev. Lett.* **95**, 076602 (2005)

124. M. Onoda, S. Murakami, N. Nagaosa, "Hall effect of light", *Phys. Rev. Lett.* **93**, 083901 (2004)

125. K. Y. Bliokh, Y. P. Bliokh, "Conservation of angular momentum, transverse shift, and spin Hall effect in reflection and refraction of an electromagnetic wave packet", *Phys. Rev. Lett.* **96**, 073903 (2006)

126. K. Bliokh, A. Niv, V. Kleiner, E. Hasman, "Geometrodynamics of spinning light", *Nature Photon.* **2**, 748 (2008)

127. O. Hosten, P. Kwiat, “Observation of the spin hall effect of light via weak measurements”, *Science* **319**, 787 (2008)

128. Y. Gorodetski *et al*., “Weak measurements of light chirality with a plasmonic slit”, *Phys. Rev. Lett.* **109**, 013901 (2012)

129. F. Falcone *et al*., “Babinet principle applied to the design of metasurfaces and metamaterials”, *Phys. Rev. Lett.* **93**, 197401 (2004)

130. S. L. Sun *et al*., “Gradient-index metasurfaces as a bridge linking propagating waves and surface waves”, *Nature Mater.* **11**, 426 (2012)

131. N. Yu *et al*., “Light propagation with phase discontinuities: Generalized laws of reflection and refraction”, *Science* **334** 333 (2011)

132. X. Ni, N. K. Emani, A. V. Kildishev, A. Boltasseva, V. M. Shalaev, “Broadband light bending with plasmonic nanoantennas”, *Science* **335**, 427 (2012)

133. Y. Zhao and A. Alù, “Manipulating light polarization with ultrathin plasmonic metasurfaces”, *Phys. Rev. B* **84**, 205428 (2011)

134. P. Genevet *et al*., “Ultra-thin plasmonic optical vortex plate based on phase discontinuities”, *Appl. Phys. Lett.* **100**, 013101 (2012)

135. F. Aieta *et al*., “Aberration-free ultrathin flat lenses and axicons at telecom wavelengths based on plasmonic metasurfaces”, *Nano Lett.* **12**, 4932 (2012)

136. M. A. Kats *et al*., “Giant birefringence in optical antenna arrays with widely tailorable optical anisotropy”, *Proc. Natl. Acad. Sci. U.S.A.* **109**, 12364 (2012)

137. V. S. Liberman, B. Y. Zel’dovich, “Birefringence by a smoothly inhomogeneous locally isotropic medium”, *Phys. Rev. E* **49**, 2389 (1994)

138. R. Y. Chiao, Y. S. Wu, “Manifestations of Berry’s topological phase for the photon”, *Phys. Rev. Lett.* **57**, 933 (1986)

139. M. V. Berry, “Interpreting the anholonomy of coiled light”, *Nature* **326**, 277 (1987)

140. D. R. Smith, J. J. Mock, A. F. Starr, D. Schurig, “Gradient index metamaterials”, *Phys. Rev. E* **71**, 036609 (2005)

141. O. Costa de Beauregard, C. Imbert, Y. Levy, “Observation of shifts in total reflection of a light beam by a multilayered structure”, *Phys. Rev. D* **15**, 3553 (1977)

142. K. Y. Bliokh, Y. Gorodetski, V. Kleiner, E. Hasman, “Coriolis effect in optics: unified geometric phase and spin-hall effect”, *Phys. Rev. Lett.* **101**, 030404 (2008)

143. Y. Gorodetski, A. Niv, V. Kleiner, E. Hasman, "Observation of the spin-based plasmonic effect in nanoscale structures", *Phys. Rev. Lett.* **101**, 043903 (2008)

144. R. H. Renard, "Total reflection: A new evaluation of the Goos-Hänchen shift", *J. Opt. Soc. Am.* **54**, 1190 (1964)

145. L. Li, C. W. Haggans, "Convergence of the coupled-wave method for metallic lamellar diffraction gratings", *J. Opt. Soc. Am. A* **10**, 1184 (1993)

146. X. Yin, Z. Ye, J. Rho, Y. Wang and X. Zhang, "Photonic spin hall effect at metasurfaces", *Science*, **339**, 1405 (2013)

147. H. J. Jeong *et al.*, "The future of optical lithography", *Solid State Technol.* **37**, 397 (1994)

148. S. Okazaki, "Resolution limits of optical lithography", *J. Vac. Sci. Technol. B* **9**, 2829 (1991)

149. G. Hughes, L. C. Litt, A. Wuest and S. Palaiyanur, "Mask and wafer cost of ownership (COO) from 65 to 22 nm half-pitch nodes", *Proc. SPIE* **7028** (2008)

150. International technology roadmap for semiconductors 2009 edition: Lithography, (2009)

151. J. Melngailis, "Focused ion-beam technology and applications", *J. Vac. Sci. Technol. B* **5**, 469 (1987)

152. D. Chao, A. Patel, T. Barwicz, H. I. Smith and R. Menon, "Immersion zone-platearray lithography", *J. Vac. Sci. Technol. B* **23**, 2657 (2005)

153. R. D. Piner *et al.*, "Dip-pen nanolithography", *Science* **283**, 661 (1999)

154. T. R. Groves and R. A. Kendall, "Distributed, multiple variable shaped electron beam column for high throughput maskless lithography", *J. Vac. Sci. Technol. B* **16**, 3168 (1998)

155. M. Muraki and S. Gotoh, "New concept for high-throughput multielectron beam direct write system", *J. Vac. Sci. Technol. B* **18**, 3061 (2000)

156. K. Salaita *et al.*, "Massively parallel dip-pen nanolithography with 55000-pen twodimensional arrays", *Angew. Chem. Int. Edit.* **45**, 7220 (2006)

157. P. Vettiger *et al.*, "The "Millipede" - More than one thousand tips for future AFM data storage", *IBM J. Res. Dev.* **44**, 323 (2000)

158. T. F. Scott *et al.*, "Two- Color single-photon photoinitiation and photoinhibition for subdiffraction photolithography", *Science* **324**, 913 (2009)

159. L. Li, R. R. Gattass, E. Gershgoren, H. Hwang and J. T. Fourkas, "Achieving l/20 resolution by one-color initiation and deactivation of polymerization", *Science* **324**, 910 (2009)

160. T. L. Andrew, H. Y. Tsai and R. Menon, "Confining light to deep Subwavelength dimensions to enable optical nanopatterning", *Science* **324**, 917 (2009)

161. P. Srisungsitthisunti, O. K. Ersoy and X. F. Xu, "Improving near-field confinement of a bowtie aperture using surface plasmon polaritons", *Appl. Phys. Lett.* **98**, 223106 (2011)

162. J. Tominaga, T. Nakano and N. Atoda, "An approach for recording and readout beyond the diffraction limit with an Sb thin film", *Appl. Phys. Lett.* **73**, 2078–2080 (1998)

163. H. J. Lezec *et al.*, "Beaming light from a subwavelength aperture", *Science* **297**, 820 (2002)

164. S. Vedantam *et al.*, "A plasmonic dimple lens for nanoscale focusing of light", *Nano Lett.* **9**, 3447 (2009)

165. E. Ozbay "Plasmonics: Merging photonics and electronics at nanoscale dimensions", *Science* **311**, 189 (2006)

166. W. Srituravanich *et al.*, "Flying plasmonic lens in the near field for high-speed nanolithography", *Nature Nanotechnol.* **3**, 733 (2008)

167. A. Sundaramurthy *et al.*, "Toward nanometer-scale optical photolithography: Utilizing the near-field of bowtie optical nanoantennas", *Nano Lett.* **6**, 355 (2006)

168. W. A. Challener *et al.*, "Heat-assisted magnetic recording by a near-field transducer with efficient optical energy transfer", *Nature Photon.* **3**, 220 (2009)

169. W. L. Barnes, A. Dereux and T. W. Ebbesen, "Surface plasmon subwavelength optics", *Nature* **424**, 824 (2003)

170. W. Srituravanich *et al.*, "Plasmonic nanolithography", *Nano Lett.* **4**, 1085 (2004)

171. T. Grosjean, M. Mivelle, F. I. Baida, G. W. Burr and U. C. Fischer, "Diabolo nanoantenna for enhancing and confining the magnetic optical field", *Nano Lett.* **11**, 1009 (2011)

172. N. C. Lindquist, P. Nagpal, A. Lesuffleur, D. J. Norris and S. H. Oh, "Three dimensional plasmonic nanofocusing", *Nano Lett.* **10**, 1369 (2010)

173. Y. M. Liu, T. Zentgraf, G.Bartal and X. Zhang, "Transformational plasmon optics", *Nano Lett.* **10**, 1991 (2010)

174. C. Ropers *et al.*, "Grating-coupling of surface plasmons onto metallic tips: A nanoconfined light source", *Nano Lett.* **7**, 2784 (2007)

175. T. Sondergaard *et al.*, "Resonant plasmon nanofocusing by closed tapered gaps", *Nano Lett.* **10**, 291 (2010)

176. V. S. Volkov *et al.*, "Nanofocusing with channel plasmon polaritons", *Nano Lett.* **9**, 1278 (2009)

177. N. Liu *et al.*, "Nanoantenna enhanced gas sensing in a single tailored nanofocus", *Nature Mater.* **10**, 631 (2011)

178. S. Kim *et al.*, "High-harmonic generation by resonant plasmon field enhancement", *Nature* **453**, 757 (2008)

179. A. Kinkhabwala *et al.*, "Large single-molecule fluorescence enhancements produced by a bowtie nanoantenna", *Nature Photon.* **3**, 654 (2009)

180. I. P. Radko, S. I. Bozhevolnyi, A. B. Evlyukhin and A. Boltasseva, "Surface plasmon polariton beam focusing with parabolic nanoparticle chains", *Opt. Express* **15**, 6576 (2007)

181. S. I. Bozhevolnyi and K. V. Nerkararyan, "Adiabatic nanofocusing of channel plasmon polaritons", *Opt. Lett.* **35**, 541 (2010)

182. A. R. Davoyan *et al.*, "Nonlinear Nanofocusing in Tapered Plasmonic Waveguides", *Phys. Rev. Lett.* **105**, 116804 (2010)

183. Y. Wang, W. Srituravanich, C. Sun and X. Zhang, "Plasmonic nearfield scanning probe with high transmission", *Nano Lett.* **8**, 3041 (2008)

184. J. N. Anker *et al.*, "Biosensing with plasmonic nanosensors", *Nature Mater.* **7**, 442 (2008)

185. J. A. Dionne *et al.*, "Plasmon slot waveguides: Towards chip-scale propagation with subwavelength-scale localization", *Phys. Rev. B* **73**, 035407 (2006)

186. R. F. Oulton *et al.*, "A hybrid plasmonic waveguide for subwavelength confinement and long-range propagation", *Nature Photon.* **2**, 496 (2008)

187. S. A. Maier *et al.*, "Local detection of electromagnetic energy transport below the diffraction limit in metal nanoparticle plasmon waveguides", *Nature Mater.* **2**, 229 (2003)

188. K. Tanaka and M. Tanaka, "Simulations of nanometric optical circuits based on surface plasmon polariton gap waveguide", *Appl. Phys. Lett.* **82**, 1158 (2003)

189. M. I. Stockman, "Nanofocusing of optical energy in tapered plasmonic waveguides", *Phys. Rev. Lett.* **93**, 137404 (2004)

190. A. Aubry *et al.*, "Plasmonic Light-Harvesting Devices over the Whole Visible Spectrum", *Nano Lett.* **10**, 2574 (2010)

191. E. Verhagen, L. Kuipers and A. Polman, "Plasmonic Nanofocusing in a Dielectric Wedge", *Nano Lett.* **10**, 3665 (2010)

192. D. K. Gramotnev and K. C. Vernon, "Adiabatic nano-focusing of plasmons by sharp metallic wedges", *Appl. Phys. B-Lasers Opt.* **86**, 7 (2007)

193. C. Genet and T. W. Ebbesen, "Light in tiny holes", *Nature* **445**, 39 (2007)

194. H. A. Bethe, "Theory of Diffraction by Small Holes", *Phys. Rev.* **66**, 163 (1944)

195. F. Chen *et al.*, "Imaging of optical field confinement in ridge waveguides fabricated on very-small-aperture laser", *Appl. Phys. Lett*. **83**, 3245 (2003)

196. J. A. Matteo *et al.*, "Spectral analysis of strongly enhanced visible light transmission through single C-shaped nanoapertures", *Appl. Phys. Lett.* **85**, 648 (2004)

197. Z. Rao, L. Hesselink and J. S. Harris, "High transmission through ridge nanoapertures on vertical-cavity surface-emitting lasers", *Opt. Express* **15**, 10427 (2007)

198. L. Wang *et al.*, "Nanolithography using high transmission nanoscale bowtie apertures", *Nano Lett.* **6**, 361 (2006)

199. T. Sakai *et al.*, "Thermal direct mastering using deep UV laser", *Jpn. J. Appl. Phys. Part 1 - Regul. Pap. Brief Commun. Rev. Pap.* **45**, 1407 (2006)

200. E. Ito *et al.*, "TeOx-based film for heat-mode inorganic photoresist mastering", *Jpn. J. Appl. Phys. Part 1 - Regul. Pap. Short Notes Rev. Pap.* **44**, 3574 (2005)

201. J. Y. Juang *et al.*, "Design and dynamics of flying height control slider with piezoelectric nanoactuator in hard disk drives", *J. Tribol.-Trans. ASME* **129**, 161 (2007)

202. L. Pan and D. B. Bogy, "Heat-assisted magnetic recording", *Nature Photon.* **3**, 186 (2009)

203. W. Hu *et al.*, "High-resolution electron beam lithography and DNA nano-patterning for molecular QCA", *IEEE Trans. Nanotechnol.* **4**, 312 (2005)

204. N. Liu *et al.*, "Three-dimensional photonic metamaterials at optical frequencies", *Nature Mater*. **7**, 31 (2008)

205. N. Liu *et al.*, "Three dimensional plasmon rulers", *Science* **332**, 1407 (2011)

206. B. Kante *et al.*, "Symmetry breaking and optical negative index of closed nanorings", *Nature Commun.* **3**, 1180 (2012)

207. A. Curto *et al.*, "Unidirectional emission of a quantum dot coupled to a nanoantenna", *Science* **329**, 930 (2010)

208. L. Novotny and N. van Hulst, "Antennas for light", *Nature Photon.* **5**, 83 (2011)